UNIVERSITY OF LONDON THESIS

Degree PhD Year 2008 Name of Author BURANAWATANACHOKE, BOONJONG

BIOPROCESS ANALYSIS USING COMPUTATIONAL FLUID DYNAMICS AND ULTRA SCALE-DOWN

Boonjong Buranawatanachoke

This thesis is submitted to the University of London for the degree of Doctor of Philosophy in Biochemical Engineering

The Advanced Centre for Biochemical Engineering
Department of Biochemical Engineering
University College London
Torrington Place
London WC1E 7JE

ProQuest LLC
789 East Eisenhower Parkway
P.O. Box 1346
Ann Arbor, MI 48106-1346

Abstract

The primary aim of this study is to develop the means to predict mechanisms and rates of material damage and especially the size of particles making up cell suspensions. Computational fluid dynamics (CFD) is employed to define experimental conditions used in ultra scale-down (USD) techniques and relate these to large-scale operations. The validity of this novel scaling methodology as applied to a large-scale membrane filtration unit and disc-stack centrifuge has been investigated.

The current state of the art predicts performance of bioprocess operation but not of material damage itself. For the membrane operation, emphasis has been given mainly to flux rate and fouling, and clarification and dewatering are key parameters during centrifugation. Conversely, the effects of hydrodynamic parameters during the operation on the process material, e.g. shear damage, have not been paid much attention. Though CFD has been currently employed to facilitate predictions of the performance of these operations by a number of research groups, the technique alone cannot provide accurate predictions for a given biomaterial. CFD data thus needs to be integrated with experimental data given by other techniques, e.g. scale-down mimics of process equipment, USD device and etc.

This study uses CFD and USD techniques to predict this damage. Following preliminary analysis of fluid stresses, the pump has been identified as the key component of the membrane rig responsible for material damage. CFD was then employed to determine the magnitude of maximum energy dissipation rate (EDR) and provide equivalent rotational speeds of the rotating disc device, or USD device, capable of generating the same engineering conditions. The USD experiment was then carried out following recommended speeds given by CFD and experimental data together with proposed mathematical models was used to predict particle characteristics in terms of size reduction. A verification process was finally performed using full-scale experiments. It was found that CFD could provide essentially similar operating conditions for USD experiments mimicking a large-scale operation, especially for operations of a few hours.

An initial investigation has also been carried out on the applicability of the CFD-USD technology to predict material damage in the discharge part of the solid-ejecting disc-stack centrifuge. The analysis shows that CFD suffered from difficulties in defining details of the problem domain in order to assess flow fields. Moreover, the exposure to gas phase during the discharge and subsequent droplet formation and an unpredictable shape of slurry made it impossible to investigate this problem further using CFD. As a result, it is concluded that this problem should be addressed by other means.

Based on findings of this investigation, prediction guidelines are proposed to facilitate the design process and process development by using a small USD device to assess the engineering environment in a large unit operation. More importantly, the concept may theoretically lay the foundation for scaling any unit operation based on key engineering parameters of the system.

Acknowledgements

First of all I would like to say a very special thank you to my supervisor, Professor Mike Hoare, for his kind and continuous support, without whom this thesis would have been less than complete.

I would also like to thank my advisor, Professor Nigel Titchener-Hooker, for all his support throughout my study at UCL from MSc to PhD and on helping me obtain Chevening Technology Enterprise Scholarship (CTES) to explore the business opportunities in scientific research.

Special thanks to Professor Parviz Shamlou who inspired me to pursue the PhD study and helped me obtain the PhD funding which is provided by the Overseas Research Students (ORS), Innovative Manufacturing Research Centre (IMRC) for Bioprocessing and Departmental scholarships.

I would like to acknowledge help and collaboration from Dr Hu Zhang, Dr Gerard Chan and other PhD students throughout my study in the Department.

I would also like to thank you Martyn Vale and the rest of the people in the Electronics Workshop who always helped me when something went wrong with my computer and software.

To other friends, e.g. Abi, Meng, Pui, P'Aom and etc., without whom living in the UK would be less fun and exciting.

Lastly, my parents who always give me supports from faraway land.

Table of Contents

List of Figures

List of Tables

List of Abbreviations

ASM	algebraic stress model
CC	cell centered
CFD	computational fluid dynamics
CHO	Chinese hamster ovary
CPU	central processing unit
CSTR	continuous stirred tank reactor
CV	control volume
DNA	deoxyribonucleic acid
EDR	energy dissipation rate
FBS	fetal bovine serum
HIC	hydrophobic interaction chromatography
HIV	human immunodeficiency virus
HPLC	high performance liquid chromatography
ICS	impeller collision severity
ISF	integrated shear factor
LDA	laser Doppler anemometer
MMD	mass median diameter
PDE	partial differential equation
PEG	polyethylene glycol
PFR	plug flow reactor
PVA	polyvinyl alcohol
RAM	random-access memory
rpm	revolution per minute
RSM	Reynolds stress model
TCS	turbulent collision severity
USD	ultra scale-down
VSEP	vibratory shear-enhanced processing system

Nomenclature

ΔH	pressure drop (meters of liquid column),	[m]
ΔP	frictional pressure drop over a small length of tubular-shaped bioreactors or transmembrane pressure,	[N m^{-2}]
Δt	small interval of time,	[s]
a	strain rate parameter,	[s^{-1}]
a	fluid acceleration,	[m s^{-2}]
A	surface area of a control volume in transport equations,	[m^2]
A_0	equation constant,	[s^{-1}]
A_m	membrane area,	[m^2]
A_t	cross section of the tank,	[m^2]
b	equation constant,	[-]
B	equation constant,	[kg W^{-1}]
c	equation constant,	[m W^b kg^{-b}]
C	overall dimensionless shape factor,	[-]
C_b	bulk concentration of particles,	[kg m^{-3}]
C_v	specific heat capacity for a constant volume process,	[m^2 s^{-2} K^{-1}]
d	diameter of spherical cell,	[m]
D	pipe diameter,	[m]
D_{10}	size of particle below which 10% by volume of the sample lies,	[μm]
D_{50}	size of particle below which 50% by volume of the sample lies,	[μm]
D_{90}	size of particle below which 90% by volume of the sample lies,	[μm]
Df_0	final value of any derived diameter under zero maximum EDR,	[μm]
Df_x	final value of any derived diameter,	[μm]
D_{im}	impeller diameter,	[m]
Di_x	initial value of any derived diameter,	[μm]
d_l	lower limit of the size band,	[μm]

d_L	diameter related to the probe position,	[m]
D_{mc}	hydraulic diameter of the tube,	[m]
d_p	particle diameter,	[m]
d_u	upper limit of the size band,	[μm]
D_x	intermediate value of any derived diameter,	[μm]
E	specific energy of a fluid,	[m^2 kg s^{-2}]
f	Fanning friction factor,	[-]
$\bar{f}_{app}$	mean apparent friction factor,	[-]
F	forces acting on a fluid particle,	[N]
g	gravitational force,	[m s^{-2}]
h	specific enthalpy of a fluid,	[J kg^{-1}]
h_0	specific total enthalpy of a fluid,	[J kg^{-1}]
h_{mc}	height of the membrane channel,	[m]
i	internal (thermal) energy,	[m^2 kg s^{-2}]
J	permeate flux,	[L m^{-2} s^{-1}]
k	heat conductivity,	[kg m s^{-3} K^{-1}]
k	total kinetic energy per unit mass at any position,	[m^2 s^{-2}]
k	turbulent kinetic energy,	[J]
K	experimentally-obtained constant for specific impeller designs,	[-]
k_1	constant of proportionality,	[-]
k_2	constant of proportionality,	[-]
k_{DS}	first order rate constant of the reduction process of derived diameters in the system,	[s^{-1}]
k_{DU}	first order rate constant of the reduction process of derived diameters in the USD system,	[s^{-1}]
k_{LP}	first order rate constant for the reduction of total volume fraction of large aggregates in the pumping system,	[-]
k_{LU}	first order rate constant for the reduction of total volume fraction of large aggregates in the USD system,	[-]
k_{MO}	constant used to calculated average shear rate,	[-]
K_v	pressure drop or loss coefficient,	[-]

L	total volume fraction of large aggregates after the process is run for a specific time,	[%]
L_0	total volume fraction of large aggregates at the start of the operation,	[%]
L_{ent}	length of tubular-shaped bioreactors at the entrance region until the flow is fully developed,	[m]
L_{in}	total volume fraction of large aggregates going into the high energy-dissipation region,	[%]
L_{min}	final value of volume fraction of large aggregates under specific shear environment,	[%]
L_{out}	total volume fraction of large aggregates going out of the high energy-dissipation region,	[%]
L_p	length of tubular-shaped bioreactors,	[m]
m	fluid mass,	[kg]
$\mathbf{n}$	outward pointing unit normal field of the control volume's boundary,	[-]
N	number of passes of particles in the system through the high energy dissipation area,	[-]
N	rotation rate,	[s^{-1}]
N_0	material quantity at time zero,	[-]
N_D	material quantity,	[-]
N_{Fr}	Froude number,	[-]
N_{im}	impeller speed,	[rev s^{-1}]
N_p	power number,	[-]
N_Q	flow or pumping number,	[-]
N_t	material quantity at time t,	[-]
p	pressure or a normal stress,	[N m^{-2}]
P_1	upstream pressure,	[Pa]
P_2	downstream pressure,	[Pa]
P_i	power input through the impeller or stirrer,	[W]
Q	volumetric flow rate,	[m^3 s^{-1}]
Q_i	volumetric flow rate from the impeller,	[m^3 s^{-1}]
Q_p	flow rate through the pump which is the high energy-dissipation device in the membrane system,	[m^3 s^{-1}]

Q_s	flow rate through the tip of the rotating disc in the shear device,	$[m^3\ s^{-1}]$
r	radius,	[cm]
R	dimensionless radius,	[-]
R	gas constant for ideal gas (8.314 J mol^{-1} K^{-1}]),	[J mol^{-1} K^{-1}]
r_0	arbitrary starting point for the cell's position at time zero,	[m]
R_c	resistance due to cake deposited on the membrane,	$[m^{-1}]$
Re_i	impeller Reynolds number,	[-]
Re_L	local Reynolds number,	[-]
R_f	resistance due to irreversible adsorption and pore plugging,	$[m^{-1}]$
R_m	resistance due to membrane itself,	$[m^{-1}]$
R_t	resistance of the total barrier between filtrate side and retentate side during membrane filtration operation,	$[m^{-1}]$
S_ϕ	source or sink term that either creates or destroys ϕ,	[-]
S_E	source or sink term that either creates or destroys ϕ,	[-]
s_{ii}	shearing component of linear deformation rate acting in the *i*-direction on a surface normal to the *i*-direction,	$[s^{-1}]$
s_{ij}	shearing component of linear deformation rate acting in the *j*-direction on a surface normal to the *i*-direction,	$[s^{-1}]$
S_M	source or sink term that either creates or destroys ϕ,	[-]
t	operating time or shearing time,	[s]
t	residence time,	[s]
$\bar{t}$	mean residence time,	[s]
T	temperature,	[K]
T_i	turbulence intensity,	[-]
t_p	processing time in the membrane system,	[s]
t_s	processing time in the shear device,	[s]
u	velocity field,	[-]
u	average fluid velocity,	$[m\ s^{-1}]$
u	velocity in the x Cartesian co-ordinate,	$[m\ s^{-1}]$
u_{max}	maximum fluid velocity,	$[m\ s^{-1}]$
U_{ref}	reference mean flow velocity,	$[m\ s^{-1}]$

u_s	superficial linear velocity,	[m s^{-1}]
v	velocity in the y Cartesian co-ordinate,	[m s^{-1}]
V	volume of the stirred bioreactor,	[m^3]
V	volume of 3D space in transport equations,	[m^3]
V_{cp}	cumulative permeate volume,	[m^3]
V_h	volume of fluid mass around the impeller,	[m^3]
v_{mc}	tangential velocity inside the membrane channel,	[m s^{-1}]
V_p	volume of liquid suspension in the membrane system,	[m^3]
V_s	volume of liquid suspension in the shear device,	[m^3]
w	velocity in the z Cartesian co-ordinate,	[m s^{-1}]
W	washout function,	[-]
y_0	Y offset or constant,	[s^{-1}]

Greek symbols

$\overline{\varphi'}$	mean of the fluctuating component φ' of turbulence,	[-]
$\overline{\varphi'\psi'}$	second moment of the flow properties φ and ψ,	[-]
$\overline{(\varphi')^2}$	variance of the fluctuating component φ' of turbulence,	[-]
$\overline{(\varphi')^3}$	third moment of the fluctuating component φ' of turbulence,	[-]
$\overline{(\varphi')^4}$	fourth moment of the fluctuating component φ' of turbulence,	[-]
ϕ	flow variable,	[-]
λ	Kolmogorov scale of mixing,	[m]
λ	second viscosity in Navier-Stokes equations,	[kg m^{-1} s^{-1}]
ν	kinematic viscosity,	[m^2 s^{-1}]
ε	the rate of dissipation of turbulent kinetic energy per unit mass,	[W kg^{-1}]
τ	shear stress,	[kg m^{-1} s^{-2}]
ρ	fluid density,	[kg m^{-3}]
μ	dynamic viscosity,	[kg m^{-1} s^{-1}]
μ	first viscosity in Navier-Stokes equations,	[kg m^{-1} s^{-1}]

η	viscosity of filtrate,	[N s m^{-2}]
γ	average shear rate,	[s^{-1}]
γ_{max}	maximum shear rate,	[s^{-1}]
θ	rotational coordinate,	[rad]
α	specific cake resistance,	[m kg^{-1}]
π	constant with a value of 3.14159,	[-]
Γ	diffusion coefficient or diffusivity,	[m^2 s^{-1}]
Φ	steady mean-value component of turbulence,	[-]
φ	flow property,	[-]
ψ	flow property,	[-]
φ'	statistical time-dependent fluctuating component of turbulence,	[-]
ω_0	verticity parameter,	[s^{-1}]
μ_a	apparent viscosity,	[kg m^{-1} s^{-1}]
γ	local shear rate,	[s^{-1}]
γ_{av}	average shear rate,	[s^{-1}]
ε_c	porosity of cake layer,	[-]
λ_D	decay constant,	[s^{-1}]
ε_i	energy dissipation rate calculated from fluid volume around the impeller,	[W kg^{-1}]
τ_{ij}	viscous stress acting in the *j*-direction on a surface normal to the *i*-direction,	[N m^{-2}]
τ_m	mean shear stress,	[kg m^{-1} s^{-2}]
ε_{max}	maximum energy dissipation rate,	[W kg^{-1}]
τ_{max}	maximum shear stress,	[kg m^{-1} s^{-2}]
φ_{rms}	root mean square of the fluctuating component φ' of turbulence,	[-]
ρ_s	particle density,	[kg m^{-3}]
τ_w	wall shear stress,	[kg m^{-1} s^{-2}]

CHAPTER 1 INTRODUCTION

The ability to predict shear damage and its subsequent effects during the process development of new biopharmaceuticals has been a challenge for biochemical and process engineers for decades. The novel approach based on both computational fluid dynamics (CFD) and ultra scale-down (USD) techniques has been proposed to assess material damage using a small-scale device and forms the basis of this thesis. In this chapter several issues related to bioprocess development and key elements leading to material damage are introduced. The first section describes the process development cycle for biopharmaceuticals and the challenges biochemical and process engineers are facing. Several aspects of hydrodynamic shear are then presented in terms of its mechanism and effect on biomaterials throughput the whole process environment in section 1.2. The applications of USD and CFD techniques are then described in section 1.3 and 1.4, respectively. Lastly, the overall organisation and aims of the thesis are provided in section 1.5.

1.1 Challenges for new bioprocess design and development

Following the advanced development of both genetic engineering and hybridoma technologies and an increasing understanding of human genome and molecular principles underlining health and disease, more biopharmaceuticals are being discovered year after year. Since most biopharmaceuticals are complex molecules, their direct chemical synthesis is economically unattractive and often 'impossible'. Direct extraction from natural sources may be one solution but only provided their quantities are high enough for medical use. However, this is often not the case. Moreover, there is a problem of accidental transmission of disease when dealing with the direct extraction from natural sources. For instance, human blood may carry with it HIV and other blood borne viruses. With the implementation of genetic engineering and hybridoma technologies, which were developed in the 1970s, the above problems were largely eliminated and the means were created of allowing the large-scale

production of protein-based and monoclonal antibody-based biopharmaceuticals in cells. The increased understanding of the 30000-gene human genome and molecular mechanisms within human body has moved the drug discovery and biomedical research from genomics towards proteomics allowing more precise targeting of human proteins. All of these factors have contributed to the proliferation of drug candidates and subsequent potential for medical use.

With the increased life expectancy of people and biopharmaceutical companies' desires to shorten time to the market and reduce the overall cost during the drug discovery process, there arises the need to identify a novel approach to process design, i.e. the establishment of the sequence of chemical or physical operations; the operating conditions; the duties, major specifications, and materials of construction of all process equipment; the general arrangement of equipment needed to ensure proper functioning of the plant; line sizes and principal instrumentation (Walas, 1990). There is a demand for new drugs to become available as soon as possible. Biopharmaceutical companies want to serve people's needs and at the same time maximise their recovery of development costs by both reducing production costs and increasing their revenues through shorter time to market. The time to market is important as this governs the phase where manufacturing is occurring during the period of patent exclusivity. One solution is to establish the process at the earlier stage of drug discovery while using only the small quantities of these high-value biopharmaceuticals available during the early stage of process development. This may be possible through a novel process design and development approach using twin technologies of USD and CFD. The vast majority of biopharmaceutical products currently on the market are produced by recombinant DNA technology in either *E. coli* or Chinese Hamster Ovary (CHO) cell lines (Walsh, 1998). Even the former can be sensitive to shear in certain applications while the latter is often regarded as highly shear-sensitive. Hence the ability to characterize fluid flow fields and their subsequent effects in bioprocesses by using small quantities of materials based on these technologies in order to predict process outcomes before performing pilot-scale trials should be beneficial to process development. Moreover, this novel approach should facilitate the regulatory approval process by allowing the expensive and time consuming large-scale trials to focus on demonstrating process reproducibility rather than process development.

1.2 Hydrodynamic shear in bioprocesses

Biological materials are often classified as being shear-sensitive and hence subject to damage in flow fields and mechanical forces generated in the unit operations employed in a manufacturing process. The nature and extent of damage can vary considerably and it is important to be able to predict this if pilot and large-scale trials are to be accelerated to help speed process development.

1.2.1 The processing environment

After bioprocess development has been successful, recombinant cells are cultured in an industrial-scale bioreactor where they are subjected to a number of physical stresses from impellers, baffles, air bubbles and even at the walls of tanks, pipes, etc. Following the fermentation process, the downstream processing may involve the following processes: microfiltration, centrifugation, flotation, solvent extraction, cell disruption (mechanical, thermal or chemical) if product is intracellular, precipitation, aqueous two-phase partitioning, chromatography and formulation. Materials are subjected to damage from harsh flow fields through these processes (Figure 1.1). The following sections provide general ideas on the fluid mixing and stresses on cells and their products.

1.2.1.1 Fermentation and cell culture

Cell culture in a well-mixed fermenter is usually carried out in either batch or fed-batch mode, where intermittent or continuous feeding of nutrients is used to supplement the reactor contents and provides good control over substrate concentration. Both operational modes impose stresses on cells through impeller movement, shear on wall and baffles as well as air bubble introduction, though the latter also entails the effects of air-liquid interaction.

In all fermenters, it is necessary to have two elements driving the mixing of fluids. The first element is an overall bulk or convective fluid flow so that stagnant regions do not exist within fermenters. The second element is a high-stress mixing region that is capable of promoting homogeneities in the system. It is this region where material damage often occurs. The movement of impellers whose tips dissipate maximum

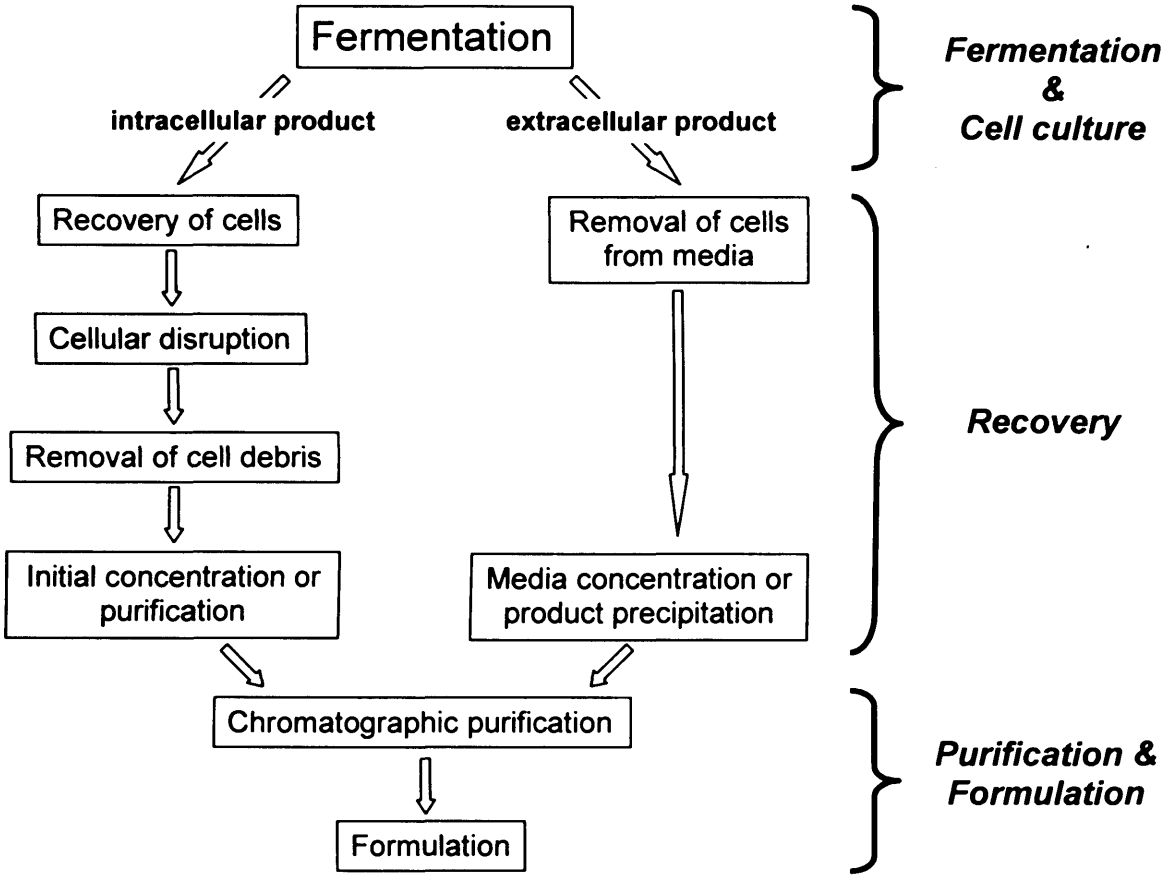

Figure 1.1 Overview of a generalised manufacturing process of biopharmaceutical products.

energy in the system generally forms the latter. Though the energy dissipation close to the impeller is generally 10 to 100 times higher than the average tank energy dissipation, typical values of energy dissipation in fermenters, or stirred tanks, are rather low compared to other unit operations in the whole process. The average values range from only about 0.2 W kg^{-1} for blending low viscosity liquids, to 4 W kg^{-1} for blending pastes and dough (Harnby et al., 1997). The ratio of 40 between average and maximum values is reported for Rushton turbines (Yim and Shamlou, 2000). As may be guessed the minimum value of energy dissipation lies in the fermenter extremities.

1.2.1.2 Recovery

Following the fermentation process, the media contains cells and the protein-based or nucleic acid-based product of interest, which may be located inside cells, in the extracellular medium or in the periplasmic compartment of the cells. Desired products, which can include the cells themselves, are then purified in order to remove virtually all contaminants from the product stream. Such contaminants may include microorganisms, DNA, pyrogens, viral particles and other non-product proteins. This purification process is carried out through a series of steps in downstream processing and is started in the primary recovery stage the objective of which is usually just one function, e.g. removal of waste solids to give a clarified broth or removal of waste liquor to give a concentrated solid phase.

Primary recovery or harvesting is a separation stage that has a dominant role in the biochemical process industries as it determines the characteristics of subsequent downstream processes. There are several techniques used in industry to recover biomass and/or extracellular protein products from the fermentation process, e.g. centrifugation and filtration and tangential-flow membrane filtration (Axelsson, 1985, Gabler, 1985, Lee, 1989). There are a number of centrifuge configurations including multichamber, tubular bowl, decanter and disk stack. For tangential-flow membrane filtration the most common formats used are flat plate, spiral wound and hollow fibre. Because each technique has its own advantages and disadvantages, combinations are sometimes used in order to achieve best results in clarifying feedstocks, e.g. centrifugation or filtration followed by absolute filtration. However, it is recommended that several factors need to be considered when making a final decision on a harvesting

approach, as each differs in terms of process development time required, capital cost, consumable cost, ease of scalability and process robustness (Wang et al., 2006). However, one of the major concerns that are found in these techniques is the material damage as a result of shear stresses.

Damage of materials due to shear stresses in the centrifuge has been of concern for decades. The primary damage location is at the inlet of industrial-scale unit where materials are subjected to an instantaneous change of directions due to the rotation of the device (Boychyn et al., 2001). Work on this part of the centrifuge has already been done at UCL (Boychyn et al., 2001, Boychyn et al., 2004, Mannweiler and Hoare, 1992). There is also evidence showing the damage during centrifuge discharge (Chan et al., 2006, Gray et al., 1972). This is believed to be the result of either shear stress generated within the discharge part itself when the discharge slot opens and the solid comes out, or the impaction of solids leaving the discharge exit onto the wall of the collection chamber or both. The latter is directed towards speeds of the sediment discharges that leave the discharge exit and hit the wall, which are estimated to be around 100 m s^{-1} (Chan et al., 2006), i.e. conditions similar to those which exist in homogenisers designed for cell disruption (Keshavarz-Moore et al., 1990).

Why is shear stress generated during centrifugation important? Valuable products, which are either extracellular or intracellular or both, are affected and damaged by shear stresses. Extracellular products are subjected to shear stresses directly and can be damaged during acceleration in the feed zone. For intracellular products, a number of cells leak as a result of shear stress leading to product loss or more complicated downstream processes. Recycling process materials through the centrifuge may also lead to additional losses and a reduction in centrifuge performance as a result of smaller particle size. Moreover, shear stress should be kept at minimum because cells must be fully intact to avoid product loss during a wash stage and the products within damaged cells will probably degrade quicker than within fully intact cells, for example due to enzyme degradation, making downstream processing more difficult.

Membrane filtration has been employed in the bioprocess industries for a wide range of applications, especially removal of cell debris, cell harvesting and protein concentration. From the literature concerning the modelling of tangential-flow

filtration it is evident that the shear stress in the rig is one of the most important operating parameters (Kim et al., 2001, Ahmad et al., 2005, Thomassen et al., 2005, Ren et al., 2002, Vasan et al., 2002). Shear stress not only damages the product of interest but also makes the membrane foul more rapidly lowering process performance, i.e. products and intracellular components are released and broken down into smaller entities which will foul the membranes. Like the centrifuge, a biomaterial being processed inside each component in the membrane rig, including the feed tank (Cherry and Papoutsakis, 1986), membrane module (Tarabara and Wiesner, 2003), valves (Vandanjon et al., 1999), pump (Kim et al., 2001) and pipework (Naili and Thiriet, 2005), is subjected to shear stress that can subsequently cause material damage. In the membrane rig the material is subject to multiple passes through a recycle loop which will include a pump, valves and the membrane itself where damage may occur (Schutte and Kula, 1990, Vandanjon et al., 1999, Save et al., 1994, Kim et al., 2001).

1.2.1.3 Purification and formulation

After products are collected from a crude sample, the purification process begins. Processes of purification are highly selective and separate the product from impurities with similar properties. Unit operations involved initially are microfiltration or ultrafiltration as a preparation stage, fractional precipitation by adding inorganic salts or organic solvents, or flocculation of certain feed components such as lipids, nucleic acids and colloidal materials. These steps are required to remove broad classes of impurity species (Ersson et al., 1989). Microfiltration allows the protein of interest to go through the membrane while retaining larger species for removal. Ultrafiltration, which lets small peptides and salts pass through the membrane and retains proteins, is employed to remove contaminating species of lower molecular size than the protein of interest. As mentioned, damage of materials during membrane operations may occur within all components of the membrane filtration rig, especially the pump. For instance, to remove large molecular weight molecules from cells, damage may occur in the flow recycle loop. Utilising the difference in protein solubility behaviour in precipitation may damage materials through adding salts and/or solvents. Like precipitation technique, reducing the amount of contaminating soluble components through selective flocculation of certain feed components also causes material damage via mixing.

Chromatography, a high-resolution technique, is employed in this step to attain acceptable protein purification levels. A number of chromatography types exist including ion-exchange chromatography, high performance liquid chromatography (HPLC), affinity chromatography, hydrophobic interaction chromatography (HIC) and membrane chromatography. The damage occurs physically through the movement of material via a high-pressure regime and by chemical means through the addition and mixing of materials with buffers.

Formulation is the last step before the product is formulated to its final form. The process is conducted to stabilise the product and preserve its activity to a maximum level. One configuration of the formulation rig may look like membrane filtration rig having a tank, valve, pump, pipework and membrane module. As a result, like the membrane rig, material damage potentially may occur in all components, especially the pump.

1.2.2 Flow stresses acting on freely suspended biomaterials

For several decades researchers have attempted to devise models explaining the effects of a specific prevailing flow condition on suspended materials. In most cases these effects are influenced by a range of flow stresses, which can arise from:

- impacts between particles and between particles and surfaces; the kinetic energy of these particles is imparted from the moving fluid whose regime is frequently assumed to be turbulent;
- laminar elongation and shear stresses caused by local velocity gradients in well-defined flow fields or at solid inserts (boundaries);
- turbulent elongation and shear stresses caused by local turbulent flow fields;
- interactions between particles and interfaces (liquid-liquid, gas-liquid, or liquid-solid).

Because turbulent conditions usually predominate in a majority of typical operations involving bioprocess equipment, turbulent conditions are more relevant to this study, and only turbulent stresses will be treated in this section.

1.2.2.1 Isotropic turbulence

The turbulent flow condition in the liquid medium is responsible for flow stresses affecting biomaterials through particle impacts and both turbulent shear and elongation stresses. When the turbulence is assumed to be homogeneous and isotropic, the nature of flow condition in the system can be analysed using the Kolmogorov's theory of turbulence. Its basic principle lies in the characteristic dimension of the smallest eddies or so-called Kolmogorov scale of mixing (λ) which is given by:

$$\lambda = \left(\frac{\nu^3}{\varepsilon}\right)^{1/4} \qquad \textbf{Eq. 1.1}$$

where ν is the fluid's kinematic viscosity and ε is the local energy dissipation rate. The theory suggests that the eddy motion in the inertial subrange of the turbulent energy band gives rise to shear forces acting on particles which are larger than Kolmogorov scale of mixing. Normal or elongational stress is thought to be the product of these forces. For those particles having the same or smaller size compared to Kolmogorov scale of mixing, flow forces are believed to originate from eddies in the viscous dissipation subrange.

The Kolmogorov's theory of turbulence allows the analysis of the flow stresses to be made and indicates that the impact forces between particles and between particles and surfaces are trivial, i.e. due to the relatively small size and similar density to that of liquid medium of most biomaterials. These impact forces, however, may become critical when considering microcarriers, e.g. for anchorage-dependent cells. In turbulent conditions, the effects on freely suspended biomaterials are either due to elongational or shear stresses. A number of models have been devised explaining the interactions between suspended biomaterials and turbulent eddies in terms of operating parameters, turbulent flow stresses and properties of biomaterials. Though there are differences in the proportionality constant, most models give the same relationship between mentioned parameters. The following shows the relationships of these parameters in terms of the mean stress in the inertial (Equation 1.2) and viscous (Equation 1.3) dissipation subrange (Shamlou, 1993):

$$\tau_m = 1.88\,\rho\,(\varepsilon d)^{2/3} \qquad \textbf{Eq. 1.2}$$

$$\tau_m = \left[\frac{2\,\mu\,\varepsilon}{15\,\nu}\right]^{1/2} = \left[\frac{2\,\rho\,\varepsilon}{15}\right]^{1/2} \qquad \textbf{Eq. 1.3}$$

where τ_m is the mean stress, μ is the dynamic viscosity of fluid, ρ is the fluid density and d is the diameter of spherical cell.

Another approach to determine flow effects on freely suspended biomaterials has been proposed based on analysing cell surface shear stress distribution and fluid shear rate (Cherry and Kwon, 1990). For suspensions having turbulent flow conditions, small biomaterials can move in and out of turbulent eddies whose configuration are assumed to be a long rotating cylinder. Materials will be subjected to a distribution of stresses when they are inside. Using above mentioned parameters and assuming that flow stresses inside turbulent eddies cause the disruption of biomaterials whose sizes are smaller than Kolmogorov scale of mixing, the group has explained the interactions between suspended biomaterials and turbulent flow fields. Their proposed expressions for fluid shear rate (γ) and cell surface shear stress (τ) whose properties depend on the position on the cell surface and time are given by:

$$\gamma = \omega_0\left[\frac{-1}{R} + \left(\frac{1}{R} + 1\right)\exp(-R)\right] \qquad \textbf{Eq. 1.4}$$

$$\tau = \frac{5}{2}\,\mu\,\gamma\,\sin\theta\left[1 - \sin^2(\gamma t)\sin^2\theta\right]^{1/2} \qquad \textbf{Eq. 1.5}$$

where

$$R = \left[\frac{a r^2}{4\nu}\right];\; a = 0.18\,(\varepsilon/\nu)^{1/2};\; \omega_0 = 7.14\,(\varepsilon/\nu)^{1/2};\; r = r_0\,\exp\left(-\frac{a t}{2}\right) \qquad \textbf{Eq. 1.6}$$

where R is the dimensionless radius, a is the strain rate parameter, ω_0 is the verticity parameter, r_0 is an arbitrary starting point for the cell's position at time zero and θ is

the rotational coordinate. At the equator of the rotating sphere where $\theta = 90°$ shear stress reaches its maximum distribution and Equation 1.5 becomes:

$$\tau = \frac{5}{2}\mu\gamma\left|\cos(\gamma t)\right| \qquad \textbf{Eq. 1.7}$$

The theory suggests that the maximum shear rate occurs at $R = 1.793$. Thus, maximum value of shear rate can be obtained by substituting this figure into Equation 1.4. By using the maximum shear rate value together with the maximum value of cosine in Equation 1.7, the maximum shear stress can be obtained:

$$\tau_{max} = 5.33\,\rho(\varepsilon\nu)^{1/2} \qquad \textbf{Eq. 1.8}$$

1.2.2.2 Turbulent flow stresses in process equipment

Practically, the energy being dissipated inside bioprocess equipment is not constant with time or position; this is in contrast to the assumptions for the above equations which assume homogenous and constant energy dissipation rate. Thus, in most cases it is necessary to have specific treatments to determine this prime parameter for each system.

Stirred bioreactors

These have been extensively studied for decades in order to elucidate the interactions between equipment configuration, operating parameters, biomaterial properties and energy dissipation rate per unit mass. For turbulent condition, these interactions usually take a general form:

$$\varepsilon = \frac{P_i}{\rho V} \qquad \textbf{Eq. 1.9}$$

where V is the volume of the stirred bioreactor and P_i is the power input through the impeller or stirrer, which depends on the flow regime and is often expressed in terms of dimensionless number, i.e. power number (N_p) and impeller Reynolds number (Re_i). The power input through the impeller can be expressed as (Doran, 1995):

$$P_i = N_p \rho N_{im}^3 D_{im}^5 \qquad \textbf{Eq. 1.10}$$

where N_{im} is the impeller speed and D_{im} is the diameter of the impeller. The experiments for specific tank and impeller configurations have to be carried out in order to determine accurate relationships between N_p and Re_i. For laminar conditions, N_p is inversely proportional to Re_i and thus the P_i can be expressed as:

$$P_i = k_1 \mu N_{im}^2 D_{im}^3 \qquad \textbf{Eq. 1.11}$$

where k_1 is a constant of proportionality. However, for turbulent condition such as those found in a typical operation, N_p is independent of Re_i and depends on a constant, K, which can be determined experimentally for specific impeller designs:

$$P_i = K \rho N_{im}^3 D_{im}^5 \qquad \textbf{Eq. 1.12}$$

and the expression for energy dissipation rate in the stirred bioreactor having turbulent regime becomes:

$$\varepsilon = \frac{K N_{im}^3 D_{im}^5}{V} \qquad \textbf{Eq. 1.13}$$

For a typical system equipped with Rushton turbines, K values range from 5 to 6 (Harnby et al., 1997). In the turbulent condition the power requirement is independent of fluid viscosity but proportional to its density as opposed to that found in laminar condition. For the transition region, both parameters affect the power requirement depending on the system configuration. For most impellers in the system equipped with baffles, laminar condition is generated when $Re_i < 10$ whereas the turbulence is fully developed when $Re_i > 10^3$ or 10^4. For systems without baffles, Re_i must reach more than 10^5 before the turbulence is fully developed.

Equation 1.13 may seem simple to apply to the stirred bioreactors. There are, however, arguments among researchers on what volume to use in order to express the nature of the turbulent stresses appropriate for such a system. To obtain the mean energy

dissipation rate, the total working volume of the system is used. This mean value is unlikely to represent the region of interest inside the system, especially in a large vessel. The energy dissipation rate around the impeller area is much higher than that calculated by Equation 1.9 (Placek and Tavlarides, 1985) and a more appropriate calculation for the energy dissipation rate is based on the fluid mass near the impeller instead (Cherry and Papoutsakis, 1988). This is because damage is likely to take place in this region of high energy dissipation. The fluid mass around the impeller (V_h) can be assumed to be proportional to the impeller diameter:

$$V_h = k_2 D_{im}^3 \qquad \textbf{Eq. 1.14}$$

where k_2 is a constant. For systems equipped with Rushton turbines and baffles, V_h can be expressed by several terms: $\rho (D_{im})^3$ (Doran, 1995); 0.075 $(D_{im})^3$ (Aloi and Cherry, 1996); and 0.17 $(D_{im})^3$ (Kresta and Wood, 1991). Due to differences in system configuration (Zhou and Kresta, 1996) and calculation algorithm for energy dissipation rate, the ratios between maximum and mean values range from 10 to 100 (Shamlou, 1993). Consequently, these inconsistencies in ways of characterising energy dissipation cause difficulties in comparing results obtained from different research groups. There is a need to find ways to establish the relationships between the different methods.

Tubular-shaped bioreactors

Fanning friction factor (f) is often employed to determine energy dissipation rate in the system having fully-developed incompressible flow in straight and smooth tubular-shaped bioreactors such as pipes and capillary devices. This dimensionless number relates to the wall shear stress (τ_w) as follows (Perry and Green, 1997):

$$\tau_w = \frac{f \rho u^2}{2} \qquad \textbf{Eq. 1.15}$$

where u is the fluid velocity in the tubular-shaped bioreactors. The frictional pressure drop per unit length ($\Delta P/L_p$), fluid density (ρ), pipe diameter (D), average fluid velocity (u) and volumetric flow rate (Q) can be related using the Fanning friction

factor and Reynolds number. Though several models exist to demonstrate these relationships, they typically take the following form (Perry and Green, 1997):

$$f = \frac{D\,\Delta P}{2\,\rho\,u^2\,L_p} = \frac{\pi^2\,D^5\,\Delta P}{32\,\rho\,Q^2\,L_p} \qquad \textbf{Eq. 1.16}$$

For smooth pipes, the friction factor depends only on the flow condition in the system through Reynolds number as follows:

$$f = \frac{16}{Re} \quad \text{for} \quad Re \le 2100 \qquad \textbf{Eq. 1.17}$$

$$f = \frac{0.079}{Re^{0.25}} \quad \text{for} \quad 4000 < Re < 10^5 \qquad \textbf{Eq. 1.18}$$

$$f = 0.0015 - 0.0045 \quad \text{for} \quad Re > 10^5 \qquad \textbf{Eq. 1.19}$$

These friction factor definitions for specific flow regimes together with the ratio of velocity and density allow the relationships between the rate of energy dissipation, operating parameters and properties of process stream and system to be established. These relationships are expressed as follows:

$$\varepsilon = \left(\frac{u}{\rho}\right)\frac{\Delta P}{L_p} = \frac{128\,Q^3\,f}{\pi^3\,D^7} \qquad \textbf{Eq. 1.20}$$

Thus,

$$\varepsilon = \frac{512\,Q^2\,\mu}{\pi^2\,D^6\,\rho} \quad \text{for} \quad Re \le 2100 \qquad \textbf{Eq. 1.21}$$

$$\varepsilon = \frac{7.24\,Q^{2.75}\,\mu^{0.25}}{\pi^{2.75}\,D^{6.75}\,\rho^{0.25}} \quad \text{for} \quad 4000 < Re < 10^5 \qquad \textbf{Eq. 1.22}$$

For Reynolds number between 2100 and 4000, the flow regime is in the transition region and the estimation of friction factor is uncertain suggesting a traditional approach should be adopted for design purposes. For rough pipes, the relative roughness, which depends on the material of construction, becomes important and must be taken into consideration to estimate accurately the value of friction factor when the flow turns into turbulence.

Practically, the flow is not fully developed at the entrance region of the pipe as opposed to that being assumed for above applications. In such a case, the length of pipe, L_{ent}, is required for the flow to be fully developed. This usually depends on the flow condition and Reynolds number at the entrance region. Approximations of this length are as follows (Dombrowski et al., 1993) for laminar conditions:

$$L_{ent} / D = 0.370 \exp(-0.148\, Re) + 0.0550\, Re + 0.260 \qquad \textbf{Eq. 1.23}$$

and for turbulent conditions:

$$L_{ent} / D = 40 \qquad \textbf{Eq. 1.24}$$

Understanding the rearrangement of flow is important as the frictional loss at the area where flow is not fully developed is greater than that having fully developed flow of the same length. For the pipe exit, though the flow pattern also changes, the distance is much shorter than that at the entrance. This distance is approximately one pipe radius for those having low Reynolds number and becomes negligible when Reynolds number is more than 100. In these regions, using flat-plate theory, the pressure drop in the developing turbulent flow at the entrance can be estimated using the mean apparent friction factor (Zhang et al., 1993). The expression of the pressure loss is given by:

$$\Delta P = 1/2\, \bar{f}_{app}\, \rho \left(L_p / D\right) u_{\max}^2 \qquad \textbf{Eq. 1.25}$$

$$\text{where } \bar{f}_{app} = \frac{0.296}{\left[Re\left(L_p / D\right)\right]^{0.2}} \qquad \textbf{Eq. 1.26}$$

and u_{max} is the maximum fluid velocity.

1.2.3 Properties of biologically active materials - shear sensitivity

Processing of biomaterials inevitably leads to exposure to shear stress. Due to differences in structure and inherent characteristics of different biomaterials, the nature and extent of their response may vary considerably.

This section will mainly focus on cells, especially bacterial and mammalian cells, since these are currently used to produce majority of biopharmaceutical products (Walas, 1990) and thus the understanding of their properties are central to the prediction of the performance of both centrifuge and membrane filtration operations.

1.2.3.1 Bacterial cells

With the advances in recombinant DNA technology, bacterial cells have been widely employed to produce a number of key biologically active substances in the biotechnology industry. These unicellular organisms are small having a typical size of 1-10 μm. They have cell wall that consists of many polymer layers of cross-linked peptidoglycan connected by amino acid bridges. Although compositions of cell wall vary among bacterial species, its functions are to maintain the cell shape and to protect the cell membrane and intracellular components from stresses such as shear and difference in osmotic pressure between the cell and its environment. Typically, these cells are robust to shear stresses due to their rigid cell wall and very small size, allowing them to be cultured in both airlift and stirred bioreactors with little to no change in morphology, biological activity and intracellular components under typical operating conditions compared to animal cells. Bacterial cells do respond to their growth environment, e.g. the composition of cell wall, which is the main structure protecting cells, depends on physical conditions during the fermentation. This affects the shear sensitivity of cells not only during the upstream but also during the downstream processing (Keshavarz-Moore et al., 1987).

The effect of shear on bacterial cells varies greatly among species and operating parameters and physical properties of the system being studied. With increasing

impeller speeds it was observed that cells increase in size and the linear relationship between the mean cell volume and agitation rate was established for several bacterial species such as *Escherichia coli*, *Saccharomyces cerevisiae* and *Staphlyococcus epidermidis* (Wase and Patel, 1985). These larger cells generated as a result of higher shear stresses, however, are more susceptible to shear damage. Interestingly, shear effects can also be beneficial. For example, product formation during the cultivation of *Clostridium acetobutylicum* can be increased by exposing cells to higher shear stresses prior to cultivation process resulting in cell activation (Afschar et al., 1986). Moderate shear helps by making the static film of liquid on the cells thinner facilitating the mass transfer between cells and outside environment and thus promoting higher growth rate. *Lactobacillus delbruckii* was investigated for shear effects under laminar stresses and it was found that moderate shear levels of 36 and 54 N m^{-2} helped improve the cell metabolism and subsequently increased biomass concentration (Arnaud et al., 1993).

1.2.3.2 Animal cells

The main disadvantage of prokaryotes, e.g. bacteria and fungi, is that they lack post-translational modification functions such as glycosylation, carboxylation, phosphorylation, etc. As a result, protein product may be different from those of natural origins and may not be functional. This makes mammalian cells important as an alternative to these prokaryotes for recombinant products since they possess post-translational systems. However, due to their relatively large size (typically around 10-20 μm in diameter) and lack of cell walls, animal cells are extremely fragile compared to other cells. They must be treated with care if the membrane is to be kept intact before the recovery process takes place. Hydrodynamic shear is known to cause death of mammalian cells (Augenstein et al., 1971). Under sublethal intensity of shear stresses, mammalian cells respond through the change of cell growth and metabolism. In the study of mammalian cells, several parameters have been used as an indicator of shear response. These include the release of intracellular components (especially enzymes), cell viability, morphology change and cell growth.

1.2.3.3 Cells grown on microcarriers

Most mammalian cells are anchorage-dependent and may be grown on surfaces of microcarriers, which are suspended in the liquid medium. Depending on the system the damage mechanism of cells grown on microcarriers and its impacts can be significantly different from those of freely suspended cells. Cells attached to microcarriers often experience greater magnitude of hydrodynamic forces than free cells as the order of magnitude of Kolmogorov scale of mixing gets closer to that of microcarrier dimensions resulting in higher relative velocities between these microcarriers and the liquid medium (Cherry and Papoutsakis, 1986, Chisti, 1993). Besides the impact of hydrodynamic shear, cell damage in the microcarrier culture may be caused by collisions between microcarriers and microcarriers and reactor's internal structures, particularly in stirred tanks. These collisions among microcarriers often have greater impacts on attached cells than do free cells as the inertia of these microcarriers is higher than that of free cells.

The unique mechanisms of cell damage in the microcarrier culture have inspired researchers to devise certain parameters describing the damage resistance of cells grown in the culture and the characteristics of the culture itself in order to determine the culture environment and to help optimise the culture performance. To establish the shear damage of mammalian cells, the tip speed of impellers may be used. However, it should be noted that its value is specific to the vessel size (Croughan et al., 1987). Instead, the strength of laminar shear rate between the impeller tip and the vessel walls, i.e. integrated shear factor (ISF), is used as a parameter describing the damaging condition of the system regardless of vessel size. It has been reported that for human fibroblasts cultured in a range of vessel sizes (channel length between 0.25 to 2.0 m and impeller diameter between 0.032 to 0.085 m) cell damage only occurs when the value of ISF exceeds 18 s^{-1} (Croughan et al., 1987). Moreover, the time-averaged shear rate can also be used and was found to have threshold values of 2.5 s^{-1} and 6 s^{-1} for human and chicken embryo fibroblasts grown on microcarriers, respectively (Croughan et al., 1987). Likewise, the Kolmogorov scale of mixing, which in turn can be linked to energy dissipation rate, may be correlated with cell damage and was found to have threshold values below which damage is observed of 125 and 100 μm for human and chicken fibroblasts, respectively (Croughan et al., 1987).

For cell damage due to collisions among microcarriers and those between microcarriers and vessel internals, some other parameters have been formulated. For instance, to determine the cell strength and thus minimise the rupture due to the impaction through system optimisation, the 'burst force' may be used. For microcarrier culture in stirred tanks, the concept of 'severity of collision' has been proposed to explain and reduce the extent of cell damage due to collisions (Cherry and Papoutsakis, 1988, Cherry and Papoutsakis, 1989). This concept is based on both the impaction energy and collision frequency and expresses their extents in terms of a turbulent collision severity (TCS) and an impeller collision severity (ICS). The former accounts for turbulence-associated impactions among microcarriers whereas the latter accounts for impactions between microcarriers and an impeller. These two collision severities are derived from some important characteristics of the culture system including energy dissipation rate per unit liquid mass, densities of liquid and solid phases, size and volume fraction of microcarriers, volume and viscosity of the liquid as well as size, number and speed of the impellers. By adapting these system characteristics, the culture performance can be optimised accordingly.

1.2.3.4 Fungi and actinomycetes

Fungi and actinomycetes can take two forms during their growth. They can form either pellet or filament-like structure. Pellets can be formed from agglomeration of either spores or hyphae or both. Pellets can be viewed as a multilayer mass that comprise of the peripheral, centre and intermediate zones. Cell growth only occurs in the first zone whereas disintegrated and lysed cell mass is found in other zones. Larger pellets are more susceptible to hydrodynamic shear compared to smaller pellets. As expected the more compact and smaller pellets are formed in the system with high shear stress. Although the morphology of pellets varies greatly with the fungal type, the understanding of the relationships between shear forces and pellet morphology/size in the specific system is very important. The functionality and metabolic activity of cells, especially those located at the centre of the pellet, are affected by supply of nutrients which is determined by the prevailing flow condition.

A more shear-sensitive filamentous form makes liquid become very viscous and behave like non-Newtonian fluid, especially at high biomass concentration. This form

is made up of short and long filaments (250 μm or more) and hyphae having diameter between 2 to 7 μm. Generally, an increase of agitation rates leads to shorter and highly-branched filaments, reduced intersepta distance and thicker hyphae. Due to their small and long cellular structure, these filament-like cells are prone to shear damage at high agitation rates, even if they have thick and rigid cell wall.

1.2.4 Equipment and devices used in shear studies

Certain equipment/devices are commonly employed in the study of shear sensitivity and effects on cells. These include:

1.2.4.1 Shake flask

Although the quantification of shear stress may not be possible in this system using traditional calculation methods, the shake flask is employed to assess effects of shear generated as a result of fluid motion. Besides increasing agitation rates, baffles can also be equipped in the shake flask to promote higher degree of turbulence environment in the flask.

1.2.4.2 Parallel plate flow chamber

One of the first parallel plate flow chambers with a well-defined flow field was employed to study the effect of flow on the adhesion of polymorphonuclear leukocytes to vascular endothelium (Lawrence et al., 1987). It has been widely employed by many research groups to study shear effects on cultured monolayers of cells, especially with endothelial cells under physiological conditions. The device consists of two rectangular plates between which are a channel holding the test specimen for fluid to flow over. During the experiment, the test fluid is forced to enter one end of the chamber and exit the opposite allowing a well-defined shear stress level under laminar condition to be generated in this simple geometry.

1.2.4.3 Cylindrical tubes

A wide range of tube diameters, i.e. from process pipe to small capillaries, has been used to characterise shear effects on cells. Fully developed laminar flow having a parabolic velocity profile can be easily achieved in the circular tubes. Due to its simple geometry and extensive study, the shear stress in the cylindrical tube is well characterised and is found to vary linearly with the radial distance from the tube axis. Thus, the level of shear stress reaches maximum along the tube wall whereas it becomes zero at the tube centre. Although they are easy to use and the characterisation of shear stress and power dissipation is well established, there are some related problems when using these tubes to assess shear effects. These problems are that sometimes long tubes are required to allow the flow to be fully developed and deliver shear effects onto test materials before shear effects can be accurately assessed and that very small capillaries may not be able to withstand high pressure during the delivery of fluids, especially those containing solid entities. Moreover, depending on the design, it may be difficult to vary the residence time of the biomaterials in the tube provided that all other parameters are kept the same.

1.2.4.4 Cone-and-plate viscometer

The cone-and-plate viscometer comprises of a rotating inverted cone and a stationary flat horizontal plate. The apex of the cone is placed very close to the stationary plate. The angle formed by these two pieces is extremely small, usually less than 3° and the test fluid is placed in this small gap. As the cone rotates, the test fluid is forced to rotate with it allowing shear stress both in laminar and turbulent conditions to be developed. To calculate shear stress, the angular velocity and rotating forces (or torque) are measured and integrated into the shear stress correlation which is system-specific. Due to the rotation of the cone and time taken for the accurate measurement of key parameters, heat is usually generated during the run and if high enough can change the rheological properties of the fluid being tested resulting in high measurement errors. This is especially true when several materials have to be tested sequentially. Nevertheless, temperature control can be achieved through passing coolants under the stationary plate, which is usually made of materials that can transmit heat efficiently. Its advantages are that the morphological characterisation of

biomaterials in the stress field may possibly be carried out using infusing fixative solution and that the viscometer uses very small volume of test materials.

1.2.4.5 Coaxial-cylinder rotary viscometer

This device is very similar to the above cone-and-plate viscometer. It comprises of two concentric cylinders, one of which rotates whereas the other is held stationary. The majority of designs allow an inner cylindrical bob to rotate inside a stationary cylindrical cup while some designs perform vice versa. The test fluid is sheared in the annulus between these cylinders allowing Couette-type flow to be developed. Again, the angular velocity and torque are measured and supplied to the experimentally-obtained correlation of that system in order to determine shear stresses. Its limitations include the temperature variation and slippage.

1.2.4.6 Impeller viscometer

When the test fluid contains the solid entity that is large and can settle out of the suspension, the impeller viscometer should be employed instead of the above mentioned standard rotational viscometers. In this device a small turbine or other impellers is used to generate shear in the test fluid. The movement of impellers will promote homogenous conditions in solid-containing fluid and thus prevent sedimentation during the test. To determine shear level in the system, torque and rotational speed are measured, and these parameters are later incorporated into a shear stress correlation, which is obtained experimentally for a specific impeller design and system using a liquid with an established relationship between viscosity and shear rate.

1.2.4.7 Agitated and/or sparged bioreactors

Practically, typical cultivation processes require that there are exchanges of nutrients and other sources with cells for the purpose of cell growth and product yield. However, none of the above devices can provide such a condition in their systems in order to assess characteristics of cells under those particular stress conditions. Instead, the agitated, sparged or air-lifted type bioreactors have been used during the normal cell cultivation to fulfil this specific purpose. Information from the literature only allows

the conclusions on the actual stress level to be drawn up to a limit due to the difference in bioreactor configuration and impeller designs. To fully understand the stress conditions in bioreactors, shear stress levels in these systems must be measured. To do so, the velocity of the system must be measured at different locations of the reactor in order to establish the whole velocity profile and its gradients. Several anemometric techniques have been utilised to determine these fluid velocities (Oldshue, 1983):

- *Hot-film anemometer*: this is based on the principle that the velocity of flow and its fluctuation affect the heat transfer rate from the heat source placed in the system (thin wire or film).

- *Photographic method*: a narrow beam is projected to the reactor. Using information regarding exposure time and the length of trajectories, the fluid velocity can be calculated. For this approach, the whole bioreactor must be placed in a black box system.

- *Electrochemical method*: because in an electrochemical reaction the boundary current intensity is proportional to the amount of ions being diffused, the flow velocity can be measured indirectly once the relationship between flow rate and mass transfer is established.

- *Laser Doppler anemometer (LDA)*: the approach is to tag the fluid using a tagged particle (added or naturally occurring) and measure the velocity of these particles based on the change in frequency (Doppler shift) of the scattered light from a fringe targeted area generated from two equal-intensity laser beams (usually split from a single beam) that intersect at a known angle. This approach is becoming more popular since the fluid velocity can be determined in real time.

Depending on the nature of biomaterials and physical condition of interest, different equipment/devices are available for specific purposes of the shear study. Nowadays, a number of novel devices have been created to facilitate the study of shear. Some of these include the disc-rotating device (or shear device) and a vibratory shear-enhanced processing (VSEP) system. The latter has been designed especially to investigate shear

effects on membrane performance. Detailed descriptions of these devices are presented in the next chapter (**Chapter 2**).

1.2.5 Mitigation of shear effects

Shear effects may be reduced by using several approaches. Some common approaches include adding cell protective agents into the culture medium; supplying oxygen through a permeable membrane; using a liquid oxygen vector; and separating the culture system into cell-free and cell-containing zones. Certain cell protective agents, when added to the culture medium, help minimise the adverse shear effects due to aeration and/or agitation. These agents include serum, Pluronic F-68, polyethylene glycol (PEG), polyvinyl alcohol (PVA), methylcellulose and dextrans. Although these agents have been investigated by many research groups, the exact molecular mechanisms upon which these agents act to protect cells are not absolutely clear. The protective mechanism may be physical, i.e. they may change physical conditions affecting shear forces in the cultured system. On the other hand, the mechanism may be biological, i.e. they may change the mechanical or physiological properties of cell and cell membrane. These agents may also act through both mechanisms. Commonly used cell protective agents are described in more details below. Other approaches mentioned above are mainly related to the mitigation of bubble-associated damage. All these are means to avoid the direct sparging of oxygen to the media and are suitable only to specific cases. Direct sparging is still the most common method to supply oxygen or other gases to the culture media.

Commonly used cell protective agents:

- *Pluronic F-68*: this is a non-ionic surfactant, which is known to protect plant, animal and insect cells in suspension from damage caused by hydrodynamic shear stresses (King et al., 1990, Zhang et al., 1992, Palomares et al., 2000). Pluronic F-68 was found to reduce surface tension and thus help the mass transfer of nutrients and metabolites promoting cell growth (Michaels and Papoutsakis, 1991). Its effect is instantaneous after the exposure suggesting a physical protective mechanism.

- *Serum*: this can be either of animal or human origin. The commonly used type is the fetal bovine serum (FBS). Its protective effects have been observed in both

bubble-free and aerated suspension cultures and generally increases with concentration up to 10% (vol/vol). It has both a direct non-specific physical protective effect (van der Pol et al., 1992) and a physiological protective effect, though this may take longer to become effective (Michaels et al., 1991). The protective mechanism is found to lie in its ability to reduce plasma membrane fluidity (Ramírez and Mutharasan, 1990).

Supplying the culture medium with actin polymerisation inducers may also improve shear resistance of cells. This is because the cytoskeleton, which is mainly made of actin, determines morphology and mechanical properties of cells and interacts closely with the cell membrane. Modifying the extent and structure of the cytoskeleton clearly has effects on cell strength and the robustness of cell to shear stresses.

It should however be noted that the application of these protective agents may be associated with negative effects during and after the cell culture. For instance, a slight toxicity was observed during a cultivation of *Tetrahymena* cells after an addition of Pluronic F-68 having a high concentration of 0.2% (Hellung-Larsen et al., 2000). Similarly, this protective agent was found to slightly decrease cell viability of TB/C3 murine hybridomas (Zhang et al., 1992). Regarding FBS, as it is chemically undefined with a high between-batch variability (Morris and Warburton, 1994), its supplementation to the culture medium thus reduces a level of reproducibility between batches of a particular culture system. Because FBS has a high protein content, its presence in the cell culture, especially that of monoclonal antibody production, also adds difficulties to the downstream process which may require additional steps to purify a protein product from FBS. Moreover, the cost of serum is high and can constitute up to 70% of the total medium cost (Jackson et al., 1999). Additionally, the inclusion of animal sera in cell culture media is a potential source of contaminants, including prions, viruses and mycoplasms (Even et al., 2006). Hence, these microorganisms have raised concerns regarding the safety of its use in the production of human therapeutic agents at present and are the key driving force towards a cell culture with a serum-free medium.

1.3 Ultra scale-down (USD)

Lower performance and productivity is usually associated with scale-up of bioprocess equipment due to the change in the engineering environment. To improve these output measurements during scale-up of a new process and modification of an existing one, a scaling methodology is required (Bylund et al., 1999). The general idea behind scale-down methods is that small-scale experiments to determine operating parameters are carried out under conditions that can actually be realised, physically and economically, at production scale (Doran, 1995). In addition to this, the methodology can be employed with process synthesis and modelling to predict the performance of a large-scale manufacturing process and accelerate process development in particular when dealing with the effect of some variables that are difficult to measure experimentally at the full scale; for example how the biological material is affected by shear stresses.

1.3.1 Basic principles

The principle of an ultra scale-down (USD) technique is that a key fluid dynamics parameter affecting unit performance in both a large-scale unit and an USD mimic is kept the same in terms of magnitude and extent. This implies that key engineering parameters must firstly be identified and that these parameters are kept the same when building USD mimics; thus providing a higher chance that outputs obtained from the USD unit will be producible in the large-scale system.

Why should USD technique be used instead of designing large-scale equipment? The design for better large-scale equipment is possible only to a certain degree. This is due to the fact that physical prototyping is expensive and testing variety of large-scale designs is time consuming. USD technique provides more process insight, e.g. poor centrifuge performance due to particle break up, low density difference or high viscosity, and thus enables the more rapid integration of unit operations into a process leading to faster prediction of process performance. The technique saves time, number of personnel and money as a result of easier handling, operation and cleaning, reduced energy consumption and smaller volume requirements of expensive biopharmaceutical materials. Moreover, USD allows more process options to be explored before progressing to pilot-scale study. USD can be used to facilitate validation of a

manufacturing process, implementation of changes to the process, troubleshooting, process synthesis, process improvement and optimisation based on large-scale experiments, assessment of process sensitivity to changes in feed stocks, and even designing a new unit operation. As a result, a USD technique would establish a better strategic approach than pilot-scale studies if the linkage between USD mimics and large-scale manufacturing equipment has been successfully established, especially in terms of time-to-market.

1.3.2 Application of ultra scale-down to shear analysis

USD devices have already been employed in the bioprocess industry. Various small-scale devices exist to assist the analysis of shear damage in a number of unit operations carried out by several research groups. Some may be physically like the large-scale unit while others may only be the reproducible of parts of the flow regime within certain sections of the equipment or process, which may or may not look like those sections of the full-scale equipment. The majority of these devices take forms such as a scale-down mimic of process equipment, viscometers, capillary devices and other designs that do not look like its full-scale counterpart, e.g. a ball-valve rig and a rotating-disc device (with and without membrane integrated). Often the scale-down mimics of a stirred tank system are found over other process equipment. This is presumably due to an ease of scaling down and fabrication. These mimics are frequently used to study an effect of changes of a system parameter or to reproduce a bioprocess event in a small scale by keeping a certain parameter constant in both scales. For instance, a scale-down version of a stirred vessel has been used to fractionate whey protein on the basis of impeller power input per unit volume resulting in similar particle sizes and turbulent conditions in further downstream, e.g. in the pump, valve and centrifuge inlet zone, have been mimicked using a ball-valve rig (Byrne et al., 2002). The ball-valve rig together with a CFD technique has also been employed to predict precipitate particle breakage in a pipeline (Zumaeta et al., 2006).

A shear device is often employed in the shear studies in order to determine and predict the effect of shear stress on material of interest and overall process performance due to its ease of use, i.e. adjustable shear intensity through varying the disc speed. Together with other analytical techniques, e.g. CFD, the device has already been employed to

predict the performance of a large-scale process for the primary recovery of a therapeutic antibody (Neal et al., 2003). The same device has also been used to reproduce the high flow forces found in the feed zone of various continuous flow centrifuges such as disc stack, multichamber bowl and CARR Powerfuge™ in order to model material damage in the feed region and overall clarification of these unit operations (Boychyn et al., 2004, Boychyn et al., 2001, Hutchinson et al., 2006). In these works the equivalent engineering environment was generated in the USD device with the aid of CFD and matched with that generated within the large-scale centrifuge leading to accurate prediction. A smaller USD device, i.e. a capillary device, has also been employed in various shear studies. For instance, it has been used to expose cells to a range of shear levels, time and impact in a way that seeks to mimic those effects that may occur during full-scale processes (Chan et al., 2006).

1.4 Computational fluid dynamics (CFD)

1.4.1 Basic principles

Computational fluid dynamics (CFD) is a computer-based analysis technique that has been developed over the past few decades to facilitate an accurate prediction of heat transfer, chemical reaction and fluid flow in complex structures based on the underlying understanding of physical and chemical phenomena. Following recent developments, the technique has progressively been applied in both industrial and non-industrial application areas in order to allow better understanding of existing technologies and to ease manufacturing design cycles. Examples include:

- biochemical/chemical engineering: fermenter, homogeniser and other unit operations
- biomedical engineering: blood flows in blood vessels
- power generation: combustion in gas turbine
- hydrology: river flows
- aerodynamics and hydrodynamics: aircraft's wings and structure of ships
- construction: wind direction/loading, lightening and ventilation
- environmental engineering: pollution distribution
- automotive: drag forces and in-car environment

In order to apply the CFD technique the problem domain is firstly drawn and its parameters specified. Numerical algorithms integrated in the CFD code are then used to solve the problem. Finally, the solutions are presented in graphics useful for further interpretation (for full details, see **Chapter 3**). However, researchers must appreciate that the application of the CFD technique to a problem is associated with a long learning period for a particular CFD code and a considerable time taken to deliver a simulation, especially one involving a complex geometry. In practice, it may take between 6-18 months to learn the code depending on the entry level of the user and the drawing of the computational domain can take up to more than 50% of the total time required (Versteeg and Malalasekera, 2007). Moreover, the cost of setup and maintenance, which involves both hardware and software, may be an issue, though this has reduced significantly over the last few years. Researchers need to invest in a compatible hardware and pay for a CFD support, which can constitute up to around £1500 per annum for one academic licence of a complete code. More importantly, numerical algorithms in the code are built upon a number of modelling assumptions which may not be fully validated under all conditions. Hence the code does not generally produce absolute results, especially those problems involving several physical and chemical phenomena, and actual experiments are still required for those flow problems.

Despite these drawbacks and its expensive setup compared to personal computers, CFD thrives over experiment-based approaches at present and in the foreseeable future because:

- the technique still offers a cheaper approach with unlimited level of detail of results compared to a high-quality experimental facility;
- the technique also reduces costs of new designs and lead times;
- design parameters of experiments under hazardous conditions can be investigated using CFD simulation prior to actual construction of prototype;
- effects of different operating conditions can be predicted and studied once a CFD model is established;
- CFD simulations are getting more and more closer to reality and are capable of handling larger problems since numerical algorithms are increasingly better and computers are getting less expensive and more powerful.

1.4.2 Applications of CFD to bioprocesses

CFD may be the way forward for detailed explanation of the complex hydrodynamic conditions in certain bioprocess applications where traditional methods are not yet applicable so that particular processes can be optimised. Many researchers have already employed this technique in various aspects of both upstream and downstream bioprocesses. Starting from an inoculation stage CFD can map the flow field in the shake flask allowing better understanding of the mixing and gas-liquid mass transfer, which may be the limiting parameter for the growth of inoculated cells (Zhang et al., 2005). During fermentation CFD has been employed in a wide range of studies including flow fields and mixing in the bioreactor (Do et al., 2002, Schäfer et al., 1998), bubble break up and coalescence in bioreactor (Lehr et al., 2002) and cell growth and biochemical reactions (Feng et al., 2007). For separation processes this numerical method can be used to map the flow intensity in the feed zone of a continuous industrial centrifuge and help predict its recovery by using a laboratory centrifuge (Boychyn et al., 2004) and to study the flow field and shear stresses at the membrane surface, which can be linked to an average inlet velocity in the case of shear-sensitive suspensions in order to minimise material damage (Tarabara and Wiesner, 2003). Adsorption separation in chromatography can also be simulated using this technique (Wu et al., 2004). More importantly, it has been employed to relate turbulent eddy dissipation rate and associated exposure time to the particle breakage in order to develop predictive models which can evaluate breakage as a result of the fluid flow through various geometries in the bioprocess system.

Moreover, CFD has been used in a design process for a number of unit operations and their ancillary devices. Some examples of these include:

- optimisation of the rotor design for controlled-shear affinity filtration (Francis et al., 2006);
- design of laboratory mimics for continuous industrial centrifuges (Boychyn et al., 2001);
- design and optimisation of static mixers (Szalai and Muzzio, 2003);
- optimisation of plate photobioreactor used for cultivation of microalgae (Perner et al., 2003).

1.5 Aims and organisation of thesis

1.5.1 Aims of the thesis

The overall aim of this thesis is to identify the key hydrodynamic parameter governing damage to biological materials and/or components in large-scale operations of membrane filtration and centrifugation and from this to investigate the feasibility of quantifying the magnitude of this parameter using the computational fluid dynamics (CFD) technique and employing an ultra scale-down (USD) approach to link a laboratory-scale device to the large-scale system. As a result, the project will study hydrodynamic conditions in the large-scale unit operations using CFD in order to mimic these conditions in the small device. Information obtained will be used to predict and improve the performance of the large-scale operation as well as to identify scale-up methodologies.

1.5.2 Basis and novelty of approach taken in the thesis study

The basis of the approach taken in this thesis study is central to the identification of the key engineering parameter and component governing damage in the system, application of twin technologies of CFD and USD and construction of predictive models (see Figure 8.1, **Chapter 8**). Once the key engineering parameter and component of the system are identified a small device (USD device) will be chosen based on an ease of manipulation of this scalable parameter. The CFD technique will then be employed to quantify a magnitude of this parameter being generated in the key component of the large scale and to calculate an equivalent operating condition, which in turn can produce the same amount of hydrodynamic extent, for a USD device. At this stage the predictive models will also be constructed to help link systems of different scales. Such models will be based on key physical and operating properties of the system governing the exposure of biomaterials to the high-shear zone. Finally, USD experiments will be performed under CFD-recommended operating conditions allowing large-scale predictions to be made using a USD device.

Novelty of the approach lies in the application of twin technologies of CFD and USD together with mathematic models to the whole membrane filtration system, which may be represented by only a key component, in order to mimic a large-scale engineering

environment using a USD device. Predictive models constructed will allow predictions to be made in the bioprocesses involving a recirculation in terms of rates of material damage and especially the size of particles making up cell suspensions.

Regarding the above basis, the work involves the following:

- Key component and/or damage-governing hydrodynamic parameter identified and possibly used to link USD and large-scale systems. Feasibility of using CFD to analyse the fluid flow field assessed (**Chapter 2** and **Chapter 7**).

- CFD techniques carried out to quantify the key parameter in the large-scale system and determine the comparable operating conditions in the USD system generating the same magnitude of the key parameter being used (**Chapter 3**).

- USD experiments performed to establish the extent of hydrodynamic damage of materials being subjected to highly turbulent conditions for various time intervals (**Chapter 4**).

- Mathematical equations developed to match both systems and lay the foundation for the prediction of material damage in the large-scale system using a USD device (**Chapter 5**).

- Pilot-scale tests performed to investigate the shear effects on particle size and size distribution and verify the prediction of material size based on a USD device (**Chapter 6**).

1.5.3 Organisation of thesis

Chapter 1: The basis for this thesis is presented along with the overall framework of the thesis.

Chapter 2 to 6: Analysis and predictions of membrane filtration operation is described. This includes preliminary analysis of each component of the membrane rig, CFD analysis of the possibly key component, USD experiment, predictive models based on mathematical equations and pilot-scale verification.

Chapter 7: The preliminary assessment of employing CFD and USD techniques to mimic material damage in large-scale centrifugation is presented.

Chapter 8: The key findings from each stage in the development of full-scale predictive models are discussed and the conclusions of the thesis are described.

Chapter 9: The future works are presented together with the knowledge transfer and business opportunities for which this thesis provides a foundation.

CHAPTER 2 MEMBRANE PROCESS MODELLING: APPROACHES AND ULTRA SCALE-DOWN DEVICE

This chapter provides information regarding the membrane system studied in this investigation and the methods which may be employed to establish the linkage between the large-scale membrane filtration system and an ultra scale-down (USD) device. The previous work done on membrane process modelling and its scale-down approaches is first described. The analyses of important elements in the membrane system and key damage-governing parameters possibly linking configurationally different systems are then presented. After that the chapter describes criteria being used for the selection of the study material. Finally, the reasons for the choice of the USD device and overall experimental design are explained marking the end of this chapter.

2.1 Introduction

2.1.1 Membrane processing of biomaterials

This section will be presented in four parts: the general application of membranes in bioprocessing; the way in which the membranes are used, especially tangential flow versus normal flow; the different forms of membranes and their use; and finally a discussion of shear effects on biological materials and filtration performance in membrane processes.

2.1.1.1 General background

Membrane filtration processes may be used to separate or recover cells and suspended particulates from liquid mixtures in many sectors including biopharmaceuticals (Wang et al., 2006), water treatment (Bissen and Frimmel, 2003) and food processing (Li et al., 2006). In the biopharmaceutical industry, membrane separations together with other purifying process steps are integrated into the manufacturing process of

biomaterials forming an important part of both upstream and downstream processing. In upstream processing, membranes are employed to facilitate fermentation as well as media exchange, synthesis and extraction. In downstream processing, besides centrifugation and normal filtration, tangential-flow membrane filtration is the first key step in the recovery of most biomaterials, especially when dealing with decreasing particle size and decreasing scale of operation. Other process steps including isolation, depyrogenation and sterile filtration also involve the use of membranes. Not only are membranes used in separation of solids from other phases, but membranes are also used in product purification and concentration by removing dissolved solutes from solutions in which they are dissolved, commonly described as diafiltration. As most biopharmaceutical products are proteins (with the exception of nucleic acid-based products) that are thermolabile and membrane separation can be achieved at or below ambient temperatures with a completely contained system, membrane operation offers great advantages over other separation methods in terms of product stability. This is especially useful when the process entails the risk of product degradation or microbial contamination of the process stream and when the processing time is long. Moreover, membrane separation is an economically feasible technique which can produce cell-free solutions and offers a higher production rate compared to other techniques.

2.1.1.2 Operation mode

Membrane systems can be managed in two operating modes depending on the direction of flow to the membrane surface (Figure 2.1). When the direction of the fluid stream is perpendicular to the membrane surface, the membrane process is said to be operated in normal-flow or dead-end filtration mode. This operation mode is employed in different stages in the manufacturing process of biological products, especially in the late stages. It is used either to filter particles or small molecules from suspensions as in the removal of bacteria and other microorganisms before the product is filled into vials or ampules, or to retrieve suspended particles as in the recovery of cells from culture broth. When the operation takes place, the fluid stream is pressed against the membrane allowing some solids that are larger than membrane's pore size to deposit on the membrane surface and some smaller particles and fluids to pass through. Solid deposited on the membrane surface then acts as a secondary membrane resulting in a decreasing flux provided the pressure driving the system is the same. The disadvantage

of this operating mode is that eventually the flux decreases until little to no fluid can pass through the membrane; though the situation can be improved by the use of filter aids to preclarify large particles. When this happens the process needs to be stopped and membranes need either cleaning or replacement. During the cleaning process, components deposited on the membrane are removed (physically, chemically or hydraulically) making the module temporarily out of order. The membrane replacement process frequently ends up with product loss and lost processing time. Consequently, the downtime resulted from these activities renders the normal-flow mode a discontinuous process, which may largely affect the production time and process economics. In practice, a number of parameters governing the cake deposition are adjusted in order to extend the filtration time to be as long as possible while the cleaning time is kept at the minimum.

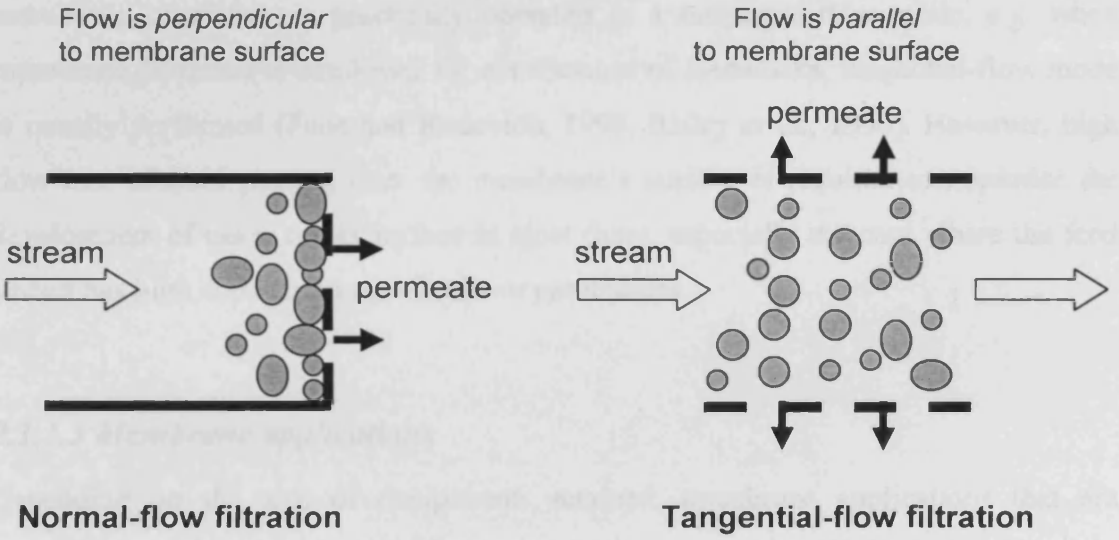

Figure 2.1 Two operation modes of the membrane separation process.

Although normal-flow filtration is often used for very dilute suspensions, the treatment of more concentrated suspensions is conducted using tangential-flow filtration (Kim and Zydney, 2006). Unlike normal-flow filtration the flow direction is parallel to the membrane surface in the tangential-flow or cross-flow mode and the pump is employed in the system. Regardless of sizes and densities, tangential-flow filtration

allows complete and continuous separation of particulates and with careful design in a plain, sterilable and fully contained system. This pressure-driven system is usually employed early in the process whereby the fluid stream is recycled for several hours, resulting in the high energy consumption. Like the normal-flow mode, the cake can still form on the membrane surface; however, increasing tangential-flow velocities over the membrane's surface helps particulates to stay in the body of fluid by reducing cake formation and concentration polarization (Mores and Davis, 2002, Thomassen et al., 2005). Consequently, a stable flux can be achieved in this operating mode provided the flow rate and other parameters are regulated appropriately, though cleaning is necessary from time to time, which may be performed via chemical cleaning and/or backwashing. Tangential-flow mode also facilitates the diafiltration to be performed in order to enhance either product yield or purity. During diafiltration, a suitable solvent such as a buffer is added into the recycle tank; thus exchanging buffers as well as reducing the amount of contaminants in the stream. In the biotechnology industry, the membrane separation is practically operated in a tangential-flow mode, e.g. when membrane filtration is employed for clarification of feedstocks, tangential-flow mode is usually performed (Fane and Rodovich, 1990, Bailey et al., 1990). However, high flow rate of fluid passing over the membrane's surface is required to minimise the development of cakes on its surface in most cases, especially the case where the feed stream has high concentrations of cells or particulates.

2.1.1.3 Membrane applications

Depending on the size of components retained, membrane applications that are commonly employed in the biotechnology industry can be classified as microfiltration, ultrafiltration, nanofiltration and reverse osmosis. Microfiltration membrane generally retains particles in a range of 0.1 μm and 10 μm in size, which include small organisms, blood cells, bacteria and pollen. It is used mainly to remove intact cells and some cell debris/lysates from process fluid and particles from air and gas during fermentation processes. In ultrafiltration, particles removed range approximately from 0.001 μm and 0.2 μm. Particles in this range include large oligopeptides, albumin, enzymes and other proteins. If ultrafiltration membrane is chosen appropriately, it is possible to separate larger particles from smaller ones, and thus in biotechnology purification and fractionation of macromolecules within above size range are

performed using ultrafiltration membranes. Regarding nanofiltration and reverse osmosis, they are employed to separate small molecules, which include salts and small molecules with a molecular weight below 1500 Daltons, from water and other solvents.

In a typical manufacturing process of biopharmaceuticals, after the fermentation processes, microfiltration is first used to remove cells and cell debris from the culture media, which often contain the product expressed by cells. To extend the life span of microfiltration membranes, clarifying filters and prefilters may be used to help clarify the culture media before microfiltration step. These filters also help increase the performance of the microfiltration process and reduce the operation time by reducing the rate of cake deposition on the membrane surface. If the product is inside cells, the disruption of cells and the removal of cell debris need to take place before the retentate can be processed further. Usually, the processed retentate stream or the permeate from the microfiltration step contains the product of interest along with a number of contaminants including other proteins, particulate biocatalysts, particulate by-products and small molecules produced during the fermentations. To separate these impurities from the desired product, the ultrafiltration method is often employed. The difference in nominated molecular weight limit of ultrafiltration membrane helps facilitate these purification processes, which may be carried out in several steps. In the biopharmaceutical industry, the chromatography and other separation and purification steps are frequently integrated with the membrane separations in the well-developed manufacturing process in order to optimise the product quality and yield, as it is usually not enough to achieve end results that meet a drug's stringent requirement using only membrane operations. However, introducing a membrane-chromatography separation method, so-called affinity membrane chromatography, may reduce process steps required to achieve the same product quality and yields. This is due to the fact that the technique allows protein purification based on biological functions rather than chemical or physical properties to be performed, thus mimicking the high-resolution separation function of chromatography. Owing to membrane's porous structure, it permits time-effective performance with high flow rates, thus achieving higher productivity and resulting in shorter processing time and higher recovery of protein activity.

2.1.1.4 Effect of shear during membrane operation

Several aspects of shear effects reported during the membrane separation of biological materials in the biotechnology industry include change in morphology, release of intracellular or extracellular components, reduction of biological activity or cell viability and alteration of suspension filterability. In tangential-flow configuration, high fluid velocities over the membrane's surface are usually generated to help prevent fouling on the membrane. However, these velocities are usually associated with high shear forces in the system, which impose stresses onto biomaterials leading to changes in structures and activities and, if high enough, can result in material damage/disruption and the creation of debris. When these debris and other particulates in the process stream reach considerable levels, the performance of the filtration operation can be impaired for example membrane fouling meaning that high flux rates cannot be sustained without increasing transmembrane pressure. Thus, besides the effects of operating conditions such as flow rate and transmembrane pressure drop, the performance of the membrane operation depends largely on the debris size or damage extent of materials in the system, which in turn is governed by a number of factors including extent of shear stress imposed, cell size and morphology, culture age and the environment to which the cells are exposed (fermentation media, temperature, pH, etc.) (Kim et al., 2001, Nipkow et al., 1989, Barbosa et al., 2003, Brindley Alías et al., 2004).

All components used in the assembly of the membrane rig, including membrane module, feed tank, valve, pipework and pump, can generate shear stress during the operation to certain extents depending on the design of each component, the design of the rig as a whole and the operating conditions. However, the extent of material damage also depends on the susceptibility of the product of interest to shear. Within the past decade the evidence has shown that pumps, which are used to deliver pressure difference within the system such that the process stream can be recirculated, generally impose higher intensity of shear stress to biological materials compared to other components in the system and are the main cause of adverse effects on membrane process performance (Jaouen et al., 1999, Vandanjon et al., 1999). The effect of shear stress due to the pumping devices has been consistently reported on various biomaterials including microalgae species (Brindley Alías et al., 2004, Vandanjon et

al., 1999, Jaouen et al., 1999), enzymes (Virkar et al., 1981) and human albumin (Gomme et al., 2006). Two main categories of pumps exist, i.e. centrifugal and others. Pumps having positive displacement action usually cover these others.

Although the type of pumps used largely depends on the rheological properties of the liquor being processed, the majority of pumps are of a centrifugal type as they are inexpensive to buy and maintain and are available in a large variety of materials. Unlike the centrifugal pump, the positive displacement pump, whose discharge rate is principally independent of pressure against which it works, is applied in specific circumstances depending on the material being processed. For installations in which suspended solids must be handled with a minimum of solids breakage or degradation, such as pumps transporting biomaterials, a low-shear positive displacement pump may be used (Perry and Green, 1997). However, material damage may still occur in this type of pump as the mechanism for fluid delivery is based on mating and meshing of its impellers and casing.

For particles larger than macromolecules, the application of shear during the membrane operation may break down these particles producing finer colloidal particles and/or releasing intracellular components into the process stream. The level of damage usually increases with recirculation cycle (or time) leading to flux decrease and reduction of the overall performance of the membrane operation by the thickening of a cake layer on the surface of the membrane. This cake-thickening phenomenon can be explained by the resistance-in-series model (Choo and Lee, 1996, Lee et al., 2000), which is shown in Equation 2.1:

$$J = \frac{\Delta P}{\eta R_t} \qquad \textbf{Eq. 2.1}$$

where J is the permeate flux (L m^{-2} s^{-1}), ΔP the transmembrane pressure (N m^{-2}), η the viscosity of filtrate (N s m^{-2}) and R_t the resistance of the total barrier between filtrate side and retentate side (m^{-1}), which composes of the membrane resistance (R_m), deposit/cake resistance (R_c) and the fouling resistance due to irreversible adsorption and pore plugging (R_f). Thus, Equation 2.1 can be rewritten:

$$J = \frac{\Delta P}{\eta\left(R_m + R_c + R_f\right)} \qquad \textbf{Eq. 2.2}$$

When the level of fine particulates reach a considerable level the permeate flux (J) will be reduced by the increase of cake deposition on the membrane surface and irreversible adsorption and plugging of particulates and smaller molecules due to the increase of cake resistance (R_c) and fouling resistance (R_f). The cake resistance (R_c) itself is directly proportional to the specific cake resistance (α), which is the cake resistance normalised to the mass of materials deposited per unit of membrane area and it is a distinctive property of particles dependent on their structure and size (Howell et al., 1993). The specific resistance is, in turn, inversely related to particle size in the process stream:

$$R_c = \frac{\alpha V_{cp} C_b}{A_m} \qquad \textbf{Eq 2.3}$$

$$\alpha = \frac{180\left(1-\varepsilon_c\right)}{\rho_s \cdot d_p^2 \cdot \varepsilon_c^{\,3}} \qquad \textbf{Eq. 2.4}$$

where V_{cp} is the cumulative permeate volume (m^3), C_b the bulk concentration of particles (kg m^{-3}), A_m the membrane area (m^2), α the specific cake resistance (m kg^{-1}), ε_c the porosity of cake layer (dimensionless), ρ_s the density of particles (kg m^{-3}) and d_p the particle diameter (m). As the mean size of particles in the system decreases, the specific cake resistance and cake resistance will increase. It is also likely that ε_c will decrease, due to mixtures of fine and large particles, again contributing to the increased resistance. As a result, the system equipped with high-shear-generating devices, which are likely to produce smaller particles in the process stream, will sequentially reduce the permeate flux with time, thus impairing the performance of the overall system. Practically, to obtain the value of fouling resistance, the clean membrane is firstly used to measure flux of ultra-pure water in order to get R_m. At the end of the run membrane is flushed with water and cake layer removed in order to get the resistance of R_m + R_f through pure water flux measurement. It has been experimentally verified that the

value of fouling resistance increases with decreasing size of particles in the process stream (Kim et al., 2001).

2.1.2 Previous work

2.1.2.1 Membrane process modelling

In membrane separation, mathematical modelling provides an important alternative tool to experimental studies for process development of membrane operations. Such modelling needs to account for prediction of flux rate and flux decline for example due to fouling. Although governing parameters related to the performance of membrane separation processes have been investigated and their effects are modelled by various research groups, most of the studies directly involve fouling and changes of fluxes resulted from several causes while the decrease in material size due to shear damage during the membrane operation has not been paid much attention. For instance, Bian *et al.* (2000) have investigated the effects of an increasing shear rate at the edge of the microfiltration and nanofiltration membrane on reducing concentration polarization and on controlling membrane fouling during filtration of river water and have employed the concentration polarization model to predict successfully the removal efficiency of humic substances from the membrane's surface. Mores and Davis (2002) created models to predict the recovered flux of the tangential-flow microfiltration after the membrane is clogged and cleaned by backpulses under different conditions of backpulse durations, transmembrane pressures and shear rates. Kyun Choi *et al.* (1999) modelled empirically cake formation in a rotating membrane filter in separation of fine silica slurry under Taylor-vortex flow and found the deposition process for particles to be two first-order steps in series of firstly particle mass transfer to the surface and then their adhesion to other parts of the fouling layer (particles). This is balanced by their rate of removal which is directly related to the wall shear stress. Another research group has also developed a mathematical model to describe flux decline behaviour during microfiltration accounting for all classical protein fouling mechanisms including pore blockage, pore constriction and cake filtration (Duclos-Orsello et al., 2006).

Numerical modelling through computational fluid dynamics (CFD) techniques has been integrated for the prediction of the hydrodynamics parameters within the membrane system and to link these parameters to the performance of the membrane processes. However, until now, there are only a few CFD simulations involving membrane systems and all of them are only dealt with the flow fields and their effects on the membrane's flux, not the effect of flow fields on the materials being processed. The effects of different configurations of spacer filaments on flow patterns in narrow channels in membrane modules using CFD code have been investigated (Schwinge et al., 2002, Cao et al., 2001). Serra and Wiesner (2000) used CFD to investigate and compare the performance of rotating membrane disc filters and stationary membrane disc filters over a range of operating conditions (flow rate and disc's angular velocity) and geometric configurations (disc radius and clearance between membrane and baffle). The numerical code has also been used for simulating concentration polarization (Ahmad et al., 2005). Ahmad and his colleagues reported the use of this numerical method to predict the profile of concentration polarization, mass transfer coefficient and wall shear stress under different types of conditions in the empty narrow membrane channel.

Despite long practical experience in membrane modelling, no generic model has been developed to predict the extent of material damage during the membrane operation. This is presumably due to the fact that it is extremely difficult to develop one single model for all biomaterials whose properties are complex and vary greatly and depend upon their nature as well as operating environment in the upstream processing.

2.1.2.2 Scale-down device

Several small-scale devices have been developed to study the effects of major parameters on the performance of large-scale membrane processes and to find optimal conditions for scale-up. Two distinctive designs exist. The first was developed by Reynolds *et al.* (2003) to predict changes with time of cake compressibility. The group successfully modified a batch-wise Nutsche filter into an ultra scale-down (USD) rotating vertical leaf filter by inserting a plunger into a filter housing, which enables a continuous flow of feed from a pump, in order to create a laboratory mimic of a production-scale continuous filter with a filtration area of 24 m^2. Another unique

device, a so-called cone-and-plate test cell, consists of an inverted wide-angle cone lowered into a cylinder where the circular membrane is mounted (Vasan et al., 2002). It was developed to allow uniform surface shear to be generated during ultrafiltration, thus enabling better validation of mathematical models for ultrafiltration processes.

Other small-scale devices generally tend to take one of two forms: a rotating-disc module or a vibratory shear-enhanced processing (VSEP) system. A rotating-disc module is a dynamic filtration having a disc rotating near a circular membrane in order to control parameters affecting the permeate flux. The dimensions and configurations of the rotating-disc system vary slightly for each research group and are dependent on the application. The VSEP system is a vibrating membrane with mechanisms of producing vibrations in order to increase and control shear rates at the membrane surface. One of its main units was introduced by New Logic International (Emeryville, CA, USA). It consists of an annular membrane of 500 cm^2 area (maximum of 151 m^2 in production units), with 13.5 cm outer radius and 4.7 cm inner radius mounted in a steel housing perpendicular to a vertical shaft which vibrates around its axis at its resonant frequency of about 61 Hz (Al-Akoum et al., 2002b). In both systems, an additional mechanical device is used to increase shear near the membrane's surface allowing very high membrane shear rates to be controlled independently of an inlet flow rate and transmembrane pressure, thus facilitating designs of large-scale process and characterisations of key parameters affecting the performance of membrane operations. Many papers have reported the use of these systems as alternatives to conventional tangential-flow filtration (Bouzerar et al., 2003, Harscoat et al., 1999, Al-Akoum et al., 2006, Vane et al., 1999).

Several research groups have utilised the rotating-disc module in many studies. For example, Lee *et al.* (1995) employed a laboratory-scale rotating disc dynamic filtration system (0.013-m^2 nylon membrane) for concentrating recombinant yeast cells containing an intracellular product in order to develop rapidly a highly effective cell harvest step by evaluating how operating conditions of cell density, disc rotating speed, filtration mode, and nominal transmembrane pressure affect the concentration factor and dynamic flux. A similar rotating-disc system was employed to investigate the fouling characteristics during the concentration of ferric hydroxide suspension in saline solution using tangential-flow filtration (Bouzerar et al., 2000). To develop a model

used to predict fouling behaviour in any tangential-flow filtration process, the rotating-disc system was also used to examine the interactions of 17 different parameters, e.g. transmembrane pressure, pH, content of antifoam and pore width, causing fouling during the dynamic microfiltration of *E. coli* suspensions (Meyer et al., 1998). The variation of the system may be seen, e.g. the installation of vane on the disc. Brou *et al.* (2002) investigated the gain in performance of the rotating disc dynamic filtration device by equipping it with eight straight vanes of various heights from 2 to 6 mm using baker yeast suspensions as a test fluid.

Like the rotating-disc system, a small vibratory shear-enhanced processing (VSEP) system has been employed in studies of hydrodynamic parameters involving the membrane flux. Al-Akoum *et al.* (2002) employed the VSEP system to investigate how the permeate flux varies with the fluid properties and shear rate on microfiltration and ultrafiltration membranes using yeast suspensions and bovine albumin solutions, respectively. The system has also been used by the same group to investigate the effect of the mean membrane shear rate on membrane flux during the concentration of total proteins by ultrafiltration and for separating casein micelles from whey proteins using microfiltration (Al-Akoum et al., 2002a). The studies using the VSEP system confirmed a strong relationship between local hydrodynamics and permeate flux obtained during crossflow filtration and hence the importance of the wall shear stress to the performance of the membrane operation.

2.1.3 Description of membrane system

A schematic diagram of the pilot-scale membrane filtration rig employed in this investigation is shown in Figure 2.2. This membrane system was at first designed by Bio-Design Ltd., UK, in 1990 and has been significantly modified since then. The rig has been continuously used and maintained in good conditions in the Department of Biochemical Engineering at University College London, UK. The system consists of a feed tank, membrane module, pump, valve and pipework.

A custom-made feed tank has a working volume of ~150 L. The diameter and height of the tank are the same and equal 0.58 m. The tank is equipped with a 45° pitched-blade turbine with six blades. The impeller is located at one third of the tank's height from

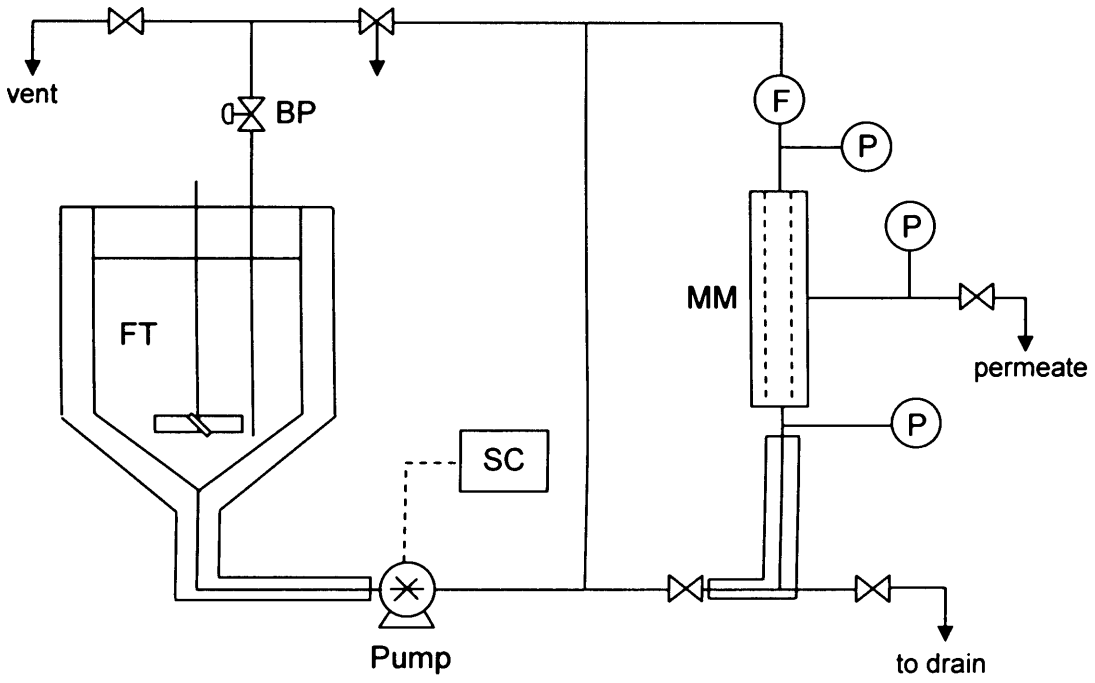

Figure 2.2 Schematic diagram of a pilot-scale membrane rig. The feed tank (FT) with cooling capacity through jackets has a capacity of 150 L and is equipped with six 45° pitched blades. The membrane is located in module MM, which can be changed to any membrane type. A variable speed vane pump is fitted in the system to give different tangential flow conditions via a speed controller (SC). The diaphragm valves are used throughout to minimise the extent of material damage. Pipework with i.d. of 6 mm was used to reduce entry and exit effects. Transmembrane pressure is controlled by adjusting a diaphragm valve (BP) on the retentate return line. Pressure gauges (P) are used throughout the rig to monitor the pressure during the operation. A pressure transducer is also fitted at the inlet (P).

the bottom. The tank also has three baffles, with the width of one twelfth the tank diameter, fitted and spaced evenly inside. With an offset of one half of the impeller diameter from the tangent line at the bottom and an offset of one sixth the baffle width from the wall, the baffle extends its length to the liquid level. The impeller diameter is 0.22 m. The temperature of materials is maintained mainly by cold water circulation through the jacket surrounded the feed tank. The original rig was fitted with Fairey Tecramics membranes having 6 mm internal diameter and 0.265 m length (Fairey Industrial Ltd., UK). However, membrane modules are interchangeable and can be of several commonly available models. The pump is a positive displacement rotary vane type (P01011, Bechtech, UK), which is connected with a speed controller (Model VS31-YAA from SKF automation systems, UK). The pump, which is used to recirculate mixed liquor, has 4 carbon vanes rotating inside, which forces liquid to move from the inlet to the outlet and has a capacity delivering liquid medium between 3.66 L min^{-1} (at 300 rpm) to 18.36 L min^{-1} (at 1500 rpm). The transmembrane pressure can be adjusted by a Saunders diaphragm valve on the retentate return line. Pipes connecting different rig components are made of stainless steel and have internal diameter of 6 mm. Cooling is also available through jacketed sections of pipework. Pressure gauges (Wika Instruments Ltd., UK) are used throughout the system, including the inlet and outlets (retentate and permeate side), to provide full monitors of the pressure during the run. Magnetic flowmeter Autolux meter (Krohne, Germany) is used to measure flow rate of fluid in the rig. The measurement of inlet pressure is achieved by pressure transducer (0-20 bar, Model 6100BG-D, TransInstruments (UK)). The bypass loop can have a membrane installed via tri-clamp fittings if necessary.

2.2 Analysis of material damage in membrane system

2.2.1 Material damage in membrane operations

As most membrane operations are operated in the tangential-flow mode and this is the configuration where the material damage normally occurs, it is important to establish a predictive model that can estimate the damage or change in properties of a process stream which may occur at scale long before the manufacturing-scale process is carried out or even before the process development is complete. Processing of biological

materials in the membrane filtration rig can lead to considerable breakage and damage, depending on the intensity of shear stresses to which materials are subjected and the strength of the biomaterials. This section reviews and analyses the flow intensity in each component of the membrane filtration system where materials may be subjected to intense flow fields that cause damage. Several flow parameters have already been used to correlate the hydrodynamic environment of the system to biomaterial damage. These may include shear rate (Molina Grima et al., 1997, Kumaresan and Joshi, 2006), shear stresses (Abu-Reesh and Kargi, 1989, Born et al., 1992), Reynolds number (Maiorella et al., 1991, Chan et al., 1991) and local energy dissipation rate (Al-Rubeai et al., 1995, Jüsten et al., 1996), Kolmogorov scale of mixing (Millward et al., 1994) (Kunas and Papoutsakis, 1990) and etc. Due to a common use and the availability of relevant data in the literature for this particular problem, the shear rate was however chosen as a mean to compare the flow intensity in components of the membrane rig and hence identify a key component responsible for material damage in this thesis study. Nevertheless, an alternative route besides using the shear rate will be taken in order to rule out a less important component if the relevant data in the literature is not yet available.

2.2.1.1 Feed tank

Besides holding a large volume of mixture, an agitated vessel is used in the membrane rig to maintain homogeneity of liquor, to keep solid particles suspended and to facilitate the heat exchange and mass transfer, with the help of impellers and baffles. The baffle prevents vortexing and swirling of the liquid mass as a whole whereas the impeller delivers a power input leading to a particular volumetric flow rate at each rotation in order to create conditions suitable for heat and mass transfer. The impeller also imparts shear (stress) to the fluid especially fluid elements close to the impeller tip; impellers with large blade area which rotate at low speeds, i.e. anchors, paddles and helical screws, may produce lower peaks of shear stress compared to high speed small diameter impellers. When the shear generated from impellers is high enough, materials in the mixed liquor will be distorted or broken down into smaller entities. If normal operating conditions of the impellers and physical properties of process materials are known, flow parameters used to correlate flow conditions to material damage such as shear rate may be calculated.

During the membrane filtration operation the impeller is usually required to operate at a low rotational speed while maintaining homogeneity of the mixture. However, the speed of the impeller also largely depends on physical properties of the process mixtures including settling velocity of the particles, solid contents of the suspension, specific gravities of the solid and liquid and shear sensitivity. To give a measure of mixing intensity, the volumetric pumping rate of the impeller per unit cross section of the tank, or **superficial linear velocity (u_s)**, may be adopted (Walas, 1990). As far as mixing solid suspension is concerned, these velocity values has been categorised to be in the range between 0.03 to 0.3 m s^{-1} (Chemineer et al., 1976). A velocity of 0.03 m s^{-1} will move solids on the tank bottom and suspend them from time to time while the velocity of 0.3 m s^{-1} will be used when the maximum feasible uniformity is needed providing slurry uniformity to 98% of the liquid level. The velocity values between 0.09 to 0.18 m s^{-1} allow for operations in most applications of solids suspension and dissolution from suspending all solids completely off the bottom of the vessel to providing uniform distribution to within 95% of liquid level. These velocities together with certain dimensionless groups and their relationships on specific impeller designs may then be used to calculate operating conditions of the impellers under defined criteria for processing specific materials. For Newtonian system these dimensionless groups may include impeller Reynolds number (Re_i), power number (N_P), Froude number (N_{Fr}) and flow or pumping number (N_Q) and are defined as follows:

$$Re_i = \frac{N_{im} D_{im}^2 \rho}{\mu} \qquad \textbf{Eq. 2.5}$$

$$N_P = \frac{P_i}{\rho N_{im}^3 D_{im}^5} \qquad \textbf{Eq. 2.6}$$

$$N_{Fr} = \frac{N_{im}^2 D_{im}}{g} \qquad \textbf{Eq. 2.7}$$

$$N_Q = \frac{Q_i}{N_{im} D_{im}^3} \qquad \textbf{Eq. 2.8}$$

where N_{im} is rotational speed of the impeller (rev s^{-1}), D_{im} is the impeller diameter (m), ρ is the fluid density (kg m^{-3}), μ is the fluid dynamic viscosity (kg $m^{-1}s^{-1}$), P_i is power input (W), g is gravitational force (m s^{-2}) and Q_i is volumetric pumping rate from the impeller (m^3 s^{-1}). However, Equation 2.5 may need to be adjusted when the calculation involves fermentation broth as most of them exhibit non-Newtonian behaviour, whose viscosity varies with shear conditions. One approach is to use an impeller Reynolds number based on the apparent viscosity (μ_a) in the correlation for ungassed fluids:

$$Re_i = \frac{N_{im} D_{im}^2 \rho}{\mu_a} \qquad \textbf{Eq. 2.9}$$

Using dimensional analysis, it can be shown that the power number is related to the impeller Reynolds number and Froude number by the following equation (Holland and Chapman, 1966):

$$N_p = C Re_i^x N_{Fr}^y \qquad \textbf{Eq. 2.10}$$

where C is the overall dimensionless shape factor which depends on the geometry of the system. As the Froude number is only relevant to the system where gravitational effect is substantial, its influence in tanks fitted with baffles can be neglected and the exponent y is zero and $N_{Fr} = 1$. Equation 2.10 can then be written for baffled systems as:

$$N_p = C Re_i^x \qquad \textbf{Eq. 2.11}$$

or

$$\log N_p = \log C + x \log Re_i \qquad \textbf{Eq. 2.12}$$

By using N_P-Re_i and N_Q-Re_i relationships (the latter can be established in a similar fashion) together with the superficial linear velocity required to generate a specific mixing condition in the system, the minimal recommended rotational speed of the

impeller can determined. Through this impeller speed together with liquid properties and tank properties, the corresponding shear rate can then be calculated.

Because the main objective of the impeller in the feed tank during membrane filtration operation is to resuspend solids, which in this investigation have a low density, at the bottom of the vessel back into suspension, a recommended superficial linear velocity of 0.09 m s^{-1} should be sufficient. As a result, by using this velocity value together with data obtained from the system having the same geometrical configuration, the operating condition of the impeller in terms of rotational speed can be calculated and thus the shear rate in the stirred tank may be determined.

Calculations for required impeller speed

Let's first determine the required impeller speed that allows the superficial linear velocity of 0.09 m s^{-1} to be established. For the sake of these calculations, the suspension liquid has a density of 1000 kg m^{-3} and a viscosity of 10^{-2} kg m^{-1} s^{-1}. From the definition of the superficial linear velocity we have:

$$u_s = Q_i / A_t = Q_i / \left[(\pi/4)(0.58)^2\right] = 0.09\ \mathrm{m\,s^{-1}} \qquad \textbf{Eq. 2.13}$$

where Q_i and A_t are the volumetric pumping rate of the impeller and cross section of the tank, respectively. This gives Q_i to be 0.024 m^3 s^{-1}. From Equation 2.8 we obtain:

$$Q_i = N_Q N_{im} (0.22)^3 = 0.024\ \mathrm{m^3\,s^{-1}} \qquad \textbf{Eq. 2.14}$$

whereas from Equation 2.5 the impeller Reynolds number equals to:

$$Re_i = N_{im} (0.22)^2 (1000)/(10^{-2}) = 4840\, N_{im} \qquad \textbf{Eq. 2.15}$$

Solving N_{im} by trials with the aid of the relationship curve between N_Q and Re_i of the system having the same configuration (Dickey, 1984) gives the impeller speed of 3 rev s^{-1}. This means that, with the impeller speed of 3 rev s^{-1}, the hydrodynamic forces in the system will be sufficient to suspend all solids completely off the bottom of the vessel in most applications of solids suspension. Because solids in the test material

under this investigation have a low density, this predetermined operating condition should clearly be valid for this particular system.

Calculations for shear rate

To calculate the shear rate, the following equations may be applied.

$$\frac{P_i}{V} = \tau \gamma \qquad \textbf{Eq. 2.16}$$

or

$$\gamma = \left(\frac{1}{\mu}\frac{P_i}{V}\right)^{1/2} \qquad \textbf{Eq. 2.17}$$

where γ is the average shear rate (s^{-1}) and V is the volume of the stirred tank (m^3). The corresponding impeller Reynolds number for the impeller speed of 3 rev s^{-1} was found to be 14520, which indicates the turbulent regime in the system. Data from the system equipped with pitched blades (Bates et al., 1963) shows that the power number equals to 1.3 when the flow condition within the stirred tank becomes turbulent. Using Equation 2.6 the power required to move the impeller can be calculated:

$$P_i = (1.3)(1000)(3)^3(0.22)^5 = 18 \text{ W} \qquad \textbf{Eq. 2.18}$$

By using Equation 2.17 the average shear rate in the stirred tank can be calculated:

$$\gamma = \left(\frac{1}{10^{-2}}\frac{18}{0.15}\right)^{1/2} = 110\,s^{-1} \qquad \textbf{Eq. 2.19}$$

Alternatively, a technique to obtain the average shear rate has been devised based on the theory that the average shear rate in a mixing system is a linear function of the impeller speed (Metzner and Otto, 1957). This can be written as:

$$\gamma = k_{MO} N_{im} \qquad \textbf{Eq. 2.20}$$

where k_{MO} is a constant which depends upon the impeller design and can be obtained from the experiments. k_{MO} observed in a stirred vessel of typical configurations equipped with pitched-blade turbines has a value of 11 (Nagata, 1975). This gives the average shear rate of:

$$\gamma = (11)(3) = 33\,s^{-1} \qquad \textbf{Eq. 2.21}$$

However, the average shear rate alone may not be adequate to assess the flow intensity in the stirred tank, as the shear rate in this mixing system depends on the distance from the impeller. The shear rate values were found to vary greatly from the impeller's tip to the tank extremities. Hence, the maximum shear rate (γ_{max}) generated in the liquid area close to the impeller should also be considered. Its formula can be written as (Robertson and Ulbrecht, 1987):

$$\gamma_{max} = 3.3 N_{im}^{1.5} D_{im} \left(\frac{\rho}{\mu}\right)^{1/2} \qquad \textbf{Eq. 2.22}$$

and its value in this system was found to be:

$$\gamma_{max} = (3.3)(3)^{1.5}(0.22)\left(\frac{10^3}{10^{-2}}\right)^{1/2} = 1200\,s^{-1} \qquad \textbf{Eq. 2.23}$$

To summarise, it can be concluded that the feed tank imposes low level of hydrodynamic stresses to materials, as the range of shear rate is only between 33 and 1200 s^{-1}. Moreover, since the tank has a dished bottom, the power requirement is even less and thus the impellers can be operated at lower speed compared to a flat-bottom one generating even lower shear rate.

2.2.1.2 Membrane module

Currently, there are five main types of membrane module geometries being used in the biopharmaceutical industry. These include plate-and-frame, tubular, hollow fiber, capillary fiber and spiral wound designs. The plate-and-frame module is one of the

earliest designs used in the membrane system. The module consists of a stack of membranes packed together with spacers and collection plates in between. The channel height can be between 0.4 and 2.5 mm and the flow may be either streamline or turbulent (Grandison and Lewis, 1996). Tubular module consists of a number of cylindrical membrane tubes with a range of diameters up to 25 mm. These modules normally operate under turbulent flow conditions with flow velocities greater than 2 m s^{-1} (Grandison and Lewis, 1996). Generally, the resistance to fouling of tubular modules are better than that of plate-and-frame modules. However, both designs are used in the separation applications where membrane fouling is severe. Hollow fiber and capillary fiber assemblies are similar to the tubular design but the fibers containing in these modules have smaller internal diameters ranging from 0.001 to 1.2 mm. They usually operate in the streamline flow regime and may not perform well with viscous feeds and those containing particulate matter (Grandison and Lewis, 1996). Spiral wound system is a thin channel module wound around a porous axial collection tube as to increase the surface area to volume ratio. Commercial spiral-wound modules are typically 36-40 inches long and have diameters of 4, 6, 8 and 12 inches and appear to be displacing hollow fiber designs because they are inherently more fouling resistant and feed pre-treatment costs are therefore lower (Baker et al., 1991). Moreover, modules with improved resistance to fouling have been developed and are increasingly displacing the more expensive plate-and-frame and tubular systems used in applications involving viscous fluids and suspended particles (Baker et al., 1991). The flow pattern generated in the spiral-wound module is usually turbulent.

Although the physical configuration of each module geometry is different, the hydrodynamic fundamentals are analogous and damage mechanisms of biomaterials within the module can either be due to cell membrane deformation into the membrane's pores under the influence of transmembrane pressure or to hydrodynamic shear. Regarding the cell deformation, cell lysis will take place when the strain induced, which is proportionate to transmembrane pressure and pore diameter, is high enough to break the cell membrane. Cell lysis is also a function of the residence time of cells over the membrane's pore which in turn depends on the wall shear rate (higher shear rate reduces the time the cell spent on a pore). To minimise the damage from cell deformation in the pore, the critical value of transmembrane pressure above which cell lysis occurs may be applied as an upper limit. The relevant data has been extensively

reported for erythrocytes whose internal structure is more fragile than other cell types and can be used as a safe limit for those with stronger internal structure (Forstrom et al., 1975, Zydney and Colton, 1984).

Concerning the hydrodynamic shear, high fluid velocities are required to minimise the cake deposition on the membrane's surface. Most designs, however, impose low stress on the process stream. To calculate the shear rate at the wall the following equations may be applied (Henry and Allred, 1972):

$$\gamma = 6 v_{mc} h_{mc}^{-1} \text{ for plate and frame type} \qquad \textbf{Eq. 2.24}$$

$$\gamma = 8 v_{mc} D_{mc}^{-1} \text{ for tubular type} \qquad \textbf{Eq. 2.25}$$

where h_{mc} is the height of the membrane channel (m), v_{mc} is the tangential velocity inside the membrane channel (m s^{-1}) and D_{mc} is the hydraulic diameter of the tube (m). For a typical module used in bioprocess applications (channel length = 30 cm) the local shear rate generated at the membrane surface was found to be 4000 s^{-1} (van Reis and Zydney, 2007), i.e. below those that could initiate damage to biomaterials. Maiorella *et al.* (1991) confirmed this by measuring the cell viability of mammalian and insect cells and found that cell damage was not detected in laminar flow at the maximum wall shear rate of up to 6000 s^{-1}. Collectively, fluid stresses in the membrane module are considered to be at low level and, for certain unique applications, damage to biomaterials may be avoided without compromising the unit's performance by applying the upper limit of stress for a specific cell type which has readily been made available by several research groups (Smith et al., 1987, Tramper et al., 1986).

2.2.1.3 Pump

As described in section 2.1.1.4, it has been consistently reported that processing a suspension through the pumping device causes damage to biomaterials (Jaouen et al., 1999, Vandanjon et al., 1999, Brindley Alías et al., 2004, Virkar et al., 1981, Gomme et al., 2006, Roy et al., 1989). By using an electrodiffusion technique, the shear rate can be measured and values as high as 10^6 s^{-1} were reported for a pump equipped with

an impeller blade with radius of 80 mm (Wichterle et al., 1996). The group also concluded that the shear rate found at the impeller blade was close to the value predicted by the Kármán theory (Schlichting, 1979) of laminar boundary layer at the rotating disc and can be predicted using the formula developed from the theory. The Kármán theory describes a laminar boundary layer developed on a rotating disc and defines the shear rate in this layer for a Newtonian fluid as:

$$\gamma = N\,6.30\,Re_L^{1/2} \qquad \textbf{Eq. 2.26}$$

where γ is the local shear rate (s^{-1}) and N is the rotational speed of the disc. Re_L is the local Reynolds number for the point in radial position and is defined as:

$$Re_L = N\,d_L^2\,\rho/\mu \qquad \textbf{Eq. 2.27}$$

where d_L is diameter related to a point in radial position, μ is the fluid viscosity, ρ is the fluid density.

Based on the dimensions of the impeller blade (vane) in the pump equipped in the system being investigated (see section 2.1.3 in **Chapter 2** and section 3.2.4.1 in **Chapter 3**) and shear rate data obtained from the rotating disc experiments that proved to follow the Kármán theory (Wichterle et al., 1996), the shear rate in the pump was estimated to be ~20,000 s^{-1} for low-speed studies, i.e. the pump speed of 600 rpm.

2.2.1.4 Pipework

For the pipework the Reynolds number was firstly estimated so that relevant correlations for a specific flow condition can be assigned to estimate the shear rate. For low-speed studies (pump speed = 600 rpm) the Reynolds number was calculated:

$$Re = \frac{Du\rho}{\mu} = (0.006)(4.32)(1000)/(10^{-2}) \approx 2600 \qquad \textbf{Eq. 2.28}$$

With the Reynolds number of 2600 the flow condition in the pipework is possibly turbulent. In such case the following equation can be applied to evaluate the shear rate in the system (Bjerkholt et al., 2005):

$$\gamma = \frac{32Q10^{-3}}{60\pi D^3} \qquad \textbf{Eq. 2.29}$$

where Q is the volumetric flow rate (L min^{-1}) and D is the pipe internal diameter (m) and the shear rate generated at the wall of a circular smooth pipe calculated:

$$\gamma = \frac{(32)(7.32)(10^{-3})}{(60)(\pi)(0.006^3)} = 5760\, s^{-1} \qquad \textbf{Eq. 2.30}$$

Because the stress and level of the energy being dissipated in the circular pipes with uniform cross-section is still lower than the damage threshold of 6000 s^{-1} (Maiorella et al., 1991), it is likely that no damage to ordinary biomaterials will be observed within the pipework during the normal operating conditions for the rig. In addition to this, pipes in the rig have been maintained in good condition and been cleaned at the end of each run, it can be reasonably assumed that these smooth pipes have little or no erosion, preventing a higher level of the turbulent condition to be generated in the system.

2.2.1.5 Valve

Valves are employed in bioprocesses to control flow in lines during the operation and provide isolation for equipment. For membrane filtration operation valves together with pumping devices are used to control flow rate and transmembrane pressure in the membrane module. Damage of biomaterials has consistently been reported when the process stream is passed through valves (Save et al., 1994, Schutte and Kula, 1990). This is mainly due to the extent of the change in flow direction and intensity of flow field inside the valve which in turn depend on the internal structure of the valve (type of valve), operating condition (fluid velocity and pressure) and its opening degree (percentage or angle of opening).

Various types of valves exist including gate valves, globe valves, check valves, butterfly valves, slide valves, diaphragm valves and etc. Though they have the same line size and pressure rating, the geometry of these valves may differ significantly from each other when produced by different manufacturers. The majority of valves used in the plant are gate valves, which use raising and lowering mechanisms to control flows, though these valves cause high pressure drop and shear stresses. The diaphragm valve should be used instead for those require low level of shear since this valve design, owing to its internal structure, allows very low pressure drop.

Although there is no relevant data on shear rate and the generic models allowing prediction of biomaterial damage in valves are not yet available in the literature, several parameters may be employed to characterise the extent of shear effects for each design. Some of these include the upstream pressure, pressure drop across the valve and flow rate in the circulation loop. However, the use of each parameter alone does not prove to be a robust approach as the extent of shear effects will change once other parameters are altered. Instead, the pressure drop or loss coefficient (K_v) has been proposed to be a more suitable parameter to evaluate the shear effects caused by a valve (Vandanjon et al., 1999, Perry and Green, 1997). The coefficient can be evaluated experimentally using upstream pressure (P_1), downstream pressure (P_2), fluid velocity (u) and fluid density (ρ):

$$\Delta H_{1\text{-}2} = (P_1 - P_2)/(\rho g) = (K_v u^2)/(2g) \qquad \textbf{Eq. 2.31}$$

where ΔH is the pressure drop (m). The unit for both upstream and downstream pressures is Pascal (Pa). The pressure drop coefficient integrates characteristics of the valve itself (valve type and its internal structure) and the system (fluid velocity and pressure) and is a function of the extent of valve's opening. This thus allows only one value of pressure drop coefficient can be obtained for a given type of valve and for a given opening percentage. However, there are limitations when applying K_v to compare shear effects from valves having different geometries. The same value of K_v calculated from different valve types does not guarantee the same resultant effect on biomaterial. Moreover, the significance and behaviour of K_v at different operating conditions

(pressure and fluid velocity in the system) needs to be further assessed (Vandanjon et al., 1999).

As the difference among valves of the same type, line size and pressure rating exists among those produced from different manufacturers and their K_v values and generic models for shear rate for specific valve types are not readily available, the assessment for the damage effect on biomaterials through valve can be difficult without performing the experiment. Nevertheless, when valves are close to fully opened or fully opened negligible damage may be assumed. For applications requiring partial opening of valve, the challenge to devise a generic model still remains and the issue will be subjected to further investigation.

2.2.2 Key component responsible for material damage

Table 2.1 shows the values of shear rate found and developed from the information available in the literature for components of the membrane filtration rig. According to Table 2.1 the pump was found to be a potential component causing material damage in the membrane filtration system. Hence, this thesis study will investigate a key engineering parameter governing the damage effect in the pump and possibly reproduce it in a very small device (an ultra scale-down device). Due to its complex structure and lack of a generalised predictive model for damage, standard analysis procedure is not possible to assess fluid stresses in the pump. Instead, the computational fluid dynamics (CFD) and ultra scale-down (USD) techniques will be employed in order to mimic the damage effect in the USD device.

From here onwards, several issues involved in this challenge will be presented to describe how the above objective of validating the application of twin technologies of CFD and USD can be achieved in order to link systems of different scales. Refer to section 2.5 and section 1.5 (**Chapter 1**) for more details on the structure of this thesis.

Component of the Membrane rig	Shear rate (s^{-1})
1. Feed tank	33 – 1200
2. Membrane module	4000
3. Pump	20000
4. Pipework	5760
5. Valve	N/A

Table 2.1 Shear rate analysis for components of the membrane filtration rig. Note that the information regarding shear rate for the valve is not yet available in the literature and that negligible damage is assumed when the valve is close to fully opened. For applications requiring partial opening of valve, further investigation may be necessary.

2.2.3 Damage-governing parameters

Different system variables have been used to correlate the extent of material damage to the flow environment. Depending on the nature of the system and problems being addressed, these can be categorised into physical parameters and hydrodynamic parameters. Due to differences in configuration of the two systems being linked, only the latter is relevant in this investigation. These parameters may include shear rate, shear stress, average wall shear stress, Kolmogorov scale of mixing and energy dissipation rate.

Because most flow patterns in the positive displacement pump are a combination of shear and extensional components, which exposes materials to both tangential (shear) and normal stresses, shear stress cannot represent the real flow intensity. Alternatively, the energy dissipation rate was chosen instead in this investigation as a key parameter used to link damage extent to engineering environment. From a practical, qualitative, point of view this term can be thought of as a measure of the 'local' rate at which the mechanical energy introduced into the system through the moving pump vane is converted to heat (Ma et al., 2002). It has been used to characterise the intensity of flow conditions acting on cells for nearly 40 years (Bluestein and Mockros, 1969) and has been extensively used in the fluid mechanical/mixing community for even longer

(Kresta, 1998). Moreover, the linkage of systems of different scales has already been successful based on its maximum value (Neal et al., 2003, Boulding et al., 2002, Boychyn et al., 2001, Boychyn et al., 2004). Hence, the maximum energy dissipation rate (EDR) will be used a key hydrodynamic parameter representing flow conditions within the system being studied and also be maintained in the shear device in order to generate equivalent environment as that in the full-scale system.

2.3 Selection of studied materials

As the magnitude of the key engineering parameter varies with operating conditions of the system, the principal criterion for good test sample is that it must show gradual-response behaviour following exposure to a range of hydrodynamic stresses generated in both USD and full-scale systems. The response of the test materials must also be measurable. In addition, the test sample must also be reproducible in order to minimise batch to batch variations and thus to get accurate results. Moreover, to better understand the breakage characteristics in the process equipment, the studied materials containing particles of different size groups are required.

For the system under investigation where the magnitude of hydrodynamic stresses is quite low for damaging proteins and the effect of air-liquid interface is presumably negligible, using the test system involving soluble groups such as a nucleic acid or protein is not suitable. Protein precipitates may be an option due to their gradual-response behaviour and reproducibility. However, their variety of size classes is quite narrow making them not perfectly suitable to study breakage characteristics in detail. Consequently, a good system may be one involving bacterial cell and mammalian cell suspensions in which cells are treated in such a way that aggregates are formed. Cell aggregates obtained will provide suspensions with a wide variety of size classes and thus allow a gradual response to be observed following the exposure to engineering conditions. In this case, the damage from flow fields are likely to cause a downward shift in particle size distribution, which may be measured directly and instantaneously using a particle sizer. Reproducibility can be maintained between batches by applying shear forces, e.g. via magnetic stirrer, to the suspensions prior to experiments until a certain specified particle size profile is obtained.

2.4 Ultra scale-down device

2.4.1 Selection of a USD device

One of key challenges in this study is to find a USD device, which is suitable for an investigation of the issues involved with a system linkage between a small test system and a large-scale unit. Using only small amount of process materials, the device is employed to mimic the turbulent processing experienced by particles in the large-scale system, thus enabling the effects of energy dissipation rate on the particle size to be assessed more accurately and predictions of large-scale operations to be developed at lower costs.

There are a number of small-scale devices used by several research groups. Some may be physically like the large-scale unit while others may only be reproducible of just part of the flow regime within the equipment and which may have no geometric similarity. Concerning the study of shear damage of materials in bioprocesses, the majority of these take the following forms: scale-down mimics of feed tanks or other process equipment, capillary devices and rotating-disc devices or shear devices.

The scale-down mimics of process equipment are commonly found throughout the bioprocess industry, especially the stirred tank system. These small devices look physically similar to their full-scale counterparts and usually have the same ratios for internal components installed as large-scale units. The advantage of these devices is that the physical properties of the unit are the same in every aspect compared to the large-scale one and thus resources, which include time, manpower, and test materials, can be enormously saved for the shear study. However, in this system only one or a few parameters can be fixed. For example, keeping the impeller speed fixed in the scale-down mimic does not result in the same magnitude of energy dissipation rate generated by the impellers in both systems. As in the present investigation where the maximum energy dissipation rate in the full-scale positive displacement pump needs to be assessed, it may not be practical to produce a scale-down mimic of the pump of smaller size. Even if this is possible, it may take a long time in designing and manufacturing it to the desired specification. As a result, the scale-down mimic approach is not suitable for this investigation.

Like these scale-down mimics, capillary devices are frequently employed in the study of shear. Capillaries have a variety of lengths and diameters allowing effects of different levels of shear and fluid velocity to be studied. The capillary system consists of a capillary itself, driving piston and a collection chamber. The driving piston is used to create high pressure in the test material chamber forcing liquid to go through the capillary whereas the collection chamber is the compartment used to collect high-speed samples. In order to increase the level of shear in the system, either the piston speed needs to be increased or the capillary diameter needs to be decreased or both. However, due to large particles having diameters of up to 2000 μm in the proposed test sample, the blockage and rupture of capillaries may occur in those having small diameters when the system is adjusted to increase the shear level in the capillary. Moreover, low sample volumes of 2-3 mL in the capillary system are inadequate for further measurement or processing. To take a measurement of size distribution using equipment in the present investigation (this shall be explained in **Chapter 4**), a sample having volume of more than 5 mL is needed. Collectively, capillary devices are not suitable for the test materials and the approach used in this study.

The rotating-disc device (Figure 2.3A) or shear device has been used by several research groups, especially at the Department of Biochemical Engineering at University College London. The device has a rotating disc inside the sample chamber. Connected to the motor at the top, the disc is capable of providing rotation between ~3000 rpm to 15000 rpm. It is the rotation of the disc that generates turbulent conditions and energy is dissipated to the fluid in the system. Unlike miniature replica, this shear device can be manufactured without any difficulties and can possibly be used to mimic environments in other process equipment also. With the power pack equipped, the device can rotate and generate a wide range of maximum energy dissipation rates in the studied system. Moreover, cooling can be achieved with ease as the construction material is stainless steel, which has very high thermal conductivity. The sizes of inlet and outlet are big enough for the proposed test materials while the sample volume of 20 mL would also be sufficient for further processing. Unlike the capillary device, the shear device is a contained system. All openings are properly sealed and the possibility of leakage is closest zero. Furthermore, the device has already been successfully used to mimic the turbulent conditions in various continuous flow centrifuges such as disc stack, multichamber bowl and CARR Powerfuge™

(Boychyn et al., 2004, Neal et al., 2003). As a result, the shear device shall be used as USD device to mimic the maximum energy dissipation rate generated in the large-scale system.

2.4.2 Description of shear device

The in-house rotating-disc device, or shear device, used in the study is showed in Figure 2.3A. The prototype of the shear device is explained elsewhere (Levy et al., 1999). To make the device more suitable for this investigation, the dimensions of the disc and the chamber were modified and the configuration of the device as a whole was explained below.

The device comprised of a working chamber, 50 mm in diameter and 11 mm height, and a rotating disc. Both parts were made from a smooth aluminium alloy (Durell, Smith Ltd., UK). The rotating disc was coated with a layer of polytetrafluoroethylene (PTFE) and mounted on a stainless steel shaft. The rotating disc used has a diameter of 40 mm with thickness of 1 mm. The shaft was extended through the top part via an airtight PTFE bearing (clearance of 0.1 mm) and was connected to a high-speed DC motor (Groupher Speed 500 BB RACE, UK). The motor was powered by an in-house power controller unit, which was capable of delivering a range of voltages, thus providing all speeds of rotation from 3000 rpm to 15000 rpm. The speed was measured and displayed digitally through this power controller unit. The top and bottom parts of the chamber also have 1.5 mm diameter ports. They were fitted to remove any air trapped in the liquid suspension during the filling operation, and then sealed with swabable valves before each run. The unit was placed on a 3-leg metal base to reduce vibration during experiments. The schematic diagram including the device's dimensions are shown in Figure 2.3B.

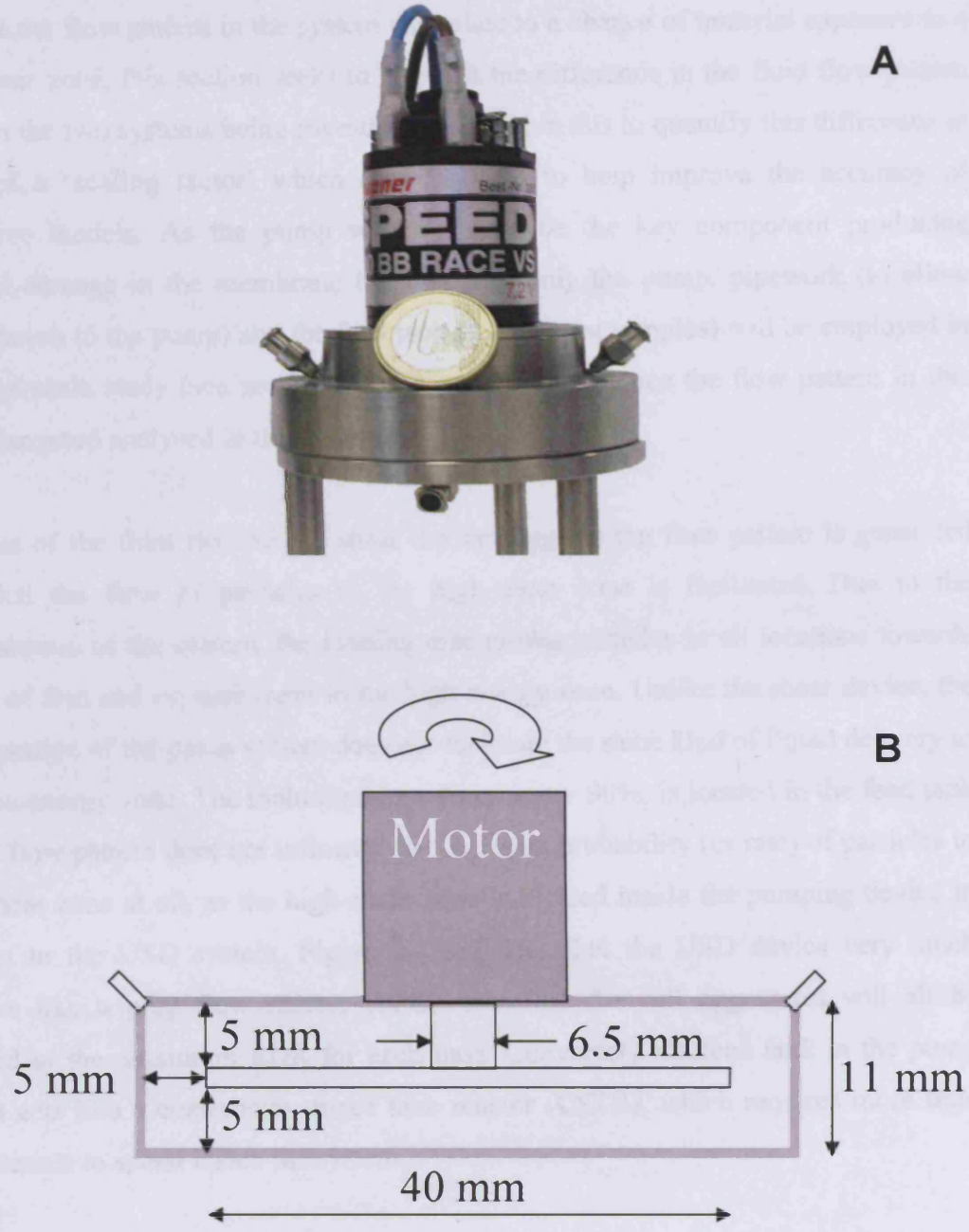

Figure 2.3 An in-house shear device used in the membrane study. The actual device has a motor at the top which draws power from a power controller to move a rotating disc in the working chamber generating shear conditions inside the system **(A)**. A schematic diagram of a shear device shows all dimensions **(B)**. A rotating disc has a diameter of 40 mm and a thickness of 1 mm and it is located at the middle of a 50 mm-diameter chamber. A shaft with diameter of 6.5 mm is connected to a motor, which drives the disc to rotate up to 15000 rpm. The Euro coin shown is 23.25 mm in diameter.

2.4.3 Analysis of flow pattern and scaling factor

Because the flow pattern in the system can relate to a chance of material exposure to a high-shear zone, this section seeks to pinpoint the difference in the fluid flow pattern between the two systems being investigated and from this to quantify this difference in terms of a 'scaling factor' which may be used to help improve the accuracy of predictive models. As the pump was found to be the key component producing material damage in the membrane filtration rig, only the pump, pipework (to allow recirculation to the pump) and the feed tank (to hold test samples) will be employed in the large-scale study (see section 6.1, **Chapter 6**) and hence the flow pattern in this particular setup analysed in this section.

Analysis of the fluid flow in the shear device suggests the flow pattern is generated such that the flow of particles to the high-shear zone is facilitated. Due to the configuration of the system, the rotating disc moves particles in all locations towards the tip of disc and exposes them to the high-energy zone. Unlike the shear device, the configuration of the pump system does not facilitate the same kind of liquid delivery to the high-energy zone. The main liquid medium, say > 90%, is located in the feed tank and its flow pattern does not influence the exposure probability (or rate) of particles to high-shear zone at all, as the high-shear zone is located inside the pumping device in contrast to the USD system. Figure 2.4 indicates that the USD device very much operates like a plug flow reactor (PFR), therefore the cell aggregates will all be exposed to the maximum EDR for each pass. Conversely the feed tank in the pump system acts like a continuous stirred tank reactor (CSTR), which requires more time for materials to spend inside the system.

The flow pattern and mixing in CSTR and PFR systems have been well studied for several decades. In a context of a chance of exposure to the high-shear region, good understanding has been acquired for the residence time distribution (RTD) in these systems. One method describing RTD is a negative step change. The negative step change is a method whereby an inert tracer is added to the system and time measured to record when its concentration approaches zero. This response to a negative step change defines the washout function, *W(t)* (Nauman, 2004):

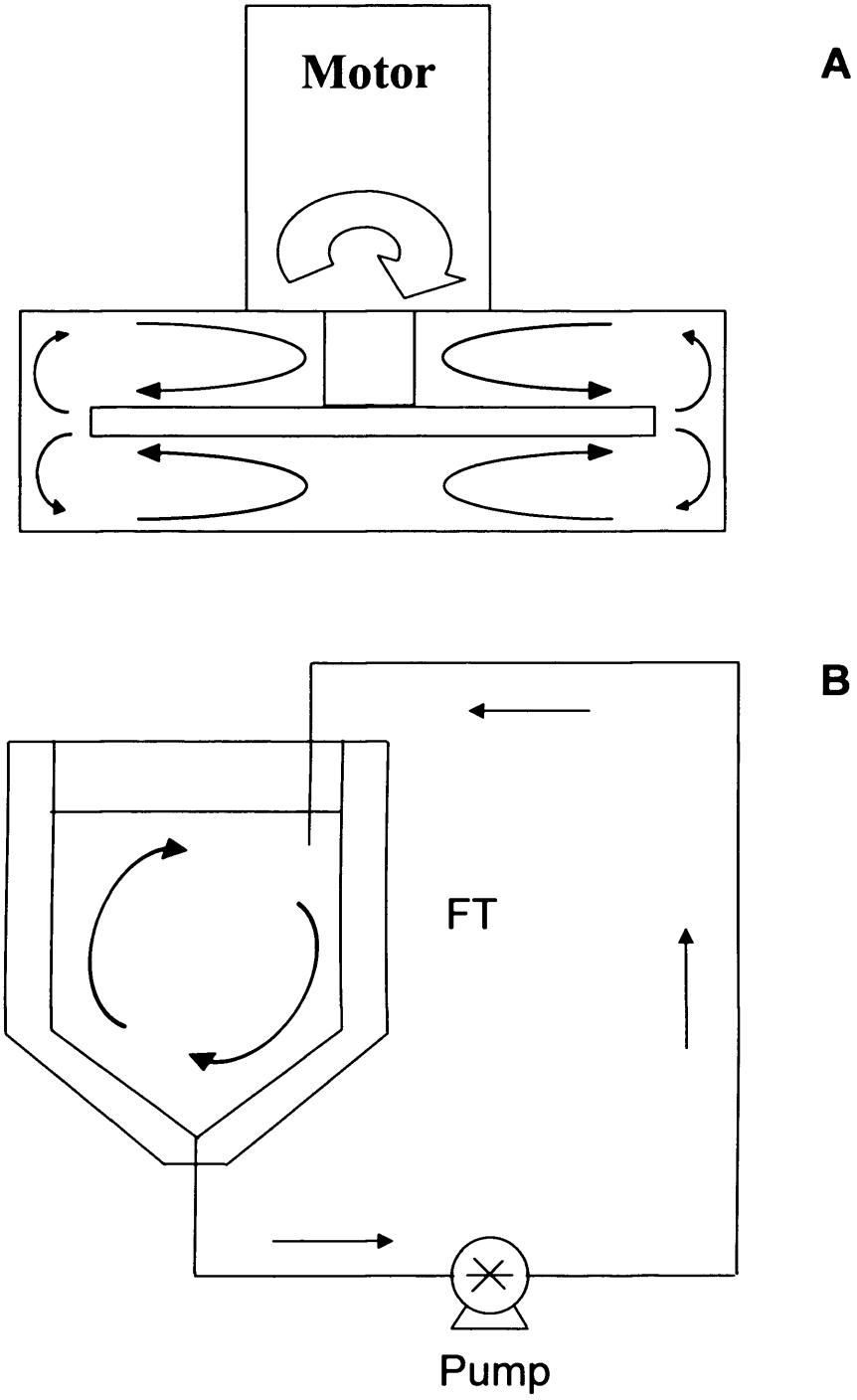

Figure 2.4 Schematics of the flow distribution in USD and large-scale pump systems. The flow pattern in the USD system always transports particles to the tip of the disc, i.e. the high-shear zone **(A)**. This facilitates the increase of the exposure rate of particles to the high-shear zone. In contrast, the configuration of the pump system does not facilitate the increase of this exposure rate. The flow of the majority of liquid, which is located inside the feed tank, does not influence the chance of exposure of particles to the high-shear zone at all compared to that occurring in the USD system **(B)**.

For CSTR, the washout function is:

$$W(t) = e^{-t/\bar{t}} \qquad \textbf{Eq. 2.32}$$

and for PFR, the washout function is:

$$W(t) = 1 \quad \text{when } t < \bar{t} \text{ or} \qquad \textbf{Eq. 2.33}$$

$$W(t) = 0 \quad \text{when } t > \bar{t} \qquad \textbf{Eq. 2.34}$$

where t is the residence time and $\bar{t}$ is mean residence time and $t/\bar{t}$ is dimensionless time. This means that the integrals of the various washout functions all have unit mean so that the various flow systems can be compared independent of system size (Nauman, 2004).

In practice the rules of thumb suggest that an ideal CSTR (continuous stirred tank reactor) behaviour is approached when the mean residence time is 5-10 times the length of time needed to achieve homogeneity (Walas, 1990). Since the tank used during the large-scale pump experiments (see section 6.1, **Chapter 6**) is assumed to be well mixed due to its small volume and high fluid flow rate from the returning stream, the factor of 5 will be applied for these systems. This means that the passage of approximately 5 reactor volumes is required for nearly complete exposure of all the cell aggregates to the pump (due to the feed tank), i.e. compared to 1 reactor volume for the USD device. Consequently, the scaling factor of 5 should later be applied to the predictive models (see **Chapter 5**) to take into account the effect of this difference in systems being compared (see section 8.2.4.3, **Chapter 8**).

2.5 Experimental design

As can be inferred from above analysis, the positive displacement vane pump may represent a key component responsible for material damage in the membrane filtration rig. The analysis of the key hydrodynamic parameter in the pump during its operation is thus essential to facilitate predictions of processing effects. Because a successful linkage requires integration of USD data and the understanding of damage behaviour in the full-scale equipment, USD experiments shall be carried out and damage-predictive models established. These models and their predictions shall then be verified with large-scale experiment using the same test materials.

The investigation is therefore divided into four parts as described below:

1. CFD analysis

Due to the lack of a generalised model for the pumping devices and the complexity of the fluid dynamics of individual pumps, the use of CFD to compute the key hydrodynamic parameter, i.e. maximum turbulence energy dissipation rate, under specific operating conditions is necessary. The technique, which involves drawing detailed structure of equipment of interest into a CFD package and simulating flow fields, would allow these engineering values in the positive displacement pump to be studied and corresponding rotational speeds of the rotating-disc device, or USD device, capable of generating equivalent full-scale conditions to be determined. The recommended disc speeds shall be applied during the USD experiments. These are described in **Chapter 3**.

2. USD experiments

USD experiments shall then be performed using chosen test materials under CFD-recommended rotational speeds. Damage behaviours following exposure of materials to flow fields generated by different disc speeds shall also be analysed. This step is essential to find the corresponding damage in the USD system producing the same magnitude of maximum energy dissipation rate as the full-scale system. Moreover, the relationships between final particle size and maximum energy dissipation rate shall be established to facilitate the predictions in the large-scale. These are presented in **Chapter 4**.

3. Analytical work on scaling methodologies

The pathway of particles recirculated in the membrane process and breakage characteristics of different size groups of particles in suspension shall be examined. Mathematical models used to predict the size change in full-scale system would then be established. These predictive models together with USD experimental data are used to predict particle characteristics of materials subjected to the key engineering parameter in the large-scale system in terms of size reductions against time. To implement these, models predicting final particle size and size changes with time for a given maximum energy dissipation rate shall be given. All these are fully explained in **Chapter 5**.

4. Large-scale verification

Full-scale experiments shall finally be performed in order to verify the predictive models. Experimental data obtained is to be compared with data supplied from predictive models. These are described in detail in **Chapter 6**.

CHAPTER 3 CFD OF PUMPING SYSTEM AND SHEAR DEVICE

Computational fluid dynamics (CFD) technique is introduced to determine the intensity of a maximum energy dissipation rate which in turn governs the damaging condition in the large-scale pumping system. These results were then used to establish the operating conditions in an ultra scale-down (USD) device producing the same damage intensity. In this chapter the underlying CFD theories are first outlined. The CFD simulation studies characterising the energy dissipated in the pump and shear device are then presented. The recommendations on the shear device experiments are also proposed for the prediction of the pumping system.

3.1 Introduction

In this section an outline will be provided of how CFD code works. This will be followed by an explanation of the underlying governing equations of flow and the several numerical solution techniques used. Finally, the theories that numerically describe flow properties in turbulent regime, which is the most commonly encountered flow condition in the process equipment, are explained.

3.1.1 How CFD code works

CFD codes are integrated with numerical algorithms which provide solutions for the flow problems. To facilitate ease of use of the codes in terms of problem parameter input and efficient analysis of results, state-of-art user interfaces are equipped in all commercial packages. The integration of user interfaces into the CFD packages allows software components to be distinguished by three main elements as described below:

3.1.1.1 Pre-processor

The function of this software element is to receive problem parameters into the program through user-friendly interfaces. These inputs include nature of the flow problem and properties of fluid and boundary conditions. Thus, activities in this stage involve:

- specifying the computational domain comprising a number of cells, i.e. the region of flow problem;
- defining boundary conditions at cells that touch domain boundary;
- creating grids (or meshes) of cells (or control volumes or elements);
- selecting physical and/or chemical phenomena for the flow problem;
- specifying fluid properties;
- transforming the problem containing above information into a more recognisable form for further processing by the next element, the solver.

The pre-processor in a certain package may be divided into several distinct sub-elements to perform specific tasks outlined above for more effective execution. Moreover, the pre-processor element in modern CFD packages usually allows access to large databases containing physical properties of common fluids and special chemical and physical process models for faster problem definitions.

3.1.1.2 Solver

This central element of the CFD package contains numerical solution algorithms. Several streams of solution techniques exist including finite difference, finite volume, finite element and spectral methods (refer to section 3.1.2). As simulations in this thesis were carried out using the CFX/ANSYS package which is built upon the finite volume method, the structure of the solver is described based on this method whose executions involve:

- integrating flow governing equations over all control volumes;
- transforming these integral equations into a structure of algebraic equations (discretisation);

- resolving algebraic equations for complex and non-linear physical phenomena through an iterative method. The most popular methods are tri-diagonal matrix algorithm (TDMA) and SIMPLE algorithm.

3.1.1.3 Post-processor

The post-processor element allows the large amount of data obtained from the solver to be visualized in graphics useful to the user. Its capabilities include some or all of the followings:

- display of geometry and its surface (2D and 3D);
- display of grids and specific control volumes;
- view manipulation;
- particle tracking;
- vector plots;
- line and shaded contour plots;
- animation for display of dynamic results;
- data export capability for further processing in other programmes.

3.1.2 Numerical discretisation techniques

The discretisation process allows each term expressed in the partial differential equations governing fluid flows to be rewritten in such the form (so-called numerical analogues) that the computer can understand and calculate their solutions. Several discretisation techniques exist as described below. The first three are the most commonly used techniques in the CFD code. The main differences among numerical discretisation techniques are in the way the flow variables are approximated and the way numerical analogues are generated (discretisation process).

3.1.2.1 Finite difference method

In this method Taylor series expansion is utilised to describe the unknown flow variable ϕ by means of derivatives of a flow variable representing the differences between its values at various node points in co-ordinate lines or time. The complete equations of Taylor series expansions, which contain infinite terms, are usually

truncated to calculate approximations of derivatives of ϕ of these points, although this may lead to errors in numerical calculations, so-called the truncation error. More points may be used in the Taylor series in order to obtain more accurate approximates. Through geometrical relationships of these points, finite difference equations, i.e. central, forward and backward difference, can be generated and then used to replace derivatives in the flow-governing partial differential equations producing the numerical analogue. In the computational domain many points are placed and, at each point, the difference form for the derivatives of flow variables is written to create relationships of flow variables between that point and its neighbouring points. After equations of all points in the domain are acquired, the flow problem can be solved numerically.

3.1.2.2 Finite volume method

Currently the finite volume method is the most popular method employed in CFD. Most recognized codes including CFX/ANSYS, STAR-CD, PHOENICS and FLUENT are constructed based on this method, which is generally a special finite difference formulation. Like the finite difference method, the numerical equations at a given point derived by the finite volume method can be obtained from values of flow variables at its neighboring points. The Cell Centered (CC) variable arrangement allows less complex implementations and is thus the most popular arrangement used to discretise the partial differential equations governing flow problems. In this technique, the finite volume (or cell), its neighboring volumes and their centroids are used as a starting point to derive the definition of variables. Through the expression of a variable in terms of its first derivatives, second derivatives and real values at the volume centroids and faces and previously described executions (see *Solver* in section 3.1.1.2), the finite volume formulation for flow variables can be obtained. However, this technique poses higher risks of generating truncation errors, especially when the mesh deviates from uniform rectangles. Overall, the fundamental based on this method, which is the conservation of a flow variable ϕ within a finite control volume, can be expressed as a balance between several processes:

$$\begin{bmatrix}\text{Rate of change of}\\ \phi \text{ in the control}\\ \text{volume with}\\ \text{respect to time}\end{bmatrix} = \begin{bmatrix}\text{Net rate of increase}\\ \text{of } \phi \text{ due to}\\ \text{convection into}\\ \text{the control volume}\end{bmatrix} + \begin{bmatrix}\text{Net rate of increase}\\ \text{of } \phi \text{ due to}\\ \text{diffusion into}\\ \text{the control volume}\end{bmatrix} + \begin{bmatrix}\text{Net rate of}\\ \text{creation of } \phi\\ \text{inside the}\\ \text{control volume}\end{bmatrix}$$

Eq. 3.1

3.1.2.3 Finite element method

In this method, the computational domain is divided into a number of 'elements' and each element has numerical equations describing flow variables, which are produced independently of all other elements. The method uses simple functions, e.g. linear, quadratic or cubic, to describe the local variation of a flow variable ϕ in each element. In order to describe the whole flow field in the computational domain, the variation of flow variables in all elements is summed up. The decoupling structure of the finite element method facilitates more comprehensible organization of the program for programmers and thus eases of new element addition.

To overcome the problem of defining a second derivative of flow variables using a linear function assumption, the partial differential equation is multiplied by an unknown function and the entire equation is then integrated by parts over the domain of interest. This process allows the transformation of the second order derivative to products of first order derivatives, though additional terms involving domain boundary are introduced and the unknown function needs to be described.

3.1.2.4 Spectral method

The Spectral method utilizes Fourier series or series of Chebyshev polynomials to estimate the unknowns. Unlike above methods, approximations used in the Spectral method are not local but valid throughout the entire flow domain. Again these series are usually truncated and used to replace the unknown in the partial differential equations describing flows. Algebraic equations for the coefficients of the Fourier series or series of Chebyshev can be obtained from a weighted residual concept or by making the approximate function to match with the exact solution at a number of grid points.

3.1.3 Flow governing equations

The mathematical equations governing fluid flow and heat transfer used to solve the time-dependent 3D flow problems can be derived from and represent the conservation principles of mass, energy and momentum (Versteeg and Malalasekera, 2007). These principles are:

1. The conservation of mass (the continuity equation)

The principle is related to a mass balance for the fluid element, i.e. the rate of increase of mass inside the fluid element equals to the net rate of flow of mass into the element. This expression can be mathematically described for a compressible fluid by the following partial differential equation (PDE):

$$\frac{\partial \rho}{\partial t} + \frac{\partial(\rho u)}{\partial x} + \frac{\partial(\rho v)}{\partial y} + \frac{\partial(\rho w)}{\partial z} = 0 \qquad \textbf{Eq. 3.2}$$

where u, v and w are the velocities in the x, y, z co-ordinates, respectively. For incompressible fluids, i.e. constant-density fluids, the equation 3.2 becomes:

$$\frac{\partial u}{\partial x} + \frac{\partial v}{\partial y} + \frac{\partial w}{\partial z} = 0 \qquad \textbf{Eq. 3.3}$$

Equation 3.3 evidently applies to the system studied in this thesis. However, for completeness the analysis will continue with a general solution for all fluid types as this is what is traditionally provided in all well-known CFD packages.

2. Newton's second law (the momentum equation)

The law states that the rate of change of momentum of a fluid particle equals to the sum of all forces F acting on it. This can be written as:

$$F = m \cdot a \qquad \textbf{Eq. 3.4}$$

where m is the fluid mass and a is the fluid's acceleration. This can be rewritten in the PDE form for each Cartesian co-ordinate (x, y, z) in terms of the rate of increase of momentum, surface forces and body forces:

$$\frac{\partial(-p+\tau_{xx})}{\partial x}+\frac{\partial \tau_{yx}}{\partial y}+\frac{\partial \tau_{zx}}{\partial z}+S_{Mx} = \rho\frac{Du}{Dt} \qquad \textbf{Eq. 3.5}$$

$$\frac{\partial \tau_{xy}}{\partial x}+\frac{\partial(-p+\tau_{yy})}{\partial y}+\frac{\partial \tau_{zy}}{\partial z}+S_{My} = \rho\frac{Dv}{Dt} \qquad \textbf{Eq. 3.6}$$

$$\frac{\partial \tau_{xz}}{\partial x}+\frac{\partial \tau_{yz}}{\partial y}+\frac{\partial(-p+\tau_{zz})}{\partial z}+S_{Mz} = \rho\frac{Dw}{Dt} \qquad \textbf{Eq. 3.7}$$

where p is the pressure or a normal stress, τ_{ij} is the viscous stress acting in the j-direction on a surface normal to the i-direction, S_M accounts for any sources or sinks that either create or destroy ϕ and $D\phi/Dt$ represents the total or substantive derivative of ϕ with respect to time following a fluid particle.

3. The first law of thermodynamics (the energy conservation equation)

The principle states that the rate of change of energy equals to the sum of the rate of work done on and the rate of heat added to a fluid particle. This can be expressed in terms of the following PDE:

$$\rho\frac{DE}{Dt} = -\text{div}(p\mathbf{u})+\begin{bmatrix} \frac{\partial(u\tau_{xx})}{\partial x}+\frac{\partial(v\tau_{xy})}{\partial x}+\frac{\partial(w\tau_{xz})}{\partial x}+ \\ \frac{\partial(u\tau_{yx})}{\partial y}+\frac{\partial(v\tau_{yy})}{\partial y}+\frac{\partial(w\tau_{yz})}{\partial y}+ \\ \frac{\partial(u\tau_{zx})}{\partial z}+\frac{\partial(v\tau_{zy})}{\partial z}+\frac{\partial(w\tau_{zz})}{\partial z} \end{bmatrix}+\text{div}(k\,\text{grad}\,T)+S_E \qquad \textbf{Eq. 3.8}$$

where E is the specific energy of a fluid, which is defined as the sum of the internal (thermal) energy i and kinetic energy $\frac{1}{2}(u^2+v^2+w^2)$. k is the heat conductivity, $\mathbf{u}$

denotes the velocity field, T is the temperature and S_E accounts for any sources or sinks that either create or destroy the unknown flow variable ϕ.

Enthalpy equation can also be obtained by rearranging the Equation 3.8:

$$\frac{\partial(\rho h_0)}{\partial t}+\operatorname{div}(\rho h_0\,\mathbf{u})=\frac{\partial p}{\partial t}+\begin{bmatrix}\frac{\partial(u\tau_{xx})}{\partial x}+\frac{\partial(v\tau_{xy})}{\partial x}+\frac{\partial(w\tau_{xz})}{\partial x}+\\ \frac{\partial(u\tau_{yx})}{\partial y}+\frac{\partial(v\tau_{yy})}{\partial y}+\frac{\partial(w\tau_{yz})}{\partial y}+\\ \frac{\partial(u\tau_{zx})}{\partial z}+\frac{\partial(v\tau_{zy})}{\partial z}+\frac{\partial(w\tau_{zz})}{\partial z}\end{bmatrix}+\operatorname{div}(k\,\operatorname{grad}T)+S_E \qquad \textbf{Eq.3.9}$$

where h and h_0 are the specific enthalpy and specific total enthalpy of a fluid respectively and can be expressed as:

$$h = i + p/\rho \qquad \textbf{Eq.3.10}$$

$$h_0 = h+\frac{1}{2}\left(u^2+v^2+w^2\right) = E + p/\rho \qquad \textbf{Eq.3.11}$$

4. Equations of state

In order to obtain the relationships among thermodynamic variables, i.e. p, ρ, i and T, the system state of thermodynamic equilibrium is assumed. The principle suggests that the fluid can adjust itself thermodynamically to a new environment so rapidly such that the changes of its properties may occur immediately. In such a condition the state of the fluid element can be described by the equation of states which relate two state variables, i.e. ρ and T, to other variables. The equations of state for pressure and specific internal energy are:

$$p = p(\rho, T) \qquad \textbf{Eq. 3.12}$$

$$i = i(\rho, T) \qquad \textbf{Eq. 3.13}$$

For an ideal gas, these equations become:

$$p = \rho RT \qquad \textbf{Eq. 3.14}$$

$$i = C_v T \qquad \textbf{Eq. 3.15}$$

where R is the gas constant and C_v is the specific heat capacity for a constant volume process.

5. Navier-Stokes equations

At this point the viscous stress component τ_{ij} is still unknown. For Newtonian fluids this is proportional to the local strain rate (or deformation rate) which consists of the linear deformation rate and volumetric deformation rate. In 3D the linear deformation rate contain nine components, six of which are independent in isotropic fluids (Schlichting, 1979). Six shearing components and three elongating components are shown as follows:

$$s_{xy} = s_{yx} = \frac{1}{2}\left(\frac{\partial u}{\partial y} + \frac{\partial v}{\partial x}\right) \qquad \textbf{Eq. 3.16}$$

$$s_{xz} = s_{zx} = \frac{1}{2}\left(\frac{\partial u}{\partial z} + \frac{\partial w}{\partial x}\right) \qquad \textbf{Eq. 3.17}$$

$$s_{yz} = s_{zy} = \frac{1}{2}\left(\frac{\partial v}{\partial z} + \frac{\partial w}{\partial y}\right) \qquad \textbf{Eq. 3.18}$$

$$s_{xx} = \frac{\partial u}{\partial x}, \quad s_{yy} = \frac{\partial v}{\partial y}, \quad s_{zz} = \frac{\partial w}{\partial z} \qquad \textbf{Eq. 3.19}$$

And the volumetric deformation rate is defined as:

$$\frac{\partial u}{\partial x} + \frac{\partial v}{\partial y} + \frac{\partial w}{\partial z} = \operatorname{div} \mathbf{u} \qquad \textbf{Eq. 3.20}$$

Viscous stresses in 3D can then be defined through the combined set of above strain rates and viscosities based on the Newton's law of viscosity for compressible flows:

$$\tau_{xy} = \tau_{yx} = \mu\left(\frac{\partial u}{\partial y}+\frac{\partial v}{\partial x}\right) \qquad \textbf{Eq. 3.21}$$

$$\tau_{xz} = \tau_{zx} = \mu\left(\frac{\partial u}{\partial z}+\frac{\partial w}{\partial x}\right) \qquad \textbf{Eq. 3.22}$$

$$\tau_{yz} = \tau_{zy} = \mu\left(\frac{\partial v}{\partial z}+\frac{\partial w}{\partial y}\right) \qquad \textbf{Eq. 3.23}$$

$$\tau_{xx} = 2\mu\frac{\partial u}{\partial x}+\lambda\,\mathrm{div}\,\mathbf{u}, \quad \tau_{yy} = 2\mu\frac{\partial v}{\partial y}+\lambda\,\mathrm{div}\,\mathbf{u}, \quad \tau_{zz} = 2\mu\frac{\partial w}{\partial z}+\lambda\,\mathrm{div}\,\mathbf{u} \qquad \textbf{Eq. 3.24}$$

From above the first viscosity μ links viscous stresses to linear deformations whereas the second viscosity λ links viscous stresses to volumetric deformations. With new expressions of viscous stresses in terms of gradients of velocity components, Equations 3.5 to 3.7 can be rearranged to give Navier-Stokes equations:

$$-\frac{\partial p}{\partial x}+\frac{\partial}{\partial z}\left[\mu\left(\frac{\partial u}{\partial z}+\frac{\partial w}{\partial x}\right)\right]+\frac{\partial}{\partial y}\left[\mu\left(\frac{\partial u}{\partial y}+\frac{\partial v}{\partial x}\right)\right]+\frac{\partial}{\partial x}\left[2\mu\frac{\partial u}{\partial x}+\lambda\,\mathrm{div}\,\mathbf{u}\right]+S_{Mx}=\rho\frac{Du}{Dt}$$

Eq. 3.25

$$-\frac{\partial p}{\partial y}+\frac{\partial}{\partial z}\left[\mu\left(\frac{\partial v}{\partial z}+\frac{\partial w}{\partial y}\right)\right]+\frac{\partial}{\partial x}\left[\mu\left(\frac{\partial v}{\partial x}+\frac{\partial u}{\partial y}\right)\right]+\frac{\partial}{\partial y}\left[2\mu\frac{\partial v}{\partial y}+\lambda\,\mathrm{div}\,\mathbf{u}\right]+S_{My}=\rho\frac{Dv}{Dt}$$

Eq. 3.26

$$-\frac{\partial p}{\partial z}+\frac{\partial}{\partial x}\left[\mu\left(\frac{\partial u}{\partial z}+\frac{\partial w}{\partial x}\right)\right]+\frac{\partial}{\partial y}\left[\mu\left(\frac{\partial v}{\partial z}+\frac{\partial w}{\partial y}\right)\right]+\frac{\partial}{\partial z}\left[2\mu\frac{\partial w}{\partial z}+\lambda\,\mathrm{div}\,\mathbf{u}\right]+S_{Mz}=\rho\frac{Dw}{Dt}$$

Eq. 3.27

6. Transport equations

The basic transport equation is used as a starting point in the finite volume method for numerical solution procedures. It emphasizes several transport processes including rate of change, convection, diffusion and sources and can be essentially expressed in words for general variable ϕ as:

$$\begin{bmatrix}\text{Rate of increase}\\ \text{of } \phi \text{ of}\\ \text{fluid element}\end{bmatrix} + \begin{bmatrix}\text{Net rate of flow}\\ \text{of } \phi \text{ out of}\\ \text{fluid element}\end{bmatrix} = \begin{bmatrix}\text{Rate of increase}\\ \text{of } \phi \text{ due to}\\ \text{diffusion}\end{bmatrix} + \begin{bmatrix}\text{Rate of increase}\\ \text{of } \phi \text{ due to sources}\end{bmatrix}$$

Eq. 3.28

Mathematically, this can be expressed as:

$$\frac{\partial(\rho\phi)}{\partial t} + \operatorname{div}(\rho\phi\,\mathbf{u}) = \operatorname{div}(\Gamma \operatorname{grad}\phi) + S_\phi \qquad \textbf{Eq. 3.29}$$

where S_ϕ accounts for any sources or sinks that either create or destroy ϕ and Γ is the diffusion coefficient or diffusivity. By integrating the Equation 3.29 over a 3D control volume (CV) and applying divergence theorem to convective term and diffusive term, the Equation 3.29 can be expressed in a useful integrated form for steady state condition:

$$\int_A \mathbf{n}.(\rho\phi\,\mathbf{u})\mathrm{d}A = \int_A \mathbf{n}.(\Gamma \operatorname{grad}\phi)\mathrm{d}A + \int_{CV} S_\phi \mathrm{d}V \qquad \textbf{Eq. 3.30}$$

where V denotes the volume of 3D space, $\mathbf{n}$ is the outward pointing unit normal field of the control volume's boundary and A is surface area of a control volume. For time-dependent flows, the transport equation can be expressed as:

$$\int_{\Delta t}\frac{\partial}{\partial t}\left(\int_{CV}\rho\phi\,\mathrm{d}V\right)\mathrm{d}t + \int_{\Delta t}\int_A \mathbf{n}.(\rho\phi\,\mathbf{u})\mathrm{d}A\mathrm{d}t = \int_{\Delta t}\int_A \mathbf{n}.(\Gamma \operatorname{grad}\phi)\mathrm{d}A\mathrm{d}t + \int_{\Delta t}\int_{CV} S_\phi \mathrm{d}V\mathrm{d}t \qquad \textbf{Eq. 3.31}$$

3.1.4 Turbulence

Steady and smooth flows can be observed at low Reynolds number and are described as laminar. Adjacent fluid layers move past each other in parallel with no disruption between layers in the laminar flow regime whose behaviour can be thoroughly described using the above equations. Many flows encountered in bioprocess equipment, however, are generally in turbulent motion having high Reynolds number. Generally, for subsonic and incompressible flows, the transition processes from laminar to turbulence involve small-disturbance amplifications, the development of areas with high shear small-scale motions and finally growth and uniting of these areas into fully turbulent flows. Turbulence is then maintained by the shear in the mean flow. Eddies of various sizes are generated facilitating exchanges of mass, momentum and heat among fluid particles in different areas of the system. The largest turbulent eddies obtain energy from the mean flow and pass it onto smaller eddies. Eventually, the smallest eddies impart their energies to surrounding fluids, which in turn convert into thermal internal energy, resulting in increased energy losses linked to turbulence. In addition, the inherited nature of velocity fluctuations associated with turbulence also creates additional turbulent stresses, i.e. Reynolds stresses, forcing the turbulent flow to be treated differently.

3.1.4.1 Descriptor of turbulent flow

Due to the random nature of the turbulent regime, the flow property is described and broken down into two parts: a steady mean-value component Φ and statistical time-dependent fluctuating component $\varphi'(t)$. This is called the Reynolds decomposition, which defines the flow property φ as the sum of these components. The definitions of mean Φ and some other important descriptors of the time varying component φ', which can be described in terms of its statistics, are shown as follows.

Mean

The mean of flow property Φ is defined as:

$$\Phi = \frac{1}{\Delta t}\int_0^{\Delta t}\varphi(t)\,\mathrm{d}t \qquad \textbf{Eq. 3.32}$$

where Δt is a small interval of time while the mean of the fluctuating component φ', which equals to zero, is defined as:

$$\overline{\varphi'} = \frac{1}{\Delta t}\int_0^{\Delta t}\varphi'(t)\,dt \equiv 0 \qquad \textbf{Eq. 3.33}$$

Theoretically, the time interval should be infinity. For steady mean flows, however, an interval that is larger than the time scale related to the slowest change of flow property due to the largest eddies would be sufficient for the time average in Equation 3.33. For time varying flows a number of identical experiments must be carried out to obtain the instant values of the flow property in order to determine its mean.

Variance and root mean square (r.m.s.)

These descriptors are used to quantify the spread of the fluctuating component φ':

$$\overline{(\varphi')^2} = \frac{1}{\Delta t}\int_0^{\Delta t}(\varphi')^2\,dt \qquad \textbf{Eq. 3.34}$$

$$\varphi_{rms} = \sqrt{\overline{(\varphi')^2}} = \left[\frac{1}{\Delta t}\int_0^{\Delta t}(\varphi')^2\,dt\right]^{1/2} \qquad \textbf{Eq. 3.35}$$

For the velocity these variances can be used to determine the total kinetic energy per unit mass at any position k, which in turn links to the turbulence intensity T_i as follows:

$$k = \frac{1}{2}\left(\overline{u'^2} + \overline{v'^2} + \overline{w'^2}\right) \qquad \textbf{Eq. 3.36}$$

$$T_i = \frac{\sqrt{\left(\frac{2}{3}k\right)}}{U_{ref}} \qquad \textbf{Eq. 3.37}$$

where U_{ref} is the reference mean flow velocity.

Moments of different fluctuating variables

Moments can be formed from pairs of different variables describing characteristics of the turbulent fluctuations. The second moment of two properties, e.g. φ and ψ, are expressed as:

$$\overline{\varphi'\psi'} = \frac{1}{\Delta t}\int_0^{\Delta t} \varphi'\psi' \, dt \qquad \textbf{Eq. 3.38}$$

Third and fourth moments

These statistical descriptors of turbulence indicate the asymmetry (skewness) and peakedness (kurtosis), respectively:

$$\overline{(\varphi')^3} = \frac{1}{\Delta t}\int_0^{\Delta t} (\varphi')^3 \, dt \qquad \textbf{Eq. 3.39}$$

$$\overline{(\varphi')^4} = \frac{1}{\Delta t}\int_0^{\Delta t} (\varphi')^4 \, dt \qquad \textbf{Eq. 3.40}$$

3.1.4.2 Turbulent governing equations

Due to the fluctuating nature of turbulence, only its time-averaged property is of great interest to most engineers and thus its mathematical description will be different from the laminar flow. Moreover, the velocity fluctuation in turbulence also created additional shear turbulent stresses, i.e. Reynolds stresses. These Reynolds stresses cause six extra stress terms, i.e. three shear stresses and three normal stresses, to be integrated in the governing equations. Subsequently, compressible turbulent flows are governed by the following equations (Versteeg and Malalasekera, 2007):

Continuity equation

$$\frac{\partial \overline{\rho}}{\partial t} + \mathrm{div}(\overline{\rho}\,\widetilde{\mathbf{U}}) = 0 \qquad \textbf{Eq. 3.41}$$

Reynolds equations

$$\frac{\partial(\bar{\rho}\tilde{U})}{\partial t}+\operatorname{div}\left(\bar{\rho}\tilde{U}\tilde{\mathbf{U}}\right)=-\frac{\partial \bar{P}}{\partial x}+\operatorname{div}\left(\mu \operatorname{grad}\tilde{U}\right)+\left[-\frac{\partial\left(\overline{\bar{\rho}u'^{2}}\right)}{\partial x}-\frac{\partial\left(\overline{\bar{\rho}u'v'}\right)}{\partial y}-\frac{\partial\left(\overline{\bar{\rho}u'w'}\right)}{\partial z}\right]+S_{Mx}$$

Eq. 3.42

$$\frac{\partial(\bar{\rho}\tilde{V})}{\partial t}+\operatorname{div}\left(\bar{\rho}\tilde{V}\tilde{\mathbf{U}}\right)=-\frac{\partial \bar{P}}{\partial y}+\operatorname{div}\left(\mu \operatorname{grad}\tilde{V}\right)+\left[-\frac{\partial\left(\overline{\bar{\rho}v'^{2}}\right)}{\partial y}-\frac{\partial\left(\overline{\bar{\rho}u'v'}\right)}{\partial x}-\frac{\partial\left(\overline{\bar{\rho}v'w'}\right)}{\partial z}\right]+S_{My}$$

Eq. 3.43

$$\frac{\partial(\bar{\rho}\tilde{W})}{\partial t}+\operatorname{div}\left(\bar{\rho}\tilde{W}\tilde{\mathbf{U}}\right)=-\frac{\partial \bar{P}}{\partial z}+\operatorname{div}\left(\mu \operatorname{grad}\tilde{W}\right)+\left[-\frac{\partial\left(\overline{\bar{\rho}w'^{2}}\right)}{\partial z}-\frac{\partial\left(\overline{\bar{\rho}u'w'}\right)}{\partial x}-\frac{\partial\left(\overline{\bar{\rho}v'w'}\right)}{\partial y}\right]+S_{Mz}$$

Eq. 3.44

Scalar transport equation

$$\frac{\partial\left(\bar{\rho}\tilde{\Phi}\right)}{\partial t}+\operatorname{div}\left(\bar{\rho}\tilde{\Phi}\tilde{\mathbf{U}}\right)=\operatorname{div}\left(\Gamma_{\Phi}\operatorname{grad}\tilde{\Phi}\right)+\left[-\frac{\partial\left(\overline{\bar{\rho}u'\varphi'}\right)}{\partial x}-\frac{\partial\left(\overline{\bar{\rho}v'\varphi'}\right)}{\partial y}-\frac{\partial\left(\overline{\bar{\rho}w'\varphi'}\right)}{\partial z}\right]+S_{\Phi}$$

Eq. 3.45

where the tilde denotes Favre-averaged or density-weighted variable and the overbar denotes a time-averaged variable.

3.1.4.3 Turbulence models

Several turbulent models exist to facilitate fluid problem solving using the CFD technique to predict the flow variables in turbulent conditions. Most of these were constructed based on the time-averaged Reynolds equations. The most common turbulence models including their advantages and disadvantages are described as follows (Versteeg and Malalasekera, 1995):

Mixing length model

This turbulence model is one of the earliest models. It is easy to implement and cheap in terms of computing resources. This model is provides good predictions for thin shear layers, e.g. jets, mixing layers, wakes and boundary layers. Although the model is well established, it is completely incapable of describing flows with separation and recirculation and can only calculate mean flow properties and turbulent shear stress.

k-ε model

Like the mixing length model, the k-ε model is very well-established and it is the most widely validated model. It is the simplest turbulence model for which only initial and/or boundary conditions need to be supplied. It has provided excellent performance for many industrial relevant flows. The disadvantage of the k-ε model is that it is more expensive than the mixing length model, based on computing time due to the extra two partial differential equations. It also gives poor performance in some unconfined flows, flows with large extra strains (e.g. curved boundary layers, swirling flows) and fully developed flows in non-circular ducts.

Reynolds stress equation model (RSM)

The model is the most general form of all classical turbulence models. Like the k-ε model, only initial and/or boundary conditions need to be supplied. The model also gives very accurate calculation of mean flow properties and all Reynolds stresses for many simple and more complex flows including wall jets, asymmetric channel and non-circular duct flows and curved flows. However, it needs a very large computing cost and it is not as widely validated as the k-ε model. Another disadvantage is that the model performs just as poorly as the k-ε model in some flows owing to identical problems with ε-equation modelling (e.g. axisymmetric jets and unconfined recirculation flows).

Algebraic stress model (ASM)

The algebraic stress model is similar to the Reynolds stress model. The main difference is that the individual stress components of the Reynolds stresses are solved algebraically. The model is a cheap model to account for Reynolds stress anisotropy because it potentially combines the generality approach of the RSM (good modelling

of buoyancy and rotation effects possible) with the economy of the k-ε model. It has successfully applied to isothermal and buoyant thin shear layers and if convection and diffusion terms are negligible the ASM performs as well as the RSM. The model has the same disadvantages as RSM applies due to the similarity in both models. It is also not as widely validated as the mixing length and k-ε models and the model is severely predicted in flows where transport assumptions for convective and diffusive effects do not apply - validation is necessary to define performance limit. It is only slightly more expensive than the k-ε model (two PDEs and a system of algebraic equations).

Large eddy simulation models

These models are used to solve the time-dependent flow equations for the mean flow and the largest eddies and where the effects of the smaller eddy are modelled. However, large eddy simulation models are at present at the research stage and the calculations are too costly to merit consideration in general purpose computation at present.

3.1.4.4 The k-ε model

The k-ε model is one of estimation methods of solving complex equations for turbulent flow. Because this well-established model is employed in both systems being studied, this section seeks to present its flow governing equations in brief in order to help the understanding of fundamentals behind this model. For a standard k-ε model, two transport equations are used to describe the turbulent kinetic energy k and the rate of dissipation of turbulent kinetic energy per unit mass ε (Launder and Spalding, 1974, Versteeg and Malalasekera, 2007):

$$\frac{\partial(\rho k)}{\partial t} + \mathrm{div}(\rho k \mathbf{U}) = \mathrm{div}\left[\frac{\mu_t}{\sigma_k}\,\mathrm{grad}\,k\right] + 2\mu_t S_{ij} . S_{ij} - \rho\varepsilon \qquad \textbf{Eq. 3.46}$$

$$\frac{\partial(\rho \varepsilon)}{\partial t} + \mathrm{div}(\rho \varepsilon \mathbf{U}) = \mathrm{div}\left[\frac{\mu_t}{\sigma_\varepsilon}\,\mathrm{grad}\,\varepsilon\right] + C_{1\varepsilon}\frac{\varepsilon}{k} 2\mu_t S_{ij} . S_{ij} - C_{2\varepsilon}\rho\frac{\varepsilon}{k} \qquad \textbf{Eq. 3.47}$$

where μ_t is the eddy viscosity and is defined as:

$$\mu_t = C\rho\vartheta\ell = \rho C_\mu \frac{k^2}{\varepsilon} \qquad \textbf{Eq. 3.48}$$

and S_{ij} is a mean component of the rate of deformation of a fluid element in a turbulent flow while C_μ, σ_k, σ_ε, $C_{1\varepsilon}$ and $C_{2\varepsilon}$ are adjustable constants. In words these equations can be written:

$$\begin{bmatrix}\text{Rate of}\\ \text{change of}\\ k \text{ or } \varepsilon\end{bmatrix} + \begin{bmatrix}\text{Transport}\\ \text{of } k \text{ or } \varepsilon \text{ by}\\ \text{convection}\end{bmatrix} = \begin{bmatrix}\text{Transport}\\ \text{of } k \text{ or } \varepsilon\\ \text{by diffusion}\end{bmatrix} + \begin{bmatrix}\text{Rate of}\\ \text{production}\\ \text{of } k \text{ or } \varepsilon\end{bmatrix} - \begin{bmatrix}\text{Rate of}\\ \text{destruction}\\ \text{of } k \text{ or } \varepsilon\end{bmatrix}$$

Eq. 3.49

To compute the additional Reynolds stresses, Boussinesq relationship was used:

$$-\rho\overline{u'_i u'_j} = \mu_t\left(\frac{\partial U_i}{\partial x_j} + \frac{\partial U_j}{\partial x_i}\right) - \frac{2}{3}\rho k\delta_{ij} = 2\mu_t S_{ij} - \frac{2}{3}\rho k S_{ij} \qquad \textbf{Eq. 3.50}$$

3.2 Materials and methods

Because of flow complexity in the pumping system being studied, the CFD technique was employed to analyse the flow in the pump and to determine the magnitude of maximum energy dissipation rate (EDR) generated in the unit under specific operating conditions. Based on the level of maximum EDR found in the pump, the same technique was later utilised to obtain the equivalent rotational speed for the shear device (USD device) causing the same damage extent. The rotation speed obtained together with USD experimental results (**Chapter 4**) will then form parts of the predictive model for large-scale operations in later chapter (**Chapter 5**).

3.2.1 Hardware

A Dell 340 Precision Workstation, with 1GB RAM, running Windows NT 4.0, was used for all computations.

3.2.2 Software

The commercial CFD package used in modelling the flow field in the pumping system and shear device is the CFX 4.4 developed by AEA Technology, Oxfordshire, United Kingdom (the company was later restructured to become ANSYS, PA, USA). The CFX 4.4 software is built upon a finite volume method in solving the discretised equations. The package comprises CFX Build, CFX Solver and CFX Analyse. It has capabilities in solving both laminar flow and turbulent flow in both incompressible and compressible problems. For turbulent flow, a number of turbulence models are available; the k-ε model and a low Reynolds number k-ε model, an RNG k-ε model, two low Reynolds number k-ω models, an algebraic Reynolds stress model, a differential Reynolds stress model and a differential Reynolds flux model (AEA-Technology, 1999).

A FORTRAN compiler (Compaq Visual FORTRAN Standard Edition 6.6.B, Compaq Computer Corporation, Texas, USA) was employed for the specification of the problem's domain and relevant boundary conditions through the FORTRAN file.

3.2.3 Equipment

The pump used in this investigation is of a positive displacement rotary vane type (P01011, Bechtech, UK). It has 4 carbon vanes rotating inside forcing liquid to move from the inlet to the outlet and has a capacity delivering liquid medium between 3.66 L min^{-1} (at 300 rpm) to 18.36 L min^{-1} (at 1500 rpm). Figure 3.1A shows the internal structure of this type of pump.

The shear device was used to represent the USD system. Its configurations and dimensions have already described in section 2.4.2 (**Chapter 2**).

3.2.4 CFD problem's specifications

For all simulations, the fluid was assumed to be Newtonian (constant μ), isothermal and incompressible and the properties of water including density and viscosity were applied as fluid properties. The test material contained 10% v/v solids (see section 4.1.1, **Chapter 4**). While this material was at rest it exhibited pseudoplastic behaviour,

i.e. the viscosity decreases with increasing rate of shear. However, once sheared its rheological behaviour changed to be that of Newtonian fluids due to size change of aggregates and particles in a suspension. The experiments measuring shear stress and velocity gradient have been carried out at time zero and a very early stage of both scales (after 15 s in the USD device and after 2 min in the large-scale pump experiment) in order to confirm this behaviour and subsequent constant viscosity of this test material. As a result, it was assumed in the CFD simulation that this material had Newtonian behaviour. Additionally, the suspended cell is assumed to have no effect on the fluid flow pattern. Following the comparisons of a succession of finer meshes, a small enough grid size was chosen for pump and shear device to ensure that results in both systems are independent of the grid size. The key parameter, i.e. maximum EDR, was then characterised in both pumping system and the shear device.

3.2.4.1 Pump

For the rotary vane pump, a rotor with radial slots is positioned off-centre in a housing bore. This rotating component has a diameter of 8 cm. Four vanes that fit closely in rotor slots slide in and out as the rotor turns clockwise and can extend from 0 cm to ~2 cm. Vane action is aided by centrifugal force, hydraulic pressure, or pushrods. Pumping action is caused by the expanding and contracting volumes contained by the rotor, vanes and housing. Vanes are the main sealing element between the suction and discharge ports. It is assumed that the fluid entering into the pump chamber with very low velocity and the vanes can successfully prevent the back flow of the fluid. In this context, the pump chamber can be divided by these four vanes into four parts (or quarters), each part will repeatedly move around by expanding and contracting volumes. Due to the symmetry of these quarters, only one quarter of the chamber was chosen to represent the fluid flow in the pump for a CFD simulation purpose (see Figure 3.1A). The chamber volume from the inlet position increases to the largest value then decreases. At the exit, the chamber volume changes to the same as that in the inlet. The rotor and vanes were treated as the moving walls with the same rotational speed, and the wall for the house chamber is stationary.

The FORTRAN file together with a command file was used to describe the geometry of the problem, its boundary conditions and the changing volumes for the pump

movement (**Appendix I**). For a simulation purpose, two pump speeds of 600 rpm and 1500 rpm were chosen representing the average and maximum delivery capacities of the pump for this system, respectively. The k-ε model was employed to describe the turbulent flow in the pumping system. Simulations of the pumping system were carried out by Dr Hu Zhang, a postdoctoral researcher who used to carry out CFD simulation work at the Biochemical Engineering Department at UCL.

3.2.4.2 Shear device (USD device)

Following the characterisation of the maximum EDR in the pumping system, the CFD technique was then employed to determine the equivalent disc speed in the shear device. The computational domain was constructed in CFX Build. The domain is divided into the (inner) rotating region and (outer) stationary region in order to apply the rotating coordinate such that the inner frame moves within the outer frame during the simulation. The surface between these two regions was defined by two unmatched boundaries. As the geometry of the shear device is symmetrical, only half of the geometry was simulated via the use of a periodic plane. The command file of the shear device is presented in **Appendix I**. In this system, the k-ε model was employed to describe the turbulent flow in the shear device. Firstly, the simulations were carried out at equivalent disc speeds to the pump operations. The USD system was then modelled under several recommended disc speeds (section 3.3.3) in order to establish the general behaviour of the biomaterial of interest for size prediction purpose (see more details in **Chapter 5**).

3.3 CFD simulation results

3.3.1 CFD simulation of pumping system

CFD simulations allowed the magnitudes of maximum EDR to be calculated and these were found to be 900 and $1.5*10^4$ W kg^{-1} for the pump speed of 600 rpm and 1500 rpm, respectively. Analysis of fluid flow in the pump operation showed that the high-shear region (maximum EDR) was found around the stationary wall which was near to the leading vane (Figure 3.1). This was due to the entangling action of pump elements

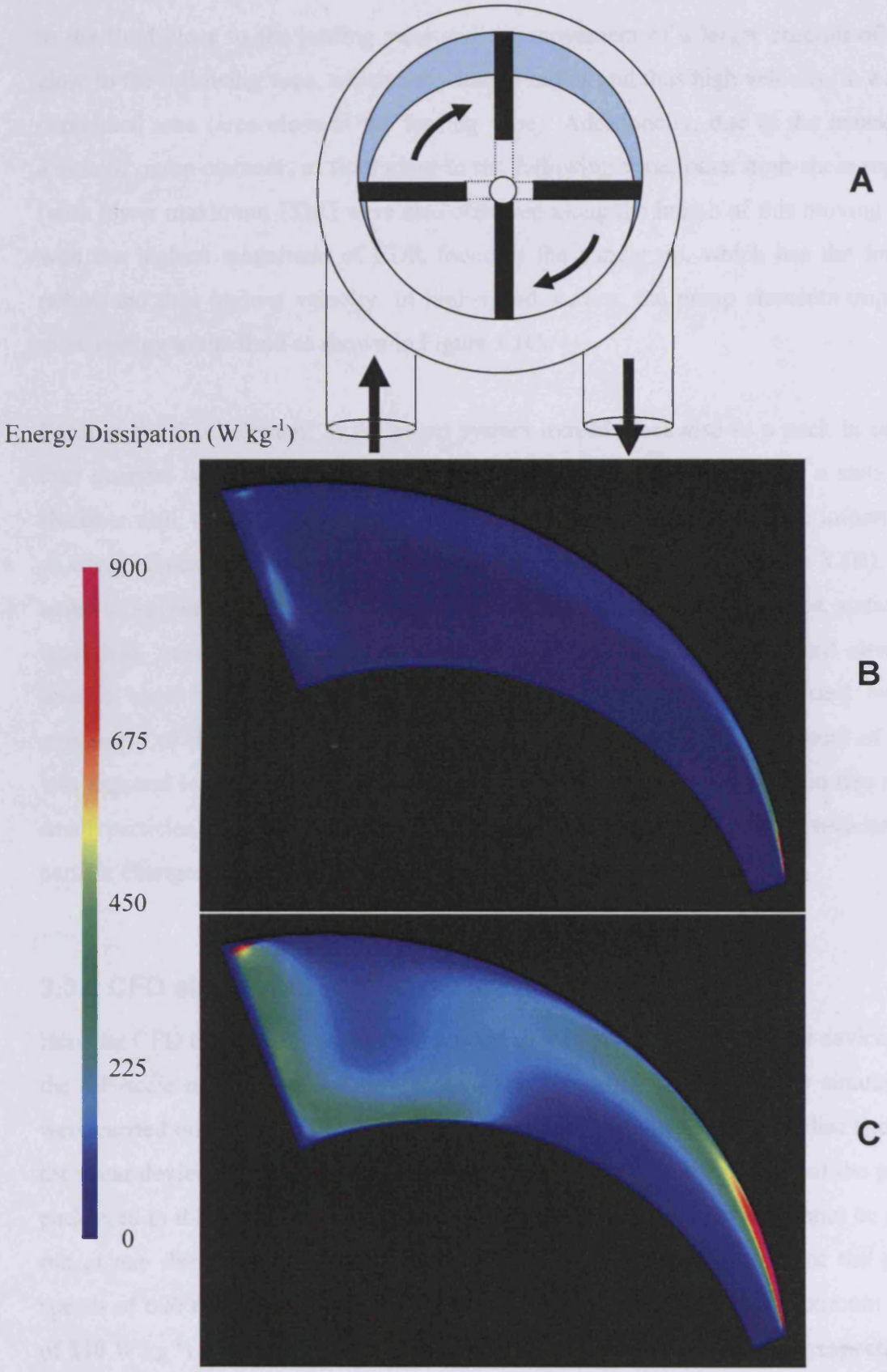

Figure 3.1 CFD simulations of the pump running at 600 and 1500 rpm. The simulated part is represented by one of four quarters **(A)** and the corresponding energy dissipation rate profile are shown for 600 rpm **(B)** and 1500 rpm **(C)**.

to the fluid close to the leading vane and the movement of a larger amount of fluid close to the following vane, which has a longer radius and thus high velocity, to a more contracted area (area close to the leading vane). Additionally, due to the entangling action of pump elements to fluid close to the following vane, other high-shear regions (with lower maximum EDR) were also observed along the length of this moving vane with the highest magnitude of EDR found at the vane's tip, which has the longest radius and thus highest velocity. In high-speed studies, the pump elements imparted more energy to the fluid as shown in Figure 3.1C.

Because the fluid element in the pump system moved clockwise as a pack in one of four quarters which were formed by a moving rotor, moving vanes and a stationary chamber wall, the majority of the fluid was found not to be affected by the impartment of energy from pump elements, especially for a low-speed study (Figure 3.1B). This situation is 'similar' to that having a stationary fluid pack, stationary vanes, stationary rotor and 'moving wall' of the house chamber. Consequently, only fluid elements located close to the stationary chamber wall were significantly affected by the movement of these pump elements. This suggested that only a small amount of fluid was exposed to high energy dissipation rate and large particles were broken into many small particles, but the majority return to the reservoir (mixing tank) without any particle change.

3.3.2 CFD simulation of USD device

Here the CFD technique was used to help match the conditions in the small device with the full-scale machine. Based on the same maximum EDR, similar CFD simulations were carried out for the USD device in order to determine the equivalent disc speed in the shear device. Due to the limitation in the speed adjustment capability of the power pack used in this study (see section 2.4.2, **Chapter 2**), the USD device cannot be set to run at any desired speed. As such the closest equivalent disc speeds for the pump speeds of 600 rpm and 1500 rpm were found to be 5000 rpm (USD's maximum EDR of 840 W kg^{-1}) and 15000 rpm (USD's maximum EDR of 15100 W kg^{-1}), respectively. Figure 3.2 shows the energy dissipation rate profile for these disc speeds. The match up of these speeds can be summarised in the Table 3.1. In the USD system, the high-energy dissipation zone is found to be at the tip of the disc. Here, the fluid layer close

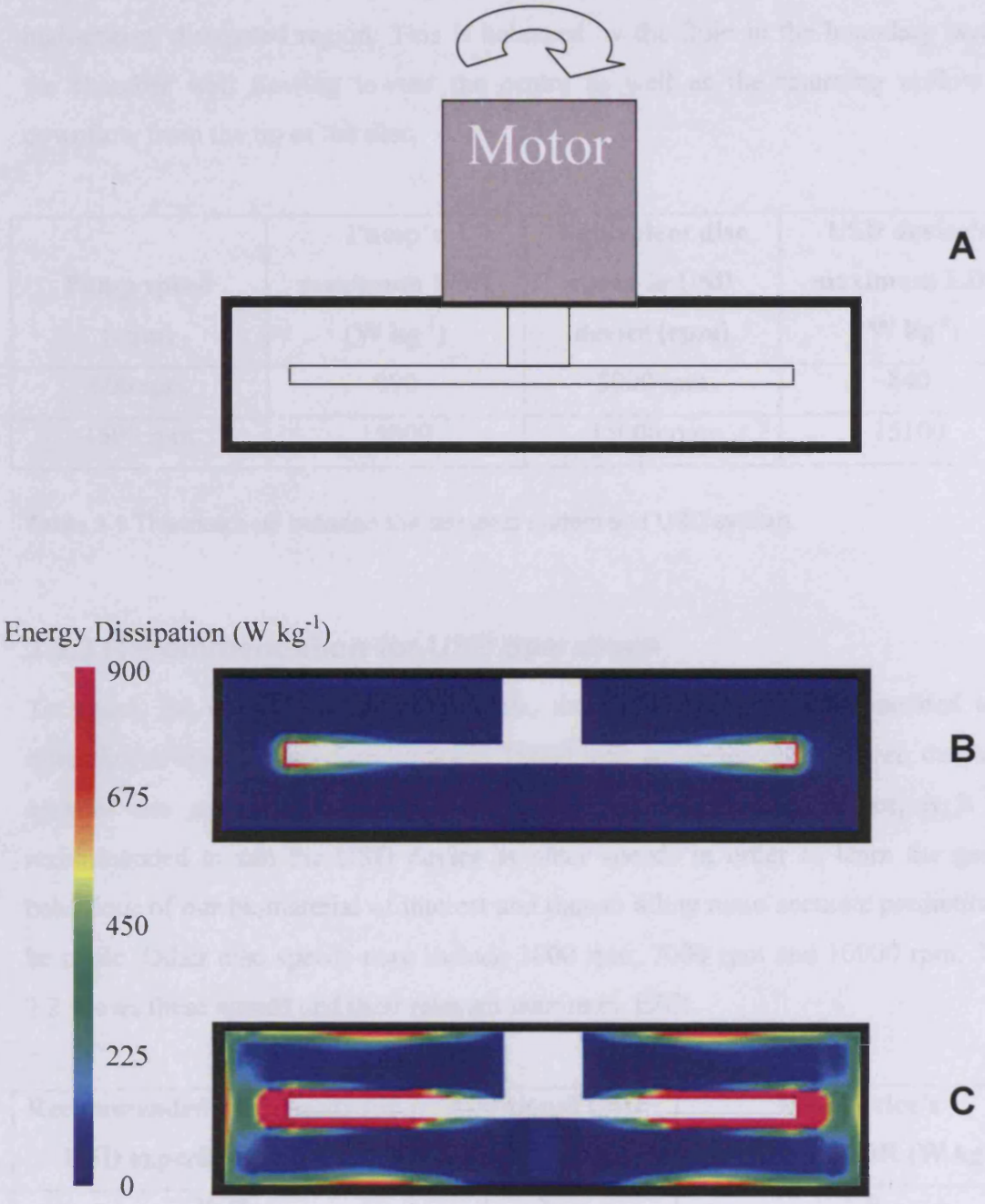

Figure 3.2 CFD simulations of the shear device rotating at 5000 and 15000 rpm. These disc speeds are equivalent to the pump speeds of 600 and 1500 rpm, respectively, which are presumably producing the same damage effect as in the pump. The simulated part of the USD system **(A)** and the corresponding energy dissipation rate profiles for 5000 rpm **(B)** and 15000 rpm **(C)** are shown.

to the rotating disc is carried tangentially outward by centrifugal forces passing the high-energy dissipated region. This is balanced by the fluid in the boundary layer of the chamber wall flowing toward the centre as well as the returning upflow and downflow from the tip of the disc.

Pump speed (rpm)	Pump's maximum EDR (W kg^{-1})	Equivalent disc speed in USD device (rpm)	USD device's maximum EDR (W kg^{-1})
600 rpm	900	5000 rpm	840
1500 rpm	15000	15000 rpm	15100

Table 3.1 The match up between the pumping system and USD system.

3.3.3 Recommendation for USD operations

To match the damage of the large scale, the USD device is recommended to be operating at the disc speed of 5000 and 15000 rpm, respectively. However, due to the ease of use and small volume of material used in the USD device, it is also recommended to run the USD device at other speeds in order to learn the general behaviour of our biomaterial of interest and thus to allow more accurate predictions to be made. Other disc speeds may include 3000 rpm, 7000 rpm and 10000 rpm. Table 3.2 shows these speeds and their relevant maximum EDR.

Recommended disc speeds for USD experiments (rpm)	Additional USD speeds (X)	USD device's maximum EDR (W kg^{-1})
3260*	X	270
5000		840
7000	X	1900
10000	X	5000
15000		15100

Table 3.2 All recommended disc speeds including the disc speeds equivalent to the pump speed of 600 and 1500 rpm for USD experiments. (*) Note that 3260 rpm was found to be the lowest speed that allows a stable operation of the shear device.

3.4 Conclusions

The CFD technique was found to successfully find corresponding impeller speeds which produced similar magnitudes of the key engineering parameter governing damage of biomaterial, i.e. maximum EDR, for USD compared with pump. The intensity of the energy dissipation rate under a specific operating condition at any location of both systems was successfully mapped by using this technique. It also helped pinpoint the location where this key parameter reached its maximum value, i.e. a place where the damage of biomaterial is likely to occur. Most importantly, the CFD technique allowed equivalent disc speeds that could reproduce the large-scale damage condition to be estimated for the small-scale (USD) operation. These recommended disc speeds were then applied in the shear device experiment whose results are presented in the next chapter.

CHAPTER 4 SHEAR DEVICE EXPERIMENT

In this chapter, the shear device is employed as an ultra scale-down (USD) device to mimic the engineering environment and hence predict the damage caused by a pump integrated in a membrane operation. The results are based on size changes of a mammalian cell suspension subjected to a range of maximum energy dissipation rates (EDR) generated by the rotating disc in this USD device. The effect of the exposure time on this suspension is also described. The key engineering parameter causing different shear environments, i.e. maximum EDR, is employed to correlate the size change of these particles and will be used to relate these results to predict break up which may occur in a pumping operation during large-scale membrane separation.

4.1 Materials and methods

4.1.1 Cell samples

A sample of mammalian cell broth with a solids concentration of 10% v/v was obtained from Lonza Biologics plc, Slough, UK. It was immediately frozen for storage at -80°C. Before use it was thawed by leaving at 4°C for 14 h and at room temperature for 6 h until fully defrosted. In order to ensure a uniform feed material and to break up loose aggregates the suspension was kept stirred (ice-cooled beaker, 1000 mL, stirred using a magnetic polytetrafluoroethylene-coated stirrer bar having rounded ends with length of 70 mm and diameter of 9.5 mm and rotating at the speed of ~800 rpm) until D_{50} of ~45 μm ± 2 μm was obtained. The particle size distribution was monitored and provided the same pattern for each batch. This stirring action usually took around 2 h ± 15 min before the desired particle size was reached. Finally, prior to experimental runs, a sample, 2 L, was diluted to 10 L with 0.15 M NaCl (Sigma-Aldrich, Dorset, UK) prepared using ultra-pure water at room temperature. A proportion of this final suspension, 400 mL, was allocated to shear experiments and the remainder, 9.6 L, was allocated to the large-scale membrane experiment. To confirm the stability of a sample

after dilution, particle sizes of a diluted sample were compared and matched with those of the non-diluted sample in both sheared and non-sheared conditions.

4.1.2 Experimental equipment

A shear device was employed in the experiment. All specifications of the shear device alone in terms of dimensions and materials of construction have been previously presented in section 2.4.2 (**Chapter 2**).

In this study the shaft of the shear device is connected to an ultra-speed DC motor (Groupher Speed 500 BB RACE, UK), which is powered by an in-house power controller unit. The controller unit, via a transformer, has a capability of supplying a wide range of voltages, thus offering adjustable speeds of rotation from 3000 to 15000 rpm. The disc speed was determined and displayed numerically on a panel on the power controller unit. Before performing experiments the shear device's base was dissembled and the disc speed was measured using a non-contact laser tachometer (model TMRT 1, SKF, Luton, UK) to verify the accuracy of the power controller unit. Throughout experiments the device was placed in a water bath. Water temperature was monitored using the temperature probe and kept at 20°C ± 0.5°C by adding ice as needed. All three openings on the device were sealed using valves (model 2452040xx, Halkey-Roberts Corp., Florida, USA) to ensure complete sample containment and elimination of air-liquid interfaces as a result of air ingress into the system during the experiment. The schematic of this operation is shown in Figure 4.1.

4.1.3 Operating parameters

A normal experimental run involved filling the device with a sample and shearing at a fixed disc speed for a specific time period and repeating this sequence for a range of different disc speeds and times. For each run the disc speed was set and samples of 20 mL were filled into the shear device through a bottom opening via a standard Becton-Dickinson plastic syringe (40 mL) at the rate of approximately 40 to 50 mL min^{-1}. Samples displaced air in the device and forced it to escape through one of top inlets via an empty syringe. The filling stopped when sample was seen in this syringe. All syringes were then removed and the device was placed in the water bath. Samples were

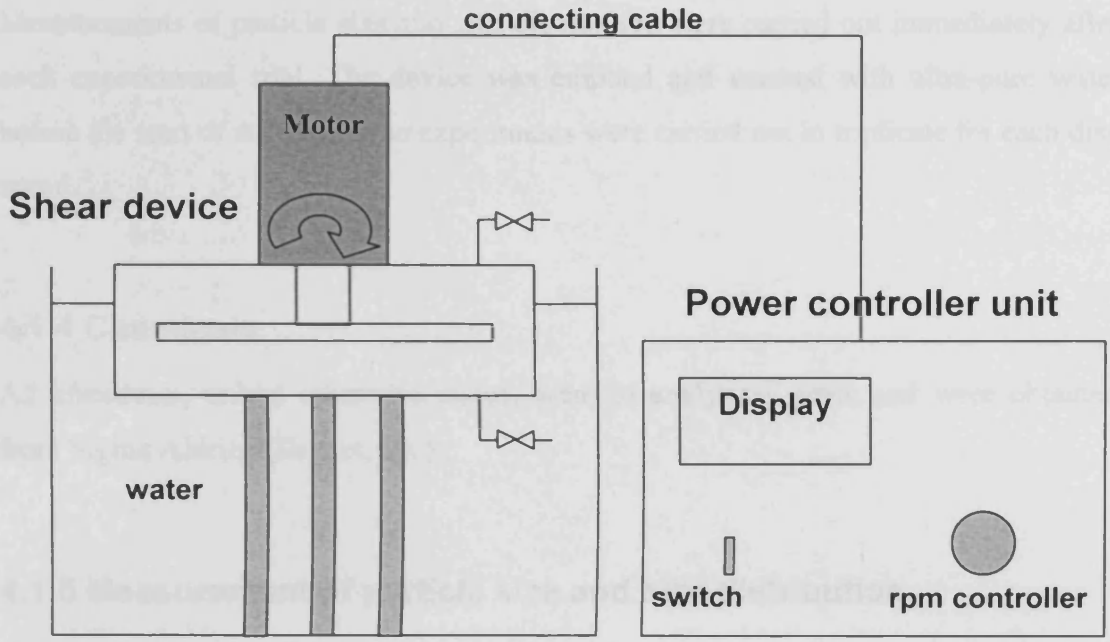

Figure 4.1 Schematic of shear device experiment. Shear device is placed on a stand in a water bath and was connected to a power controller unit, which controlled the speed of the shear device (in rpm) through the DC motor. The speed was set before samples were introduced and time measurement started when the power controller unit was turned on. The study of disc speeds, which included 3260, 5000, 7000, 10000 and 15000 rpm, was carried out at various time periods, i.e. 15, 30, 60, 120 and 300 s. After each run, the particle size and size distribution were measured using Malvern Mastersizer 2000 particle analyser.

sheared at various fixed disc speeds including 3260, 5000, 7000, 10000 and 15000 rpm. For each disc speed samples are sheared for 15, 30, 60, 120 and 300 s. A non-sheared sample was used as a control. Time measurements started when the power controller unit was turned on. After each run samples were collected from the bottom opening of the device with the help of positive pressure from an air-containing syringe inserting through one of the top inlets at the rate of approximately 40-50 mL min^{-1}. Measurements of particle size and size distribution were carried out immediately after each experimental trial. The device was emptied and washed with ultra-pure water before the start of each run. The experiments were carried out in triplicate for each disc speed.

4.1.4 Chemicals

All chemicals, unless otherwise stated, were of analytical grade and were obtained from Sigma Aldrich (Dorset, UK).

4.1.5 Measurement of particle size and size distribution

The suspension size distribution was measured using a laser light scattering method. All measurements were achieved using Malvern Mastersizer 2000 particle analyser and Hydro 2000SM sample dispersion accessory (Malvern Instruments, Worcestershire, UK). A user-defined Standard Operating Procedure (SOP) was set with the help of software's SOP Wizard according to sample properties and the procedures for making a measurement given by Mastersizer 2000 Operators guide were followed for all measurements. NaCl solution having a normal physiological concentration, i.e. 0.15 M, was used to wash the unit between each measurement and to set the measurement background. All measurements were carried out in triplicate at room temperature.

Distribution data obtained was expressed in a set of size bands which was optimised to match the physical design of the detector and optical configuration for the best resolution. The fundamental distribution data from each size band was used to calculate all distribution parameters and derived diameters. In performing this calculation, the geometric mean of the size band limits, i.e. the root mean square of the product of upper limit and lower limit of the size band ($\sqrt{d_u \cdot d_l}$), was used as a

representative diameter, as it is more suitable to the logarithmic spacing of the particle size bands than the arithmetic mean. In this study the size distribution was characterised in two ways: (a) the volume fractions for each group of particles (debris, cells and aggregates); (b) the derived diameters below which 10%, 50% and 90% by volume of the sample lies, i.e. D_{10}, D_{50} and D_{90} respectively. Refer to **Appendix II** for data regarding volume fraction of particles.

4.1.6 Data analysis

All distribution data was obtained through software provided with Malvern Mastersizer 2000 particle analyser. Data was given in terms of both volume percent (vol %) and derived diameters (D_{10}, D_{50} and D_{90}). All data analyses, including graphical representations, were achieved using computer programmes: Microsoft® Office Excel 2003 and Origin 6.0 (MicroCal, LLC, Northampton, MA, USA).

4.2 Experimental results and discussions

4.2.1 Shear causes particle size change

The sample preparation procedure used (section 4.1.1) yielded a suspension with a bimodal size distribution with a main peak of mean diameter 12 μm and a small peak of mean diameter of 2 μm (non-sheared, Figure 4.2). The resultant suspension contained particles of various sizes ranging coherently from 2 μm to more than 1000 μm in diameter with no unusual or random peaks. It is obvious that the processed suspension at this point contained several components according to their sizes, i.e. aggregates, cells and cell debris. Aggregates with the size larger than 100 μm in diameter were formed to which several hundreds of cells may contribute. The suspension also contained cells that are 10 μm in diameter. Cell debris was also formed as a remnant of sample preparations and this is shown in the left region of the size distribution curve with particle sizes of less than 10 μm in diameter. Due to its reproducibility and consistency, this material was used as a starting material in the shear device experiments.

Following the exposure of samples to a disc speed of 3260 rpm (equivalent to a maximum EDR of 270 W kg^{-1}) for 15 s, large aggregates were broken down and their sizes decreased. The particle size distribution shifted to the left (into a smaller-particle region) and was still bimodal with more noticeable peaks of cells and small particles of less than 4 μm in diameter (Figure 4.2). The processes of disassembly of large aggregates into cells and breakage of cells into debris best can be explained graphically through the linear-scale plots in Figure 4.3 where the areas under the curve are directly proportional to the volume of particles in a particular size range. Figure 4.3A shows the break up of the large cell aggregates to form single cells of mean size 10 μm – the decrease in area of large aggregates above 60 μm is approximately equal to the increase in cell volume. Also evident is the growing amount of cell debris which probably results from breakage of the whole cells or may be a byproduct of the break up of the aggregates (Figure 4.3B). This material is important as it typically remains after high speed centrifugation and for example it may be estimated that the effect of shear is to at least double the size of a polishing filter required for debris removal before any high resolution chromatography. Figure 4.3 also shows that the most prominent changes of particle properties were noticed by the reduction of large aggregates, e.g. those with diameter larger than 60 μm and by simultaneous increase of smaller aggregates, e.g. those with diameter smaller than 60 μm, and cells. In addition, the reduction of large aggregates also contributed to the formation of cell debris. Sizes of particles could also be represented in a more practical way in terms of derived diameters including D_{10}, D_{50} and D_{90}. These are defined as the sizes of particles below which 10%, 50% and 90% of the sample lies, respectively. Based on this context, it was found that the exposure of a suspension to maximum EDR of 270 W kg^{-1} resulted in the decrease of derived diameters; D_{10} decreased from 11.1 μm to 10.1 μm, D_{50} decreased from 45 μm to 33 μm and D_{90} changed from 171 μm to 119 μm (Figure 4.4). If calculated in percentage, the reductions of D_{10}, D_{50} and D_{90} are 9%, 27% and 30%, respectively. As might be expected a delicate nature of large aggregates allows a higher proportion to be affected by shear compared to smaller particles resulting in greater reductions of the D_{90} value.

These phenomena can be seen as the resultants of the input of energy into the system through the rotation of the disc, which allows at least 2 processes to occur. One

mechanism permits input energy to dissemble large aggregates into individual cells while another mechanism lets dissipated energy to disrupt cells into debris. According to this, the disruption of large aggregates became more evident at higher speeds and hence higher maximum EDR (energy). For example, the disc speed of 5000 rpm (equivalent to a maximum EDR of 840 W kg^{-1}) running for 15 s caused D_{10}, D_{50} and D_{90} to decrease from 11.1 μm, 45 μm and 171 μm to 8.7 μm, 19 μm and 48 μm, respectively, and in percentage terms reductions of 22%, 58% and 72%, respectively (Figure 4.4). The effects of different disc speeds on the particle sizes and their distributions are shown in terms of volume frequency based on logarithmic scale in Figure 4.2. The figure shows that exposure of the suspension to a range of maximum EDR, generated by the shear device, leads to different degrees of solid disruptions and that the higher the magnitude of maximum EDR, the smaller the particle size and the more the distribution curve shifts to the left. The most marked change of particle size was in the case of 15000 rpm running for 15 s where D_{10}, D_{50} and D_{90} decreased to 5.7 μm, 11.2 μm and 20.3 μm, giving the size reduction of 49%, 75% and 88%, respectively (Figure 4.4). Using linear-scale representation it can be clearly seen that when the maximum EDR in the system increased the disruption rate of large aggregates also increased and thus accounted for the greater increment of smaller aggregates, cells and cell debris (Figure 4.5).

Since these phenomena involves a process of imparting the energy from pump elements to the fluid in the system and the intensity of the imposed energy to aggregates can be represented by the maximum EDR (see section 2.2.3 in **Chapter 2** for evidences), the maximum EDR of the system, which is a scalable parameter, was adopted instead of the disc speed for the rest of this investigation. Besides the energy dissipation of the system, other factors also affect the size change of these particles. The effects of maximum EDR together with these factors causing specificity in size characteristics of a suspension will be investigated and described in detail in the next section.

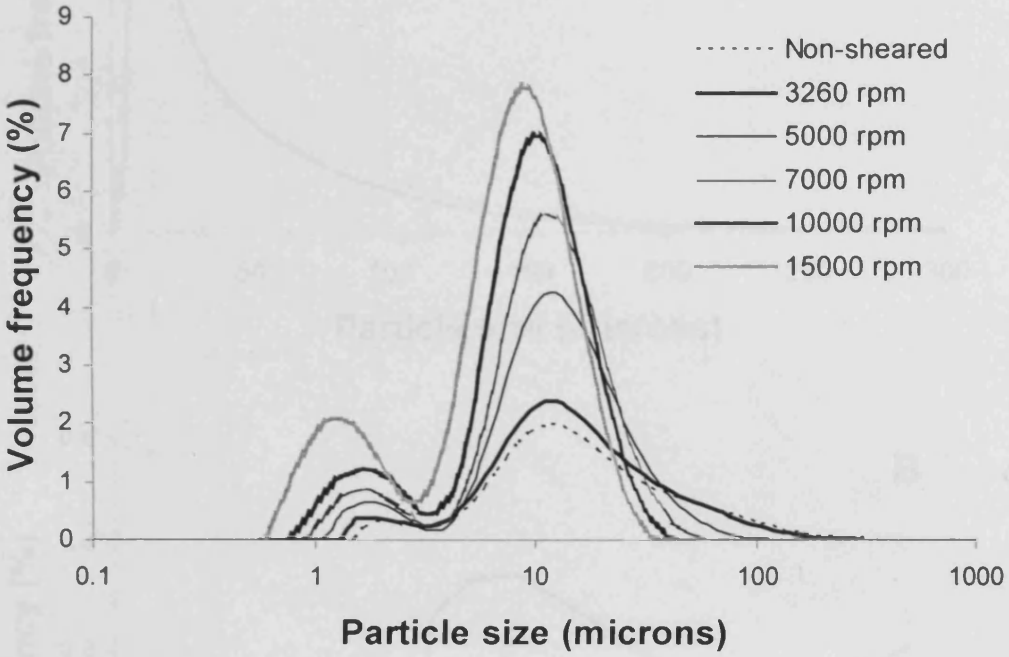

Figure 4.2 Comparison of the particle size distributions of cell suspension after being subjected to a range of disc speeds starting from 3260 rpm to 15000 rpm for 15 s based on logarithmic scale. Different disc speeds caused the particle size distribution curve to have specific characteristics. The higher the magnitude of maximum EDR, the smaller the particle size and the more the distribution curve moves to the left. This speed range covers the maximum EDR from 270 to 15100 W kg^{-1}. The most evident change of particle size distribution occurred when the EDR reached 15100 W kg^{-1} where D_{10}, D_{50} and D_{90} decreased from 11.1 μm, 45 μm and 171 μm to 5.7 μm, 11.2 μm and 20.3 μm, respectively. At the same time, the small-particle peak was also highest among results from other magnitudes of dissipated energy.

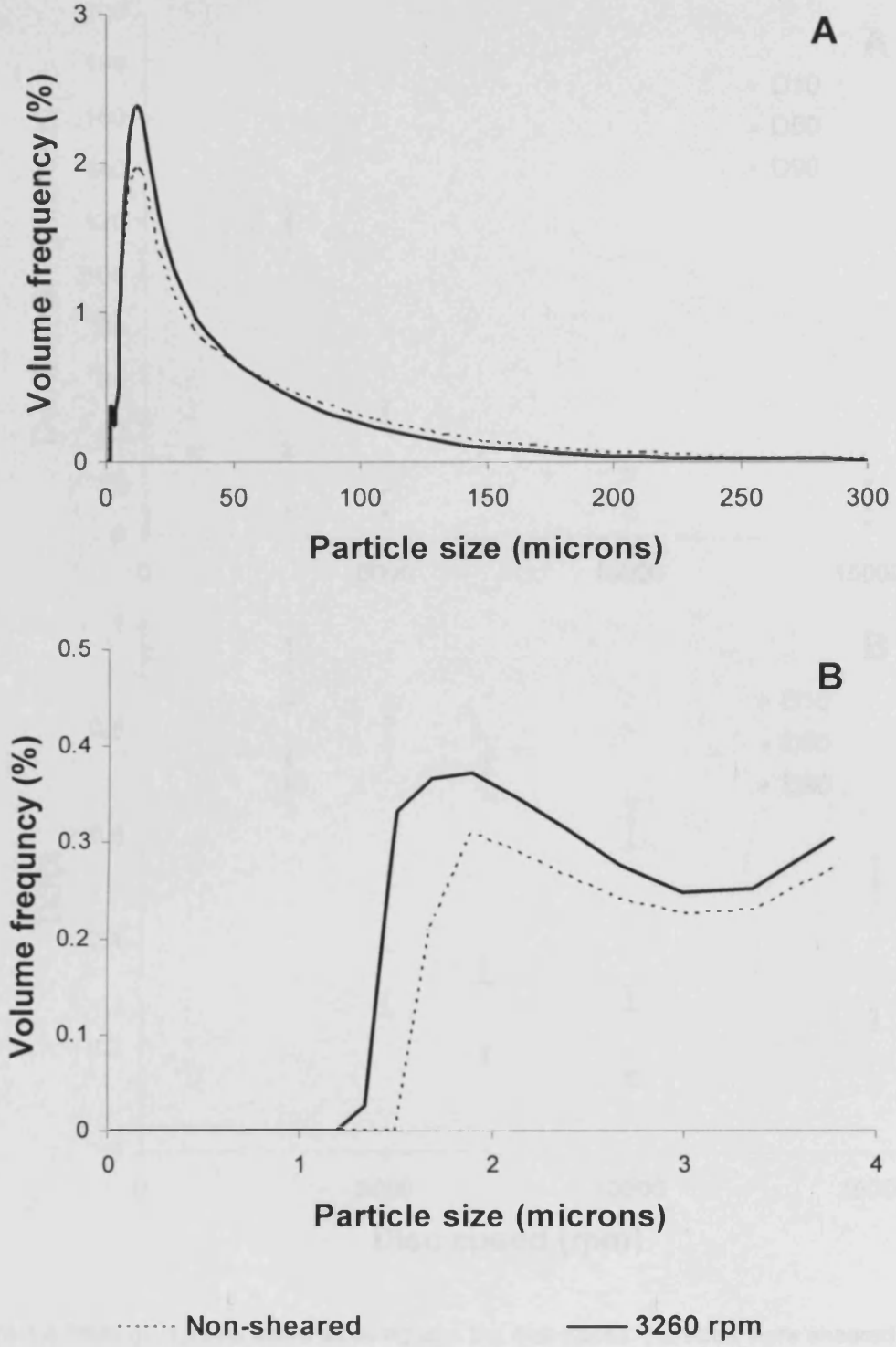

Figure 4.3 Changes of particle size distribution of suspension after being subjected to shear at 3260 rpm for 15 s compared to the non-sheared sample based on linear scale. Large aggregates having diameter larger than 60 μm were broken down **(A)**. Reduction of large aggregates contributed to the increase of (cells and) cell debris **(B)**.

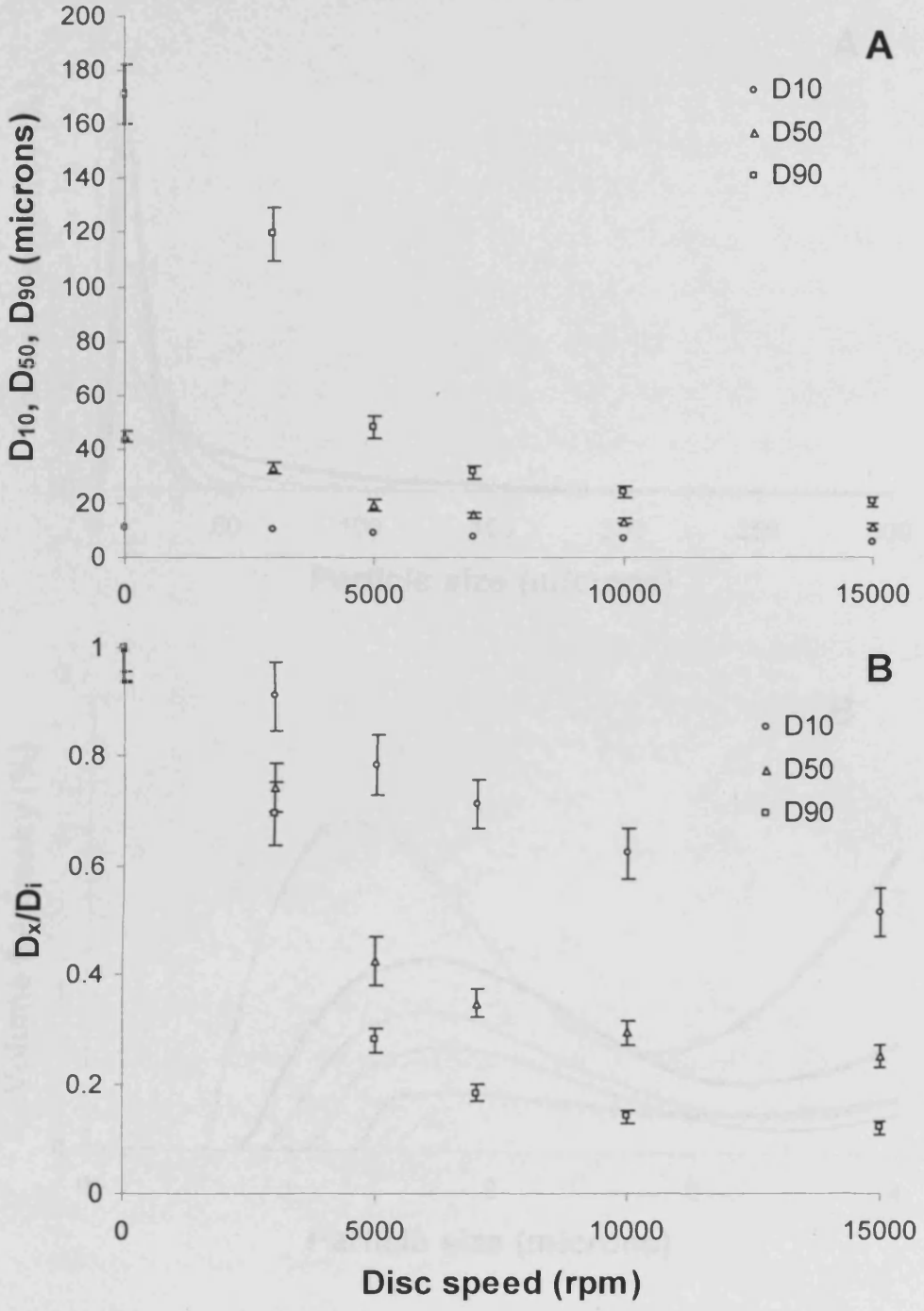

Figure 4.4 Plots of representative sizes against the disc speed. Particles were sheared for 15 s at different disc speeds ranging from 3260 to 15000 rpm. Both the derived diameter **(A)** and the ratio between the derived diameter and its initial size **(B)** are shown. Following the exposure to shear generated by the disc speed of 15000 rpm, D_{10}, D_{50} and D_{90} decreased from 11.1, 45 and 171 μm to 5.7, 11.2 and 20.3 μm, respectively. Size decrease was dependent on particle size itself and disc speed with the higher speed resulting in smaller particles. Particle sizes were represented by derived cumulative undersize diameters by volume%, namely D_{10} (-o-), D_{50} (-Δ-) and D_{90} (-□-).

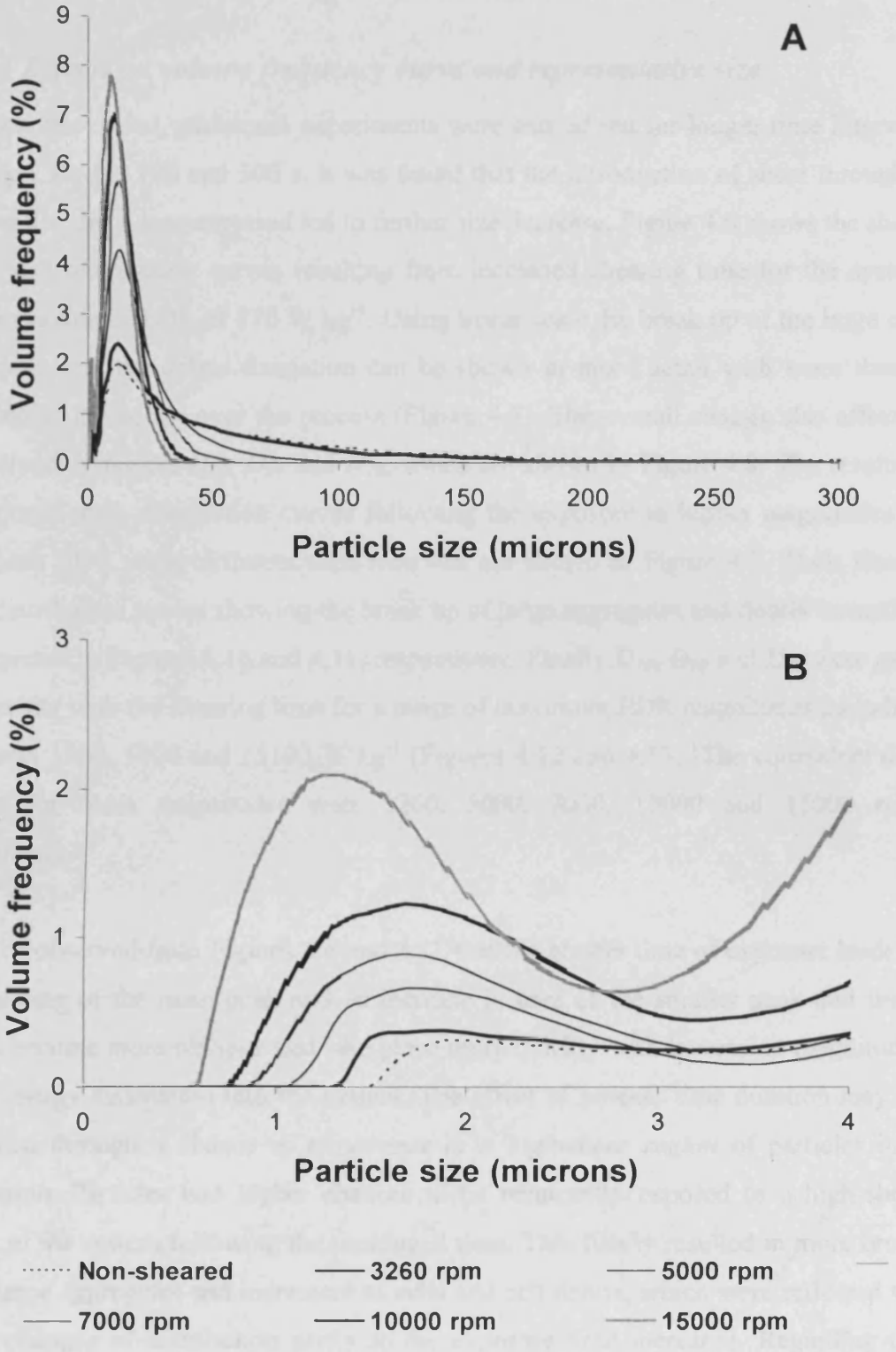

Figure 4.5 Changes of particle size distributions of suspension after being subjected to shear at different disc speeds for 15 s compared to the non-sheared sample based on linear scale. Changes of large aggregates and cells **(A)** and cell debris **(B)** are shown. It was found that the higher the magnitude of maximum EDR to the system, the higher the change of these particles. Data for 3260 rpm was taken from Figure 4.3.

4.2.2 Effects of the shearing time and maximum EDR

4.2.2.1 Effects on volume frequency curve and representative size

For each disc speed, additional experiments were carried out for longer time intervals including 30, 60, 120 and 300 s. It was found that the introduction of shear through a rotating disc for a longer period led to further size decrease. Figure 4.6 shows the shifts of the size distribution curves resulting from increased shearing time for the system having maximum EDR of 270 W kg^{-1}. Using linear scale the break up of the large cell aggregates and the debris formation can be shown in more detail with more than a doubling of the debris over the process (Figure 4.7). The overall change also affected the derived diameters D_{10}, D_{50} and D_{90}, which are shown in Figure 4.8. The resultant logarithmic-scale distribution curves following the exposure to higher magnitudes of maximum EDR under different time intervals are shown in Figure 4.9. Their linear-scale distribution curves showing the break up of large aggregates and debris formation are depicted in Figures 4.10 and 4.11, respectively. Finally D_{10}, D_{50} and D_{90} were used to correlate with the shearing time for a range of maximum EDR magnitudes including 270, 840, 1900, 5000 and 15100 W kg^{-1} (Figures 4.12 and 4.13). The equivalent disc speeds for these magnitudes were 3260, 5000, 7000, 10000 and 15000 rpm, respectively.

It can be observed from Figures 4.6 and 4.11 that the greater time of exposure leads to a narrowing of the main peak and an increase in area of the smaller peak and these effects become more obvious and take place more quickly with increasing magnitudes of the energy dissipation into the system. The effect of process time duration may be explained through a *chance of recurrence to a high-shear region* of particles in a suspension. Particles had higher chances to be recurrently exposed to a high-shear region in the system following the prolonged time. This finally resulted in more break up of large aggregates and increment of cells and cell debris, which were reflected via above changes of distribution peaks as the exposure time increased. Regarding the effect of increased magnitudes of maximum EDR, the phenomenon may be explained through an increase of both maximum EDR of the system itself and the flow rate expelling particles from the tip of the rotating disc. Higher magnitudes of maximum EDR generated from the higher disc speed cause damage to a wider range of particles. Smaller particles that do not break at certain magnitudes of maximum EDR may be

disrupted in the system having a higher magnitude. At higher speeds the flow rate at which materials are expelled from the tip of the disc is also greater; thus leading to higher recurrence of materials to a high-energy zone. As a result, these two factors derived from the operation condition of the disc speed account for more solids break-up when the maximum EDR increased.

Following the change of the volume frequency distribution curve, the derived diameters D_{10}, D_{50} and D_{90} changed accordingly – they decreased in size with the shearing time and at a faster rate as maximum EDR increased (Figures 4.12 and 4.13). Again the explanation of a chance of recurrence to a high-shear region may be used to describe decreasing trends of all derived diameters after the prolonged time of exposure. As maximum EDR increased, size decreases occurred more quickly due to an increase in both maximum EDR and flow rate from the tip of the disc. These results suggest the dependence of the degree of size reductions on maximum EDR and more importantly allow the final values of all derived diameters to be observed after the exposure to shear for 300 s which are specific for each magnitude of the maximum EDR.

4.2.2.2 Rate of change of volume fraction with time

According to the above results, the rate of change of particle size in a suspension, i.e. the decrease of large aggregates and increase of cells and cell debris, was very rapid even after a short period of exposure – for example after only 15 s the volume fraction of cells and cell debris, i.e. those having diameter equal to or smaller than the cell diameter ($\leq$ 10 μm), swiftly increased from 10.2% to 20% when the suspension was exposed to the maximum EDR of 840 W kg^{-1}. The situation is reversed for large aggregates. However, after 15 s of exposure to shear the rate of change of these particles gradually decreased with time, i.e. with the same shearing condition the volume fraction of cells and cell debris increased to only 21.2%, 23.5%, 24.9% and 26.3% following the exposure for 30, 60, 120 and 300 s, respectively. With increasing magnitudes of EDR of the system, the difference in the rate of change between early stage and late stage became more prominent. For example, the volume fraction of cells and cell debris largely increased from 10.2% to 50.3% following the exposure to the maximum EDR of 15100 W kg^{-1} for 15 s and gradually increased to 71.3% after 300 s.

The explanation to a rapid change during early stage and slow change during late stage is probably central to the availability of the solids left to be disrupted in the system. The more rapid decrease of large aggregates and increase of cells and cell debris were observed after only a short exposure to shear in the system. As time passed, solids left to be disrupted in the system were depleted and the rate of aggregate disassembly and debris formation gradually decreased with time. As a result, though it was demonstrated that longer exposure of aggregates to energy transmitted from the rotating disc leads to higher degree of size change of particles, solid break-up may not be directly proportionate to the shearing time. This is due to the fact that the degree of breakage depends on the maximum energy dissipation of the system and the amount of solids left to be broken, which would be depleted with time. The following table shows the reduction pattern of rates of changes of volume fraction per unit time of cells and cell debris under influence of different magnitudes of maximum EDR.

Operating time interval (s)	**Rates of changes of volume fraction of cells and cell debris under different maximum EDR magnitudes (percent per sec)**				
	Max EDR 270 W kg^{-1}	**Max EDR 840 W kg^{-1}**	**Max EDR 1900 W kg^{-1}**	**Max EDR 5000 W kg^{-1}**	**Max EDR 15100 W kg^{-1}**
0-15	0.1736	0.6540	1.1322	1.8564	2.6677
15-30	0.0450	0.0794	0.1852	0.1802	0.2811
30-60	0.0442	0.0762	0.0489	0.0712	0.1358
60-120	0.0227	0.0227	0.0505	0.0716	0.0948
120-300	0.0033	0.0077	0.0168	0.0231	0.0392

Table 4.1 Rates of changes in volume fraction of cells and cell debris in a mammalian cell suspension following the exposure to different magnitudes of maximum EDR for different time intervals. These rates decreased with the shearing time for all conditions due to the amount of solids left to be disrupted becoming less.

Table 4.1 implies that the system would eventually reach the state where there is little or no solid left to be broken and the shift in size distribution cannot be observed. This concept is similar to other breakage concepts concerning breakage of whey protein

precipitates (Zumaeta et al., 2005), drop break-up in stirred vessels (Kumar et al., 1998), breakage of single particles in a single impact event (Brown et al., 1996, Thornton et al., 1999, Austin, 2002) and breakage of latex flocs in a stirred tank (Kobayashi, 2004). Depending on the system's shearing conditions and nature of experimental materials, at this state small particles may collide and form larger particles and the rate of particle aggregation may equal to the rate of particle breakage. However, it is also possible that the minimum energy required to break the majority or all of particles in the system became equal to or greater than the maximum EDR of the system and thus solid disruption no longer takes place. According to above concepts concerning the breakage, it might be assumed that either mechanism would stop the distribution curve from changing and that, for a particular set of shearing conditions and experimental materials, specific characteristics of the size distribution would eventually be observed after specific shearing time duration.

To summarise, the change of particle size is dependent on the time of exposure to shear and maximum EDR. Prolonged exposure to shear allowed particles to have higher recurrent opportunities to be exposed to high-shear regions; thus leading to a higher degree of solid disruptions and size decreases. However, depending on the system's maximum EDR and the amount of solids left, the extra shearing time might not always lead to proportionate breakages of solids and their size changes. It was observed that as the shearing time increased the amount of solids left to break was depleted resulting in the decrease of the rate of changes in their volume fraction and the distribution curve having tendencies to reach a state where the shearing conditions of the system could not disrupt particles any further. These occurrences were shown by an initial rapid decrease of large aggregates and rapid increase of cells and cell debris followed by more gradual changes of these particles towards the end. These characteristics became more obvious with increasing disc speeds when magnitudes of both the system's maximum EDR and the flow rate expelling particles from the tip of the disc had increased. This is because the higher maximum EDR allowed particles of smaller sizes to break and the coupled higher flow rate from the disc reduced the mixing time and increased the degree of recycle of the liquid in the system. These changes following an increase in maximum EDR of the system ultimately lead to a higher recurrent opportunity of biomaterials to a high-shear region and thus a more rapid change at the early stage of the process compared to a case of lower maximum EDR.

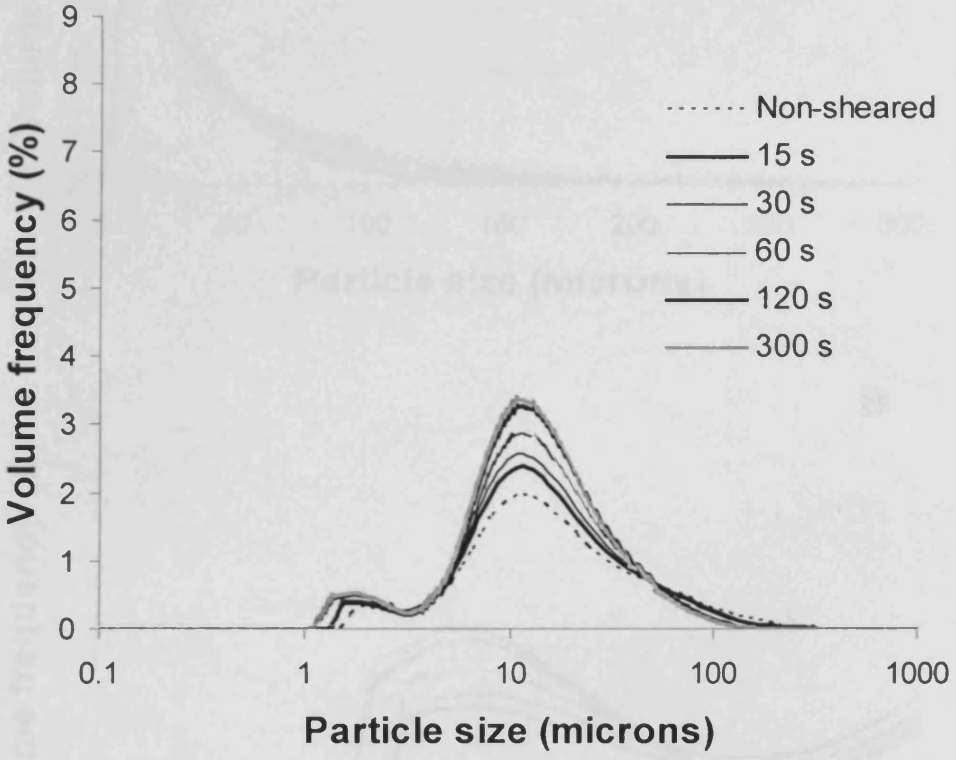

Figure 4.6 Particle size distribution curves resulted from the exposure of mammalian cell aggregates to the system generating maximum EDR of 270 W kg^{-1} for different time periods ranging from 15 to 300 s based on logarithmic scale. Data for 15 s was taken from Figure 4.2. It was found that longer shearing time resulted in more solid disruption and thus made the distribution curve shifted more to the left.

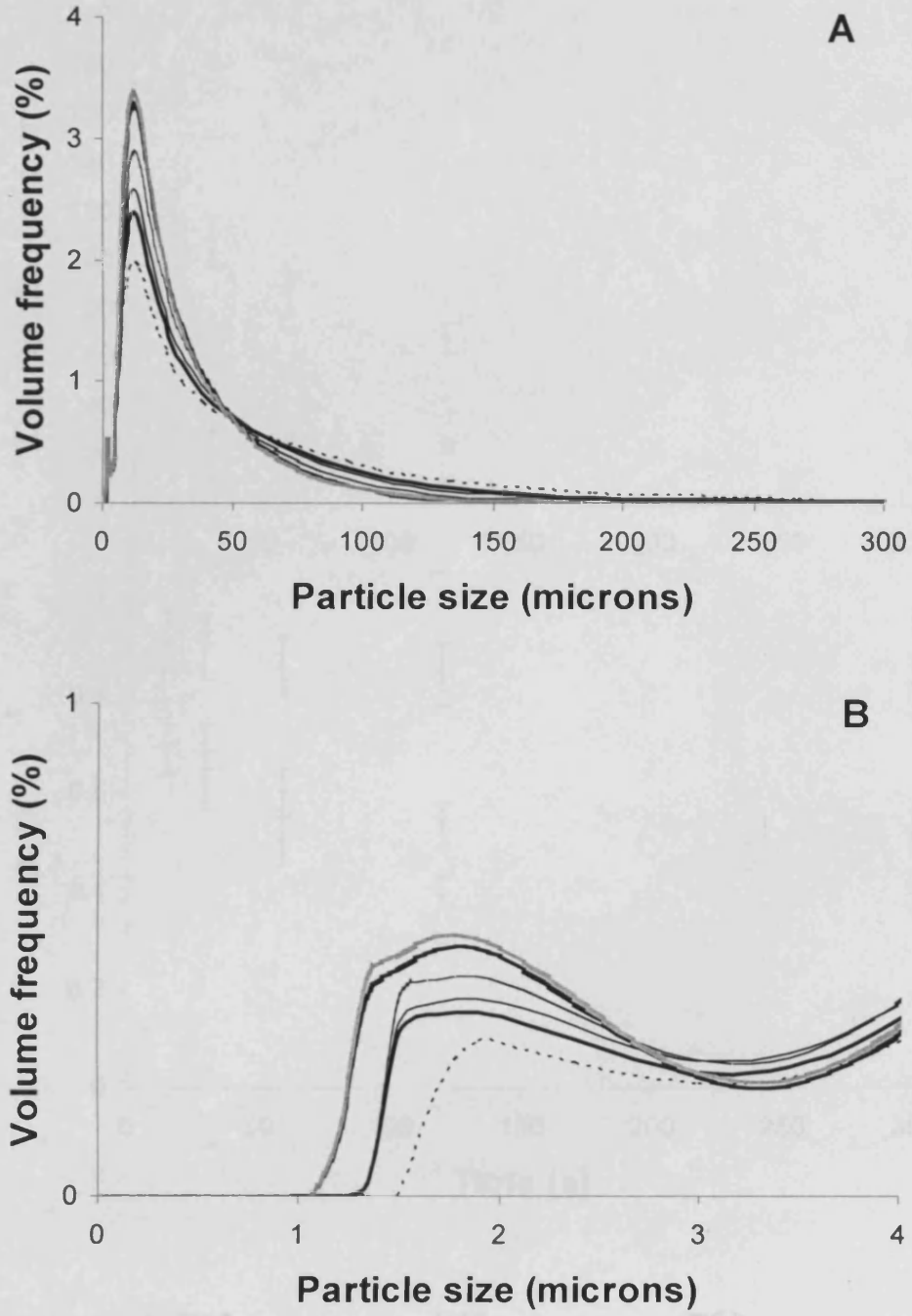

Figure 4.7 Changes of distribution curves of a suspension after being subjected to maximum EDR of 270 W kg^{-1} under the shearing time ranging from 15 to 300 s based on linear scale. Data for 15 s was taken from Figure 4.3. More disassembly of large aggregates and formations of small aggregates and cells took place as shearing time increased **(A)**. Prolonged time also caused an increase in the formation of cell debris which can be observed through an increase of the height of the smaller peak of the curve **(B)**.

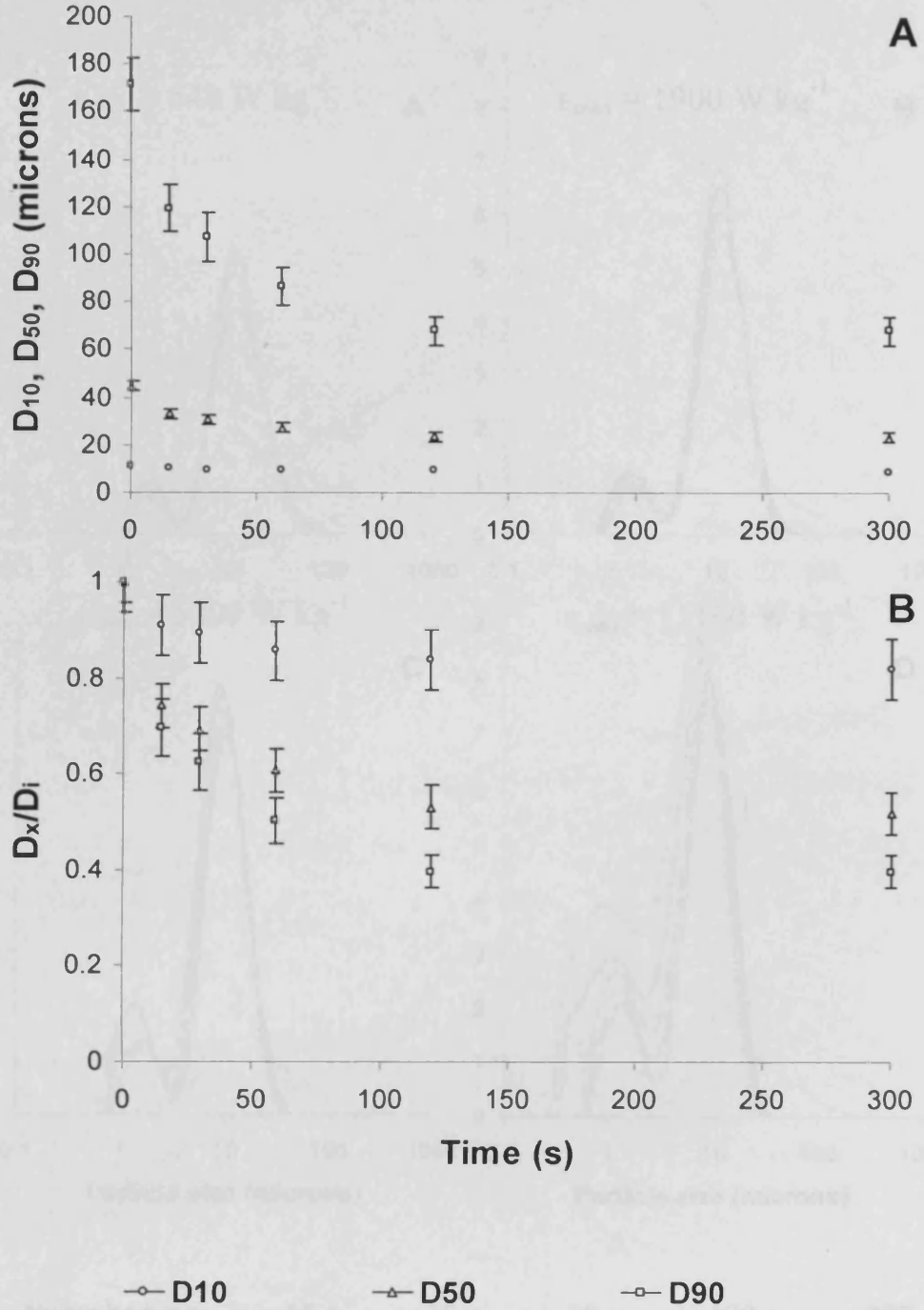

Figure 4.8 Changes of representative sizes of a suspension with time in the shear device having maximum EDR of 270 W kg^{-1}. Data for 15 s was taken from Figure 4.4. Both the derived diameter **(A)** and the ratio between the derived diameter and its initial size **(B)** are shown. It was found that changes with time is specific to particle size representatives of the fine, medium and large end of mammalian cell aggregates exposed to shear in this USD device. Sizes given are the equivalent particle diameters at which they are by volume 10% (D_{10}; -o-), 50% (D_{50}; -Δ-) and 90% (D_{90}; -□-) of particles of smaller size. The equivalent disc speed is 3260 rpm.

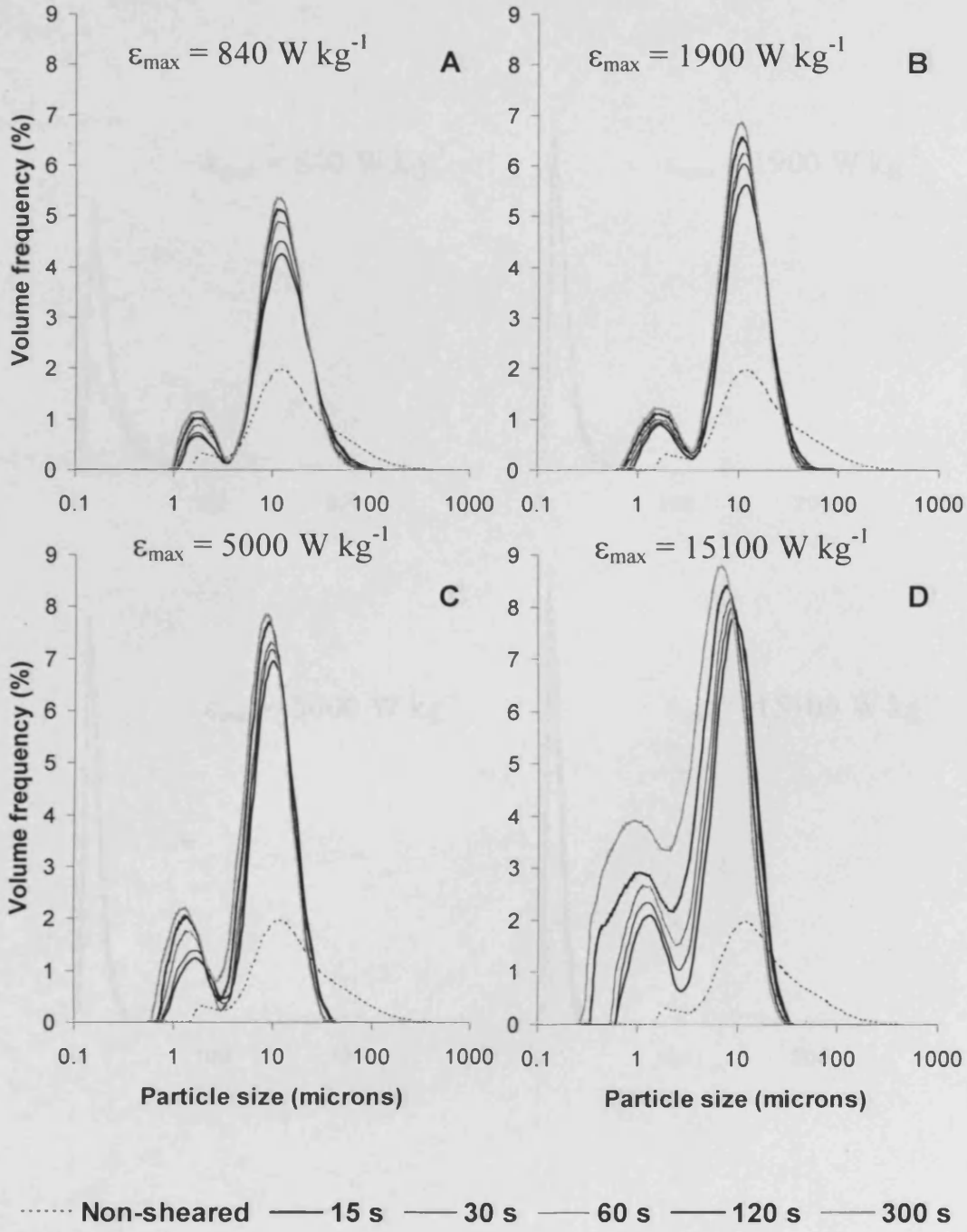

Figure 4.9 Changes of distribution curves of a suspension being subjected to different magnitudes of maximum EDR under the shearing times ranging from 15 to 300 s based on logarithmic scale. Data for 15 s was taken from Figure 4.2. These magnitudes include 840 **(A)**, 1900 **(B)**, 5000 **(C)** and 15100 W kg^{-1} **(D)**.

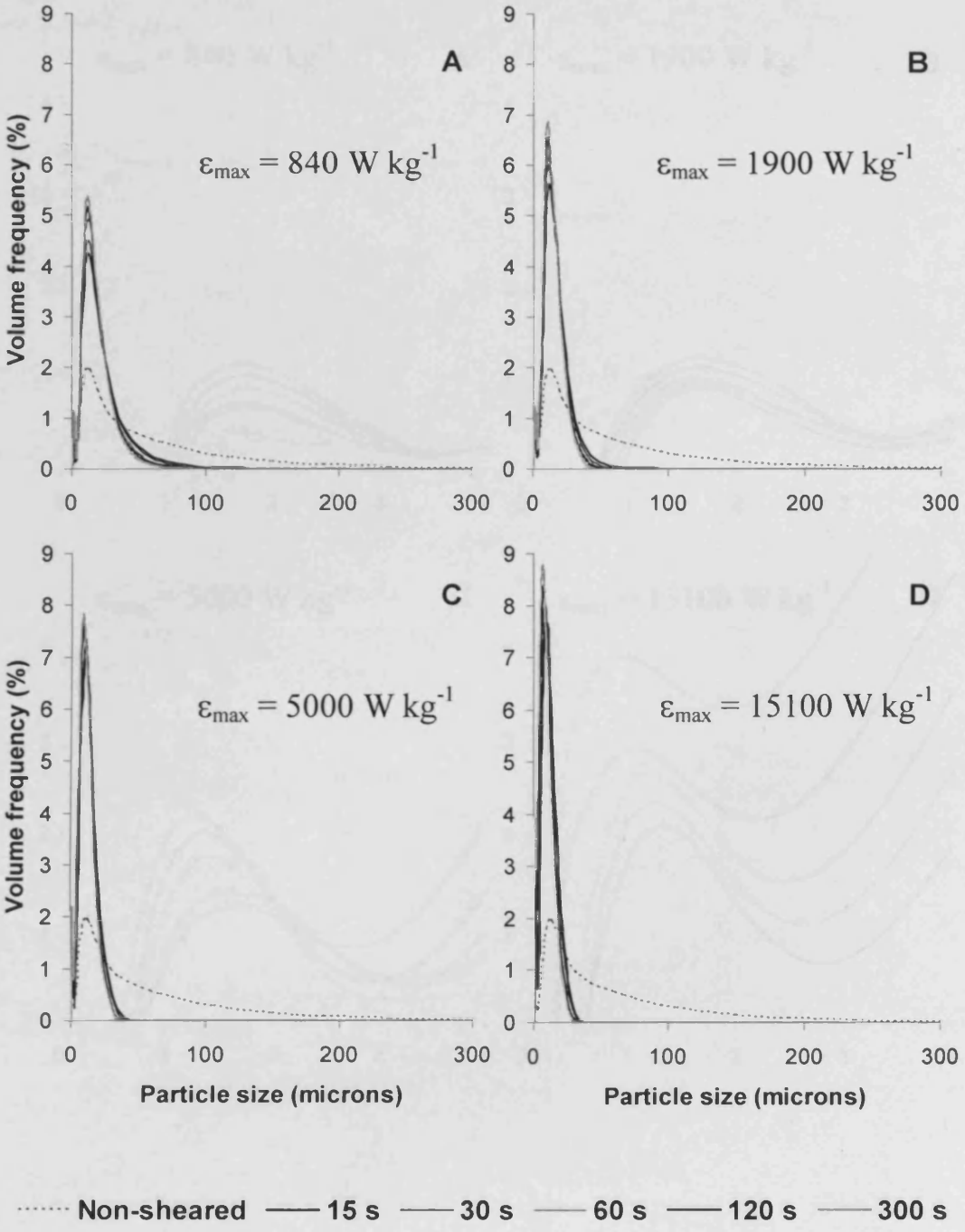

Figure 4.10 Changes of distribution curves of a suspension being subjected to different magnitudes of maximum EDR resulted from disassembly of large aggregates and formations of small aggregates and cells under the shearing times ranging from 15 to 300 s based on linear scale. Data for 15 s was taken from Figure 4.5. These magnitudes include 840 **(A)**, 1900 **(B)**, 5000 **(C)** and 15100 W kg^{-1} **(D)**.

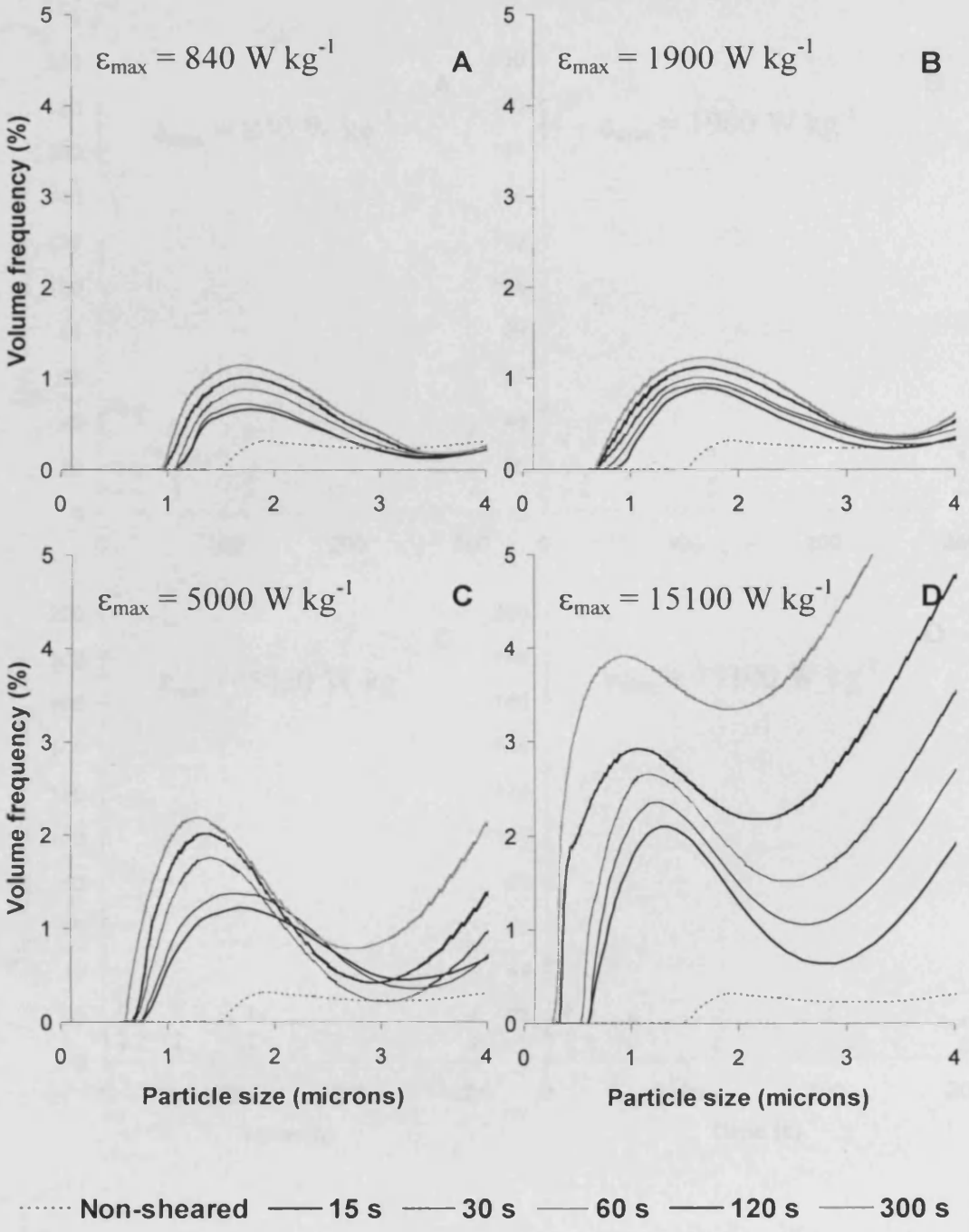

Figure 4.11 Changes of distribution curves of a suspension being subjected to different magnitudes of maximum EDR resulted from the debris formation under the shearing times ranging from 15 to 300 s based on linear scale. Data for 15 s was taken from Figure 4.5. These magnitudes include 840 **(A)**, 1900 **(B)**, 5000 **(C)** and 15100 W kg^{-1} **(D)**.

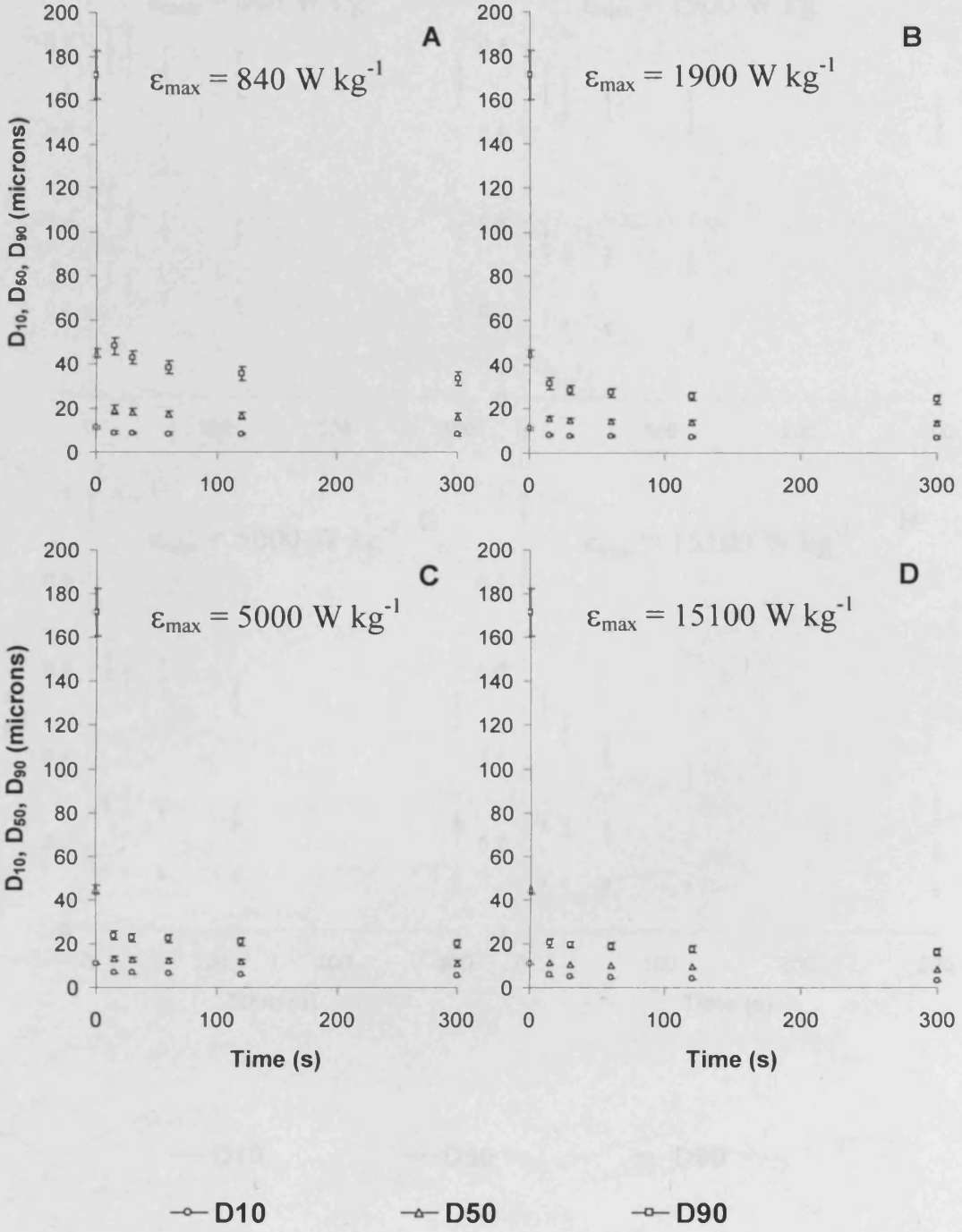
A
ε_{max} = 840 W kg^{-1}
B
ε_{max} = 1900 W kg^{-1}
C
ε_{max} = 5000 W kg^{-1}
D
ε_{max} = 15100 W kg^{-1}
D_{10}, D_{50}, D_{90} (microns)
Time (s)
D10
D50
D90

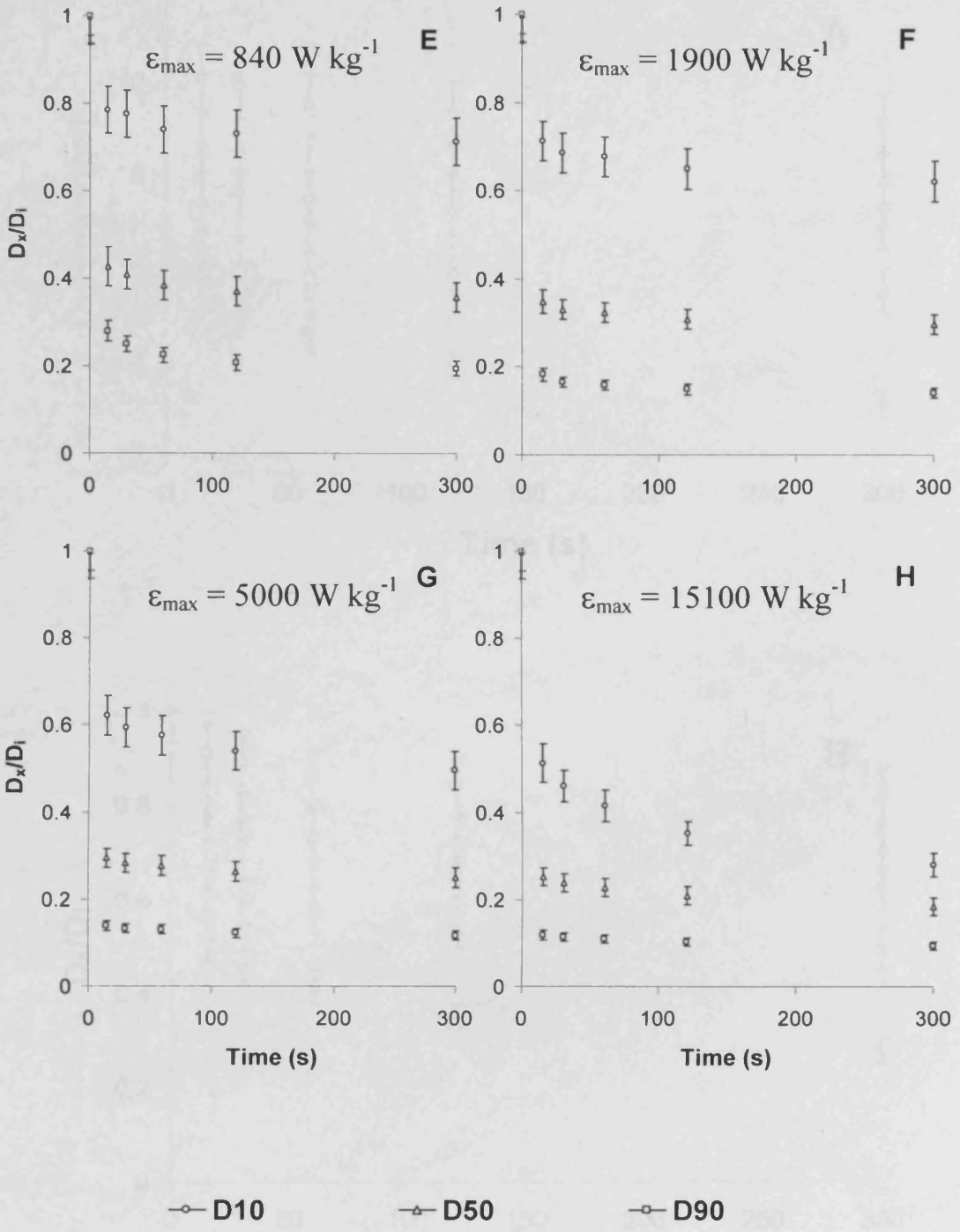

Figure 4.12 Changes of representative sizes of a suspension with time after being subjected to different magnitudes of maximum EDR in the USD device. These magnitudes include 840 **(A, E)**, 1900 **(B, F)**, 5000 **(C, G)** and 15100 W kg^{-1} **(D, H)**. Sizes given are the equivalent particle diameters at which they are by volume 10% (D_{10}; -o-), 50% (D_{50}; -Δ-) and 90% (D_{90}; -□-) of particles of smaller size.

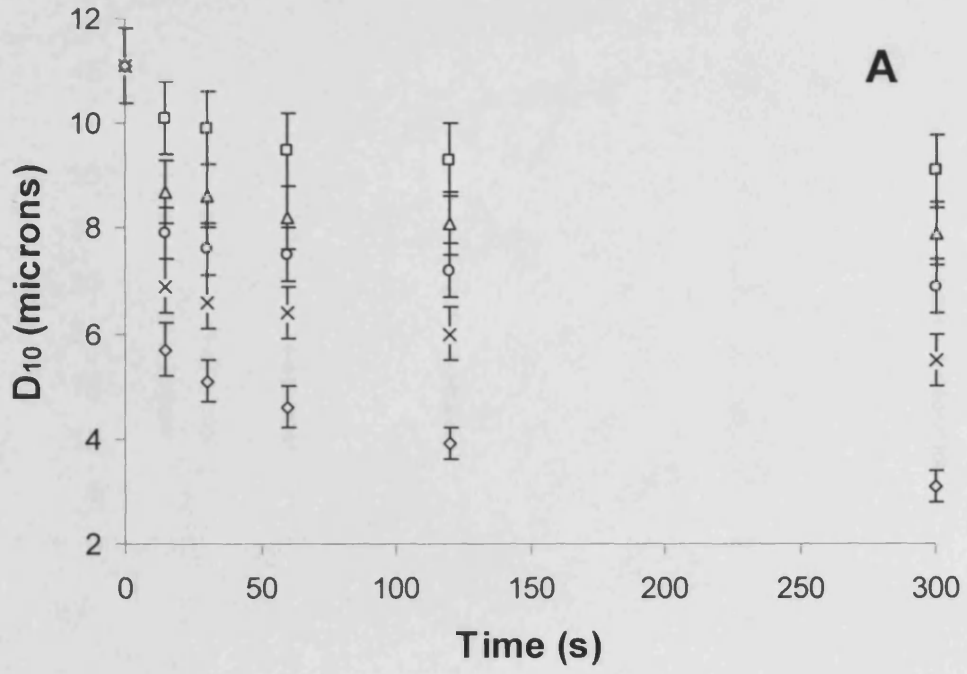

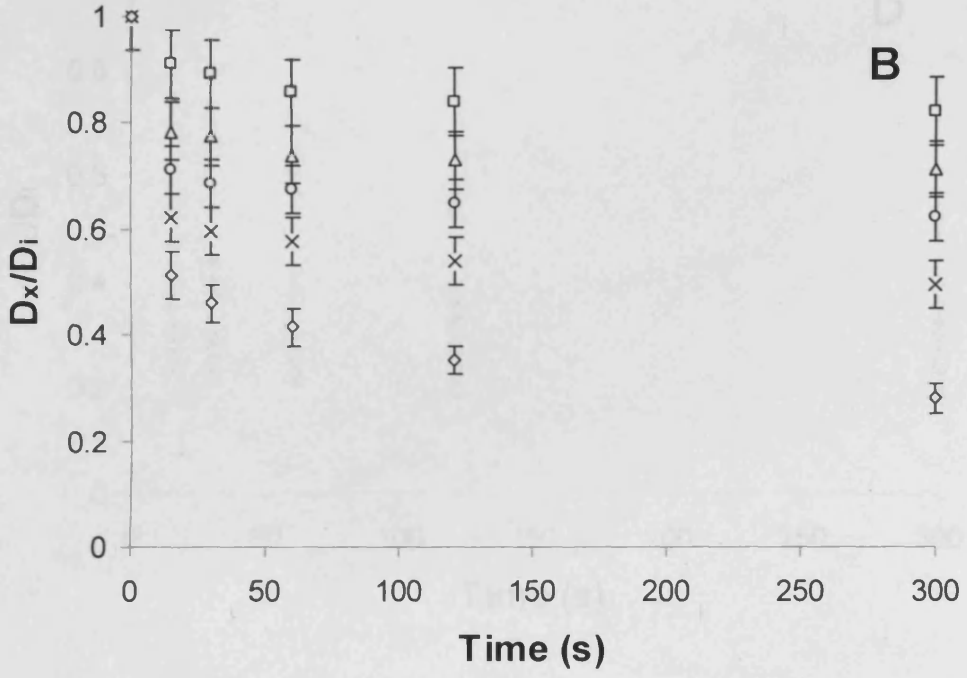

270 W kg-1 840 W kg-1 1900 W kg-1

5000 W kg-1 15100 W kg-1

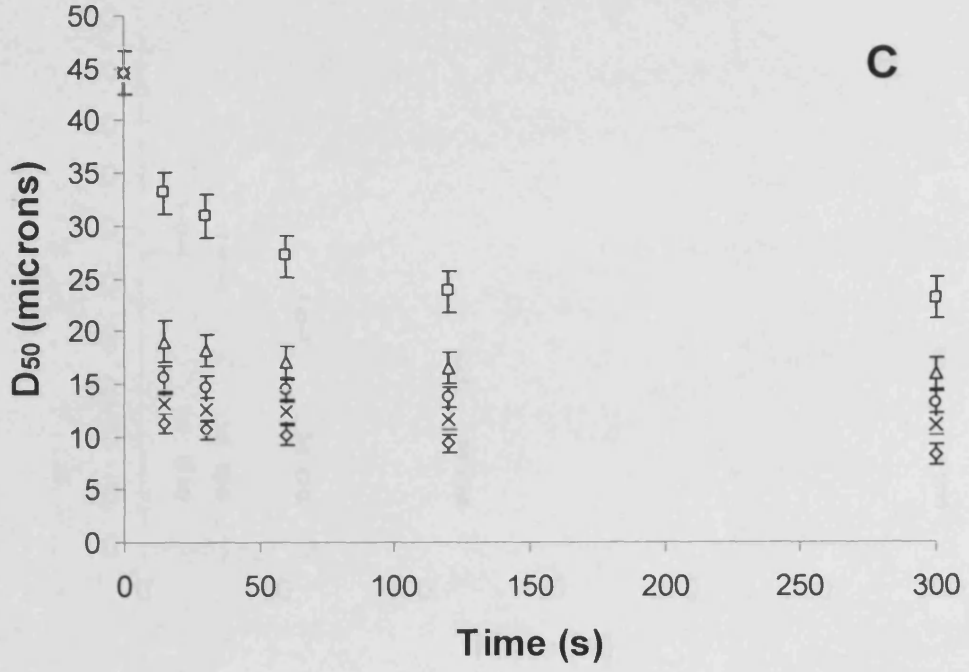

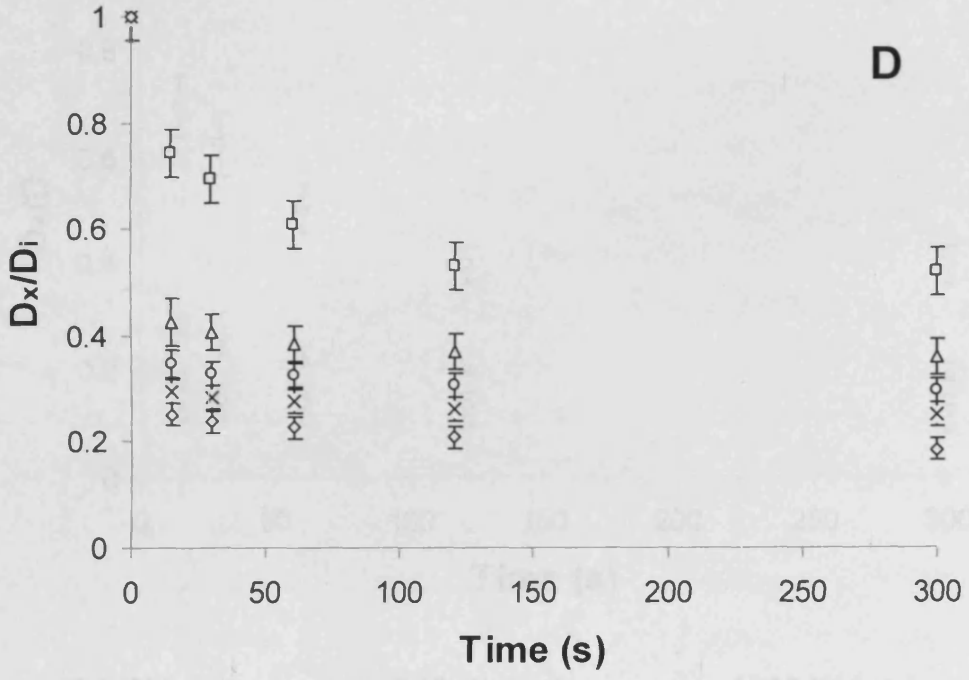

270 W kg-1 840 W kg-1 1900 W kg-1

5000 W kg-1 15100 W kg-1

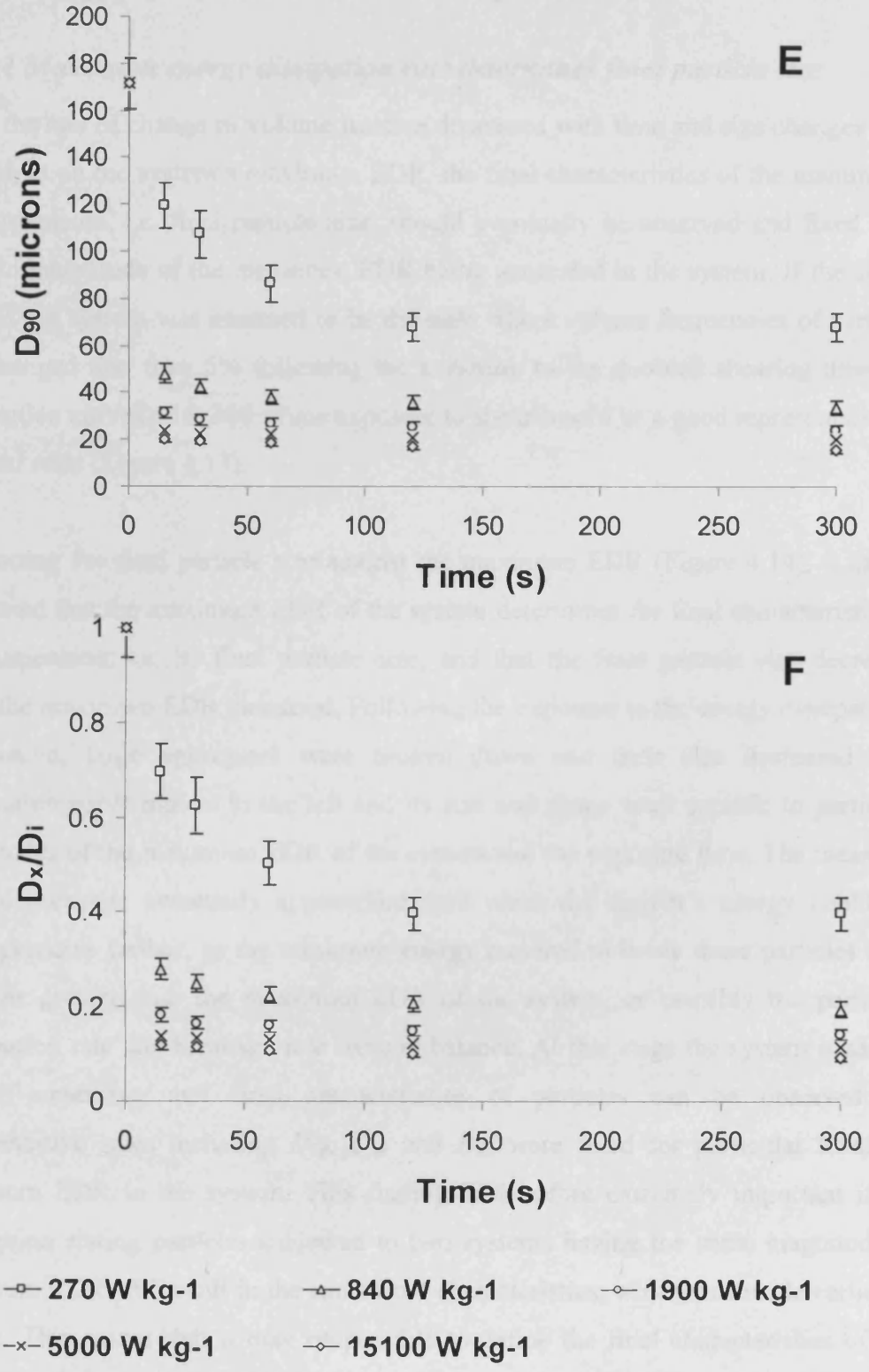

Figure 4.13 Changes of particle size representatives in the shear device with time. These changes of D_{10} **(A, B)**, D_{50} **(C, D)** and D_{90} **(E, F)** are specific to the maximum EDR of the system at which materials are subjected. Maximum EDR included 270 (-□-), 840 (-Δ-), 1900 (-o-), 5000 (-x-) and 15100 W kg^{-1} (-◇-).

4.2.3 Energy dissipation rate and final particle size

4.2.3.1 Maximum energy dissipation rate determines final particle size

Since the rate of change of volume fraction decreased with time and size changes were dependent on the system's maximum EDR, the final characteristics of the mammalian cell suspension, i.e. final particle size, should eventually be observed and fixed for a specific magnitude of the maximum EDR being generated in the system. If the steady state of the system was assumed to be the state where volume frequencies of particles had changed less than 5% following the exposure to the doubled shearing time, the distribution curves after 300 s runs exposure to shear would be a good representative of the final state (Figure 4.13).

By plotting the final particle size against the maximum EDR (Figure 4.14), it can be confirmed that the maximum EDR of the system determines the final characteristics of cell suspension, i.e. its final particle size, and that the final particle size decreased when the maximum EDR increased. Following the exposure to the energy dissipated in the system, large aggregates were broken down and their size decreased. The distribution curve moved to the left and its size and shape were specific to particular magnitudes of the maximum EDR of the system and the exposure time. The measured particle breakage eventually approached zero when the system's energy could not break particles further, as the minimum energy required to break these particles were equal or greater than the maximum EDR of the system, or possibly the particles' aggregation rate and breakage rate were in balance. At this stage the system is said to be self-preserving and final characteristics of particles can be observed; all representative sizes including D_{10}, D_{50} and D_{90} were fixed for particular levels of maximum EDR in the system. This finding is therefore extremely important if the assumption stating particles subjected to two systems having the same magnitude of maximum EDR will result in the same final characteristics, which was made earlier, is correct. This means that it may be possible to define the final characteristics of cell suspension in the large-scale operations having the equivalent magnitude of maximum EDR by processing small volumes of materials in the shear device.

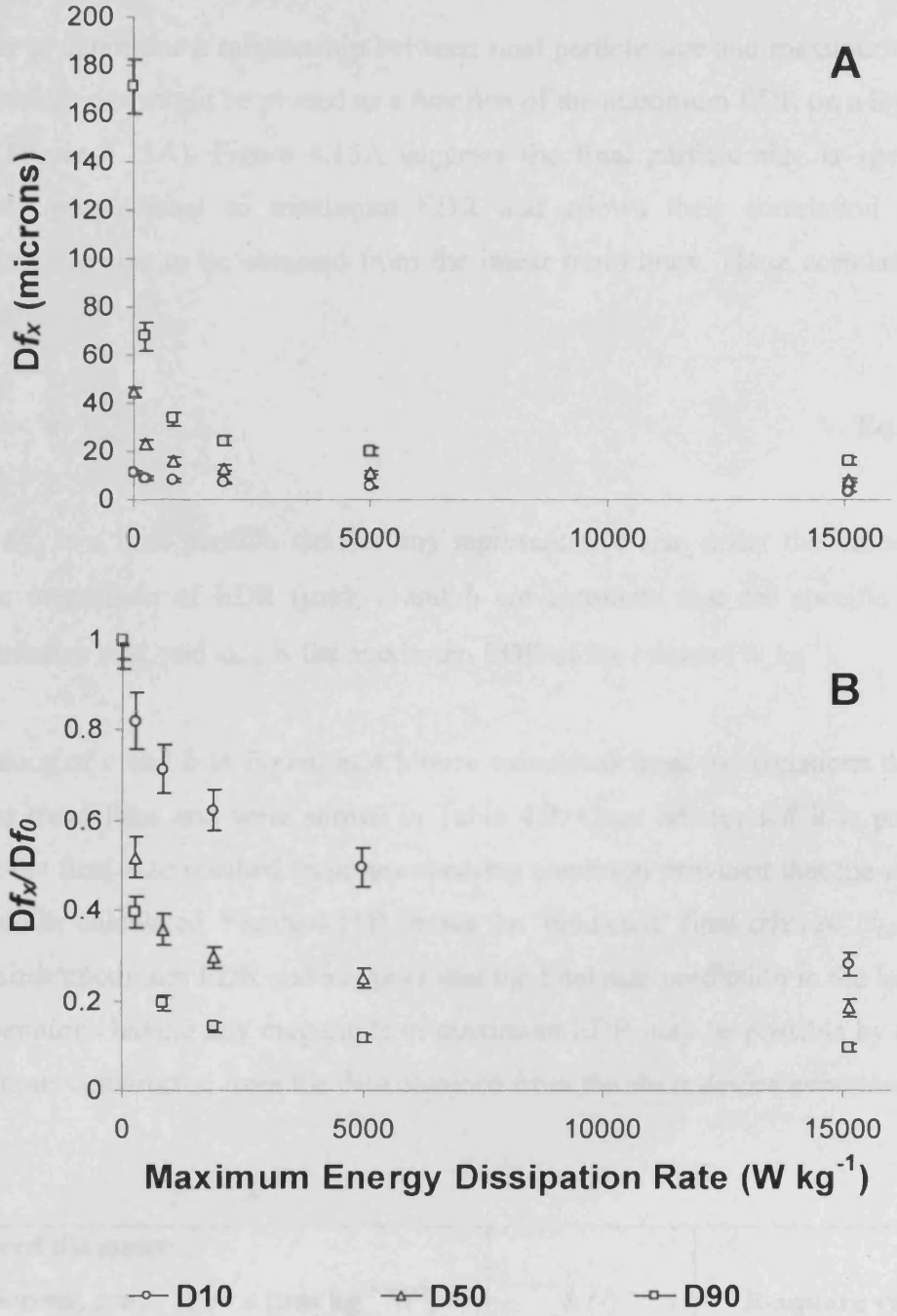

Figure 4.14 Final particle sizes (Df_x) and the ratios between the final size and the initial size (Df_x/Df_0) under various EDR for D_{10}, D_{50} and D_{90} after being subjected to different magnitudes of maximum EDR in the shear device. Data was taken from Figure 4.13. It was found that the higher the magnitude of maximum EDR, the smaller the final size **(A)** and that the size reduction is most prominent in large particle size representative **(B)**. Sizes given are the equivalent particle diameters at which they are by volume 10% (D_{10}; -o-), 50% (D_{50}; -Δ-) and 90% (D_{90}; -□-) of particles of smaller size.

4.2.3.2 Predictive model for final particle size

In order to determine a relationship between final particle size and maximum EDR, he final particle size might be plotted as a function of the maximum EDR on a logarithmic scale (Figure 4.15A). Figure 4.15A suggests the final particle size is specific and inversely proportional to maximum EDR and allows their correlation for each representative size to be obtained from the linear trend lines. These correlations take the form:

$$Df_x = c \cdot \varepsilon_{max}^{-b} \qquad \textbf{Eq. 4.1}$$

where Df_x is a final particle size for any representative size under the influence of a specific magnitude of EDR (μm), c and b are constants that are specific for each representative size, and ε_{max} is the maximum EDR of the system (W kg^{-1}).

The values of c and b in Equation 4.1 were calculated from the equations describing relevant trend lines and were shown in Table 4.2. Once determined it is possible to predict the final size resulted from any shearing condition provided that the maximum EDR can be calculated. Figure 4.15B shows the 'predicted' final sizes of D_{10}, D_{50} and D_{90} against maximum EDR and suggests that the final size prediction in the large-scale unit operations having any magnitude of maximum EDR may be possible by using the correlations constructed from the data obtained from the shear device experiments.

Derived diameter (microns, μm)	**c (μm kg^{-b} W^b)**	**b (-)**	**R-square values**
D_{10}	$10^{-0.2569}$	-43.024	0.9027
D_{50}	$10^{-0.2477}$	-88.443	0.9896
D_{90}	$10^{-0.3462}$	-390.51	0.9206

Table 4.2 The values of c and b in the equation describing a relationship between the final particle size and maximum EDR (Equation 4.1: $Df_x = c \cdot \varepsilon_{max}^{-b}$). These values were calculated from the trends lines from the logarithmic plots of the final particle size against maximum EDR.

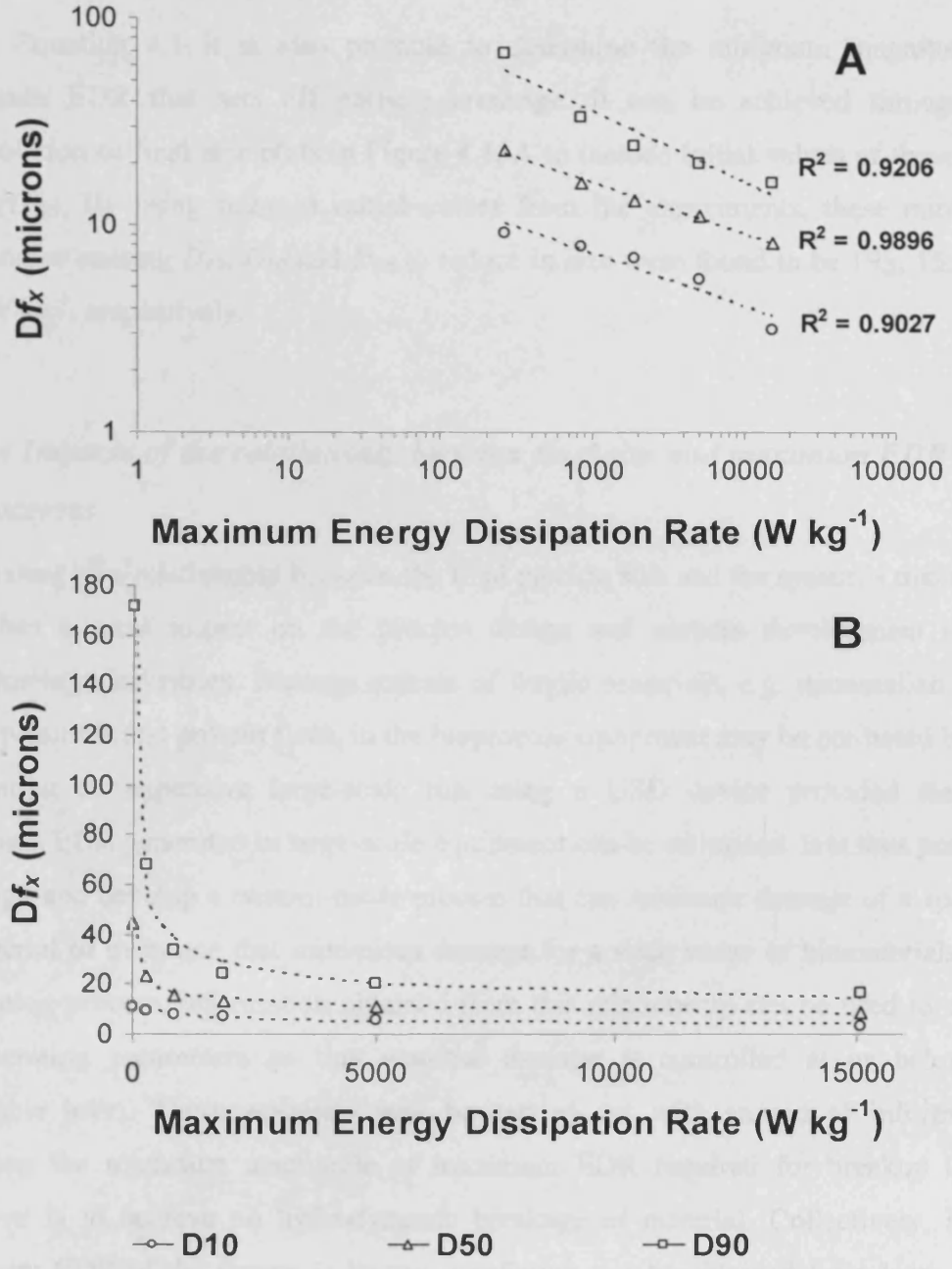

Figure 4.15 Logarithmic plots of the final particle size (Df_x) against maximum EDR **(A)** and corresponding prediction plots of the final particle size based on Equation 4.1: $Df_x = c \cdot \varepsilon_{max}^{-b}$ **(B)**. In **(A)** the dotted lines represent trends for each representative size, which provides equations to correlate final size and maximum EDR. Note that the R-squared value for each trend line was shown next to the associated line and that data points at zero EDR were not included for the calculations of these correlations. In **(B)** the final particle sizes were predicted using Equation 4.1 which in turn used constants '*c*' and '*b*' obtained from plots in **(A)**. Predictions, represented by dotted lines, are good for all representative sizes. Open data points represent final sizes obtained from shear device experiments.

4.2.3.3 Minimum EDR for particle breakage

Using Equation 4.1 it is also possible to determine the minimum magnitude of maximum EDR that sets off particle breakage. It can be achieved through the extrapolation of final size plots in Figure 4.15A to include initial values of those final sizes (Df_0). By using relevant initial values from the experiments, these minimum magnitudes causing D_{10}, D_{50} and D_{90} to reduce in size were found to be 195, 15.9 and 10.8 W kg^{-1}, respectively.

4.2.3.4 Impacts of the relationship between final size and maximum EDR on bioprocesses

The finding of a relationship between the final particle size and the system's maximum EDR has a great impact on the process design and process development in the biotechnology industries. Damage extents of fragile materials, e.g. mammalian cells, DNA, plasmids and protein flocs, in the bioprocess equipment may be predicted before performing an expensive large-scale run using a USD device provided that the maximum EDR generated in large-scale equipment can be estimated. It is thus possible to design and develop a custom-made process that can minimise damage of a specific biomaterial or even one that minimises damage for a wide range of biomaterials. For an existing process, information obtained from this relationship can be used to adjust the operating parameters so that material damage is controlled at or below an acceptable level. These activities may be carried out with an aid of information regarding the minimum magnitude of maximum EDR required for breakup if the objective is to achieve no hydrodynamic breakage of material. Collectively, if the maximum EDR of the system is known, prediction can be obtained for a large-scale bioprocess in terms of the final particle size, information which can be employed during process design and process development in order to develop economically a process that can minimise material damage using the USD device.

4.3 Conclusions

Results from experiments confirm that the materials used in the study are suitable due to its size-change consistency and reproducibility. Provided the maximum EDR of the system is higher than the minimum energy required for breakup, shear causes the size of aggregates to change. Following the exposure to shear, large aggregates were broken apart into smaller particles, cells and cell debris, which seems to be remnants of the solid disruption process. This resulted in the shift of the size distribution curve towards a smaller-particle region as well as the increase in the amount of particles having a diameter of smaller than 4 μm. These results of size changes are dependent on the shearing conditions and are more pronounced in the system having higher magnitudes of maximum EDR, as solids are broken into smaller entities compared to solids in the system having lower dissipated energy. The exposure time of solids to shear also affects the behaviour of particles. The extra shearing time allows solids to repeatedly flow back to the high-shear region causing more solids break up. A higher flow rate expelling liquid from the tip of the disc following an increase of maximum EDR further improved a chance of recurrence to the high-shear region and increased solid disruption.

It was also found that the final size of particles in a suspension was correlated well with the maximum EDR of the system and that the final size can be estimated once the magnitude of maximum EDR of the system is known and predictive equation applied. Moreover, it is recommended that the information regarding the relationship between the final size and maximum EDR should be integrated during stages involving process design and process development in order to minimise material damage in the system.

As most biologicals and pharmaceuticals are classed as shear-sensitive materials, which are expensive and unfavourably affected by engineering flow in the bioprocesses, the above findings are important and should be used to develop a strategy as a basis for process development, which includes process scale-up; process innovation and research; design, construction and operation of laboratory units or pilot plant; and process optimisation, in order to minimise shear damage.

CHAPTER 5 PARTICLE SIZE PREDICTIONS IN MEMBRANE FILTRATION PROCESS

This chapter presents the methodologies of linking two unique systems that are different in scale and configuration but have certain engineering parameters in common. The key fundamentals used to link these systems are described. Data obtained from the shear device experiments from the previous chapter together with certain hydrodynamic parameters from the two systems is used to devise models linking the large-scale membrane filtration unit with the ultra scale-down (USD) device based on the size change with time. These models are then used to predict large-scale operations based on the particle characteristics following the exposure of particles to shear. The chapter ends by introducing the approaches for modelling the particle size change with time under a range of shear environments by means of mathematical methods.

5.1 Predictive models for membrane operations

Often biomaterials are subjected to shear for only a very brief period in the process equipment and this period is also varied depending on the nature of the process and the equipment itself. Thus, it is advantageous to have models that could predict these corresponding shear effects, e.g. particle size change or damage extent, for specific time periods. Besides the model predicting the final particle size (Equation 4.1, **Chapter 4**), it is also possible to derive the predictive model for the change of particle size with time through the use of data obtained from the USD device in order to facilitate these prediction purposes.

This section will be presented in three parts. The first part describes the fundamentals used to derive predictive models for the change of volume fraction of large aggregates in mammalian cell suspension being processed in large-scale system. The findings from this part are then used to devise a model predicting the change of particle size in

the system in terms of equivalent particle diameter and a method linking systems of different scales, the derivations of which are explained in the second part and third part, respectively. The last part will also explain how small-scale (USD) data is used to predict large-scale operations in the system having the same magnitude of maximum energy dissipation rate (EDR).

5.1.1 Total volume fraction models

Because a mammalian cell suspension was subjected to essentially the same engineering environment when the maximum EDR in both USD and full-scale systems is kept the same, the size group of suspension particles given by particle size analyser (Malvern Mastersizer 2000) might be expected to show a similar pattern of change in volume percent (vol %) for both systems. These specific processes or changes in size might probably be correlated in terms of a rate constant (for example a first order rate constant) for the reduction of the sum of vol % (or total volume fraction, **TVF**) of large aggregates in the large-scale membrane system (k_{LP}) and the proportion of large aggregates left to be disrupted (L - L_{min}) where L is the proportion of large aggregates after the process is run for a specific time and L_{min} is the minimal or final value of the proportion of large aggregates under a specific shear environment. These hypotheses were similar to those of breakage models of enzyme release following cell disruption (Keshavarz-Moore et al., 1987) and of breakage models of whey protein precipitate particles in different flow geometries (Zumaeta et al., 2005) and based on assumptions:

- that large aggregates would be broken into smaller entities when they are subjected to a region where the energy dissipated is higher than the minimum required for break up;
- that the change of large aggregates will become less with time until the final value, i.e. L_{min}, is reached; and
- that the reduction process of large aggregates in the system depends on both the amount of large aggregates remaining to be disrupted (L - L_{min}) and the extent of energy dissipated in the high-energy zone which may be expressed in terms of the rate constant (k_{LP}).

As described later in this section, the extent of change will also be governed by other parameters including the flow rate through high energy-dissipation region (Q_p), the

volume of the large-scale membrane system (V_p) and the operating time (t_p). These correlations are later used to construct subsequent predictive models for size change during the membrane operation.

By looking at the analysed distribution expressed in a set of size classes by particle size analyser, there are a number of size classes ranging from 0.02 μm to 2000 μm, which are optimised to match the detector geometry and optical configuration. Any particles that lie in larger size classes than final size class of D_{50} are defined as large aggregates where D_{50}, also known as mass median diameter (MMD), is the size in microns at which 50% by volume of the sample is smaller and 50% is larger. Ultimately, the analysis assumes that aggregates with sizes larger than final size of D_{50} will be subjected to disruption following exposure to shear in the system.

Reduction of TVF of large aggregates in the large-scale membrane system

Here the reduction of the TVF of large aggregates (L) in the membrane filtration system where the pumping device is the key element responsible for critical shear environment is considered. A first-order process is assumed, i.e. the rate of change of the TVF of large aggregates per pass through the high-shear zone (dL/dN) is proportional to the TVF of large aggregates subjected to damage (L - L_{min}) where L_{min} is the minimal value of the TVF of large aggregates under specific operating (shearing) conditions. This may be written:

$$\frac{dL}{dN} = -k_{LP}\left(L - L_{\min}\right) \qquad \textbf{Eq. 5.1}$$

where k_{LP} is the first order rate constant for the reduction of the TVF of large aggregates in the membrane system; L is the TVF of large aggregates at any time; and N is the number of passes of aggregates in the system through the high energy dissipation area, i.e. the pump. Rearranging Equation 5.1 and integrating from pass N ($N = N$, $L = L_{in}$) to pass $N+1$ ($N = N+1$, $L = L_{out}$):

$$\int_{L=L_{in}}^{L=L_{out}} \frac{dL}{\left(L - L_{\min}\right)} = -k_{LP} \int_{N=N}^{N=N+1} dN \qquad \textbf{Eq. 5.2}$$

where L_{in} is the TVF of large aggregates *going into* the high energy-dissipation region and L_{out} is the TVF of large aggregates *going out of* the high energy-dissipation region (Figure 5.1). We then have:

$$\ln\left(\frac{L_{out} - L_{\min}}{L_{in} - L_{\min}}\right) = -k_{LP} \qquad \textbf{Eq. 5.3}$$

This can also be written:

$$\left(\frac{L_{out} - L_{\min}}{L_{in} - L_{\min}}\right) = e^{-k_{LP}} \qquad \textbf{Eq. 5.4}$$

Equation 5.4 can then be rearranged in terms of L_{out}:

$$L_{out} = \left(L_{in} - L_{\min}\right) e^{-k_{LP}} + L_{\min} \qquad \textbf{Eq. 5.5}$$

Mass balance in feed tank

Now, let's consider a feed tank in the membrane system (Figure 5.1). Complete the mass balance in terms of the TVF of large aggregates:

In : $Q_p \cdot L_{out}$

Out : $Q_p \cdot L_{in}$

Tank : $V_p \cdot \frac{dL_{in}}{dt_p}$

where Q_p is the flow rate through the pump, i.e. high energy-dissipation region in the membrane system ($m^3\ s^{-1}$); V_p is the liquid volume in the feed tank or the system volume (m^3); and t_p is the operating time (s). The feed tank is in unsteady state with respect to the TVF of large aggregates; it is assumed that the feed tank is well mixed such that the properties of the process stream exiting the tank are the same as that in

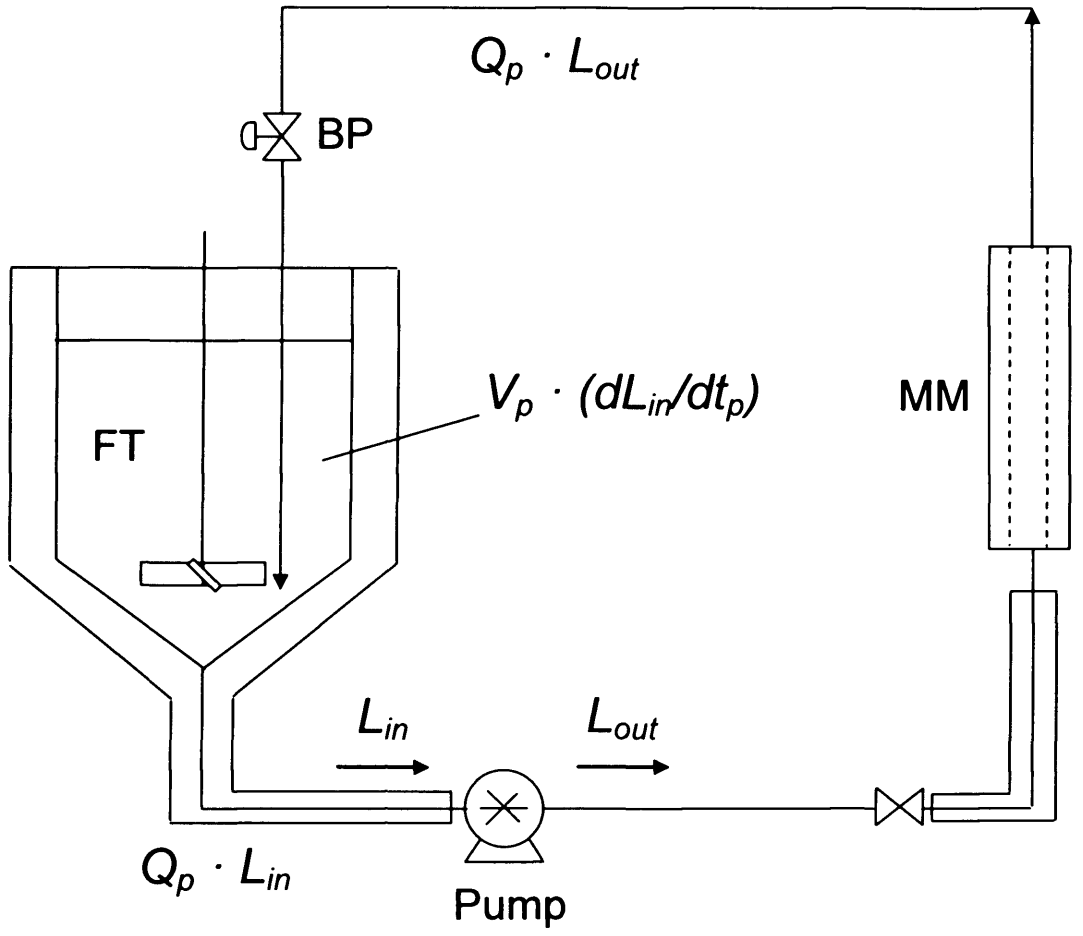

Figure 5.1 Schematic diagram of the membrane filtration system used to devise predictive models for size reduction. In this system the pumping device is the key element responsible for generating critical shear environment and thus the whole system can be viewed as a pumping system. Here membrane module (MM), feed tank (FT) and valve (BP) are assumed to cause no damage. After a cell suspension is passed through the pump, total volume fraction (TVF) of large aggregates entering the pump (L_{in}) is reduced to the TVF of large aggregates exiting the pump (L_{out}). By considering the mass balance in the feed tank, the flow rate through the pump (Q_p), the volume of the membrane system (V_p) and the operating time (t_p) can be correlated to help devise predictive models for size change of aggregates during membrane operation.

the tank. According to mass balance theory, the relationship of above terms can be written:

$$In = Out + Accumulation \qquad \textbf{Eq. 5.6}$$

Based on Equation 5.6 we have:

$$Q_p \cdot L_{out} = Q_p \cdot L_{in} + V_p \cdot \frac{dL_{in}}{dt_p} \qquad \textbf{Eq. 5.7}$$

Rearranging Equation 5.7:

$$Q_p \left(L_{out} - L_{in}\right) = V_p \cdot \frac{dL_{in}}{dt_p} \qquad \textbf{Eq. 5.8}$$

Mass balance integration

Substituting L_{out} from Equation 5.5 into Equation 5.8 we have:

$$Q_p \left[\left(L_{in} - L_{\min}\right) e^{-k_{LP}} + L_{\min} - L_{in}\right] = V_p \cdot \frac{dL_{in}}{dt_p} \qquad \textbf{Eq. 5.9}$$

Rearranging Equation 5.9 and integrating from time zero ($t_p = 0$, $L_{in} = L_0$) to time t_p ($t_p = t_p$, $L_{in} = L_{in}$) where L_0 is the TVF of large aggregates at time zero:

$$-\int_{t_p=0}^{t_p=t_p}\left(\frac{Q_p}{V_p}\right)\left(1-e^{-k_{LP}}\right)dt_p = \int_{L_{in}=L_0}^{L_{in}=L_{in}} \frac{dL_{in}}{\left(L_{in} - L_{\min}\right)} \qquad \textbf{Eq. 5.10}$$

$$\frac{L_{in} - L_{\min}}{L_0 - L_{\min}} = e^{-\left(\frac{Q_p}{V_p}\right)\left(1-e^{-k_{LP}}\right)t_p} \qquad \textbf{Eq. 5.11}$$

Rearranging Equation 5.11 in terms of L_{in} we have:

$$L_{in} = (L_0 - L_{\min}) e^{-\left(\frac{Q_p}{V_p}\right)\left(1-e^{-k_{LP}}\right)t_p} + L_{\min} \qquad \textbf{Eq. 5.12}$$

As might be expected Equation 5.12 suggests that the total volume fraction of large aggregates in the system at any specific time depends on several factors including recurrent rate of fluid material to the high-shear zone (Q_p/V_p), intensity of fluid flow fields in the system (k_{LP} and L_{min}), initial volume fraction of large aggregates (L_0) and operating time (t_p).

5.1.2 Equivalent particle diameter models

5.1.2.1 Characterisation of break up

The above analysis examines the change in volume fraction of aggregates in a given size range. However, it is more common and useful to consider size distributions in terms of the characteristic sizes at which there is a fixed volume of particles of lower size, e.g. D_{90} is the diameter at which 90% by volume of particles are of smaller size. Small changes in size distribution may be approximated as a simple shift in the overall size distribution profile with respect to particle diameter. In this case by geometrical equivalence:

$$\frac{dD_x}{dt} \alpha \frac{dL}{dt} \qquad \textbf{Eq. 5.13}$$

where L is the volume fraction of large aggregates initially represented by the size range given by D_x.

On this basis, let's consider all the parameters involved in the change of derived diameters with time in any particular system. Similar to the change of total volume fraction of large aggregates, these parameters include the initial value of any derived diameter (Di_x), the final value of any derived diameter (Df_x), the intermediate value of any derived diameter (D_x), the shearing time (t) and the maximum EDR of the system. Arranging and plotting these parameters may provide important insights into key relationships between them. Figure 5.2 shows one arrangement where the ratio of (Di_x-

Df_x) and (D_x-Df_x) was plotted against the shearing time for the shearing condition having maximum EDR of 270 W kg^{-1}. This figure suggests that the rate of reduction of D_{10}, D_{50} and D_{90} with time follows the first-order process. According to Figure 5.2 and Equation 5.13, the equivalent particle diameter models may be derived in a similar fashion to that for the TVF of large aggregates (L) as shown in the next section.

5.1.2.2 Reduction of derived diameters in the system

Assume a first-order process, i.e. the rate of reduction of D_x per unit time after passing through the high-shear region (dD_x/dt) is proportional to the value of D_x susceptible for reduction ($D_x - Df_x$). This may be written:

$$\frac{dD_x}{dt} = -k_{DS}\left(D_x - Df_x\right) \qquad \textbf{Eq. 5.14}$$

where k_{DS} is the first order rate constant of the reduction process of derived diameters in either USD or large-scale system (s^{-1}). Rewrite Equation 5.14 and integrate from time zero ($t = 0$, $D_x = Di_x$) to time t ($t = t$, $D_x = D_x$):

$$\int_{D_x=Di_x}^{D_x=D_x} \frac{dD_x}{\left(D_x - Df_x\right)} = -k_{DS}\int_{t=0}^{t=t} dt \qquad \textbf{Eq. 5.15}$$

$$\ln\left(\frac{Di_x - Df_x}{D_x - Df_x}\right) = k_{DS}\cdot t \qquad \textbf{Eq. 5.16}$$

Consequently, k_{DS} may be evaluated from a slope of the plot of $\ln\left(\frac{Di_x - Df_x}{D_x - Df_x}\right)$ against the shearing time (t), e.g. plots in Figure 5.2. Equation 5.16 can then be rearranged to provide the value of D_x at any time ($t = t$):

$$\frac{Di_x - Df_x}{D_x - Df_x} = e^{k_{DS}\,t} \qquad \textbf{Eq. 5.17}$$

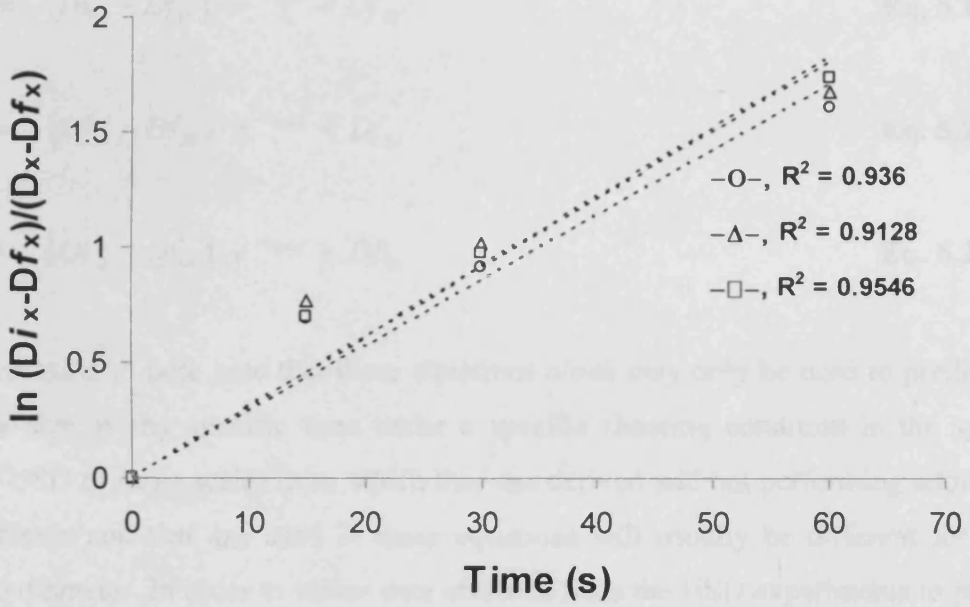

Figure 5.2 Plots of intermediate values of any derived diameter (D_x), the initial value of any derived diameter (Di_x) and the final value of any derived diameter (Df_x) in terms of $\ln\left(\frac{Di_x - Df_x}{D_x - Df_x}\right)$ against the shearing time. The plots give linear trends for all derived diameters in the shearing condition having maximum EDR of 270 W kg^{-1} generated by the disc speed of 3260 rpm. Sizes given are the equivalent particle diameter at which they are by volume 10% (D_{10}; -o-), 50% (D_{50}; -Δ-) and 90% (D_{90}; -□-) of particles of smaller size.

$$D_x = (Di_x - Df_x)\, e^{-k_{DS}\, t} + Df_x \qquad \textbf{Eq. 5.18}$$

As a result, the values of D_{10}, D_{50} and D_{90} in the system at any time may be evaluated from the following equations:

$$D_{10} = (Di_{10} - Df_{10}) \cdot e^{-k_{DS}\, t} + Df_{10} \qquad \textbf{Eq. 5.19}$$

$$D_{50} = (Di_{50} - Df_{50}) \cdot e^{-k_{DS}\, t} + Df_{50} \qquad \textbf{Eq. 5.20}$$

$$D_{90} = (Di_{90} - Df_{90}) \cdot e^{-k_{DS}\, t} + Df_{90} \qquad \textbf{Eq. 5.21}$$

It is important to note here that these equations *alone* may only be used to predict the particle size at any specific time under a specific shearing condition in the system (either USD or large scale) from which they are derived without performing additional experiments and that k_{DS} used in these equations will usually be different for each derived diameter. In order to utilise data obtained from the USD experiments to predict large-scale operations, one approach is to determine the time in the USD device (t_s) running at equivalent speed that allows the same damage to that in the large scale and then use this corresponding time in Equations 5.19 to 5.21 in order to obtain D_{10}, D_{50} and D_{90}, respectively. Full details of this matching method are explained in the next section.

5.1.3 System linkage methodologies

5.1.3.1 Equivalent USD time

To link USD to full-scale membrane system, the shear device may be viewed as a membrane separation system where the pump and feed tank are equivalent to the high-shear region at the tip of the rotating disc and the total chamber volume of the shear device, respectively. This can be viewed as in Figure 5.3, which shows schematic diagrams of membrane unit reactor and shear cell reactor models. From the analogy presented in this figure, the behaviour of TVF of large aggregates in the USD system may be characterised in the same fashion to that of Equation 5.12 as:

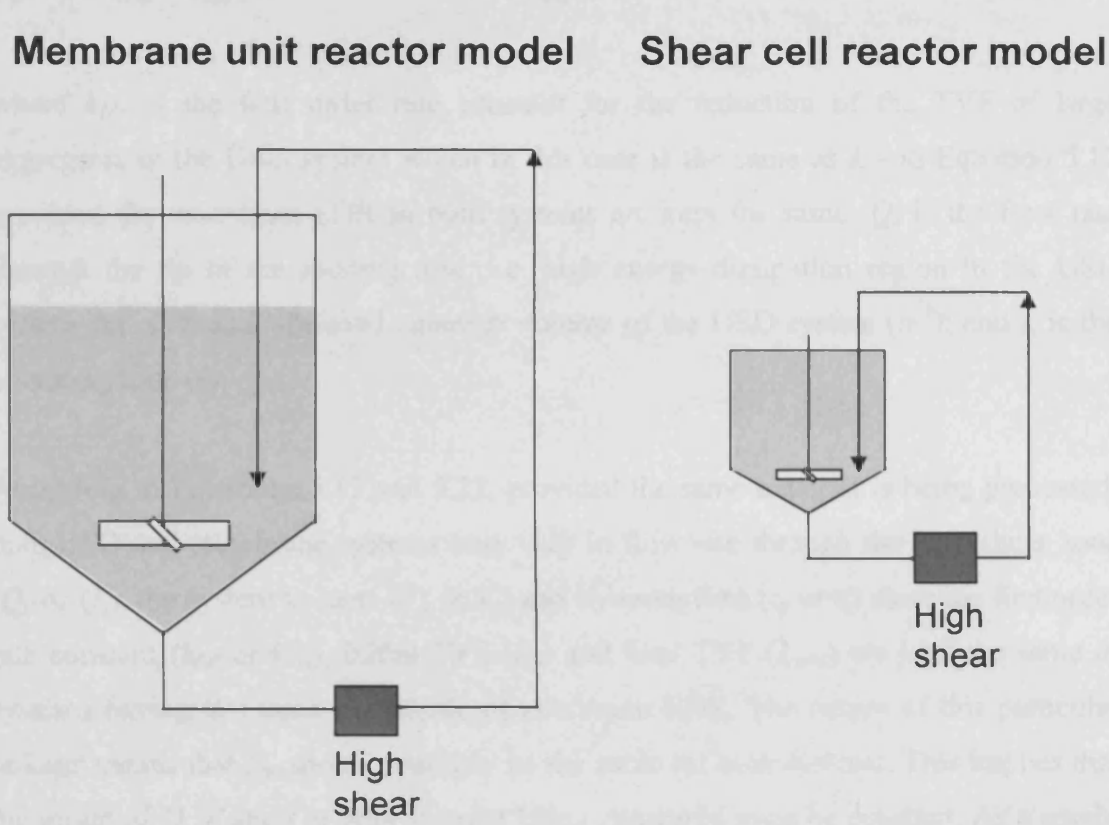

Total volume:	High	Low
Recurrence to high-shear zone:	Low	High
Process time:	High	Low

Figure 5.3 Schematic illustration of large-scale membrane rig and USD device having high energy-dissipation region that can be matched up provided maximum energy dissipation rate in both systems is kept constant. The high-shear region is shown in dark grey shade with the light grey shade representing the rest of the equipment components and process fluid. In the membrane rig the total volume is very large compared to that of the USD device resulting in a lower rate of recurrence of the process stream to the high-shear zone and thus a longer operating time (hours) if the same amount of damage to be achieved. In contrast, the total volume of the USD device is very low resulting in a higher recurrent rate to the high-shear zone and shortened operating time (seconds) to reach the set level of damage.

$$L_{in} = (L_0 - L_{\min})\, e^{-\left(\frac{Q_s}{V_s}\right)\left(1-e^{-k_{LU}}\right)t_s} + L_{\min} \qquad \textbf{Eq. 5.22}$$

where k_{LU} is the first order rate constant for the reduction of the TVF of large aggregates in the USD system which in this case is the same as k_{LP} in Equation 5.12 provided the maximum EDR in both systems are kept the same; Q_s is the flow rate through the tip of the rotating disc, i.e. high energy-dissipation region in the USD system ($m^3\ s^{-1}$); V_s is the total chamber volume of the USD system (m^3); and t_s is the operating time (s).

According to Equations 5.12 and 5.22, provided the same material is being processed, both USD and membrane systems only vary in flow rate through the high-shear zone (Q_p or Q_s), the system volume (V_p or V_s) and shearing time (t_p or t_s) since the first order rate constant (k_{LP} or k_{LU}), initial TVF (L_0) and final TVF (L_{min}) are kept the same in systems having the same magnitude of maximum EDR. The nature of this particular linkage means that L_{in} should probably be the same for both systems. This implies that the group of Q, V and t in both systems being compared must be constant. As a result, Equations 5.12 and 5.22 can be derived and expressed to allow the matching of USD and full-scale membrane systems:

$$\left[\frac{Q_p \cdot t_p}{V_p}\right]_{Full\ scale} = \left[\frac{Q_s \cdot t_s}{V_s}\right]_{USD} \qquad \textbf{Eq. 5.23}$$

Using Equation 5.23, if relevant parameters are known for systems having different scales, the damage of materials can be matched. Ultimately, predictions of the TVF of large aggregates going into the high energy-dissipation region (L_{in}) in the large-scale membrane system can be achieved through the use of operating time in USD device (t_s) that makes corresponding damage:

$$t_s = \left(\frac{Q_p \cdot t_p}{V_p}\right) \cdot \left(\frac{V_s}{Q_s}\right) \qquad \textbf{Eq. 5.24}$$

5.1.3.2 Prediction methodology based on USD data

Once the equivalent USD time (t_s) is obtained the size prediction in large-scale operations may be achieved by either direct USD experiments or predetermined predictive models. The USD experiments can be directly performed for a specific time (given by the Equation 5.24) allowing size characteristics to be determined in terms of both TVF of large aggregates (L_{in}) and a more useful term, derived diameter (D_x). Otherwise, predictive models are also readily available to estimate L_{in} (Equation 5.22) and D_x (Equation 5.18) if all relevant parameters have previously been established. On this basis Equations 5.22 and 5.18 can alternatively be viewed as follows:

$$[L_{in}]_{Full\ scale,t_p} = \left[(L_0 - L_{\min}) e^{-\left(\frac{Q_s}{V_s}\right)\left(1-e^{-k_{LL}}\right)t_s} + L_{\min} \right]_{USD,t_s} \qquad \textbf{Eq. 5.25}$$

$$[D_x]_{Full\ scale,t_p} = \left[(Di_x - Df_x) e^{-k_{DL} t_s} + Df_x \right]_{USD,t_s} \qquad \textbf{Eq. 5.26}$$

As the derived diameter D_x is a more common and useful form presenting particle size, the rest of the analysis will mainly present the particle size in terms of D_x.

5.2 Large-scale predictions of membrane operations

5.2.1 Essential parameters for large-scale predictions

As described a number of process hydrodynamic parameters and material properties are required by the predictive models to determine the size change of a mammalian cell suspension in the large-scale system once two systems being compared generate the same magnitude of maximum EDR. The prediction method principally concerns the time taken in the USD device (t_s) to produce the same effects as in the large-scale unit and the values of derived diameters at any specific time in the USD device (D_x), which in turn correspond to those in large scale. Thus, these steps mainly involve using Equations 5.24 and 5.26; the equation parameters are detailed below:

1. Flow rate through the pump (Q_p)

The pump was determined to represent the high-shear zone in the system and thus the flow rate through it is considered. The flow rate depends on its rotational speed, which varies from 300 to 1500 rpm. Two speeds, i.e. 600 and 1500 rpm, were chosen in the study. These speeds deliver liquid at the rates of 7.32 and 18.36 L min^{-1}, respectively ($1.22*10^{-4}$ and $3.06*10^{-4}$ m^3 s^{-1}).

2. Total volume of the large-scale system (V_p)

This includes all the liquid in the pump itself, reservoir (feed tank) and pipes. In this study this is 9.6 L or $9.6*10^{-3}$ m^3.

3. Operating time in the large-scale system (t_p)

This depends on the process objective. As the verification process (see **Chapter 6**) was carried out for 4 hours, the maximum operating time for this system is 4 h or 14400 s. However, for prediction purposes, the time suspension was processed in the system will be chosen between 0 to 14400 s.

4. Flow rate expelling fluid from tip of the disc (Q_s)

The equivalent speeds of the shear device are 5000 and 15000 rpm for the pump speed of 600 and 1500 rpm, respectively. The expelling flow rates were found using CFD to be $9.4*10^{-6}$ and $25.6*10^{-6}$ m^3 s^{-1} for the speeds of 5000 and 15000 rpm, respectively. Note that in the CFD simulations a two-dimension patch of 1 mm high (same as disc's height) was drawn around and next to the tip of the rotating disc and simulation parameters were specified such that the flow rate in the direction outward the disc could be calculated. In this way the flow rate through the high-shear zone can be obtained.

5. Total volume of USD device (V_s)

This is 20 mL or $2*10^{-5}$ m^3.

6. Operating time in USD device (t_s)

This is calculated using Equation 5.24.

7. Initial particle size (Di_x)

These include Di_{10}, Di_{50} and Di_{90} (Equation 5.26).

8. Final particle size (Df_x)

While the initial particle size can be measured directly from the test sample, the final particle size has to be obtained at the state where a little or no change of particle size can be observed. In this investigation this state was assumed to be after 300 s of the USD operation. This assumption has been justified using information obtained from Figure 4.13 and Table 4.1 (see **Chapter 4**). Again, this parameter will be used in Equation 5.26.

9. First order rate constant (k_{DU})

This depends on the shearing condition of the USD system and can be evaluated from a plot of $\ln\left(\frac{Di_x - Df_x}{D_x - Df_x}\right)$ against the shearing time (t_s). It will also be used in Equation 5.26.

5.2.2 Large-scale predictions

Once all required parameters are obtained procedures to achieve large-scale size predictions can be followed (refer to Figure 5.9 for a flowchart of this process).

5.2.2.1 Calculation of equivalent USD time (t_s)

The objective of this first step is to calculate the equivalent time in the USD device (t_s) that causes theoretically the same damage to aggregates in the large-scale system. This can be achieved using the Equation 5.24. All parameters resulting from pump speeds of 600 and 1500 rpm and the disc speeds of 5000 and 15000 rpm allow the equivalent USD times to be calculated. As the principal change of particle size was observed to take place early in the process, the differences of chosen times for the pumping system (t_p) will be very small within the first hour of the process and will become larger after the first hour until the process stops. Table 5.1 shows the corresponding times in the USD device for specific times in the large-scale system for both pump speeds of 600

rpm and 1500 rpm. The equivalent USD time obtained will then be used to determine derived diameter in the large-scale system when the processing time is given.

5.2.2.2 Evaluation of derived diameters in the large-scale system (D_x)

After the equivalent USD time is obtained it is possible to predict the derived diameter in the large-scale system using Equation 5.26. Di_x and Df_x are fixed whereas k_{DU} is obtained from the corresponding USD experiments. Time used in these equations will be the equivalent time in the USD device (t_s). Figure 5.4 shows the prediction of the size change of mammalian cell suspension in terms of derived diameters with the processing time in the large-scale system for both pump speeds of 600 and 1500 rpm.

Time in large-scale system (t_p, s)	**Time in USD device (t_s, s)**	
	Pump speed of 600 rpm (USD speed = 5000 rpm)	**Pump speed of 1500 rpm (USD speed = 15000 rpm)**
0	0	0
120	3	3
240	6	6
420	11	10
600	16	15
900	24	22
1200	32	30
1800	48	45
2400	65	60
3000	81	75
3600	97	90
7200	194	180
10800	292	270
14400	390	360

Table 5.1 The equivalent USD times (t_s) for specific processing times in the large-scale system (t_p) for pump speeds of 600 and 1500 rpm. Data was obtained using the Equation 5.24 and parameters described in section 5.2.1. This table is presented for convenience and purposes of experimental design.

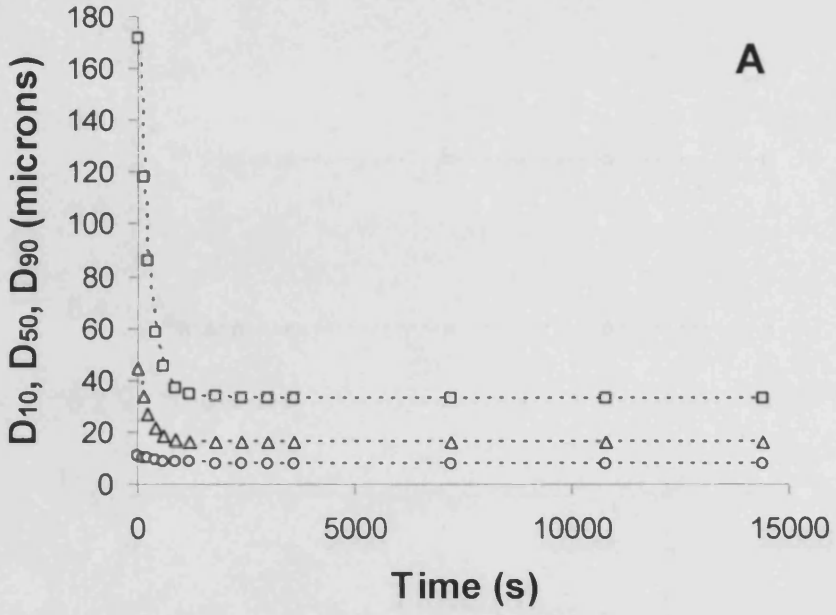
A
180
160
140
120
100
80
60
40
20
0
D10, D50, D90 (microns)
0
5000
10000
15000
Time (s)

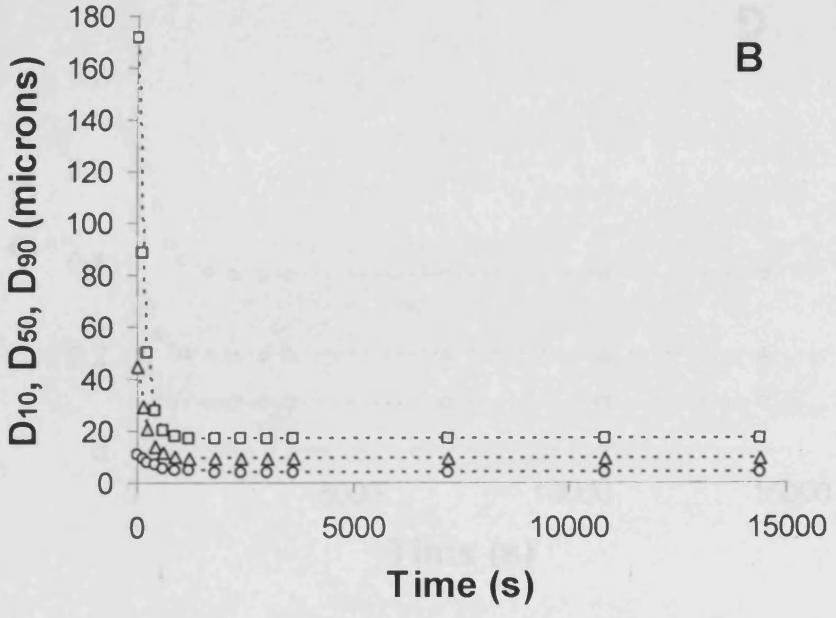
B
180
160
140
120
100
80
60
40
20
0
D10, D50, D90 (microns)
0
5000
10000
15000
Time (s)

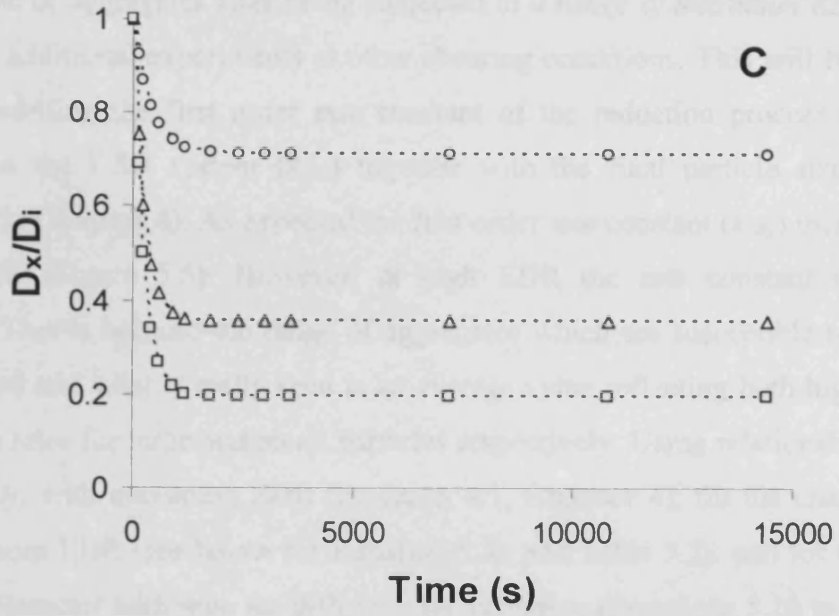

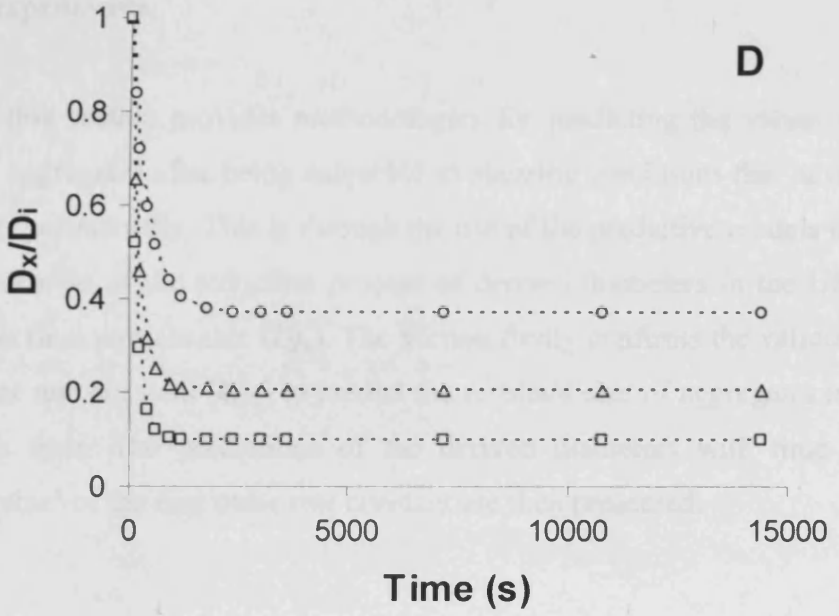

Figure 5.4 Predictions of the change of D_{10}, D_{50} and D_{90} in the large-scale system against processing time using k_{DU} obtained from the USD experiment and equivalent time in the USD device (t_s). The pump speeds include 600 rpm **(A, C)** and 1500 rpm **(B, D)**. Note that the initial (Di_x) and final values (Df_x) were fixed in the predictive curves. The values in between were calculated from Equations 5.19 to 5.21 using corresponding t_s, Di_x, Df_x and k_{DU}. The predictive curves are for D_{10} (-o-), D_{50} (-Δ-) and D_{90} (-□-).

5.3 Predictive model extensions

The predictive model may be extended further to include the predictions of the resultant size of aggregates after being subjected to *a range of maximum EDR* without performing additional experiments at other shearing conditions. This will be achieved through modelling the first order rate constant of the reduction process of derived diameters in the USD system (k_{DU}) together with the final particle size (Df_x, see Equation 4.1, **Chapter 4**). As expected the first order rate constant (k_{DU}) increases with greater EDR (Figure 5.5). However, at high EDR the rate constant tends to a maximum. This is because the range of aggregates which are susceptible to breakage has increased and what is really seen is an average value reflecting both high and low degradation rates for large and small particles respectively. Using relationships for the change in Df_x with maximum EDR (Equation 4.1, **Chapter 4**); for the change in k_{DU} with maximum EDR (see below for Equation 5.31 and Table 5.2); and for the change in derived diameter with time for different rate constants (Equations 5.19 to 5.21), it is possible to predict a wider range of equivalent particle diameters from a limited number of experiments.

Ultimately, this section provides methodologies for predicting the values of derived diameter of aggregates after being subjected to shearing conditions that have not been carried out experimentally. This is through the use of the predictive models for the first order rate constant of the reduction process of derived diameters in the USD system (k_{DU}) and the final particle size (Df_x). The section firstly confirms the validity of using the first order rate constant (k_{DU}) to predict the resultant size of aggregates in the USD system with time. The predictions of the derived diameters with time using the 'predicted value' of the first order rate constant are then presented.

5.3.1 Validity of using 'experimental k_{DU}' for predicting derived diameters

Applying the values of k_{DU} from Figure 5.5 and corresponding final particle sizes (Df_x) to Equations 5.19, 5.20 and 5.21 makes it possible to predict behaviours of particle sizes in terms of D_{10}, D_{50} and D_{90} respectively in the system having a specific magnitude of the maximum EDR for a time range of interest. Figure 5.6 shows the data

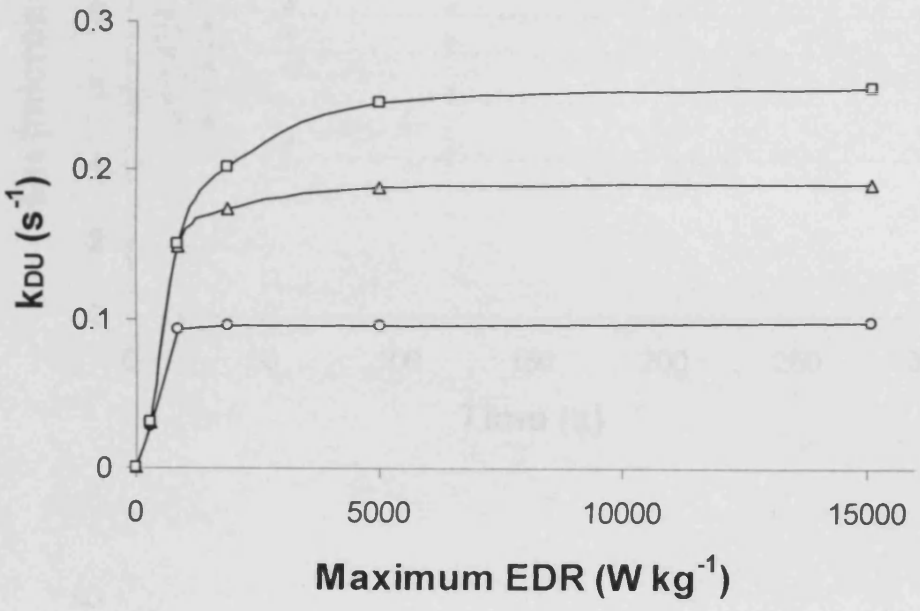

Figure 5.5 Plots of the first order rate constants (k_{DU}) obtained from USD experiments against the maximum EDR. The rate constant is dependent on the maximum EDR and is specific to the particle size. The higher rate constant of large aggregates, which are represented by D_{90}, is to their delicate nature compared to that of small particles and fines, which are represented by D_{10}. The rate constants shown are for D_{10} (-o-), D_{50} (-Δ-) and D_{90} (-□-). Note that, through Equation 5.16, each k_{DU} was calculated using the early data of derived diameters (D_x) and different final particle sizes (Df_x) obtained from specific shearing conditions, i.e. maximum EDR of the system, at t = 300 s. Lines drawn are best fit by smoothed lines generated via the XY (Scatter) chart function in Excel.

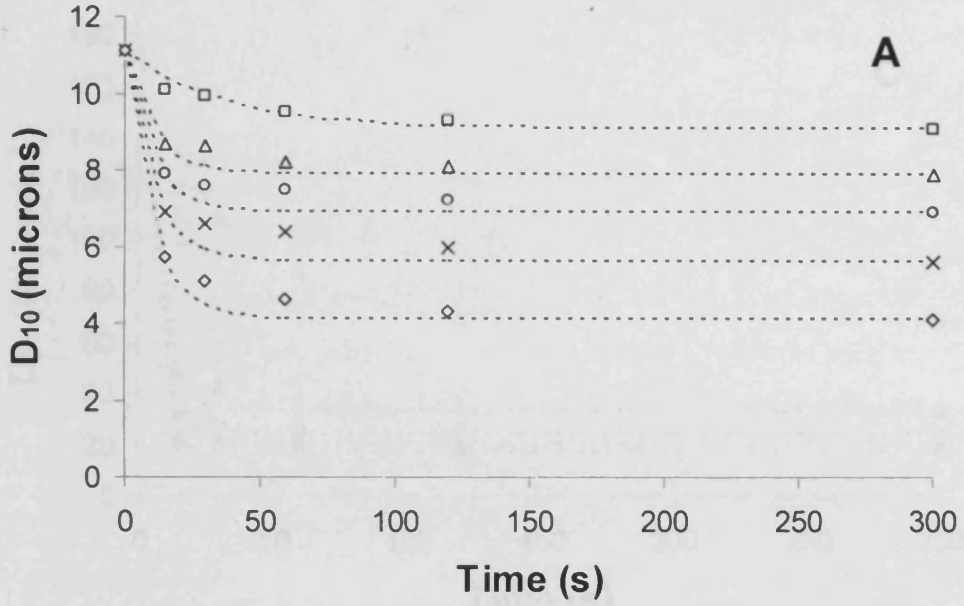
A
D10 (microns)
Time (s)
0
2
4
6
8
10
12
0
50
100
150
200
250
300

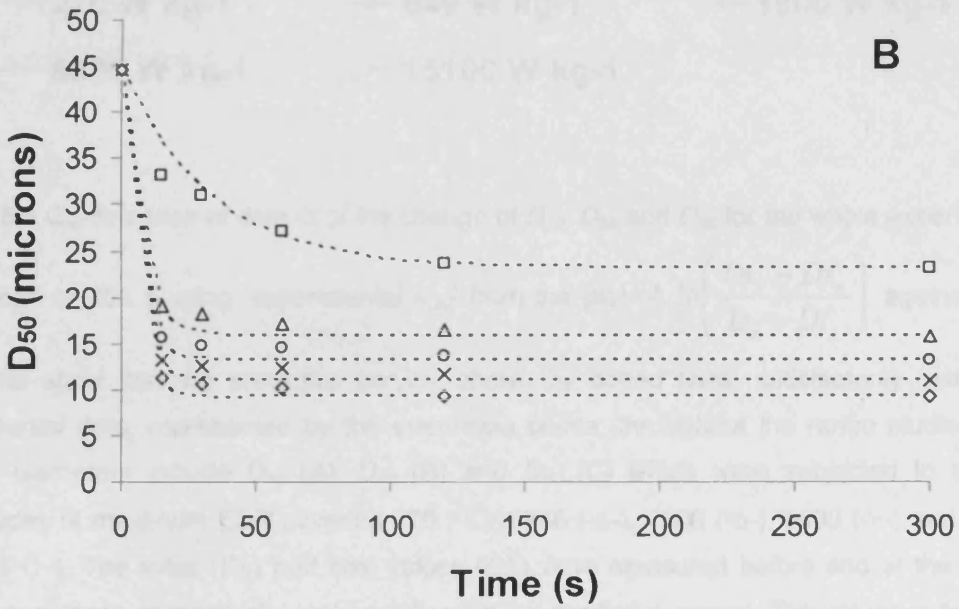
B
D50 (microns)
Time (s)
0
5
10
15
20
25
30
35
40
45
50
0
50
100
150
200
250
300

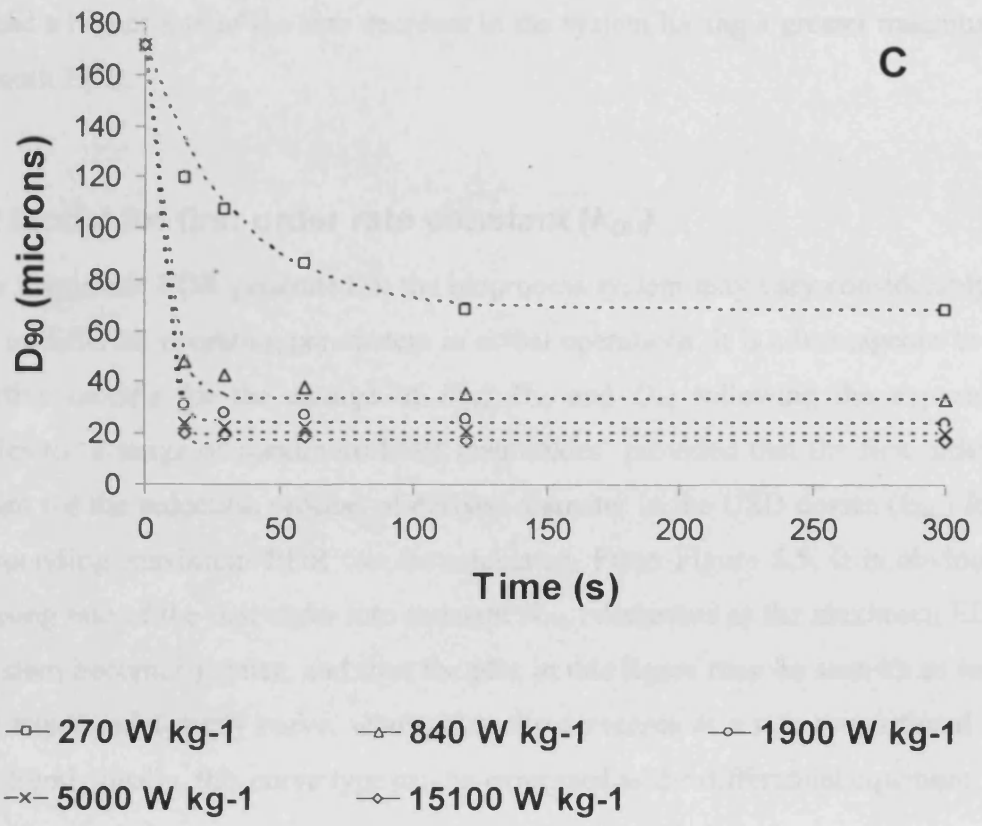

Figure 5.6 Confirmation of data fit of the change of D_{10}, D_{50} and D_{90} for the whole experimental time range of 300 s using 'experimental k_{DU}' from the plot of $\ln\left(\frac{Di_x - Df_x}{D_x - Df_x}\right)$ against time.

The plots show that the predictive curves, shown by dotted lines, satisfactorily match the experimental data, represented by the open data points, throughout the range studied. The derived diameters include D_{10} **(A)**, D_{50} **(B)** and D_{90} **(C)** which were subjected to specific magnitudes of maximum EDR covering 270 (-□-), 840 (-Δ-), 1900 (-o-), 5000 (-x-) and 15100 W kg^{-1} (-◇-). The initial (Di_x) and final values (Df_x) were measured before and at the end of USD experiments, respectively, and were fixed in the predictive curves. The values in between were calculated from Equations 5.19 to 5.21 using above two parameters, the shearing time and the experimentally-derived rate constant, which was experimentally obtained for specific shearing condition and size group.

fit confirmation of the values of D_{10}, D_{50} and D_{90} covering the time from 0 to 300 s under the influence of shear having maximum EDR of 270 to 15100 W kg^{-1} using k_{DU} obtained from USD experiments. The figure demonstrates that the predictive curves match the experimental data showing the decrease of representative diameters with time and a higher rate of the size decrease in the system having a greater magnitude of maximum EDR.

5.3.2 Model for first order rate constant (k_{DU})

As the maximum EDR generated in the bioprocess system may vary considerably as a result of different operating parameters in actual operations, it is advantageous to have predictive models for the change of D_{10}, D_{50} and D_{90} following the exposure of particles to 'a range of maximum EDR magnitudes' provided that the first order rate constant for the reduction process of derived diameter in the USD device (k_{DU}) for the corresponding maximum EDR can be calculated. From Figure 5.5, it is obvious the increasing rate of the first order rate constant (k_{DU}) decreases as the maximum EDR of the system becomes greater, and thus the plot in this figure may be seen as an inverse of the exponential-decay curve, whose quantity decreases at a rate proportional to its value. Symbolically, this curve type can be expressed as the differential equation:

$$-\frac{dN_D}{dt} = \lambda_D \cdot N_D \qquad \textbf{Eq. 5.27}$$

where N_D is the material quantity and λ_D is a decay constant. The solution to Equation 5.27 is therefore:

$$N_t = N_0 \cdot e^{-\lambda_D t} \qquad \textbf{Eq. 5.28}$$

where N_t is the material quantity at time t and N_0 is the material quantity at $t = 0$. The equation is then modified to include an offset:

$$N_t = N_0 \cdot e^{-\lambda_D t} + y_0 \qquad \textbf{Eq. 5.29}$$

where y_0 is the Y offset. To take into account the mirror image of the exponential-decay curve, the minus sign on the right-hand side is added:

$$N_t = -N_0 \cdot e^{-\lambda_D t} - y_0 \qquad \textbf{Eq. 5.30}$$

As a result, the equation for the prediction of the first order rate constant for the reduction of derived diameters in the USD device (k_{DU}) may possibly be expressed as:

$$k_{DU} = -A_0 \cdot e^{-B\varepsilon_{max}} - y_0 \qquad \textbf{Eq. 5.31}$$

where ε_{max} is the maximum EDR of the system and A_0, B and y_0 are constants. Figure 5.7 shows the prediction plots of the first order rate constant in the USD system (k_{DU}) against the maximum EDR based on the Equation 5.31. These predictions were found to match with their experimentally-derived values. Based on the Equation 5.31, all converged values of constants including A_0, B and y_0 might be obtained from the computer software (Origin 6.0, MicroCal, LLC, Northampton, MA, USA) and were shown in Table 5.2.

5.3.3 Size predictions using 'predicted k_{DU}' obtained from k_{DU} model

Once all constants in the Equation 5.31 are obtained, the predicted values of k_{DU} can in turn be used to construct the curves estimating values of derived diameters being subjected to a range of maximum EDR magnitudes and operating times. Figure 5.8 confirms the validity of this rational and shows the data fit confirmation of the values of D_{10}, D_{50} and D_{90} being subjected to a range of maximum EDR from 270 to 15100 W kg^{-1} and operating time up to 300 s based on their 'predicted k_{DU}' values.

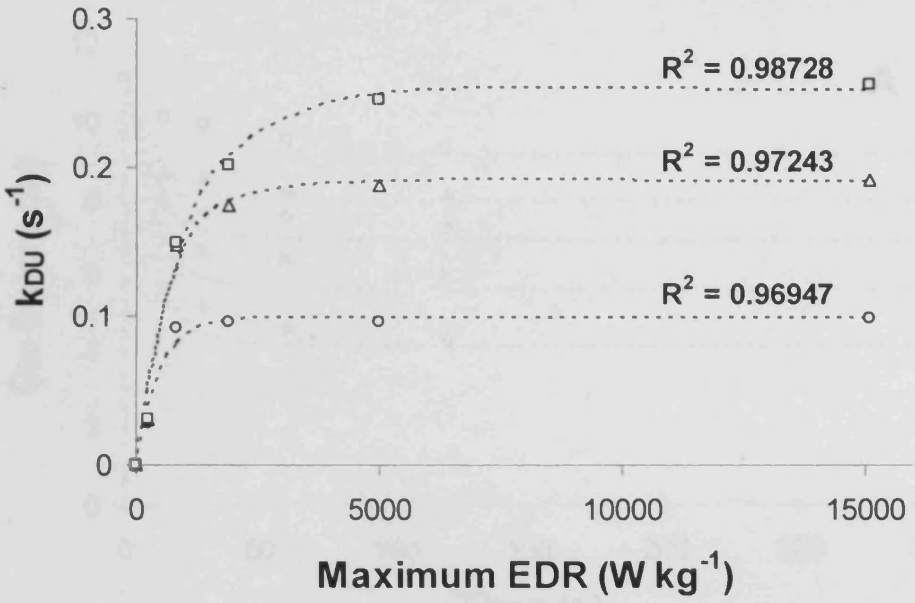

Figure 5.7 Prediction plots of k_{DU} against the maximum EDR. The predictions were based on the Equation 5.31: $k_{DU} = -A_0 \cdot e^{-B\varepsilon_{max}} - y_0$. Dotted lines and open data points represent the predicted and experimental values, respectively. The experimentally-derived rate constants shown are for D_{10} (-o-), D_{50} (-Δ-) and D_{90} (-□-). R-square values are shown next to the corresponding predicted curve. All constants including A_0, B and y_0 were obtained from converged equations for each size group.

Derived diameter (microns)	A_0 (s^{-1})	B (kg W^{-1})	y_0 (s^{-1})	R-square values
D_{10}	0.103	0.00205	-0.099	0.96947
D_{50}	0.202	0.00142	-0.191	0.97243
D_{90}	0.260	0.00094	-0.252	0.98728

Table 5.2 Converged values of A_0, B and y_0 in the predictive model: $k_{DU} = -A_0 \cdot e^{-B\varepsilon_{max}} - y_0$ for D_{10}, D_{50} and D_{90}. R-square values are also shown for each size group.

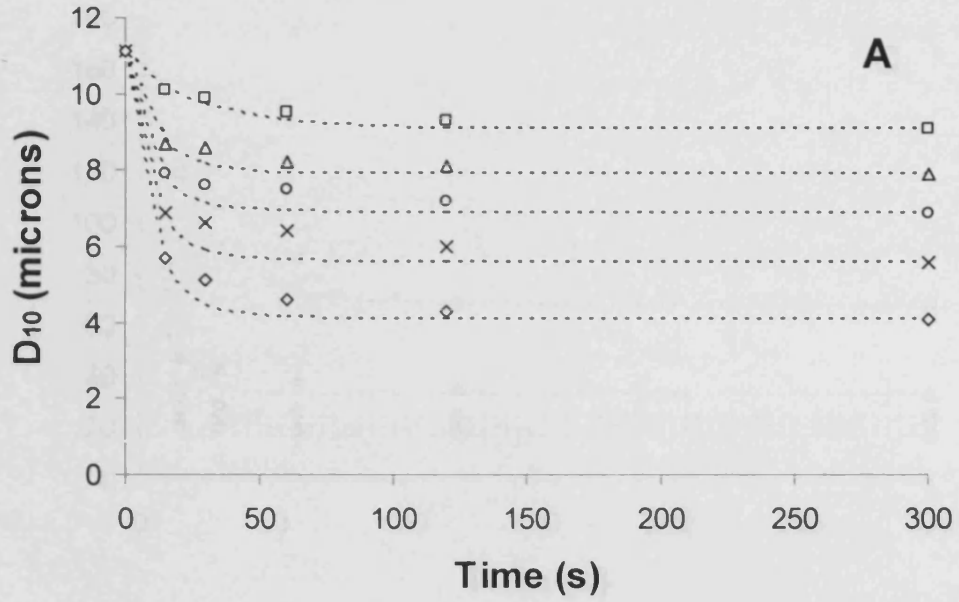
A
D10 (microns)
12
10
8
6
4
2
0
0
50
100
150
200
250
300
Time (s)

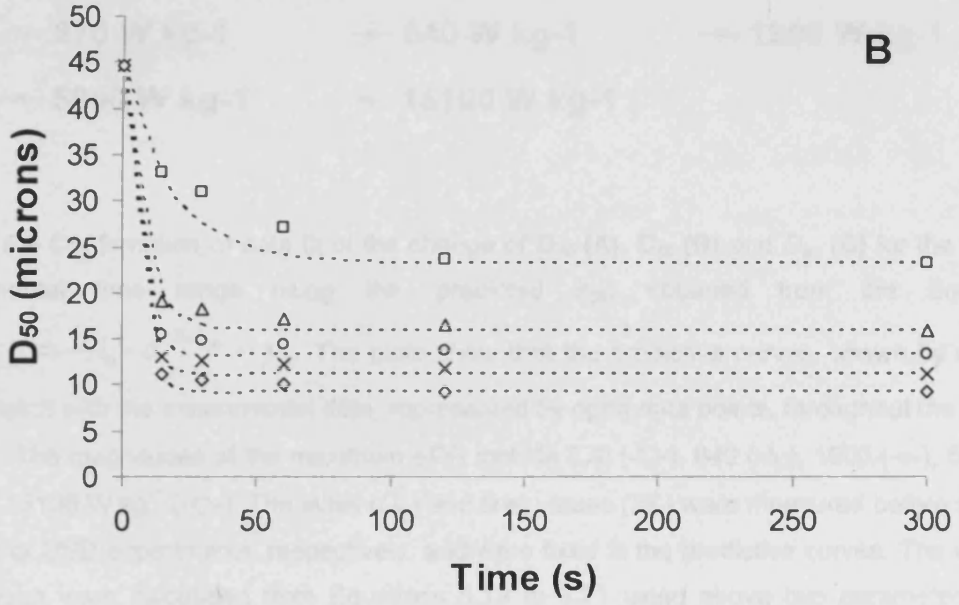
B
D50 (microns)
50
45
40
35
30
25
20
15
10
5
0
0
50
100
150
200
250
300
Time (s)

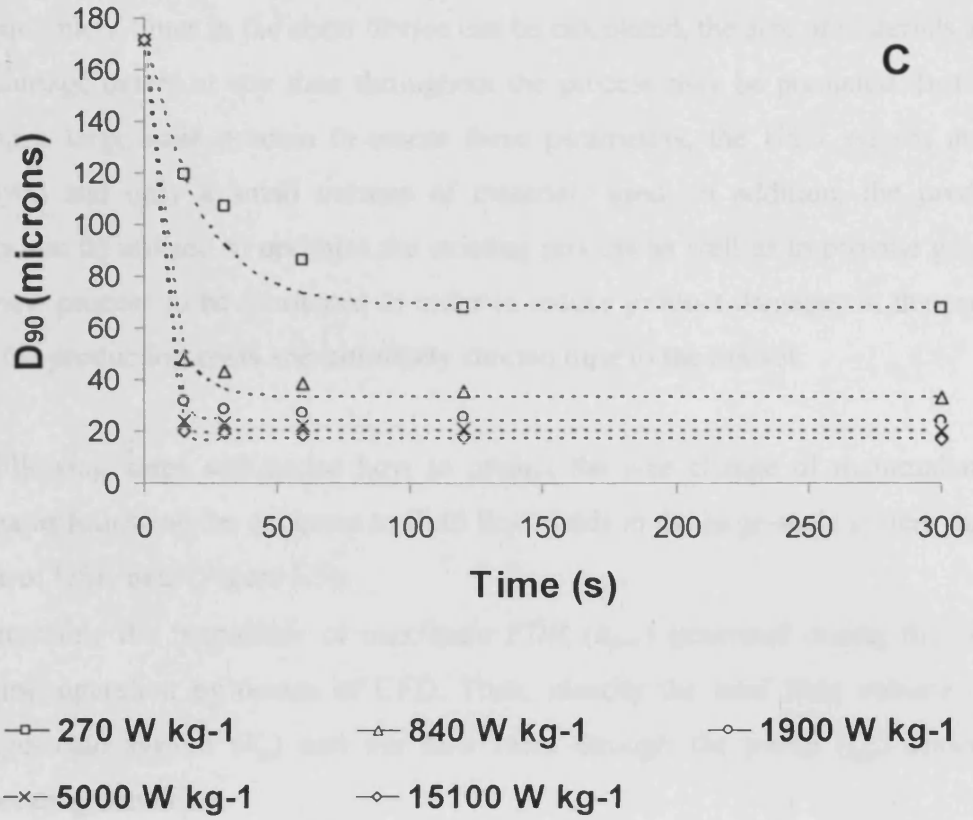

Figure 5.8 Confirmation of data fit of the change of D_{10} **(A)**, D_{50} **(B)** and D_{90} **(C)** for the whole experimental time range using the 'predicted k_{DU}' obtained from the Equation 5.31: $k_{DU} = -A_0 \cdot e^{-B\varepsilon_{max}} - y_0$. The plots show that the predictive curves, shown by dotted lines, match with the experimental data, represented by open data points, throughout the range studied. The magnitudes of the maximum EDR include 270 (-□-), 840 (-Δ-), 1900 (-o-), 5000 (-×-) and 15100 W kg^{-1} (-◇-). The initial (Di_x) and final values (Df_x) were measured before and at the end of USD experiments, respectively, and were fixed in the predictive curves. The values in between were calculated from Equations 5.19 to 5.21 using above two parameters, the shearing time and the 'predicted' rate constant, which was obtained from the above equation for specific shearing condition and size group.

5.4 Size prediction methodologies for membrane system

The above findings undoubtedly have potential to impact on bioprocess development and optimisation. If the maximum EDR inside all equipment in the bioprocess and their equivalent times in the shear device can be calculated, the size of materials and/or their damage extent at any time throughout the process may be predicted. Instead of running a large-scale process to assess these parameters, the USD system may be employed and only a small volume of materials used. In addition, the predictive models can be utilised to optimise the existing process as well as to provide guidance for a new process to be fabricated in order to reduce product damages in the process, lower the production costs and ultimately shorten time to the market.

The following steps summarise how to predict the size change of mammalian cell aggregates following the exposure to fluid flow fields in the large-scale system through the use of USD data (Figure 5.9):

1. Determine the magnitude of maximum EDR (ε_{max}) generated during the normal pump operation by means of CFD. Then, identify the total fluid volume of the large-scale system (V_p) and the flow rates through the pump (Q_p) under that operating condition.
2. Employ CFD to calculate the equivalent disc speed that generates the same magnitude of the maximum EDR in the shear device, i.e. USD system, as well as the flow rate expelling fluid from the tip of the disc (Q_s) under that particular disc speed together with the total volume of the shear device (V_s).
3. Calculate the equivalent time used in the USD device (t_s) via Equation 5.24: $t_s = \left(\frac{Q_p \cdot t_p}{V_p}\right) \cdot \left(\frac{V_s}{Q_s}\right)$ for specific times operated in the large-scale system (t_p).

From here the size prediction may be achieved by either direct USD experiments or predetermined predictive model (Equation 5.26). If relevant data from previously-run experiments is not available, USD experiments must be directly carried out to obtain these predicted values. Otherwise, the predetermined predictive model may be employed to allow size predictions to be made. For the latter, the following steps apply:

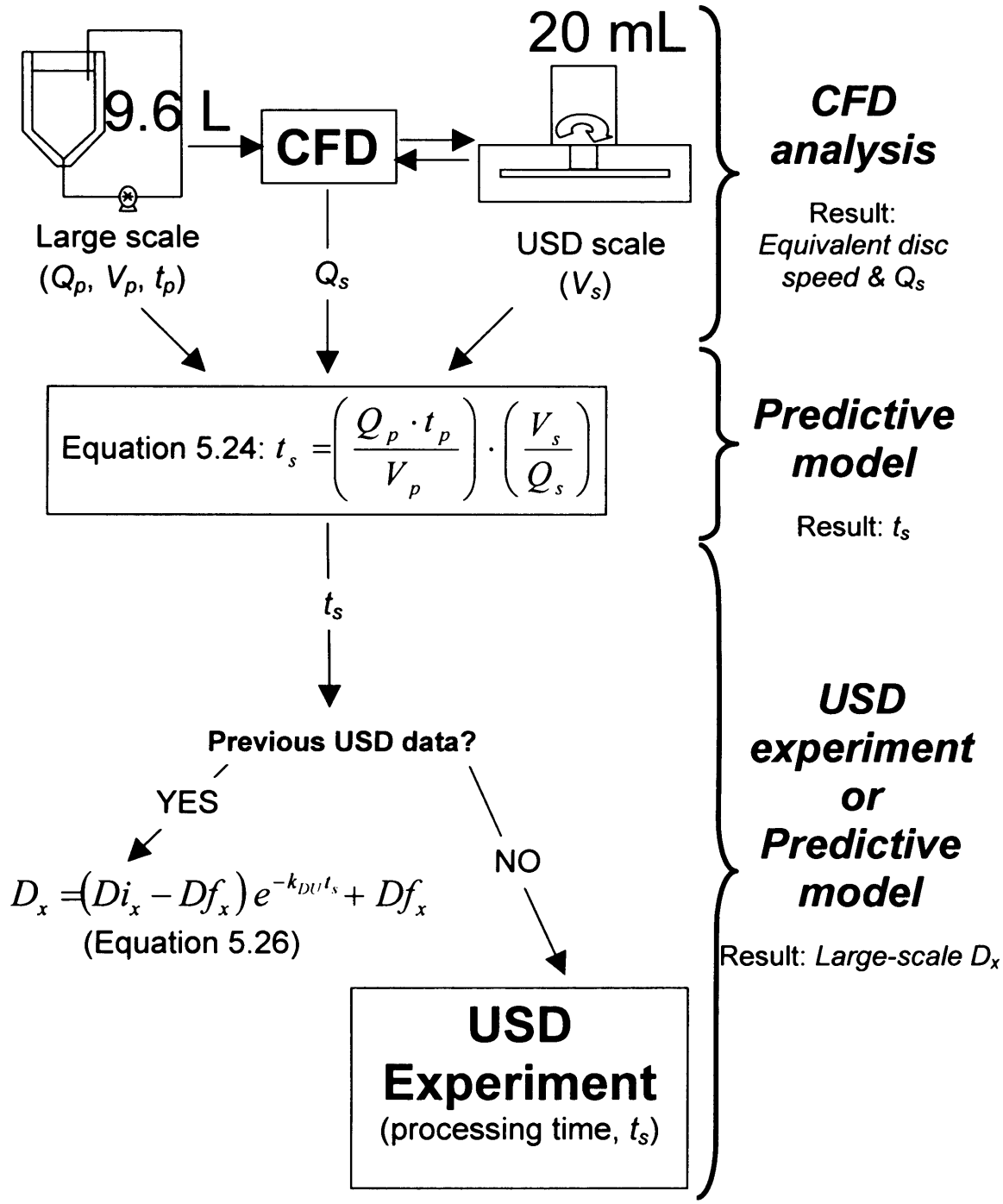

Figure 5.9 Flowchart summarising key steps and options available for the prediction of particle size change in large-scale membrane filtration system. The maximum EDR is firstly determined by CFD, which in turn calculates an equivalent disc speed for the USD system and thus Q_s. This flow rate from the disc together with other variables is then used to calculate t_s via Equation 5.24. This equivalent USD time can then be used in Equation 5.26 to give D_x provided that previous USD information is sufficiently available, or it can provide information regarding the processing time in the USD device and D_x measured directly.

4. Calculate the first order rate constant for the reduction of the derived diameters in the USD system (k_{DU}) from either the plot of $\ln\left(\frac{Di_x - Df_x}{D_x - Df_x}\right)$ against the shearing time or the equation: $k_{DU} = -A_0 \cdot e^{-B\varepsilon_{max}} - y_0$ (Equation 5.31) provided a number of experiments have already been carried out in order to gather sufficient information. The initial value of derived diameters (Di_x) can be measured prior to the experiment while the final value of these derived diameters (Df_x) under specific shearing condition may be obtained from either the state where little or no change of the size distribution curve can be detected or the equation: $Df_x = c \cdot \varepsilon_{max}^{-b}$ (Equation 4.1, **Chapter 4**).
5. Substitute the first order rate constant (k_{DU}) and other relevant parameters into the equation: $D_x = (Di_x - Df_x)\, e^{-k_{DU} \cdot t_s} + Df_x$ (Equation 5.26) in order to predict the change of derived diameters with time in the large scale.

5.5 Conclusions

It was proposed that, by preserving the magnitude of maximum energy dissipation rate, the two systems having totally different configurations and of different scales may produce the similar engineering environment and generate equivalent extent of material damage and changes in particle size. Using the system properties such as volumetric flow rate through high-energy dissipated region, total volume of the system and the processing time, predictive equations have been defined to estimate the change of aggregate sizes during the course of exposure to shear in the large-scale system by using the USD device. The results of size changes and final particle size produced from shear device experiment were employed as a scale-down mimic to supply information to these models in order to make predictions on size changes of materials in the large-scale system. Consequently, this study investigated the validity of scaling based on the maximum energy dissipation rate of the system, which shall be verified in the next chapter.

CHAPTER 6 PUMP EXPERIMENT AND VERIFICATION

The pump has been identified as the likely main source of exposure of the process stream to high energy dissipation rates (EDR). In this chapter large-scale experiments were carried out to study the effect of the pump. In this study the membrane module and valve were removed from the rig. The feed tank was reduced in size to reduce the amount of material used in the experiment. Data from a large-scale system was then compared and verified with those obtained from ultra scale-down (USD) experiments and predictive models.

6.1 Materials and methods

6.1.1 Cell samples

Cell samples and the sample preparation procedures have already been described in detail in section 4.1.1 (**Chapter 4**) of this thesis. The total volume of diluted samples used during the large-scale pump experiment was 9.6 L.

6.1.2 Experimental equipment

For the verification experiment, the membrane module and valve were removed (Figure 6.1). A 15-litre tank with cooling jackets was used instead of the 150-litre feed tank and was connected to the pump using flexible tubes with an inner diameter of 1.0 cm. The mammalian cell suspension was pumped out of the feed tank at the bottom and back to the top of the tank where the connecting tube was partly submerged into the process fluid during the experiment. The tank has an inclined propeller-type impeller but this was not used during the experiment. To determine accurately the speed of the pump, a non-contact laser tachometer (model TMRT 1, SKF, Luton, UK) was used. The equipment was washed with detergent, and then ultra-pure water, before the start and the end of each run.

6.1.3 Operating parameters

The pump was pre-calibrated using timed studies for flow of water. The feed tank was then filled with 9.6-litre process material and flow studies carried out for 4 h. Two pump speeds, i.e. 600 rpm and 1500 rpm, were used during this verification process. Samples, 40 mL, were collected from the tank for analysis at fixed times. A non-sheared sample was used as a control collected before the onset of the experiment. Measurements of particle size and size distribution were carried out immediately after each sample collection. The reduction of volume due to sample collection was assumed to be negligible compared to the fluid volume in the system. The suspension temperature was controlled to 20°C during the experiment by using 10°C cooling water on the tank jacket. Table 6.1 and Figure 6.2 show the results of pump calibration experiments.

6.1.4 Chemicals

All chemicals, unless otherwise stated, were of analytical grade and were obtained from Sigma Aldrich (Dorset, UK).

6.1.5 Measurement of particle size and size distribution

Size measurement methods and the nature of size and size distribution data have already been explained in detail in section 4.1.5 (**Chapter 4**).

6.1.6 Data analysis

All distribution data was obtained through software provided with Malvern Mastersizer 2000 particle analyser. Data was given in terms of both volume percent (vol %) and derived diameters (D_{10}, D_{50} and D_{90}). All data analyses, including graphical representations, were achieved using computer programmes: Microsoft® Office Excel 2003 and Origin 6.0 (MicroCal, LLC, Northampton, MA, USA).

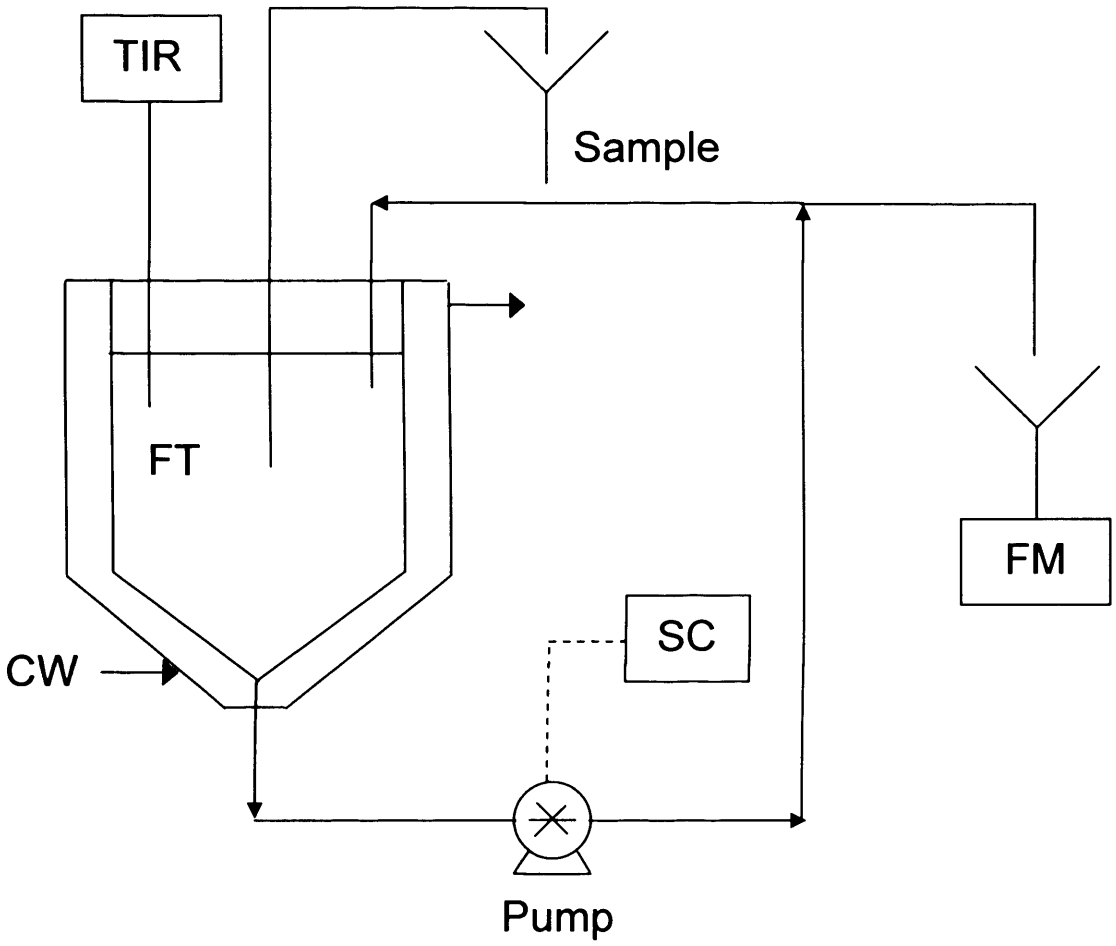

Figure 6.1 A schematic diagram of a large-scale pump experiment. The experimental setup consisted of a tank with a working volume of 15 L, a positive displacement pump and connecting tubes. Samples taken from tank were considered to be well-mixed. Representations are abbreviated as follows: SC – speed controller, FT – feed tank, FM – flow measurement, TIR – temperature indicator recorder and CW – cooling water.

Speed controller readout (hertz or %)	Rotational speed of pump (rpm)	Volumetric flow rate (L min^{-1})
10	298.0	3.66
20	598.0	7.32
30	897.1	10.98
40	1196	14.76
50	1494	18.36

Table 6.1 The volumetric measurement of the pump used in the experiment. The system consists of the pump and the speed controller. The results show that the speed controller provides good control over the rotational speed.

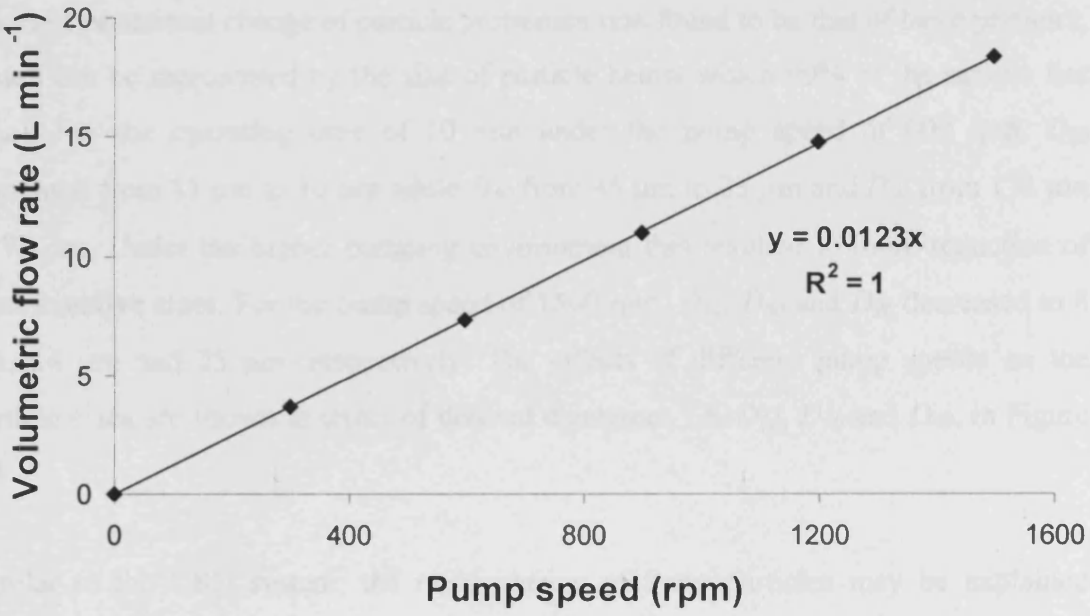

Figure 6.2 The relationship between the volumetric flow rate and the pump's rotational speed. The results show that the pump is in good working order with no leakage of fluid from the pump at high rotational speeds.

6.2 Experimental results

6.2.1 Pumping effects

The variations of aggregate sizes were monitored throughout 4-hour experiments for both runs of 600 rpm and 1500 rpm (equivalent to maximum EDR of 900 and 15000 W kg^{-1}, respectively). Following to the exposure of a mammalian cell suspension to the pump, large aggregates were disrupted and their reduction accounted for the increment of small aggregates, cells and cell debris - the phenomena that seems to be specific to each shearing condition. Changes of these different size groups can clearly be shown on both logarithmic scale (Figure 6.3) and linear scale (Figure 6.4). For the operating time of 10 min under the pump speed of 600 rpm, the volume fraction of cells and cell debris, i.e. those having size equal or below 10 μm, had increased from 10.2% to 15.8% by volume. As might be expected, the size change was more pronounced when the operating conditions became more intense. At the pump speed of 1500 rpm, the volume fraction of cells and cell debris after 10 min of exposure was increased to 33% by volume, compared to 15.8% by volume under 600 rpm.

Following the pump exposure, representative sizes also reduced correspondingly and the most prominent change of particle properties was found to be that of large particles, which can be represented by the size of particle below which 90% of the sample lies (D_{90}). For the operating time of 10 min under the pump speed of 600 rpm, D_{10} decreased from 11 μm to 10 μm while D_{50} from 45 μm to 23 μm and D_{90} from 171 μm to 75 μm. Under the higher pumping environment this resulted in more reduction of representative sizes. For the pump speed of 1500 rpm, D_{10}, D_{50} and D_{90} decreased to 8 μm, 14 μm and 25 μm, respectively. The effects of different pump speeds on the particle sizes are shown in terms of derived diameters, i.e. D_{10}, D_{50} and D_{90}, in Figure 6.5.

Similar to the USD system, the rapid change of these particles may be explained through the alteration of the magnitude of maximum EDR and volumetric flow rates to the high-shear component of the system operating at different speeds. The magnitude of maximum EDR increased to 15000 W kg^{-1} when the pump speed was 1500 rpm, compared to 900 W kg^{-1} when the speed was 600 rpm. With higher maximum EDR,

the system operating at 1500 rpm would cover a wider range of particle sizes subjected to damage. Small particles that did not break at lower maximum EDR might be disrupted in the pump system running at 1500 rpm. At the pump speed of 1500 rpm, the volumetric flow rate of the pump also increased to 18.36 L min^{-1}, compared to 7.32 L min^{-1} at 600 rpm. This leads to a higher recurrent rate of particles to the high-shear zone and thus more solid disruption in the system. As a result, the system operating at a higher pump speed would allow greater changes of these particles to be observed within the same time frame.

It can be concluded from above results that the positive displacement pump imposes shear to aggregates in the study causing the change in their size distribution – the same phenomenon occurring in the USD system. When particles were subjected to EDR generated by the pump component, large aggregates were disrupted and smaller entities formed resulting in the left shift of the volume distribution curve. Like the USD system, the degree of size change depends on the operating condition of the pump system and is more pronounced at a higher speed or higher magnitude of maximum EDR; thus giving unique characteristics of the particle size distribution for specific operating conditions. As might be expected, the pumping time also affects the change in particle size and shall be discussed in the following section.

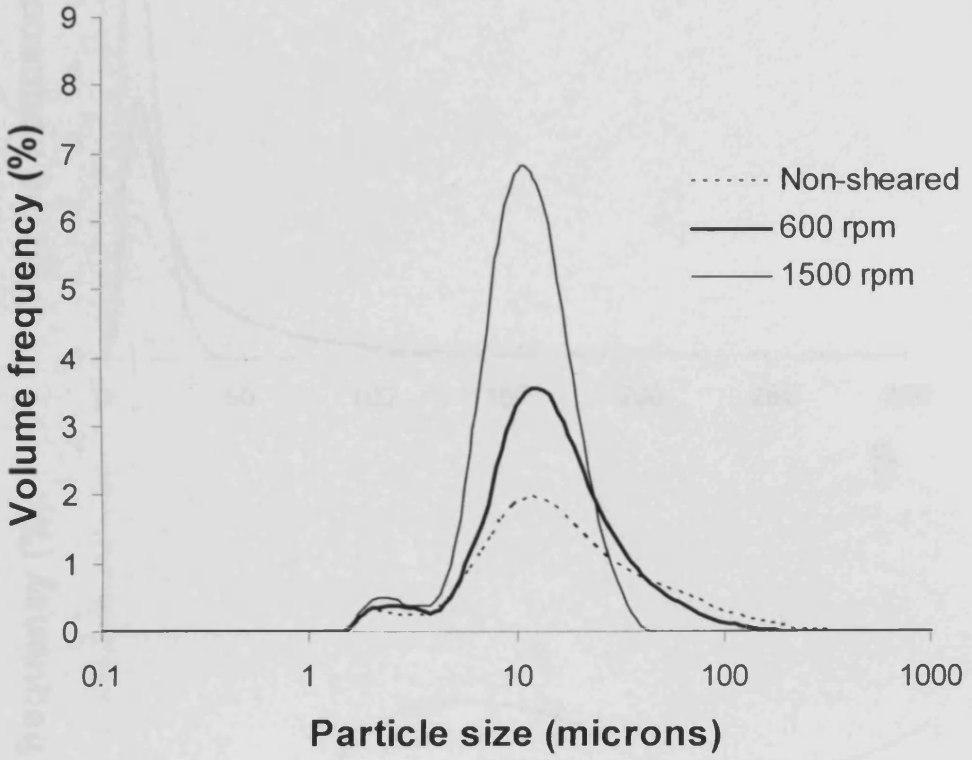

Figure 6.3 Particle size distributions of a mammalian cell suspension after being subjected to the positive displacement rotary pump running at 600 rpm and 1500 rpm for 10 min compared to the non-shear sample based on logarithmic scale. The equivalent magnitudes of maximum EDR for these speeds were 900 and 15000 W kg^{-1}, respectively. Solids were disrupted into smaller entities making the size distribution shifted to the left and the smaller peak became more noticeable. Due to higher solid break up at 1500 rpm, the size distribution shifted more to the left compared to the distribution resulted from the speed of 600 rpm. (NB Linear size scales were used for analysis of volume fractions over different size ranges).

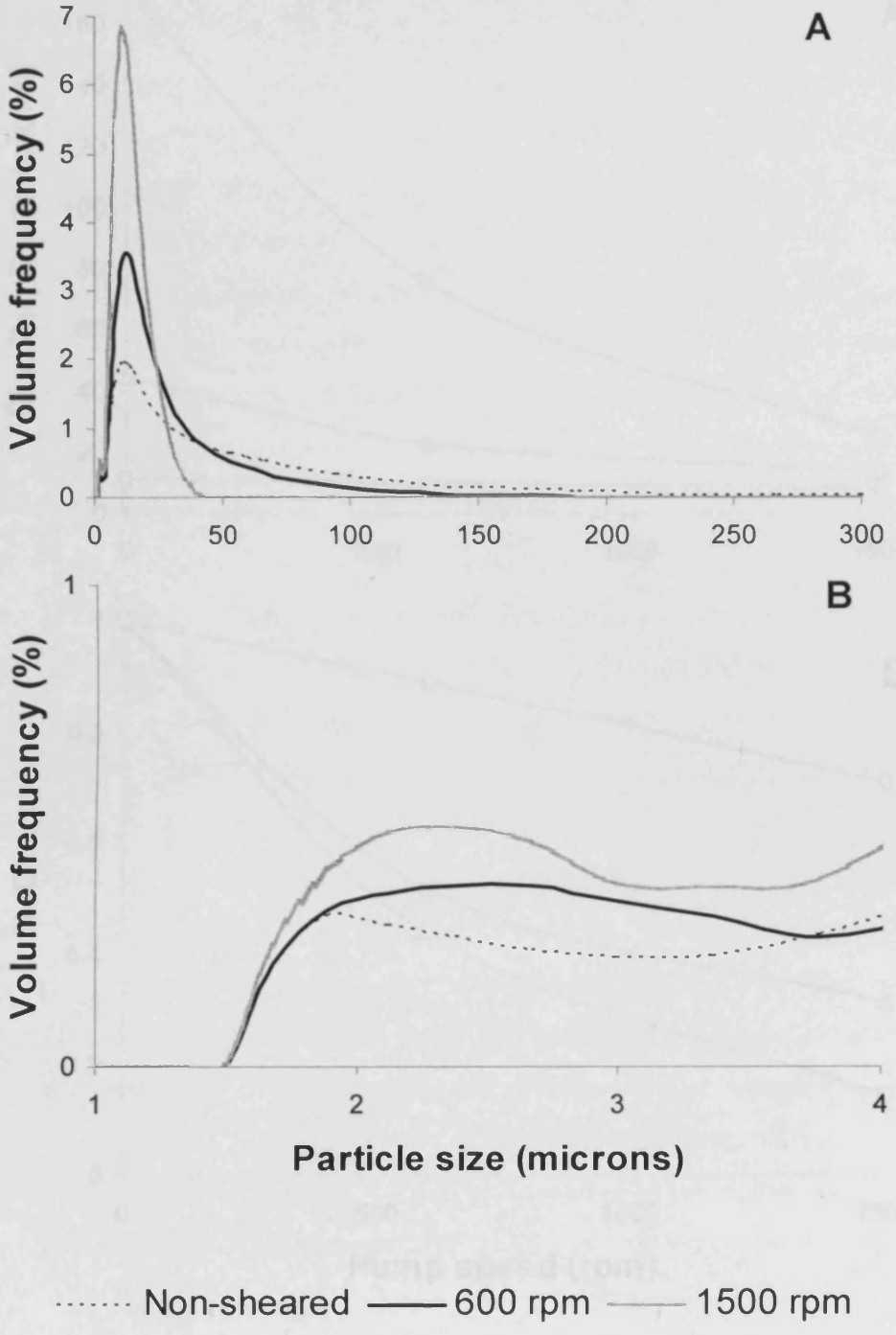

Figure 6.4 Changes of particle size distribution of a suspension after being subjected to the pump having speeds of 600 and 1500 rpm for 10 min compared to the non-sheared sample based on linear scale. Large aggregates were broken down resulting in the formation of smaller aggregates and cells **(A)** as well as cell debris **(B)**. It was found that the higher the pump speed (higher magnitude of maximum EDR to the system), the greater the change of these particles.

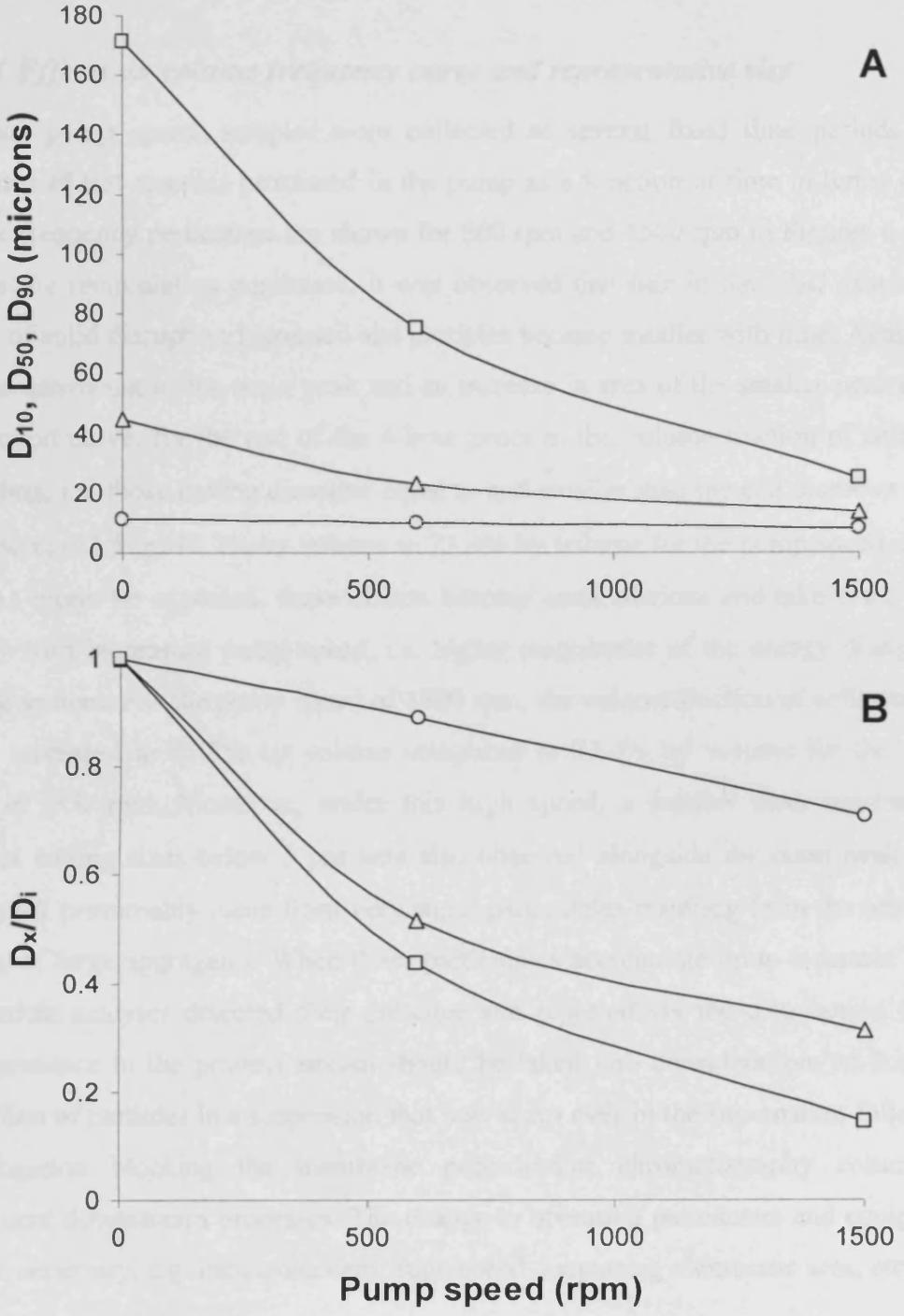

Figure 6.5 Plots of representative sizes against the pump speed. Particles were sheared through the pump for 10 min at 600 rpm and 1500 rpm. Both the derived diameter **(A)** and the ratio between the derived diameter and its initial size **(B)** are shown. Results show that the pumping device caused particle size change and that the size decrease was dependent on the rotational speed of the pump with the higher speed resulting in smaller particles. Particle sizes were represented by derived diameters, namely D_{10} (-o-), D_{50} (-Δ-) and D_{90} (-□-). Lines drawn are best fit by smoothed lines generated via the XY (Scatter) chart function in Excel.

6.2.2 Effects of the pumping time

6.2.2.1 Effects on volume frequency curve and representative size

For each pump speed, samples were collected at several fixed time periods. The variations of test samples processed in the pump as a function of time in terms of the volume frequency percentage are shown for 600 rpm and 1500 rpm in Figures 6.6 and 6.7. As the recirculation continued, it was observed that like in the USD system the degree of solid disruption increased and particles became smaller with time. Again this led to a narrowing of the main peak and an increase in area of the smaller peak of the distribution curve. By the end of the 4-hour process, the volume fraction of cells and cell debris, i.e. those having diameter equal to and smaller than the cell diameter ($\leq$ 10 μm), increased from 10.2% by volume to 23.4% by volume for the pump speed of 600 rpm. As might be expected, these effects become more obvious and take place more quickly with increasing pump speed, i.e. higher magnitudes of the energy dissipation into the system. For the pump speed of 1500 rpm, the volume fraction of cells and cell debris increased to 52.5% by volume compared to 23.4% by volume for the pump speed of 600 rpm. Moreover, under this high speed, a smaller peak representing particles having sizes below 3 μm was also observed alongside the main peak. This small peak presumably came from very small particulates resulting from the breakage process of large aggregates. When these particulates accumulate up to a certain level, the particle analyser detected their presence and reported via the distribution curve. Their presence in the process stream should be taken into consideration, as it is this proportion of particles in a suspension that may carry over in the supernatant following centrifugation blocking the membrane pore and/or chromatography column in subsequent downstream processes. The change to operating parameters and equipment may be necessary, e.g. increasing centrifuge speed, increasing membrane area, etc.

The behaviour of the representative sizes below which certain percentages of particles lie (D_{10}, D_{50} and D_{90}) during the pump operation allow interpretations of a different aspect of the process. Though it is clear that these derived diameters coincide well with the size distribution based on volume percent, the analysis of their patterns with time will permit understanding of how the process environment interacts with different size groups. Figure 6.8 shows the alteration of these representative diameters with time for

the pump speeds of 600 rpm. Like the USD system, the change with time following the exposure to shear in the pumping device is specific to particle size representatives of the fine, medium and large end of mammalian cell aggregates. It was observed that particle sizes decreased rapidly during the early stage of the pump operation and their change gradually dropped towards the end of the 4-hour process with the greatest size change lying in large-particle size group, D_{90}. This situation was very similar to that occurring in the USD system and its mechanism may again be described through the solid availability in the system during operation (see section 4.2.2). As might be expected, the size changes became more rapid with an increased pump speed of 1500 rpm, i.e. increased magnitude of maximum EDR (Figure 6.9). Again this increased rate of change of particles can be explained through the magnitude of maximum EDR and volumetric flow rates to the high-shear component of the system as previously described in section 6.2.1. To make these size alterations more distinguishable under different engineering conditions for each size group, Figures 6.8 and 6.9 were rearranged to show the relationships of derived diameters resulted from exposure to the pump running at 600 rpm and 1500 rpm, which are equivalent to maximum EDR of 900 and 15000 W kg^{-1}, with the operating time for each derived diameter, i.e. D_{10}, D_{50} and D_{90}. These are shown in Figures 6.10. The figure clearly shows the dependence of size and size-reduction characteristics on the maximum EDR. Moreover, it can be observed that the rate of size reduction increased as the maximum EDR increased for all size groups. For example, for the exposure time of 1 h, D_{10} decreased from 11.1 μm to 9.2 μm under the maximum EDR of 900 W kg^{-1} whereas D_{10} decreased to 6.9 μm under the maximum EDR of 15000 W kg^{-1}.

6.2.2.2 Rate of change of volume fraction with time

Another characteristic that the pump system has in common with the USD system is that the change in volume fraction of a specific size range (and thus particle size) decreased with time and would eventually reach a steady state. Comparing the rates of the volume fraction change of cells and cell debris between different operating time intervals allows the characteristic of the breakage process to be understood (Table 6.2).

Operating time interval (min)	Rates of changes of volume fraction of cells and cell debris under different pump speeds (percent per min)	
	600 rpm	1500 rpm
0-10	0.5784	2.4448
10-60	0.0995	0.2860
60-120	0.0509	0.1650
120-180	0.0255	0.1899
180-240	0	0.0627

Table 6.2 Rates of changes in volume fraction of cells and cell debris in a mammalian cell suspension after being subjected to different magnitudes of maximum EDR generated from two pump speeds for different time intervals. These rates decreased with the operating time for both speeds due to the amount of solids left to break becoming less.

To summarise, particle characteristics similar to those observed in the USD system were found in a suspension being processed in the large-scale pump system helping affirm the validity of the linkage methodology between two scales. Firstly, the dependence of particle size on both maximum EDR and time of exposure was observed in both systems. A rapid decrease of large aggregates and corresponding increase of cells and small particulates at the beginning of the run and gradual changes of these particles with the processing time leads us to draw a conclusion on the second common characteristic that the rate of change of volume fraction (frequency) and thus particle size of particles in a suspension being subjected to dissipated energy in these systems would decrease with time and that such system would eventually reach a steady state, i.e. a state where final characteristics of particles from the USD system may be used to predict those in the large-scale system. Ultimately, these findings allow us to confirm the rationale used to devise the linkage methodology between the two scales whose verification is presented in the next section.

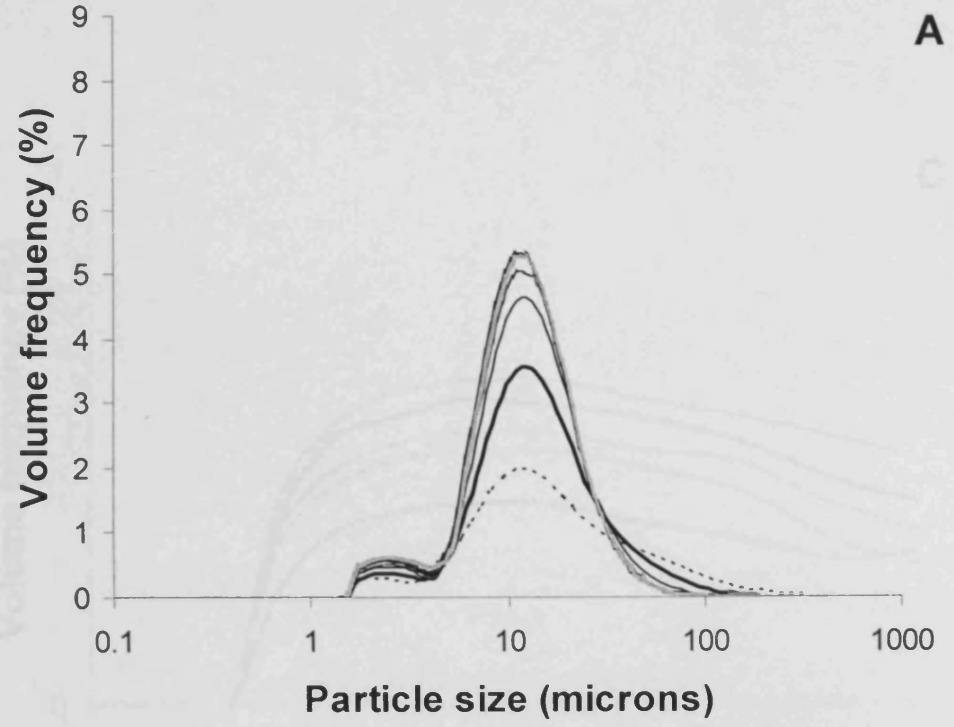
A
Volume frequency (%)
0
1
2
3
4
5
6
7
8
9
0.1
1
10
100
1000
Particle size (microns)

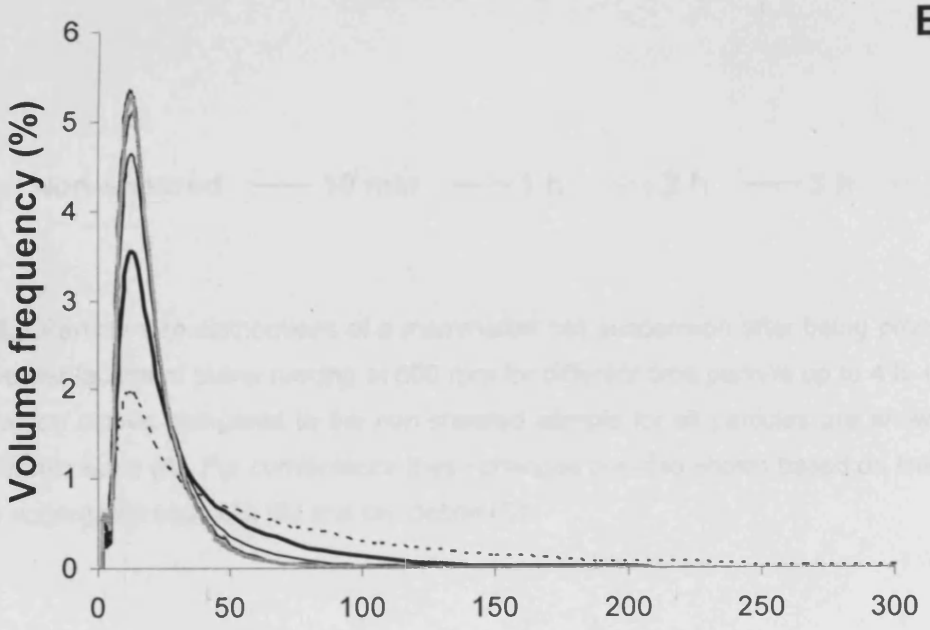
B
Volume frequency (%)
0
1
2
3
4
5
6
0
50
100
150
200
250
300

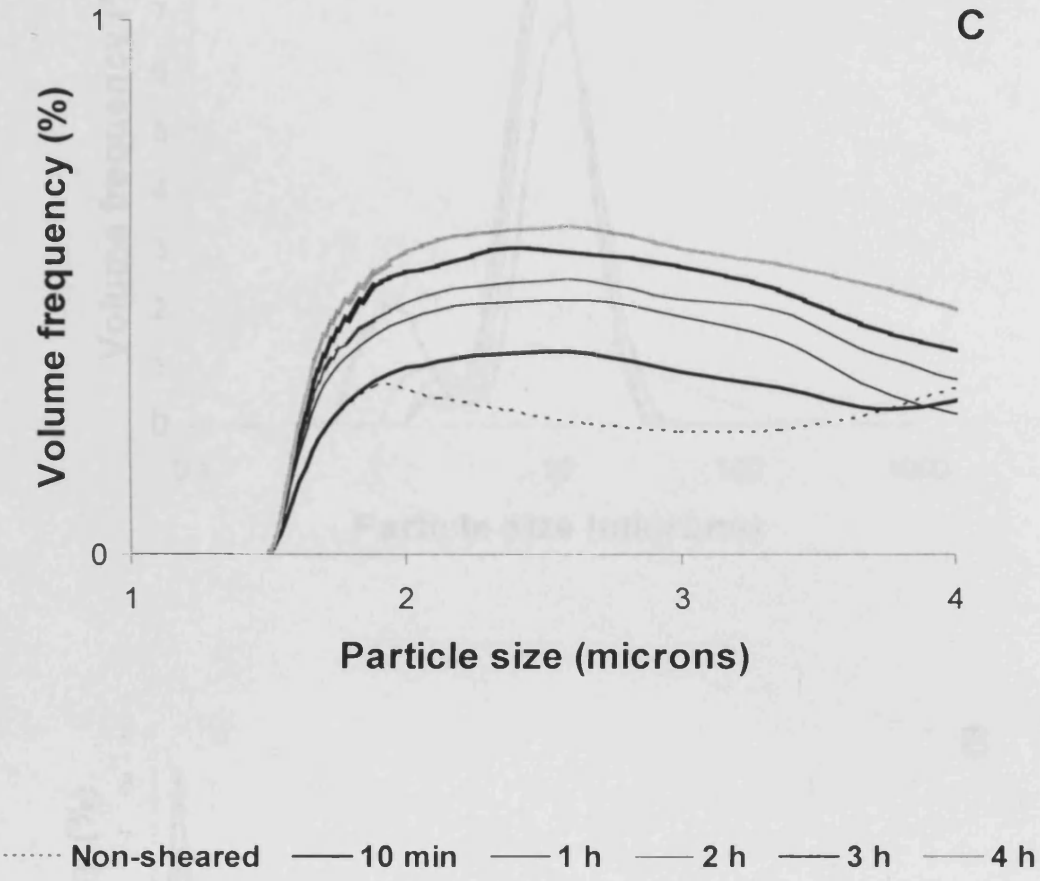

Figure 6.6 Particle size distributions of a mammalian cell suspension after being processed in a positive displacement pump running at 600 rpm for different time periods up to 4 h. Changes of distribution curves compared to the non-sheared sample for all particles are shown based on logarithmic scale **(A)**. For convenience these changes are also shown based on linear scale for large aggregates and cells **(B)** and cell debris **(C)**.

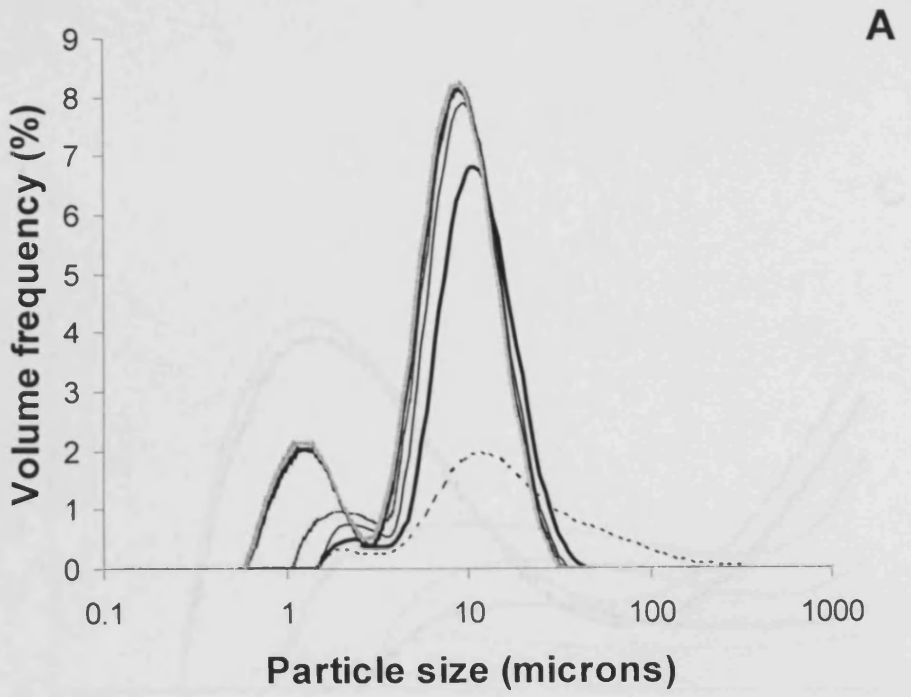
A
Volume frequency (%)
9
8
7
6
5
4
3
2
1
0
0.1
1
10
100
1000
Particle size (microns)

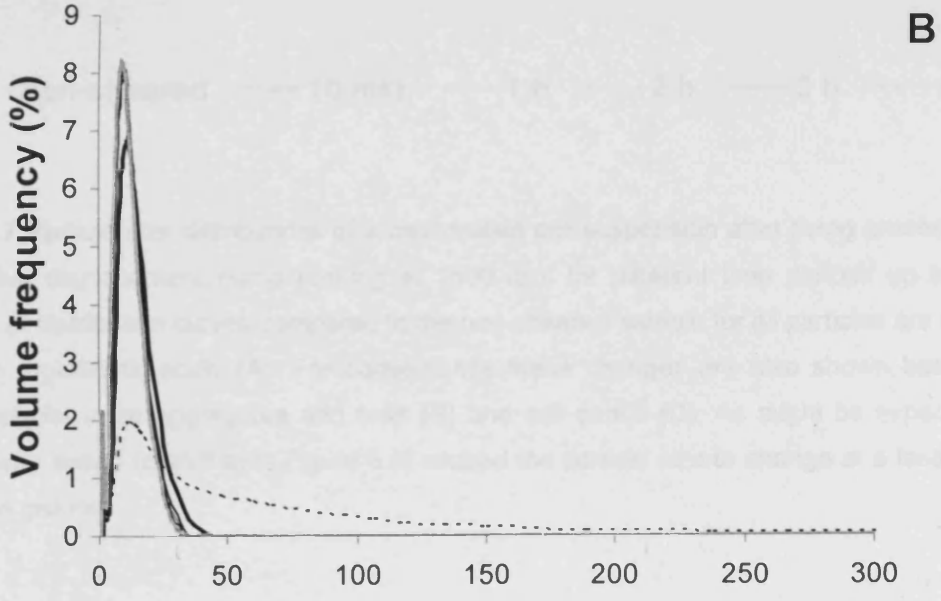
B
Volume frequency (%)
9
8
7
6
5
4
3
2
1
0
0
50
100
150
200
250
300

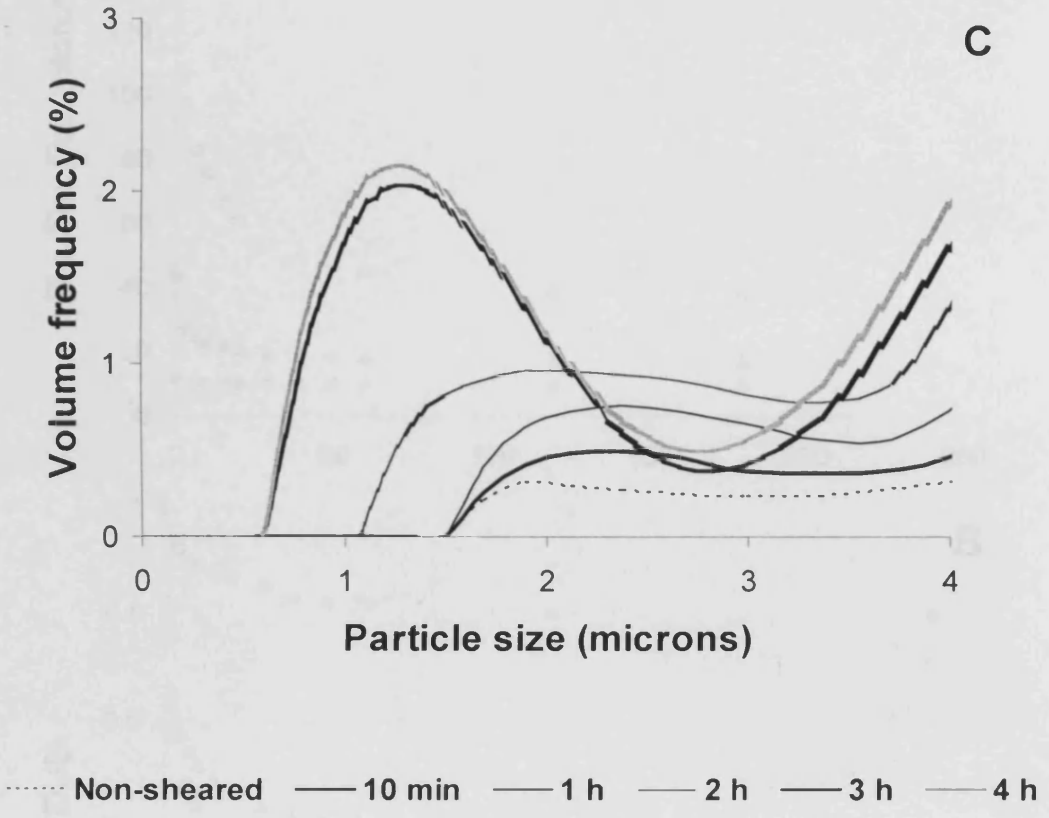

Figure 6.7 Particle size distributions of a mammalian cell suspension after being processed in the positive displacement pump running at 1500 rpm for different time periods up to 4 h. Changes of distribution curves compared to the non-sheared sample for all particles are shown based on logarithmic scale **(A)**. For convenience these changes are also shown based on linear scale for large aggregates and cells **(B)** and cell debris **(C)**. As might be expected, a higher pump speed (than that in Figure 6.6) caused the particle size to change at a faster rate for all size groups.

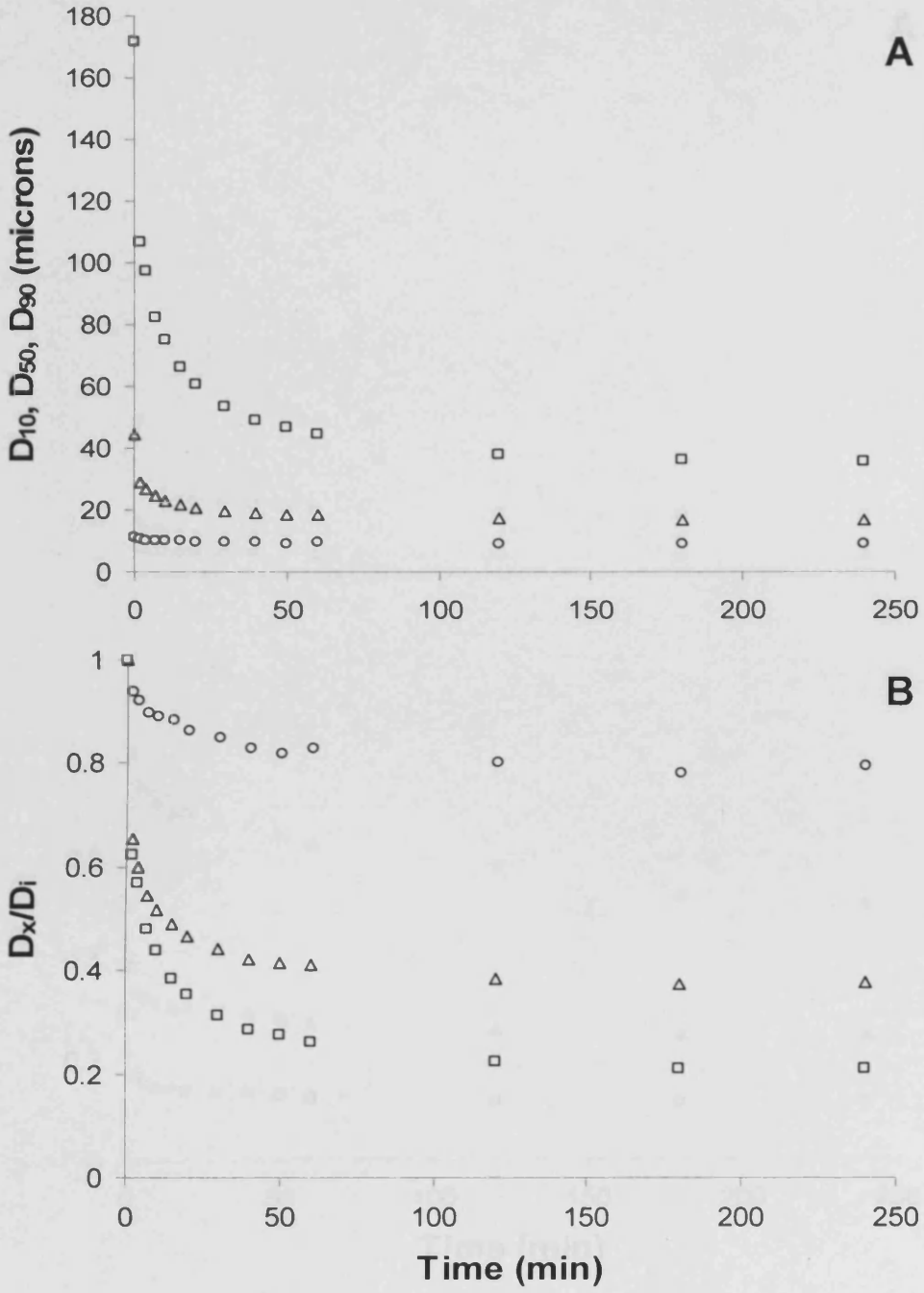

Figure 6.8 Variations of aggregate sizes as a function of time during the pump experiment running at 600 rpm (equivalent to maximum EDR of 900 W kg^{-1}). Sizes given are the equivalent particle diameters at which they are by volume 10% (D_{10}; -o-), 50% (D_{50}; -Δ-) and 90% (D_{90}; -□-) of particles of smaller size **(A)**. Sizes are also represented in terms of the percent of particle size after being processed for a particular time period to its initial size **(B)**.

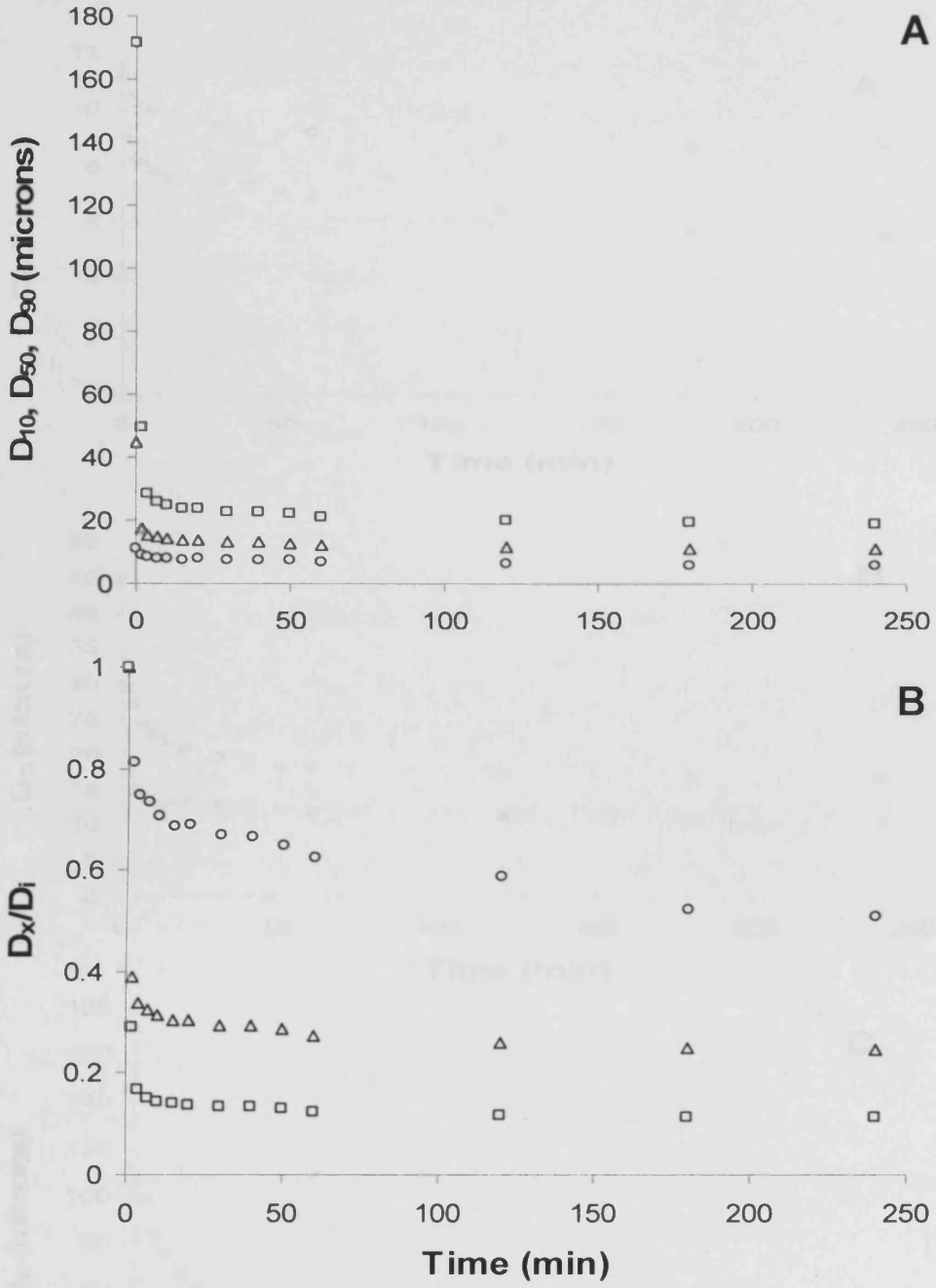

Figure 6.9 Variations of aggregate sizes as a function of time during the pump experiment running at 1500 rpm (equivalent to maximum EDR of 15000 W kg^{-1}). Sizes are represented in terms of both equivalent particle diameter **(A)** and the percent of particle size after being processed for a particular time period to its initial size **(B)**. Large aggregate (D_{90}) was shown to be the most affected size group under the shearing condition in the pump. Refer to Figure 6.8 for labels.

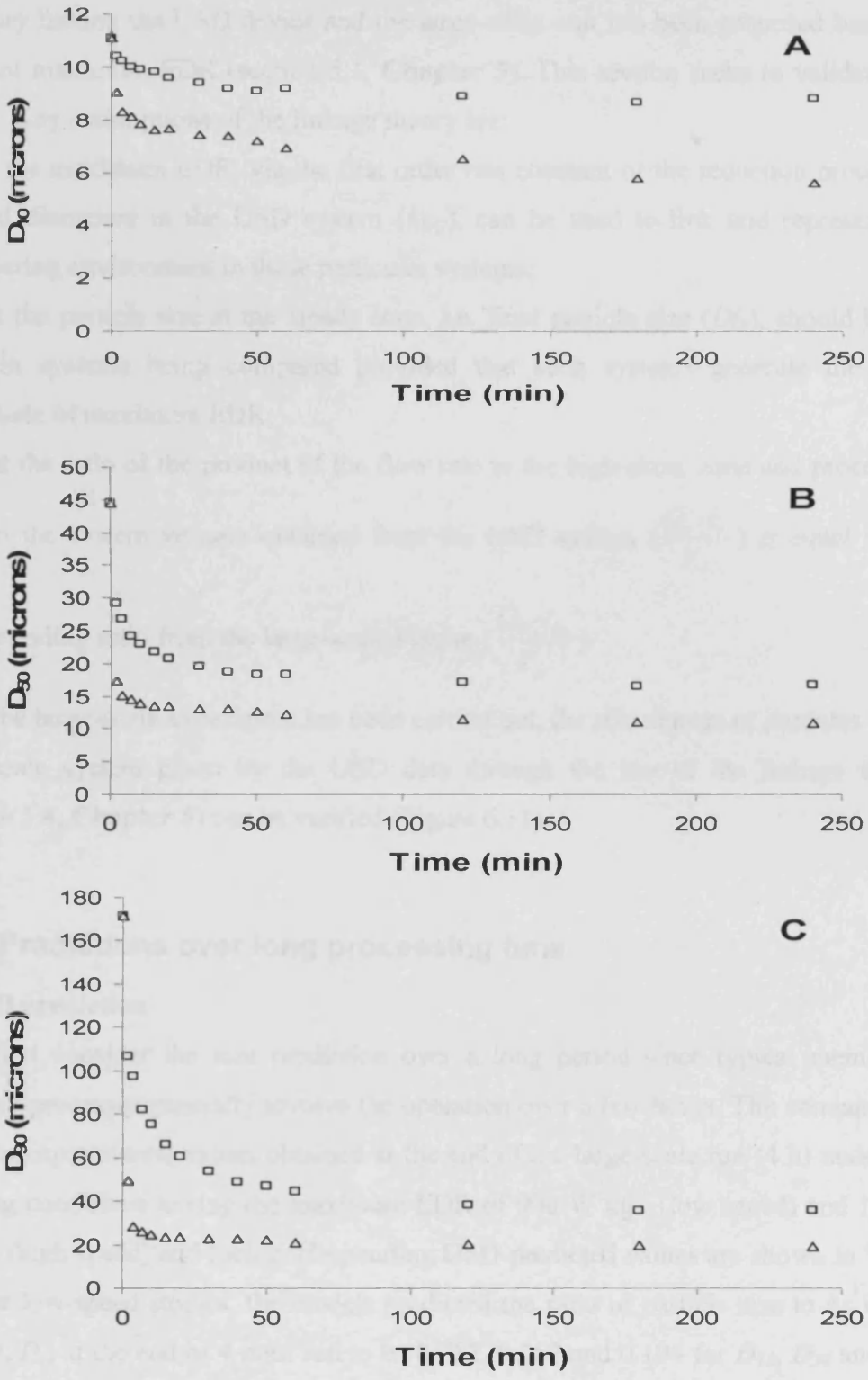

Figure 6.10 Changes of D_{10} **(A)**, D_{50} **(B)** and D_{90} **(C)** during the pump experiments running at 600 rpm and 1500 rpm with time. The equivalent magnitudes of the maximum EDR are 900 W kg^{-1} (-□-) and 15000 W kg^{-1} (-Δ-), respectively.

6.3 Experimental data versus predictive data

A theory linking the USD device and the large-scale unit has been proposed based on constant maximum EDR (section 5.1, **Chapter 5**). This section seeks to validate this theory. Key assumptions of the linkage theory are:

i) that the maximum EDR, via the first order rate constant of the reduction process of derived diameters in the USD system (k_{DU}), can be used to link and represent the engineering environment in these particular systems;

ii) that the particle size at the steady state, i.e. final particle size (Df_x), should be the same in systems being compared provided that such systems generate the same magnitude of maximum EDR;

iii) that the ratio of the product of the flow rate to the high-shear zone and processing time to the system volume obtained from the USD system ($\frac{Q_s \cdot t_s}{V_s}$) is equal to the corresponding ratio from the large-scale system ($\frac{Q_p \cdot t_p}{V_p}$).

Once the large-scale experiment has been carried out, the size change of particles in the large-scale system given by the USD data through the use of the linkage theory (section 5.4, **Chapter 5**) can be verified (Figure 6.11).

6.3.1 Predictions over long processing time

Overall prediction

Let's first consider the size prediction over a long period since typical membrane filtration processes generally involve the operation over a few hours. The comparisons between experimental values obtained at the end of the large-scale run (4 h) under the shearing conditions having the maximum EDR of 900 W kg^{-1} (low speed) and 15000 W kg^{-1} (high speed) and their corresponding USD-predicted values are shown in Table 6.3. For low-speed studies, the models predicted the ratio of particle size to its initial size (D_x/D_i) at the end of 4-hour run to be 0.712, 0.357 and 0.194 for D_{10}, D_{50} and D_{90} respectively whereas the experimental data gave corresponding values of 0.795, 0.376 and 0.207. For high-speed studies, the models predicted this ratio at the end of 4-hour run to be 0.369, 0.206 and 0.099 for D_{10}, D_{50} and D_{90} respectively whereas the

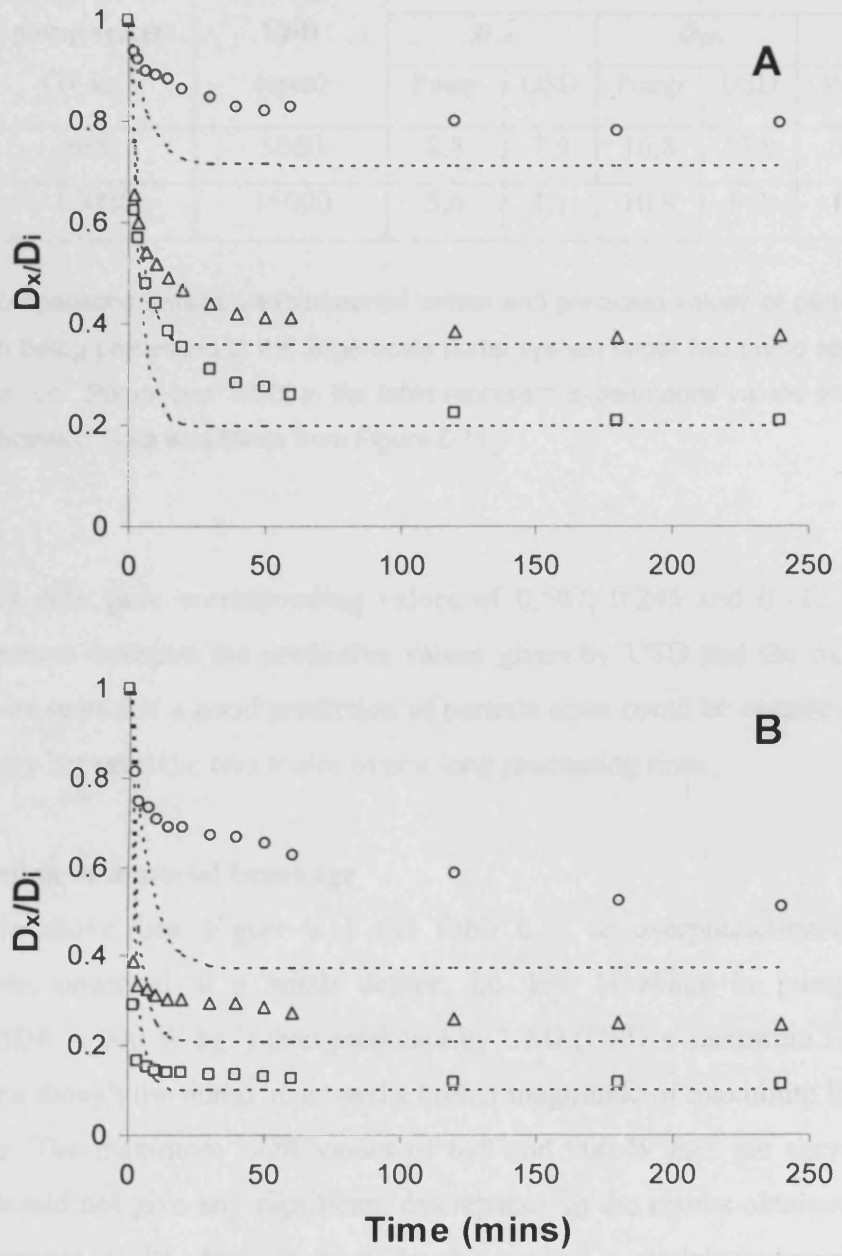

Figure 6.11 Comparisons between the experimental data and predicted data for the pump speed of 600 **(A)** and 1500 rpm **(B)**. Dashed lines in above figures represent predictions whereas data point represents experimental data. Refer to Figure 6.8 for labels. Large-scale data was taken from Figures 6.8 and 6.9 while USD data was taken from Figure 5.4 (**Chapter 5**).

Rotational speed of pump (rpm)	Maximum EDR of pump system (W kg^{-1})	Equivalent speed of USD (rpm)	Particle size at the end of large-scale pump experiment (microns)					
			D_{10}		D_{50}		D_{90}	
			Pump	USD	Pump	USD	Pump	USD
600	900	5000	8.8	7.9	16.8	15.9	35.5	33.3
1500	15000	15000	5.6	4.1	10.9	9.2	19.2	17.0

Table 6.3 Comparisons between experimental values and predicted values of particle sizes in a suspension being processed in the large-scale pump system under two pump speeds at the end of 4-hour run. 'Pump' and 'USD' in the table represent experimental values and predicted values, respectively. Data was taken from Figure 6.11.

experimental data gave corresponding values of 0.507, 0.245 and 0.112. Based on small differences between the predictive values given by USD and the experimental data, it can be seen that a good prediction of particle sizes could be obtained using the linkage theory between the two scales over a long processing time.

Overprediction of material breakage

According to above data (Figure 6.11 and Table 6.3), an overprediction of material breakage was observed at a small degree, i.e. less breakage in pump (pump's maximum EDR is 900 W kg^{-1}) than predicted by USD (USD's maximum EDR is 840 W kg^{-1}), even though the pump generated a higher magnitude of maximum EDR than a USD device. The maximum EDR values of 840 and 900 W kg^{-1} are very much the same and should not give any significant discrepancy in the results obtained from the system; otherwise results obtained should be vice versa, i.e. models underpredicted the breakage if a small difference in the maximum EDR values makes such discrepancy. One reason for this difference may be that the final particle size in the pump system might not yet be reached. In this study the analysis assumes that after 4 hours of a pump operation the mammalian cell suspension should already be in the steady state and that the final size of particles will be the same in systems having the same magnitude of maximum EDR. In practice, the steady state might not be reached in the pump system and this might contribute to particles having size larger than those being expected at the steady state.

Prediction accuracy of D_{10} and D_{90}

It was observed that the models predicted D_{90} more accurate than D_{10}. This may possibly owe to the difference in the breakage mechanisms for small-sized particles and large-sized particles which may be contributed by the breakage mechanism itself or other factors affecting the mechanism. For instance, particles having different sizes may be distributed uniquely in a system generating a specific flow pattern. This may in turn lead to a unique breakage mechanism for a specific particle size in a specific system. Since the test material was processed in two systems that have different flow patterns, it is possible to see the difference in results that predicted the breakage of particles having difference sizes.

Other reasons may also contribute to the overprediction and difference in the prediction accuracy between D_{10} and D_{90}. These are explained in the next section.

6.3.2 Predictions over short processing time

Regarding the size prediction during the early stage of the process (within 1 h), noticeable discrepancies in values obtained from two sources were observed for all representative sizes (Figure 6.11). During the first few minutes of the operation, the predictive model given by the USD data underpredicted the material breakage in the large-scale system, especially in high-speed studies. After this initial period the model then overpredicted the material breakage; however, the difference between two sources became less with increased processing time.

Two possible explanations of these differences are the limitation of the USD device to collect early data for an accurate calculation of k_{DU} and the difference between the actual breakage processes occurred in the experiments and that being assumed in the predictive models. The current design of the USD device used in this study does not allow the sample collection earlier than 15 s (the shortest possible experiment in this study). As the breakage of aggregates occurred very rapidly within the first 15 s in the USD device, especially in the high-speed studies, it is possible that a major change of aggregates might have taken place before 15 s. Since k_{DU} has a strong effect on the predicted value of a derived diameter (see Equation 5.26, **Chapter 5**), the actual values of k_{DU} could have been higher than those being calculated, as the operation under 15 s

might result in very close or equal values of derived diameters to those obtained from 15-second process. As a result, this limitation of the USD device might adversely affect the accuracy of the predictive model. Equally important, the whole process may consist of several sub-processes, which may or may not be the first-order ones and thus only one first-order process equation used in the predictive models might not be adequate to describe the change of these particle sizes for the whole process accurately. These two possibilities might eventually contribute to the mismatch between data given by predictive models and experimental data.

Other possibilities and parameters beside maximum EDR may also play an important role in the breakage mechanism and cause the discrepancy between different sources during the early stage (and late stage). These include the volume of the high-shear zone, flow pattern in the system and hence exposure time of aggregates to the high-shear zone. All these will be presented and further discussed in **Chapter 8**.

6.4 Conclusions

Following the processing in the large-scale pump system, particles in a mammalian cell suspension were found to behave in a similar fashion to those in the USD system; their size reduced with time and increased magnitude of maximum EDR. By keeping the same magnitude of maximum EDR in both USD and large-scale pumping units, it was found that predictive models together with data from the USD device running at equivalent speed to the pump can be employed to estimate the resultant size of particles in a suspension being processed in the large scale. Processing materials in the USD device was found to represent a good mimic for the large-scale operation over a long processing time (3-4 h). However, predictions over a short time, i.e. within 30 min, required further investigation which will be discussed in the last chapter.

CHAPTER 7 CENTRIFUGE MODELLING: PRELIMINARY ASSESSMENT AND USD DEVICE

A brief study is presented on a second complex flow problem encountered in bioprocessing with a view to applying the same solution as with the pump. This study involves sediment discharge from intermittent discharge disc stack centrifuge where again the challenge was to explore the combined use of computational fluid dynamics (CFD) and ultra scale-down (USD) experimental devices. The feasibility of applying CFD technique to estimate the flow field and identify the key engineering parameter(s) in the discharge zone of the CSA-1 disc stack centrifuge is assessed in this chapter. A detailed examination of the structure of the discharge zone is presented. The current capability of computer hardware and software packages on solving the relevant flow pattern is assessed and shown to be insufficient. Some limited centrifuge experiments are presented to help discuss the relevance of this challenge.

7.1 Introduction

7.1.1 Centrifugation of shear-sensitive biomaterials

Traditional techniques, which are still commonly used for clarification of fermentation broth, are membrane filtration and centrifugation (Lee, 1989). Membrane filtration is usually employed as an early process step in downstream processing to recover valuable cell products during harvesting and to clarify lysate stream after homogenisation. Filtration of product-containing suspensions however usually encounters many problems attributed to several mechanisms including filter cake formation, membrane fouling, pore blocking and concentration polarization. As these drawbacks of membrane filtration often make this recovery method a less economical for cell recovery particularly for high cell density recovery, large-scale cell harvesting and protein recovery can alternatively be carried out using centrifuges. This choice is often employed especially with increasing scale of operation and increasing particle

size. The main reasons for its widespread usage are due to its being suitable for high throughput, continuous and, for new models, well-contained operation.

Depending on the physical properties of process materials, the efficiency of centrifugation varies considerably. In most cases intact cells can be removed without great difficulties whereas disrupted cells and resultant particulates cannot be completely removed by using centrifuge alone, making direct application to chromatography difficult. Shear-sensitive materials, such as mammalian cells, are often damaged in a centrifuge as a result of centrifugal forces and shear stresses. These forces are mainly responsible for attributed damage of materials being processed in the unit and account for the increase of cell debris, which includes cell membrane and cell wall fragments, and thus the reduced efficiency of centrifuges, particularly the continuous-flow industrial ones.

For the disc stack machine damage of shear-sensitive materials can occur at several locations (Axelsson, 1985), especially where there is a liquid-gas interface, the flow field is disrupted or the rapid change of main flow direction takes place. The centrifugation process commences once the non-rotating process stream enters the rotating centrifuge. At this starting point the liquid stream forms an interface with air in the receiving chamber at the centre of the bowl. Turbulence is generated as the nonrotating incoming stream runs into the rotating interface resulting in damage of shear-sensitive materials. It has been confirmed that by processing a precipitate suspension in the disc stack centrifuge the feed zone is found to be the primary location for material damage (Mannweiler and Hoare, 1992). The same observation has also been reported in other centrifuges, e.g. multichamber-bowl centrifuge (Boychyn et al., 2001). Very fine particles produced by the strong flow field generated in the feed zone makes the separation more difficult and reduces the clarification of material and process throughput. The increase of throughput rate can be achieved through flocculation of these fines (Bentham et al., 1990). However, the best approach may be to minimise the effect of liquid-air interface created in the receiving chamber. For this purpose, a full-hermetic inlet is usually employed as this gives the least breakage (Mannweiler, 1990) or the inner radius of the interface must be reduced through a new design.

As the liquid stream is transported to the main separating part, i.e. the discs, damage can also take place at the underside of the disc. This is due to shear forces generated from the fluid movement in the Ekman layer that drag particles toward the centre. The magnitude of velocity and thus shear forces increases with increasing disc spacing, increasing bowl speed, increasing disc angle and decreasing viscosity. This may contribute to further damage restricting the maximum operational speed to be adjusted accordingly in order to minimise material damage.

Once enough sediment is accumulated at the bowl's periphery and is ready to be discharged, it is subjected to additional damage due to high kinetic energy taken by the discharge stream. The movement of a high-velocity stream through the discharge zone sets off the conversion of kinetic energy to heat whose increase is proportional to the square of the radius of the discharge 'exit' and to the square of the bowl speed. Moreover, the impaction of the high-velocity stream on the collection chamber also contributes to further damage. Previous observations have shown approximately 10% disruption of *E. coli* cells grown in complex media (Chan et al., 2006) and 20% in defined media (Gray et al., 1972). For processes where products are extracellular and the centrifuge is used to separate the two phases, the effects at the discharge zone may not be of great importance. However, for intracellular products, the effects may involve cell damage and thus the loss of great-value products which usually are obtained at very low volume. It is this particular part of the centrifuge which will be assessed for the application of CFD and USD which may be applied to mimic key characteristics in a small scale.

7.1.2 Previous work

7.1.2.1 Centrifuge modelling

The hydrodynamics, particle dynamics and separation process occurring inside industrial-scale centrifuges can be modelled using several techniques. These theoretical models together with practical studies help the selection of the centrifuge in terms of its type and size. Traditionally, most modelling techniques used are based on equations describing flow patterns and interactions among particles and particles and fluid medium under the centrifugal forces within the settling distance in the bowl. Due to the

complexity of the machine and thus the flow field generated, these mathematical equations however cannot provide a complete description based on machine configuration and properties of process materials. Moreover, change of particle size due to material damage during operation adds more uncertainties into these modelling equations.

Despite these difficulties, some mathematical models and theories can still be successfully applied to the centrifugal recovery of structurally-robust species and allow for complex configurations of the machine and its flow phenomena. The most simple and common theory used to characterise centrifuges is the mathematical theory of equivalent settling area (Ambler, 1959). The theory was devised on the basis of the viscous resistance through unhindered settling of a small single particle that does not move too rapidly and has reached an equilibrium velocity. According to this, the capability of the centrifuge is described in terms of sigma value Σ which is the calculated equivalent area of a settling tank theoretically capable of doing the same amount of work in a unit gravitational field. This index of centrifuge size depends on parameters of the specific centrifuge; generally this includes volume of the liquid in the centrifuge, radius, rotational speed and settling distance. The sigma value is usually used to compare machines with identical or similar geometry but different sizes and determine the throughput rate for the industrial-scale machine based on data obtained from pilot-scale ones. In this instance, the ratio of the throughput rate and equivalent settling area is kept constant for both scales and a small model is constructed to facilitate understanding and predict the effects of flow field generated in the large-scale machine. Though, at present the most-used definition is the separation of all particles having critical diameter (100%) instead of only half (50%) as the original derivation, the theory has been successfully applied in many applications provided that the ratio of the throughput rate and sigma value should generally be used to compare the performance of centrifuges of the same type. For disc machines, there should also be similarities of disc spacing, number of feed holes and cone angle between both machines.

Although the sigma theory has been applied extensively in the industry, it however does not take into account important parameters which may have profound effects on

performance predictions and subsequent design and operation. Some of these parameters include the hindered settling effects and actual separation efficiency. The hindered settling involves the complex interactions between particles when dealing with high concentration of solids. Increased concentration of solid particles prevents free movement of these particles and thus greatly reduces their settling rates (Clarkson et al., 1996, Aiba et al., 1964). The actual separation efficiency relates the desired separation performance to the actual throughput rate. It is suggested that the efficiency factor should be included in the sigma theory in order to help accurately determine the extent of throughput reduction in practice. Consequently, it can be seen that these parameters add more difficulties in theoretically estimating the performance of the centrifuge and sigma theory alone may not be able to provide accurate predictions in certain applications.

The accuracy of predictions based on the sigma theory alone becomes worse when the shear-sensitive species are processed resulting in large differences in clarification between actual pilot values and predictive values obtained from laboratory centrifuges (Boychyn et al., 2000). The processing of such materials, especially through the feed zone, leads to size reduction of particles and significantly reduces the overall clarification of the machine. This size change thus invalidates the sigma theory, especially during the scale-up process where data from small-scale machines having a low-shear feed zone is used to predict the performance of large-scale ones having high-shear feed zone. Moreover, the damage of such materials in the discharge zone in the solid-ejecting machines is not included in the theory leading to further difficulties in estimating the actual outcomes in large-scale operations. As a result, the sigma theory alone may not be adequate to provide sound predictions for shear-sensitive materials, which are being processed widely in the biotechnology industries, in the large-scale machine. This suggests that alternative methods must be sourced.

By integrating above parameters and phenomena originally excluded in the sigma theory into the model, simulations of the feed zone, and thus the overall performance, of the disc stack centrifuge has successfully been achieved at higher accuracy. For instance, a computer-based model for the separation of a range of biological materials has been developed for a pilot-scale disc stack centrifuge (Clarkson et al., 1996). The model is based on the sigma theory and grade efficiency concept which helps predict

the particle sedimentation in the unit. Both effects of hindered settling at high biomass concentrations and material breakage at the feed zone have also been integrated into the model.

With recent CFD applications to centrifugation together with integration of key parameters into the model, the complex flow field generated in the machine has been elucidated allowing better analyses and predictions to be made on the feed zone, which is the primary site for breakage. Boychyn *et al.* (2001) demonstrated that the CFD technique can be applied to determine the profile of the energy dissipation rate in the feed zone of the industrial multichamber-bowl centrifuge, which would have never been obtained using traditional mathematical analysis, and reproduced this engineering characteristic in a laboratory-scale high-speed rotating-disc device. A few millilitres of materials were sheared in this small device and small-scale data was then used to assess the impact of the flow field in the feed zone on properties of studied precipitates. Recovery prediction was subsequently made based on sheared materials using a laboratory-scale centrifuge. The reduction of clarification of protein precipitates from the originally predicted values (88%) to observed values (39%) has been explained by this approach. The validity of this predictive technology has been proved by extending this technology to other centrifuges including disc stack and CARR Powerfuge^{TM} (Boychyn et al., 2004). The above findings prove that clarification performance of shear-sensitive species in the industrial machine can be mimicked by processing such species in the rotating-disc device and laboratory centrifuge in sequence, with the aid of CFD to map the engineering flow field. On the broader view, this predictive technology involves determining and characterising the key engineering parameter in the large-scale unit operation and then mimicking it in the USD device with or without the aid of other techniques, e.g. CFD or mathematics-based models. The challenge still remains to assess the applicability and validity of these twin technologies to the discharge zone of the centrifuge in order to determine the impact of its flow fields in the small device and possibly to establish a fast-track approach to process selection and process development.

7.1.2.2 Ultra scale-down device

As it is difficult to predict accurately how hydrodynamic forces generated in bioprocess equipment will affect cell lines having different mechanical properties (Garcia-Briones and Chalmers, 1994), the understanding of the actual complex interactions between the material of interest and processing environment acquired through industrial-scale development may be needed. However, at this scale the operating cost is very high and the time consumed may put the company into disadvantageous position, especially for those producing biopharmaceutical products. As a result, there are needs to quantify these forces or preferably mimic their effects onto a smaller system, e.g. a small-scale mimic or USD device, in order to reduce operating cost and time of pilot-plant development.

The benefits of test data obtained from small-scale equipment are several fold. The main advantage of using data from small-scale machines is that small quantities of materials can be used to assess potential process options at the very early stages in the development cycle through better understanding of the impact of the flow fields generated in the large-scale machines. This greatly shortens the time to the market, especially for the biopharmaceutical products. In addition, Ambler (1959) has described the advantages of applying small-scale data together with sigma theory to centrifuge applications. Firstly, the throughput rate of the large-scale machine at which satisfactory removal of solid phase can be obtained in terms of both quantity and physical properties of sedimented solids on a given centrifuge rotor based on a constant ratio of the throughput rate and sigma value of both small- and large-scale machines. Secondly, the terminal concentration can be determined in a specific centrifuge. In addition, for solid-ejecting machines, the approximate number and size of discharge nozzles required to concentrate the solids into the required portion of the feed stream can be established.

In the past the most commonly-used scale-down device for the modelling of continuous-flow industrial centrifuges is a laboratory centrifuge. This approach has been successful in operations involving robust materials. However, using laboratory-scale centrifuges alone to reproduce the impaction of the flow conditions generated in the industrial centrifuges on shear-sensitive species usually does not provide accurate

predictions on the machine's performance. This is mainly due to the mismatch of the clarification and dewatering conditions between laboratory and industrial machines, especially in the feed zone. Accordingly, researchers have attempted to overcome this problem and recently became successful when employing an additional device, e.g. the rotating-disc USD device, to represent the hydrodynamic forces encountered by shear-sensitive species in the feed zone in the large-scale machine prior to laboratory centrifugation. The application of both the rotating-disc device and standard laboratory centrifuge has been successfully validated in several centrifuges including the disc stack (Boychyn et al., 2001, Boychyn et al., 2004), as described in previous section. Both devices have also been employed in a separate study in order to simulate one of the sub-processes involving large-scale recovery of flocculated immunoglobulins used in the manufacture of snake venom-specific Fab fragment through the disc stack centrifuge (Neal et al., 2003). The combined use of both devices also successfully predicted the clarification of mammalian cell culture broths using the industrial-scale disc stack centrifuge (Hutchinson et al., 2006). Unlike the feed zone, the impacts of the flow condition in the discharge zone including the collection chamber however have not yet been modelled, even with above USD devices. As the mechanism of breakage may be different from that occurring in the feed zone, the applicability of the CFD technique together with USD devices is to be assessed and will be discussed later in the chapter.

7.2 Details of large-scale centrifuge

7.2.1 CSA-1 disc stack centrifuge

The CSA-1 disc stack centrifuge (Westfalia Separators AG, Oelde, Germany) was used in the analysis in this study (Figures 7.1 and 7.2). A hydro-hermetic feed zone is used to minimise the effects of entry on cell breakage; the model has a bowl liquid capacity of 0.6 L and its rotational speed range of 6100 to 9800 rpm. Its maximum speed is equivalent to a settling area (Σ) of 1710 m^2. During its operation, the more dense solid phase is separated from the less dense liquid phase in the disc zone before being transported under the influence of centrifugal forces to the periphery of the centrifuge bowl. The liquid phase exits the centrifuge through a centripetal pump located at the top with the backpressure of 0.5 to 1.5 bar. Another pump (Grundfos CR 2-50, Grundfos pumps Ltd., Leighton Buzzard Beds, UK) is used to supply water at 2-bar pressure into the internal structure of one of the units forming the central centrifuge bowl in order to control the sediment discharge mechanism. As the discharge mechanism is triggered, one of the units forming the centrifuge bowl moves downward creating an opening 'slot' for the sediment to move from the rotating chamber to the discharge zone. The solid then travels through a small space prior to the discharge nozzle into the nozzle. It eventually leaves the nozzle exit and impinges onto the wall of the collection chamber.

7.2.2 Centrifuge discharge zone

Six discharge nozzles (Figures 7.1B and 7.2) with the direction of discharge in an anti-clockwise motion allow the release the solid cell paste from a clockwise-rotating chamber when the bowl reaches its maximum solid capacity of ~250 g. At this point the pump was immediately switched off, the bowl speed reduced and the sediment discharged into the collection chamber. As a result, the discharge zone is defined as the region starting from the inner side of the bowl and ending at the wall of the collection chamber. Figure 7.3 shows a simplified diagram of the whole length of the discharge zone comprising several different flow regions as the solid is transported before impacting onto the wall. These areas include the slot, a small space prior to the nozzle, discharge nozzles and the collection chamber area including wall.

Figure 7.1 CSA-1 centrifuge and its discharge nozzles. **(A)** The CSA-1 centrifuge with the cover of the collection bowl. **(B)** Discharge nozzles (only three of the six nozzles are visible here) together with the distance between the nozzle exit and the collection-bowl inner wall form part of the discharge zone. Note that in **(B)** the cover of the collection bowl was removed in order to expose these nozzles.

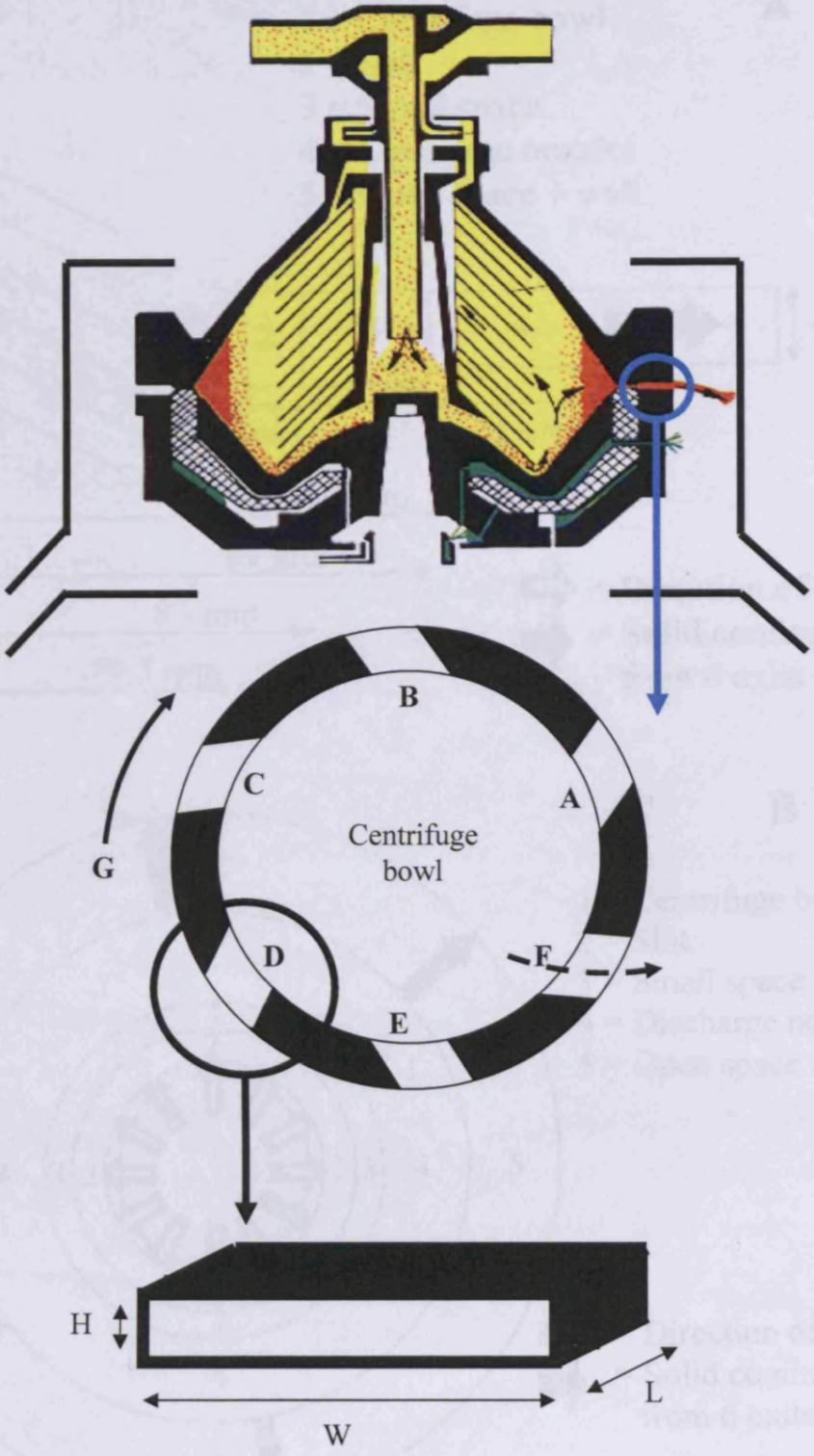

Figure 7.2 Diagrams showing the location of sediment cell paste and discharge nozzles (length L, height H, width W). The directions of centrifuge rotation and discharge are clockwise and anti-clockwise, respectively. At the start of the discharge process, cell paste passes through the discharge nozzles (courtesy of Gerard Chan).

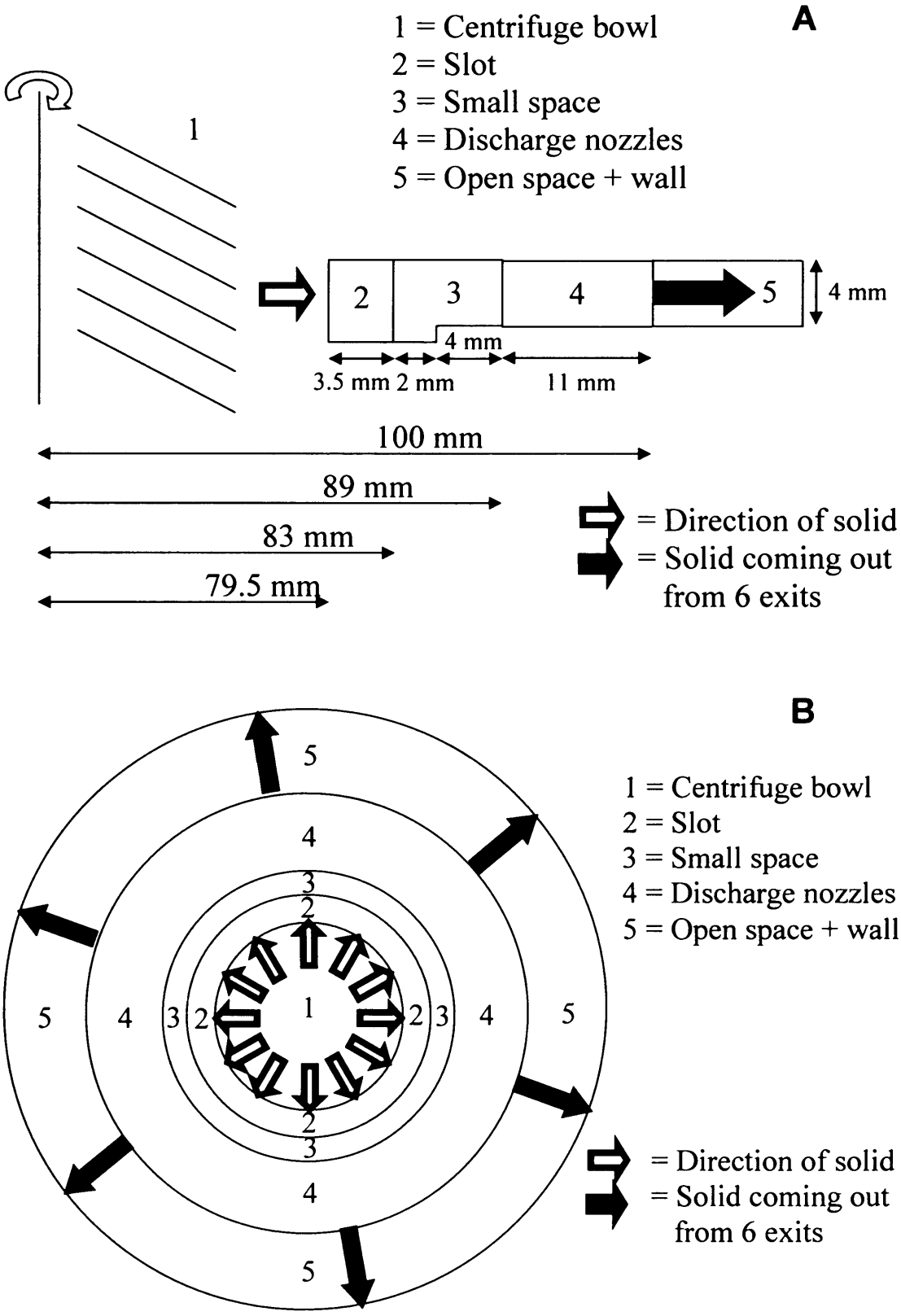

Figure 7.3 Diagrams showing the side view **(A)** and top view **(B)** of the discharge zone. Once the centrifuge bowl (1) is full the discharge process begins by releasing solid cell paste to the discharge zone, which comprises 4 areas including the slot (2), small space prior to the nozzle (3), discharge nozzles (4) and the collection chamber area including wall (5).

7.3 Materials and methods

In order to mimic the damaging effects posed by the flow through the discharge zone of the CSA-1 disc stack centrifuge, two approaches were proposed: to find a suitable USD device directly and to use CFD technique to understand fundamental flow behaviour in this specific zone and, if successful, to mimic this behaviour in the USD device to allow a better match. Collaborative work was initiated and carried out in parallel by two PhD students at the beginning of the project. The first approach was investigated by Dr Gerard Chan, a former PhD student in the Department of Biochemical Engineering, UCL. The second approach has been followed by myself and is detailed here.

The analysis of the feasibility of applying CFD and USD techniques to map detailed flow fields in the discharge zone and mimic them in the small device has been divided into four parts as follows:

- detailed examination of the structure of the discharge zone;
- estimation of the form of cell paste transported in each sub-zone and determination of variations of its density and viscosity at the bowl's periphery through centrifuge experiments and theoretical analysis based on water jet;
- feasibility of applying CFD technique to assess the flow field in the discharge zone based on results and understanding from above;
- recommendation of solution steps to discharge problem if CFD application is feasible. Otherwise, suggestion on an alternative method will be provided.

Each of these parts requires different resources. The first part requires only the CSA-1 disc stack centrifuge (section 7.2) whereas the third requires merely the specifications of computer hardware and software (section 3.2, **Chapter 3**). The rest of resources required for the second part are detailed below:

7.3.1 Experimental equipment

All examinations and experiments were carried out using a CSA-1 disc stack centrifuge. Full details of this centrifuge are presented in section 7.2.

The viscosity of the cell paste collected from the bowl's periphery was measured using a Contraves Rheomat 115 viscometer with a concentric cylinder (Contraves Industrial Product, Middlesex, UK). Within the unit, the sample was exposed to a series of torques providing relevant information for plotting a graph of shear stress against shear rate. The temperature was kept at 4°C by circulating cold water through the cooling jacket. All readings were performed twice and the average value obtained.

The density of the cell paste was measured through the sampling of 1-mL cell paste into a pre-weighed Eppendorf. The Eppendorf was then weighed and the difference between the empty and full ones calculated in order to determine its weight and thus density.

7.3.2 Cell samples

DH5α *E. coli* cell paste was obtained from Oxoid Ltd (Hampshire, UK). Cell samples were stored at –80°C. Feed suspensions were prepared by re-suspending frozen cell pastes using PBS buffer (pH = 7). Suspensions with concentration of 30 g L^{-1} were prepared for large-scale experiments.

7.3.3 Operating parameters

For all experiments, the feed suspension was continuously hand mixed to ensure homogeneities of the feed stream entering the centrifuge and the temperature was controlled to be less than 10°C using cooling water through the centrifuge hood. With a pressure of 0.5 to 1 bar and a flow rate of 56 L hr^{-1}, a peristaltic pump (model 605DI, Watson Marlow, Falmouth, Cornwall, UK) were used to deliver a feed stream into the centrifuge whose speed was set at 9800 rpm. The sample was collected after the system reached the steady state, i.e. after processing 3.6 L, or 6 bowl volumes, through the centrifuge. The overall procedure involved shutting down the centrifuge followed by dismantling the bowl and collecting a number of sediment samples from the inner bowl rim and at 1 cm away from the rim. The density and viscosity were immediately measured after sample collection in duplicate.

7.3.4 Chemicals

All chemicals, unless otherwise stated, were of analytical grade and were obtained from Sigma Aldrich (Dorset, UK).

7.4 Results

This result section will be presented in four parts. The first part of the examination determines the key infrastructure of the flow problem. The second part is to combine the jet theory with the data obtained from centrifuge experiments in order to allow better understanding on the nature of cell paste in terms of form, velocity, density and viscosity. Results and understandings from the first two parts together with the limited capacity of the computer hardware and CFD software form the third part which describes the overall assessment of CFD application on flow analysis at the discharge zone of the CSA-1 centrifuge. Finally, an alternative USD device obtained from a direct method is also presented.

7.4.1 Structure of the discharge zone

The discharge zone is divided into four areas based on the uniqueness of the configuration of each area, which may affect the shape of the cell paste as it travels and thus its flow characteristics and subsequent effects on material damage. The first area, i.e. the slot (No. 2 in Figure 7.3), has a cylindrical shape as this area is formed by the up and down motion of one of the cylindrical-edge bowl units. This first area is thus very simple to draw in the CFD program. The difficulties arise when considering the second area, i.e. a small space prior to the nozzle (No. 3 in Figure 7.3). This small space area consists of irregular contours between nozzle entries (Figure 7.4A). The discharge nozzle itself (No. 4 in Figure 7.3) is not built based on commonly found geometries. Its left part has a triangular shape facilitating the entry of solid stream into the nozzle and redirects the stream to the left as the stream travels through the nozzle (Figure 7.4A). On its right, irregular-shaped grooves guide the stream to move towards the left-hand side (Figure 7.4A). Looking from the outside, the shape of the nozzle exit also shows a little depression on the top and right edges in order to facilitate the exit of the solid stream (Figure 7.4B). Finally, the solid stream reaches an air medium and

collides onto the wall (No. 5 in Figure 7.3), which is formed from a sloped wall of the collection bowl. The flat slope here minimises damaging effects caused by the impaction of material onto the wall (Figure 7.4C). Collectively, these irregularities found in the shape of these structures, especially No. 3 and 4 in Figure 7.3, require the CFD drawing to be extremely precise if the CFD technique is to be used and accurate results are to be achieved.

7.4.2 Characteristics of cell paste during discharge

The discharge process starts with the slot opening of the rotating chamber to release dense cell paste to the discharge nozzle and subsequent areas in the discharge zone. At this stage, it is important to realise that the space around and inside the nozzles may contain an air medium as well as cell paste and such condition will increase difficulties to CFD simulation. With the standard operating speed of ~8000 rpm and its diameter of 200 mm, the velocity of cell paste coming out from the discharge nozzle was estimated to be almost 100 m s^{-1}. At this high velocity, the interaction of drag forces reshape the cell paste to become narrower as it leaves the nozzle exit and form a jet impinging onto the wall of the collection bowl. Provided the high-speed jet is assumed to behave like a water jet, based on the water jet theory the solid-containing cell paste is assumed to spread widening its diameter along the distance between the nozzle exit and the wall of the collection bowl. Along the way the periphery of the jet allows a number of droplets containing different sizes to be formed. Finally, these droplets and the jet hit onto the wall. Though, the understanding of the characteristics and detailed structure of the water jet is limited (Haller et al., 2002), the overall process of shape change of cell paste before hitting onto the wall can be assumed to involve the following, which is based on water jet work by Yanaida and Ohashi (1978):

1. the continuous flow region: the area corresponds to that near the nozzle exit where the structure of cell paste is coherent and its velocity remains approximately constant. There is little or no change occurring in this region. Further away from the exit the fine droplets begin to form, as the solid passes through a medium having different velocity.

2. the droplet flow region: the velocity of the solid decreases as the aerodynamic forces dominate. More droplets with larger sizes are formed.

3. the diffused flow region: a number of droplets are formed and the solid stream is diffused and blended in the air medium.

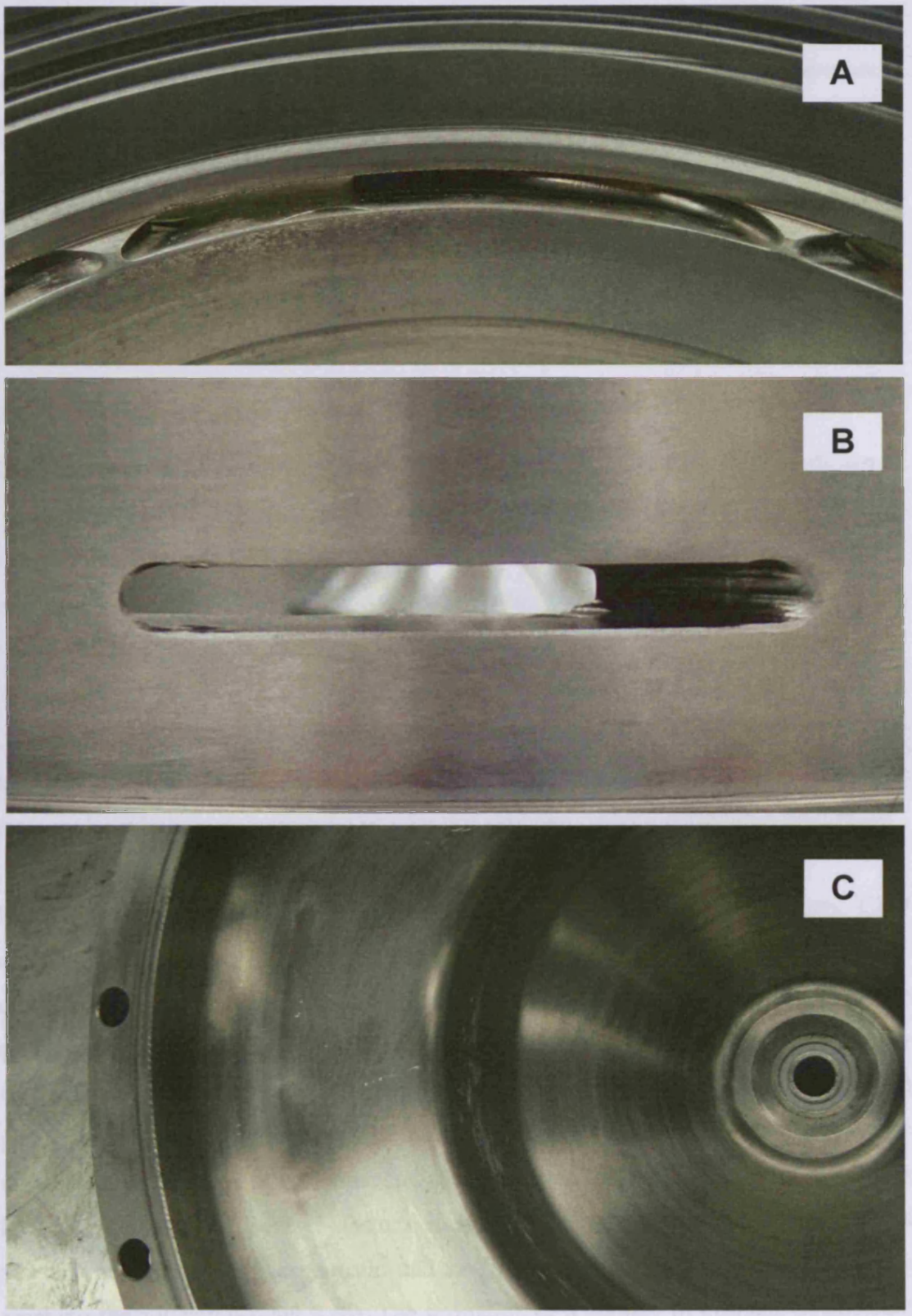

Figure 7.4 Diagrams showing the small space prior to the nozzle **(A)**, nozzle exit **(B)** and sloped wall of the collection bowl **(C)**. Most areas contain irregular curved structures forming parts of the discharge zone making CFD drawing and calculation more difficult.

Regarding the centrifuge experiments, the viscosity and density used were $2*10^{-3}$ N s m^{-2} and 1050 kg m^{-3}, respectively. However, for the sediment discharge there are a wide range of viscosities and densities. For the system studied here the cell concentration in the sediment was still relatively low leading to viscosities ranging from $4\text{-}9*10^{-3}$ N s m^{-2} and densities from 1200 to 1450 kg m^{-3}. It is unlikely these relatively small increases will affect the CFD pattern but in the future the higher values should be used in CFD analysis.

7.4.3 CFD application on the discharge zone

The observations and results obtained from above allow an assessment to be drawn of the feasibility of CFD application to study the discharge zone. As over 50% of the time spent in industry on a CFD project is devoted to the definition of the domain geometry and grid generation (Versteeg and Malalasekera, 2007), irregularities found in the structure of a majority of areas in the discharge zone clearly slow down CFD simulations if the technique is to be applied. Uncommon shapes suggest more time consumed on drawing, computation and thus simulations as a whole. Moreover, some key structures may be impossible to draw accurately. As a result, the CFD technique may not be suitable to obtain solutions for this problem under a reasonable timeframe.

Better understanding of the assumed shape of the solid stream indicates CFD application may not be applicable to this problem at present. No such model at present can accurately predict the shape of the high-velocity cell paste coming out from the rotating chamber (No. 1 in Figure 7.3) to the nozzle exit, as an air medium may occupy certain proportion of these spaces depending on the actual operating conditions and physical properties of the stream. The spreading of the cell paste stream when it leaves the discharge nozzles also contribute to difficulties. The extent of the spreading however depends on several factors including the stream velocity, density and viscosity of both the process stream and air (intermediate medium before the stream reaching the collection-bowl wall). The formation of a number of droplets of different sizes in the air medium essentially invalidates the CFD application on this problem. This is firstly due to the inability of CFD to predict accurately a wide range of droplet sizes. Secondly, even if the first problem can be solved, it may take too much computing resource to solve this particular problem. Regarding the variation of fluid

properties, though the difference of CFD results and its resource consumptions from variations of density and viscosity should be small in this case, the large variations of these properties may be observed in certain process conditions with specific biomaterials. This makes the simulations to be more difficult and may lead to inaccurate results. As a result, it can be concluded that CFD technique is not suitable to assess the magnitude of maximum energy dissipation rate in the discharge zone of the disc stack centrifuge and hence the technique was not employed for this problem.

Despite the above difficulties, an alternative method assessing the effect of shear damage in the discharge zone exists. The method provides a direct-mimic based on using a USD device which is presented in the next paragraph.

7.4.4 Alternative method for predicting discharge effects

In order to generate equivalent 'effects' found in the discharge zone, an Instron capillary rheometer model 1026 (Instron, Ltd, High Wycombe, UK) was proposed as USD device (Figure 7.5). Originally, the device was designed for testing material properties including tensile or compressive shear strength and rheology. To fit the purpose of this study the device was modified by replacing the central units with a long piston and mounting station for a wide range of stainless steel capillaries. These capillaries were manufactured by UCL workshop to have internal diameters ranging from 0.1 to 0.575 mm. For this investigation, only capillaries of 30 mm in length were used, though different lengths are available including 30, 50, 75, 100, 150 and 200 mm. The piston and holding chamber were made of an aluminium alloy (Durell, Smith Ltd, UK). A chamber, which holds a total of 15-mL fluid, has a diameter and length of 20 mm and 60 mm, respectively. This setup is capable of delivering fluid velocities up to 85 m s^{-1}. The PTFE beaker with a removable stainless steel impingement stub having diameter and height of 30 mm positioned at the centre was placed at the bottom to collect samples. During the experimental trials, 10-mL sample was processed through the capillaries over varying shear rates, shear stresses, viscosities, residence times in the capillary, impact distances and impact velocities with a lid covering the beaker to contain aerosol release. The study has been carried out to understand the effect of flow and impact conditions found during the discharge process of the disc stack centrifuge. Details of these experiments can be found in Chan *et al.* (2006).

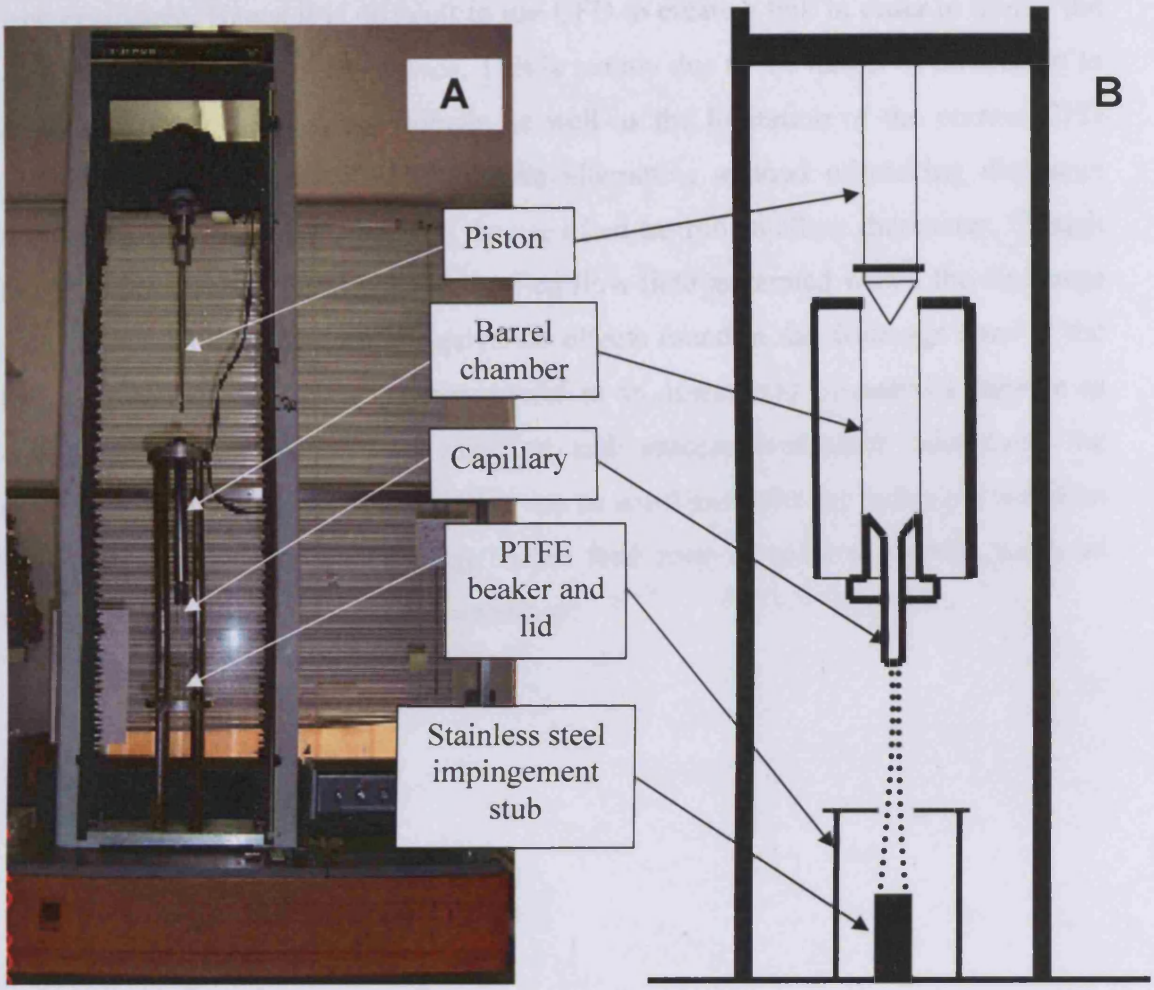

Figure 7.5 Instron capillary USD device. The actual setup, shown in **(A)**, was employed to study the effects of shear and impaction of cells. A predictive model has been proposed to estimate the shear damage occurred in the full-scale discharge zone of the disc stack centrifuge. As shown in a schematic diagram **(B)**, during the experiment a piston moves down to a sample-containing chamber forcing the liquid medium to pass through a capillary of different sizes. The sample then impacted a stainless steel target, which is used to mimic the wall of the collection chamber, and was collected for further investigations.

7.5 Conclusions

Within the confines of this project the CFD technique is found to be inapplicable for the assessment of the flow field generated in the discharge zone of the CSA-1 disc stack centrifuge. Hence it is difficult to use CFD to create a link in order to mimic the equivalent effects in the USD device. This is mainly due to the length of time taken to define accurately the problem domain as well as the limitation of the current CFD capability on hardware and software. An alternative method mimicking discharge effects is however available through the use of an Instron capillary rheometer. Though this USD device cannot provide the detailed flow field generated within the discharge zone, it allows the generation of equivalent effects found in the discharge zone of the disc stack centrifuge, which are very useful in an assessment of material damage as well as equipment design and selection and process evaluation. Moreover, the matching technique based on the Instron can be combined with the technique based on USD device to predict the breakage in the feed zone in order to provide the total material breakage in the disc stack centrifuge.

CHAPTER 8 DISCUSSIONS AND CONCLUSIONS

This chapter draws together and discusses the key findings of this thesis study as well as the important issues raised in each stage in the development of full-scale predictive models. The flowchart is firstly presented to give the overall view of the methodology employed in this study to mimic large-scale engineering environment and reproduce it in a small scale. The key issues in each stage are then discussed. The overall conclusions are presented at the end to provide a broad view on what has been achieved.

8.1 CFD-USD methodology to membrane filtration system

Key steps in the CFD-USD methodology used to assess the magnitude of the key engineering parameter (maximum energy dissipation rate) in the most relevant component (pump) and mimic this in the USD device allowing size predictions to be made in the large-scale system by using only small volume of biomaterial are summarised in the flowchart in Figure 8.1.

During the early stages an identification of the key engineering parameter responsible for changes of biomaterial is required such that it can be used to link systems of different scales, i.e. small and large scales. Equally important an identification of key component and/or part of the system responsible for most changes of biomaterial during the operation is necessary, so that its flow environment can be analysed and mimicked in detail without wasting time perform the match-up on less-relevant components. Moreover, a selection of suitable USD device to the problem is also crucial as to facilitate the ease of use (during testing and once the predictive models have been established) and ease of adjustment of the magnitude of key engineering parameter (maximum energy dissipation rate) imposed onto biomaterial.

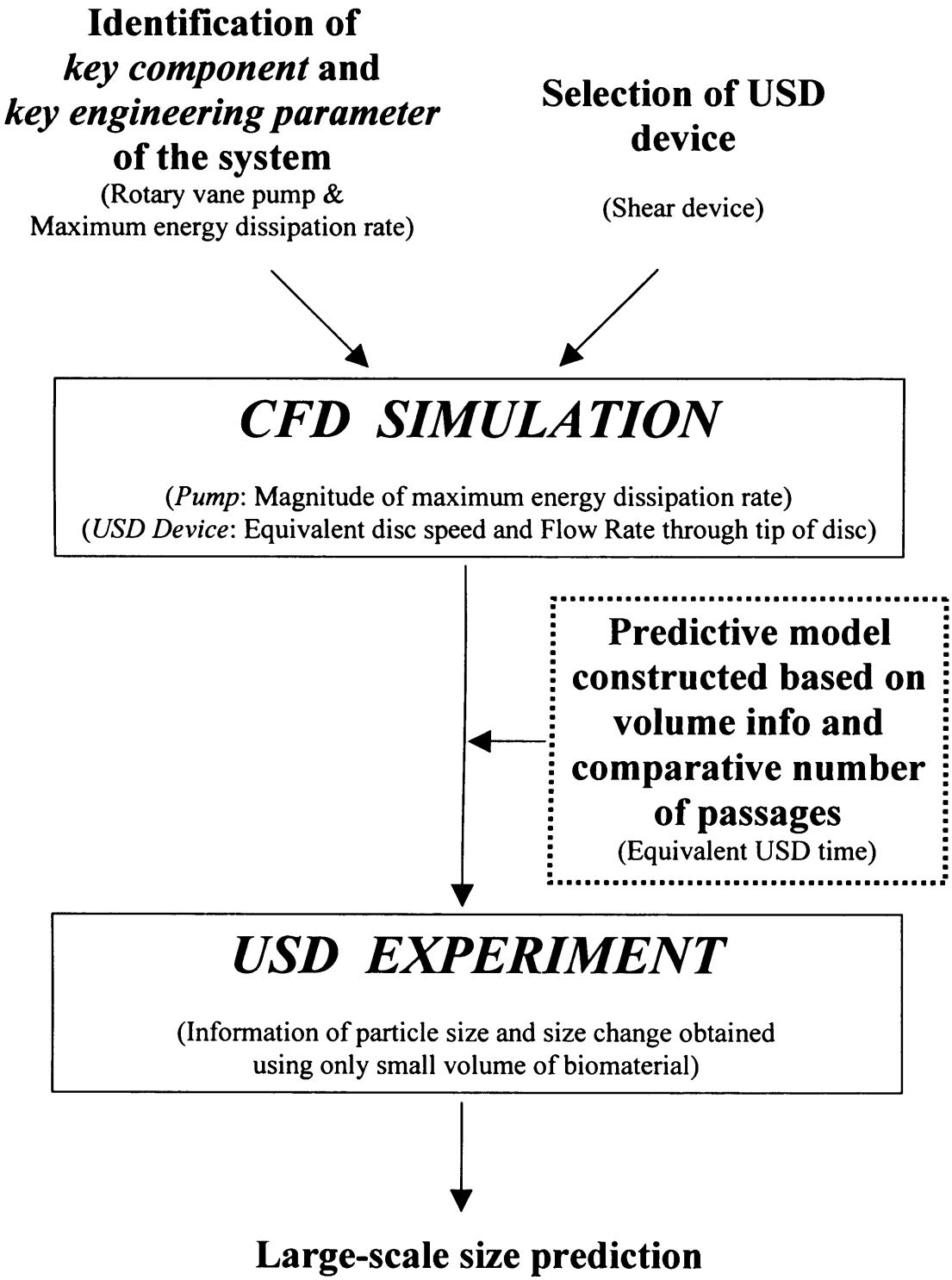

Figure 8.1 Flowchart summarising CFD-USD methodology employed for the prediction of particle size change in large-scale membrane filtration system.

Following these early stages, CFD simulations are carried out to assess the magnitude of maximum energy dissipation rate (EDR) in the pump and determine the equivalent disc speed that produces the same magnitude of maximum EDR in the USD device. Flow rate through the tip of the disc in the USD device is also calculated and used as an input into the predictive models (see **Chapter 5** for details). Predictive models together with CFD data and data (physical and operational) from both systems are then used to establish an equivalent USD time, a time required to run a USD device for the same damage to that of the large scale to be realised. Finally, USD experiments are performed based on this equivalent USD time. Size and size change in the USD device are used to link to those in the large-scale system allowing large-scale prediction to be made.

8.2 Discussions

This section will be presented in four parts: the applicability of CFD technique to assess the key engineering parameter in the pumping device; the suitability of using mammalian cell suspension and shear device in this study; an introduction of a concept of the 'direct use' of USD data which utilises an empirical calibration factor as a benchmark parameter to improve an accuracy of the existing predictive kinetic models; and finally the modification of predictive models based on the flow pattern, volume info and comparative number of passages.

8.2.1 CFD simulations

The computational fluid dynamics (CFD) technique has been shown to be a suitable tool to assess the intensity of the flow field in terms of the maximum EDR in full-scale process equipment as well as in the USD device. The technique pinpoints both location of the high energy dissipation zone and its intensity, i.e. maximum EDR. This is used as the key parameter to determine the damage of biomaterials. Its magnitude in turn is used to estimate the equivalent operating disc speeds in the USD device such that it generates the same magnitude of this flow parameter producing similar damage extents.

In this study two pump speeds, i.e. 600 and 1500 rpm, were used. The CFD estimated the maximum EDR generated at the tip of a moving vane to be 900 and 15000 W kg^{-1}, respectively. Using these magnitudes of maximum EDR, the technique has calculated equivalent disc speeds to be 5000 and 15000 rpm, respectively. These USD disc speeds should allow similar damage to be detected. A discussion of the results of this comparison will follow later.

However, experimentation over a range of disc speeds is suggested provided the cost and time of doing so is acceptable. This is to learn the general behaviour of the biomaterial of interest and to obtain some key relationship(s) between behaviour of biomaterial and operating conditions, e.g. the final particle size and maximum EDR (Equation 4.1, **Chapter 4**). It should also be noted that CFD can be applied to assess not only the maximum EDR but other operating variables such as temperature, pressure and etc. and a similar approach can be used to link USD and full scale operations. This suggests the importance of choosing the key parameters of the system being analysed. For instance, materials that are very sensitive to temperature may be efficiently assessed and tested with a temperature-based USD device. Similarly, the laminar flow field may be more suitable with the USD constructed from either two flat plates or cylindrical viscometer.

The drawbacks of using CFD include the considerable time in delivering the simulation, especially in the complex-geometry equipment. This can take several months for very detailed and complicated problems. The drawing of the computational domain, i.e. the flow problem itself, can take up to more than 50% of the total time required (Versteeg and Malalasekera, 2007). Moreover, it may also not be possible to simulate certain processes using the current system setup under a reasonable timeframe such as the movement of several droplets. Equally important, the cost of operating CFD is of great concern, which mainly involves the cost of personnel. Generally, the learning period is between 6-18 months depending on the entry level to a specific CFD code.

Due to the improvement of computer hardware and CFD software packages within the last decade, the CFD technique has become more accessible. The CFD software can now be run on personal computers and even on laptops. Thus, the cost of hardware has

been reduced from £7,500 to £2,500 over the last few years. Moreover, user-friendly interfaces and the number of flow models included in the package allow much faster implementation of the relevant problems. In this study, CFD can be applied to redesign the pumping device and the shear device in order to provide a more suitable environment for the future material or process of interest. For instance, CFD can be used to assess the maximum EDR or other flow variables in these devices equipped with different shapes and sizes of vanes and discs. As a result, CFD can be used as a powerful research and design tool. This is especially where it is not possible to measure directly within the equipment.

8.2.2 USD data

A suspension of mammalian cell aggregates provided the test material for this study. It was a useful material in that it allowed us to examine in detail both the break up of aggregates and the formation of debris; i.e. two issues of relevance to the bioprocess sector. Through a measurable and gradual change of its size after being subjected over a range of shear field and time period, the validity of the proposed principle of linking the two systems having totally different configurations based on equivalence of maximum EDR has been successfully assessed. More importantly by using frozen material we were able to ensure a reproducible start point for the studies and establish the relationship between USD and full scale operations.

However, it is recognised that the material being studied is not one commonly encountered in bioprocessing except where a freeze thaw stage has been deliberately used to introduce a holding stage. Further, more is needed to extend the research to a wider range of materials where different break up mechanisms may be of importance, e.g. loss of cell integrity, damage of polymers such as plasmid DNA, etc.

In this study the USD experiment together with the method detecting the size change of mammalian cell aggregates provides the understanding of the material characteristics in terms of size change and final size under certain processing parameters when being processed in the full-scale equipment. Two key parameters, i.e. the intensity of maximum EDR of the system and time of exposure, influence the size changes. As might be expected it was found that the higher maximum EDR and the

longer the time of exposure, the smaller the particle size and thus more fines produced and the more aggregates break up. Again as might be expected the rate of size change reduces with time and the size eventually reaches an equilibrium. Quantifying the relationships governing these size changes is crucial in the design of key stages in bioprocesses, e.g. pumps prior to centrifuges or filters.

To summarise, it is recommended that the effect of EDR and time is studied in the USD device over a wide range of conditions – this gives the properties of the material in terms of effect of shear. These results can then be used to predict what may happen in full-scale equipment once the EDR and residence time are determined.

The shear device, which has been used as a USD device, has several advantages over other USD devices. These include ease of use and sample handling, self-containment, adjustable speed (thus adjustable maximum EDR), ease of redesign and fabrication, cooling capability and small-volume consumption of samples. However, the USD device also poses limitations, especially on an early data collection. Currently, the device allows the collection of data at the earliest at 15 s. Data collection earlier than 15 s is not recommended for the current design due to the limited capability of its motor and power pack. Though very brief, the motor still takes a finite time to reach a desired disc speed and to stop, so it is difficult to ensure reproducible operations for shorter times.

8.2.3 Size predictions

In this section the concept of the 'direct use' of the experimental data from the USD device is introduced. According to this 'direct use' concept, the processing times used in both USD and large-scale experiments were compared and the USD time was adjusted (scaled up) such that the particle sizes (D_{10}, D_{50} and D_{90}) being observed in the USD experiment were closely matched with those observed in the large scale. This 'direct use' of the experimental data from the USD device allowed an 'adjusted' USD time to be determined and 'empirical calibration factor' to be calculated. Size predictions corresponding to a new 'adjusted' USD time based on the direct use concept were then verified (Figure 8.2) and compared with those obtained from existing predictive models (Figure 6.11, **Chapter 6**). The empirical calibration factor

derived from this concept was later used as a benchmark parameter upon which the existing predictive models can be improved (see section 8.2.4 for details).

Size-related phenomena in bioprocessing

From the viewpoint of bioprocessing of particulate materials we can, for convenience, separate the analysis into:

(i) loss of large-sized materials, for example where we want to preserve structures such as aggregates of cells, e.g. for use in fluidized reactors;

(ii) creation of small-sized materials, for example where we are concerned at carry over of 'biological fines' in the supernatant from a centrifuge or increased resistance during filtration for solids recovery/removal and again transmission of 'biological fines.' Such fines might, for example, cause blockage of expensive packed columns.

The above two size-related phenomena can be characterised by D_{90} and D_{10}, respectively, and from the viewpoint of prediction of the effects of bioprocessing it is useful if we consider short-term and long-term effects for these size groups. For the former this may be indicative of the results of passage through a pump or centrifuge feed zone; a combination of which may apply during feed to a centrifuge. For the latter this will be characteristic of operation of filters and membrane units in recycle mode.

8.2.3.1 'Direct use' concept verification and empirical calibration factor

According to above size-related criteria, the concept of the 'direct use' of USD data was verified (Figure 8.2, D_{50} was also included for completeness). The figure compares the particle size change with 'adjusted' time for the USD device and 'real' time for the large-scale pump system. Empirical calibration factors of 160 for low-speed studies and 500 for high-speed studies have been calculated and applied to allow this comparison (attempts will be made later to compute the calibration factor using fluid dynamics and volume information for USD and large scale). Note that the calculations of the empirical calibration factors were based on the Equation 8.1:

$$Real\ USD\ time \times Empirical\ calibration\ factor = 'Adjusted'\ USD\ time \qquad \textbf{Eq. 8.1}$$

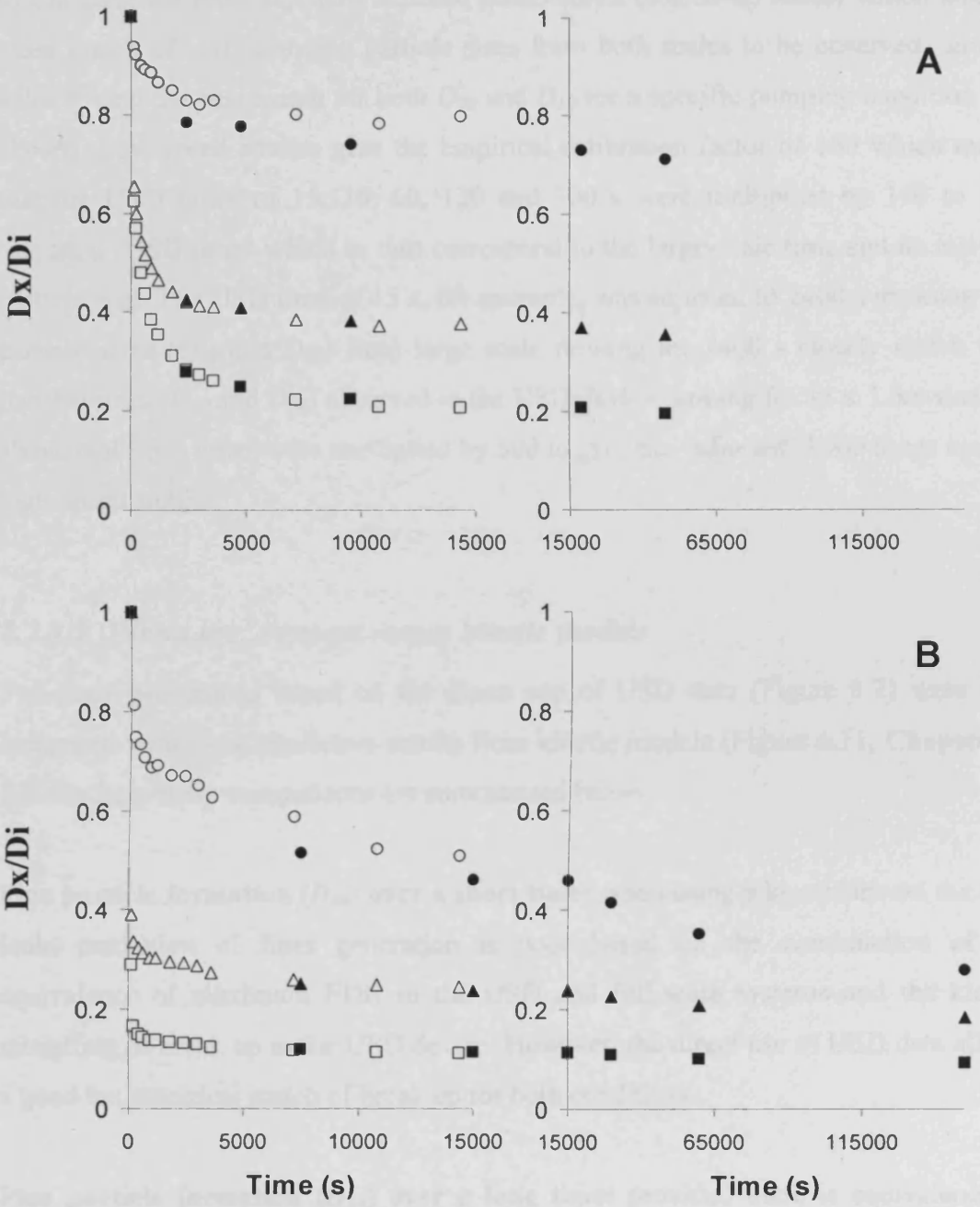

Figure 8.2 Full-scale predictions (closed points) of particle sizes in terms of derived diameters (D_{10}, D_{50}, D_{90}) based on the direct use of the experimental data from the USD device compared with experimental data from the large-scale pump system (open points). The x-axis represents the real time for the full-scale pump system and 'adjusted' time for the USD device. The adjusted times for the USD device matching the pump speeds of 600 rpm **(A)** and 1500 rpm **(B)** were obtained by multiplying the real USD times using empirical calibration factors of 160 and 500 respectively. The data from both systems were then plotted on the same x-axis time scale. Note that the scales of the left-handed graph and right-graph are different.

Different values of empirical calibration factors were applied (trialled) in Equation 8.1 to calculate the most suitable 'adjusted' USD times (scaled-up times) which allow a close match of corresponding particle sizes from both scales to be observed, and the value giving the best match for both D_{90} and D_{10} for a specific pumping condition was chosen. Low-speed studies give the empirical calibration factor of 160 which means that the USD times of 15, 30, 60, 120 and 300 s were multiplied by 160 to give 'adjusted' USD times which in turn correspond to the large-scale time and its relevant particle size. The USD time of 15 s, for example, was adjusted to 2400 s meaning that particle sizes (D_{90} and D_{10}) from large scale running for 2400 s closely match with particle sizes (D_{90} and D_{10}) observed in the USD device running for 15 s. Likewise, the above real USD times were multiplied by 500 to give the 'adjusted' USD times used in high-speed studies.

8.2.3.2 'Direct use' concept versus kinetic models

Full-scale predictions based on the direct use of USD data (Figure 8.2) were then compared with those predictive results from kinetic models (Figure 6.11, **Chapter 6**). Results from these comparisons are summarised below:

Fine particle formation (D_{10}) over a short time: when using a kinetic model the full-scale prediction of fines generation is poor based on the combination of the equivalence of maximum EDR in the USD and full-scale systems and the kinetic modelling of break up in the USD device. However, the direct use of USD data allows a good but empirical match of break up for both conditions.

Fine particle formation (D_{10}) over a long time: provided there is equivalence of maximum EDR in the USD and full-scale systems, there is a good prediction of the particle size in the full-scale equipment from both approaches.

Large particle break up (D_{90}) over a short time: here the prediction is poor when based on kinetic information derived from the USD device. However, the use of the actual experimental data from the USD device allows a good match of events at the full scale.

Large particle break up (D_{90}) over a long time: provided there is equivalence of maximum EDR in the USD and full-scale systems, there is a good prediction of the particle size from both approaches.

Collectively, the methodology based on the direct use of USD data allows a good match of events for both small-sized (D_{10}) and large-sized (D_{90}) materials over short and long processing time in the large scale. Therefore, its derived calibration factor may be used as a benchmark parameter upon which the kinetic models can be improved. This is described in the next section.

8.2.4 Modification of predictive models

While we have been successful in predicting the final size which will result from a large number of passages from the pump head, it is also important to be able to predict how the size changes with lower numbers of passages. This section aims to improve an existing predictive model which is based on kinetics (see Equation 5.23, **Chapter 5**), such that it could provide a better prediction of size change in the large-scale system, especially over a short processing time. The analysis based on analogy of systems of difference scales in terms of operating parameters (flow rate, volume info and processing time) is firstly presented. Differences in terms of volume of the high-shear zones and flow pattern of the two systems are then investigated and the model is further modified. The results from each developmental stage of a new model are shown using graphs, which contain large-scale pump data, along with a specific value of empirical calibration factor, which in turn is used to indicate the deviation of a specific model from the one giving the closest match of particle sizes in systems of different scales (Figure 8.2).

8.2.4.1 Analogy of systems of different scales

Based on the key finding from the kinetic derivation of change of aggregate size following the exposure to the high-shear zone (see Equation 5.23, **Chapter 5**), the relationship between flow rate, volume info and processing time of the two systems was analysed. We first consider the flow of liquid in the USD system and visualise it to be a small-scale pump system having total volume of 20 mL (Figure 8.3A). Using the

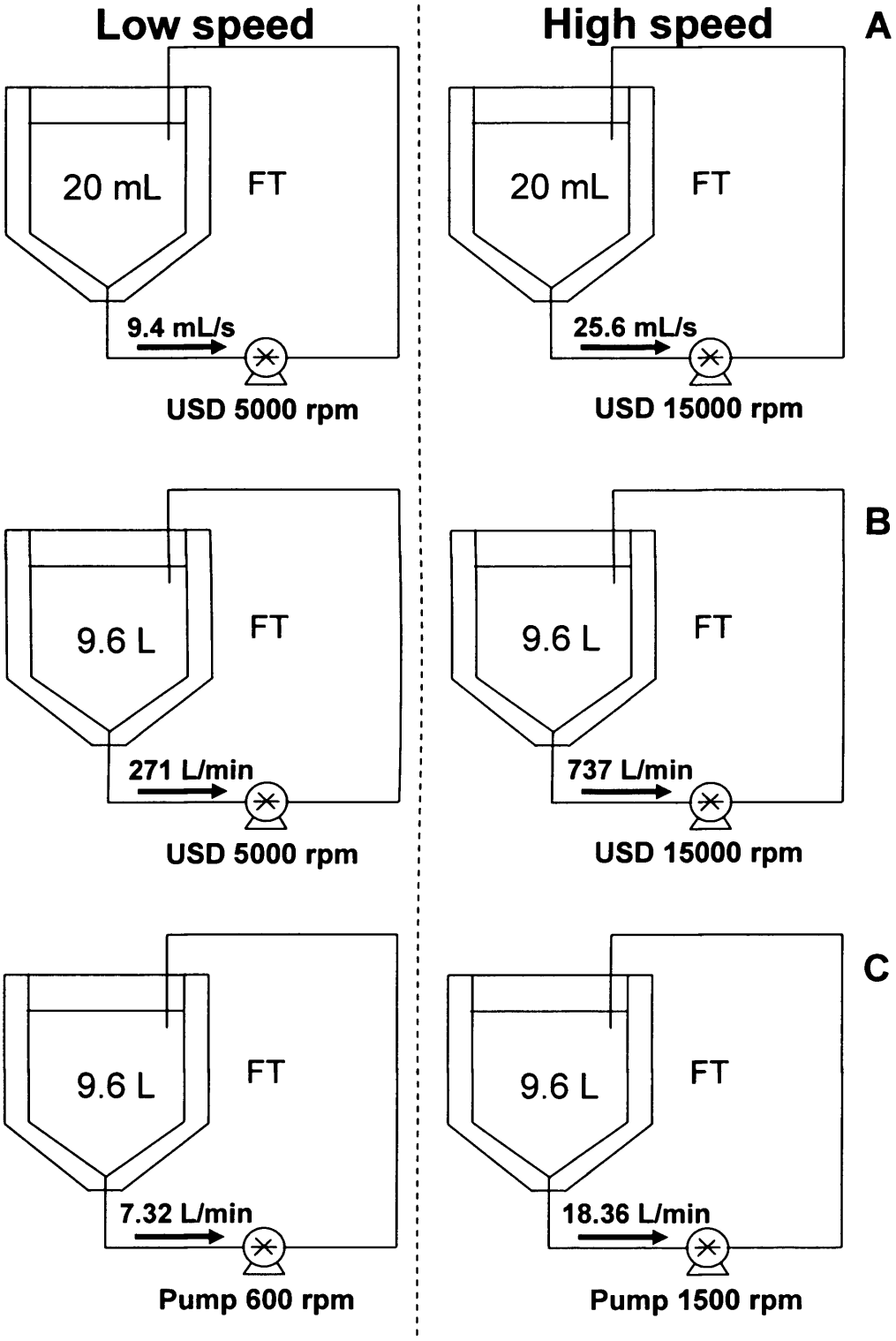

Figure 8.3 The USD system as a small-scale pump system. The USD device is visualised as a small-scale pump system with the pump representing the high-shear zone generated at the tip of the disc **(A)**. Scaling up from 20 mL to 9.6 L, it acts like a large-scale pump system **(B)**. This large-scale pump system is then compared with the actual large-scale rig **(C)**.

same liquid flow rate delivered from the tip of the rotating disc, the pump in this small-scale pump system is able to deliver the flow rate of 9.4 and 25.6 mL s^{-1} for low-speed and high- speed conditions, respectively. If we use for scale up the ratio of the total volume of the large-scale pump system (9.6 L) and the total volume of the USD device (20 mL), then the corresponding flow rates through the pump in this system would become 271 and 737 L min^{-1}, i.e. scale up by 480 (Figure 8.3B). We then compare this scaled-up system with the actual large-scale pump system that has the same total volume and the liquid delivery capability of 7.32 and 18.36 L min^{-1} for low-speed and high-speed conditions, respectively (Figure 8.3C). If particle breakage is assumed to occur for every pass through the pump in these systems, then the calibration factors should be 37 and 40 for the USD device when mimicking the low-speed and the high-speed pumping, respectively. These are considerably lower than the values of 160 and 500 observed experimentally (Figure 8.2) and do not allow good predictions to be made (Figure 8.4).

8.2.4.2 Volumes of high-shear zones in the system

One explanation for this difference may arise from the volumes of the high-shear zones for the two systems. This leads us to consider the extent of exposure of material to the high-shear region of the pump and explore if the equivalent extent of exposure in the USD device leads to the same level of break up. The extent of exposure in its simplest form may be the product of overall process time and the fraction of volume of the USD device or the pump and tank and pipework which is considered to be at high shear, i.e. sufficient shear to break the particles. This fraction of volume may be gained from CFD analysis. If we consider an energy dissipation rate of 500 W kg^{-1} to be representative of a critical level above which breakage occurs then we have Table 8.1.

This evidently does not match with the calibration factors obtained experimentally. A more detailed analysis of fluid exposure to the high-shear region is needed for both systems and it may be that time of exposure and the nature of hydrodynamic stress are also crucial.

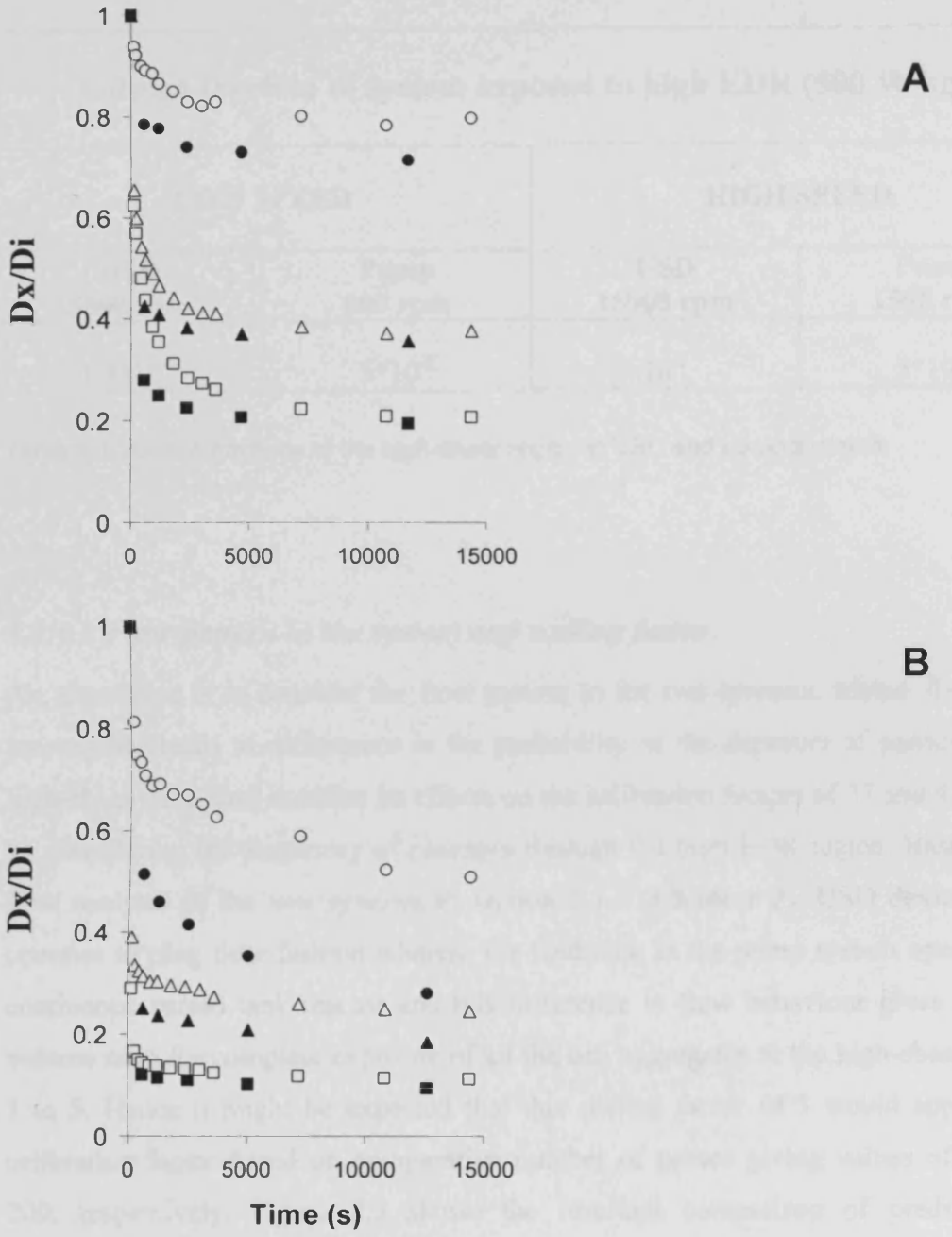

Figure 8.4 Full-scale predictions (closed points) of particle sizes (D_{10}, D_{50}, D_{90}) based on the use of USD data by means of scaled-up flow rate and total volume alone. These results were compared with experimental data from the large-scale pump system (open points). The x-axis represents the real time for the full-scale pump system and 'adjusted' time for the USD device. The adjusted times for the USD device matching the pump speeds of 600 rpm **(A)** and 1500 rpm **(B)** were obtained by multiplying the real USD times using the theoretical calibration factors of 37 and 40 respectively. The data from both systems were then plotted on the same x-axis time scale.

Volume fraction of system exposed to high EDR (500 W kg^{-1})			
LOW SPEED		**HIGH SPEED**	
USD 5000 rpm	**Pump 600 rpm**	**USD 15000 rpm**	**Pump 1500 rpm**
$1.3*10^{-2}$	$5*10^{-8}$	10^{-1}	$5*10^{-6}$

Table 8.1 Volume fractions of the high-shear region in USD and pump systems.

8.2.4.3 Flow pattern in the system and scaling factor

An alternative is to consider the flow pattern in the two systems, whose discrepancy presumably leads to differences in the probability of the exposure of particles to the high-shear zone, and examine its effects on the calibration factors of 37 and 40 derived by considering the frequency of passages through the high EDR region. Based on the flow analysis of the two systems in section 2.4.3 (**Chapter 2**), USD device greatly operates in plug flow fashion whereas the feed tank in the pump system operates like continuous stirred tank reactor and this difference in flow behaviour gives a reactor volume ratio for complete exposure of all the cell aggregates to the high-shear zone of 1 to 5. Hence it might be expected that this scaling factor of 5 would apply to the calibration factor based on comparative number of passes giving values of 185 and 200, respectively. Figure 8.5 shows the resultant comparison of predicted cell aggregate size change from the USD device results based on these values with those obtained in the large-scale pump system. The predicted results for all particle sizes are good for both low-speed and high-speed conditions except for those fines (D_{10}) under high-speed conditions. There may be other possible causes for this discrepancy which need to be addressed and analysed in the future work.

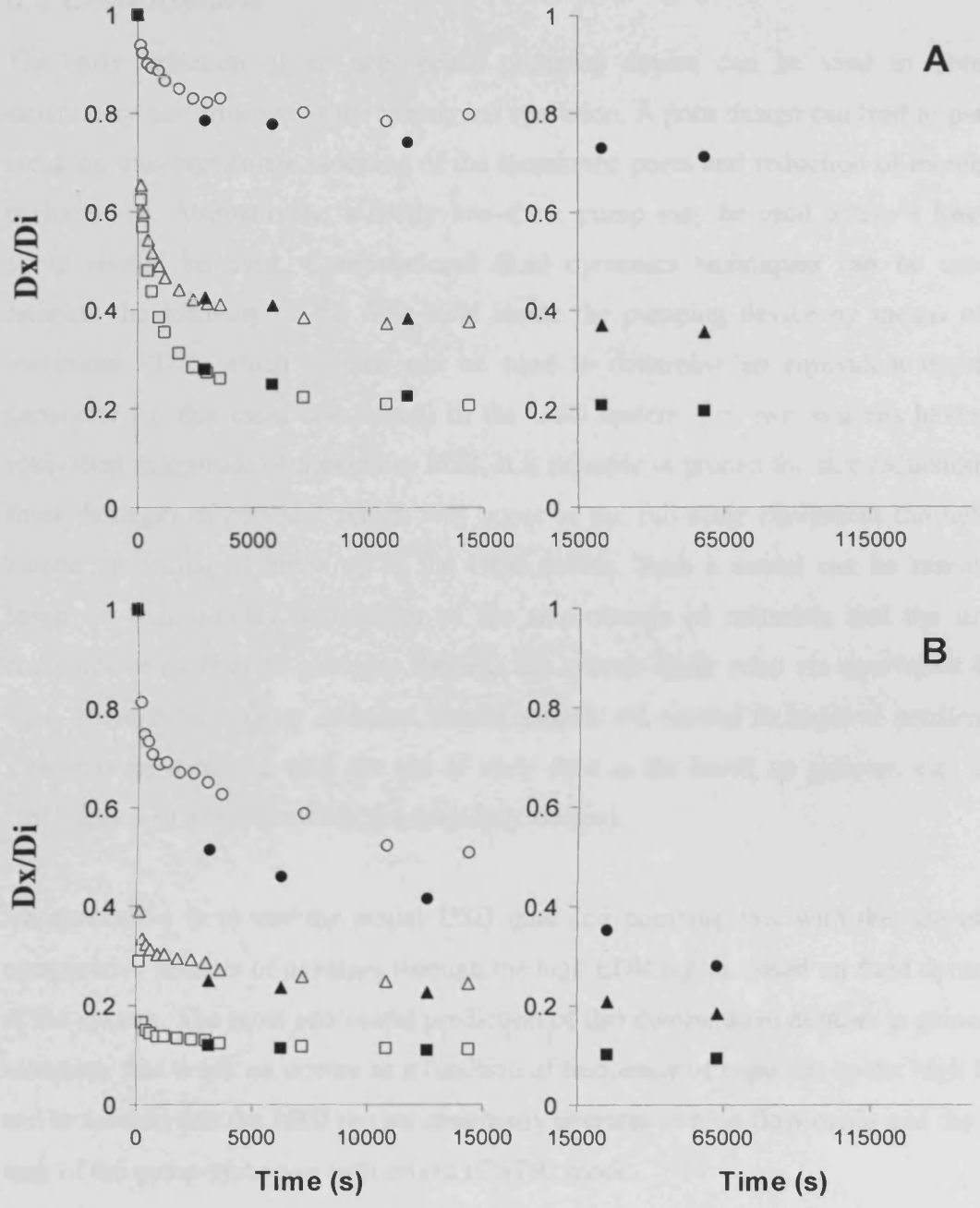

Figure 8.5 Full-scale predictions (closed points) of particle sizes (D_{10}, D_{50}, D_{90}) based on the new calibration factors, i.e. 185 and 200. These values were obtained from the combined use of the experimental data from the USD device and time of exposure through number of passes based on volume information and flow pattern. Predicted data was then compared with experimental data from the large-scale pump system (open points). The x-axis represents the real time for the full-scale pump system and 'adjusted' time for the USD device. The adjusted times for the USD device matching the pump speeds of 600 rpm **(A)** and 1500 rpm **(B)** were obtained by multiplying the real USD times using these new calibration factors. The data from both systems were then plotted on the same x-axis time scale. Note that the scales of the left-handed graph and right-graph are different.

8.3 Conclusions

The early selection of an appropriate pumping device can be vital to obtain a satisfactory performance of the membrane operation. A poor design can lead to particle break up thus particulate blocking of the membrane pores and reduction of membrane performance. Alternatively, a costly low-shear pump may be used where a low-cost pump should be used. Computational fluid dynamics techniques can be used to estimate the intensity of the flow field inside the pumping device by means of the maximum EDR, which in turn can be used to determine an equivalent operating parameter (in this case, disc speed) in the USD system. For two systems having an equivalent magnitude of maximum EDR, it is possible to predict the size reduction (i.e. shear damage) of particles which will occur in the full-scale equipment through the kinetic modelling of break up in the USD device. Such a model can be essentially based on a first-order description of the size change of materials and the use of comparative number of passages through the intense shear zone via equivalent USD time. Nevertheless, more complex kinetic models are needed to improve predictions. This may be achieved with the aid of early data in the break up process, e.g. using USD device of alternative designs (capillary device).

An alternative is to use the actual USD data and combine this with the use of the comparative number of passages through the high EDR region based on fluid dynamics of the system. The most successful prediction of this comparative number is gained by assuming that break up occurs as a function of frequency of exposure to the high EDR and to assume that the USD device essentially operates in plug flow mode and the feed tank of the pump system in well mixed (CSTR) mode.

As the hydrodynamic shear generated during a bioprocess plays an important part in determining damage to biological materials, its intensity and effect should be studied long before the actual process is developed. Based on this thesis study three vital steps are required: CFD, USD and prediction (Figure 8.1). In the CFD step, the intensity of maximum EDR (or other flow variables) of the process system is determined, and this in turn is used to estimate the operating parameters in the USD system. The biomaterial of interest is then processed in the USD system under different operating conditions (in this case, different disc speeds giving various EDR values and for different time

periods). Finally, key characteristics obtained from the USD experiments are applied to the predictive models suggesting the effect of maximum EDR or other flow variables on the change in the aggregate size.

The following summarises steps involved in the large-scale predictions of size change in the pump system:

1. Evaluate maximum EDR in the system, i.e. pump.
2. Run the USD device at same maximum EDR as large scale.
3. Characterise the USD device by its volume and its pumping rate.
4. Increase the pumping rate by the ratio of volume of full-scale operation and USD device.
5. Time in large scale equals time in USD device multiplied by pumping rate USD and divided by pumping rate large scale.
6. Each USD pumping rate should be multiplied by a 'scaling factor,' which is dependent on the flow pattern of both systems. For the systems studied, this was taken to be 5.

These steps can be mathematically rewritten:

$$t_p = t_s \cdot \left(\frac{V_p}{V_s}\right) \cdot \left(\frac{Q_s}{Q_p}\right) \cdot 5 \qquad \textbf{Eq. 8.2}$$

and can be used to answer the central challenge posed in the membrane filtration process, i.e. the prediction of material breakage or size change with time (Figure 8.6).

Predictions based on CFD technique, however, is not applicable for all existing equipment. Alternative matching method or technology must be sourced for certain equipment or part of it, e.g. the discharge zone of the centrifuge. In such a case, the discharge of the centrifuge represents the configurationally-complex system. Moreover, the flow of cell paste through air and the final impaction onto the wall of the unpredictable-shaped droplets makes such damage prediction based on CFD to be very resource-consuming in terms of time and computer power and possibly beyond the capacity of much of the CFD software currently available.

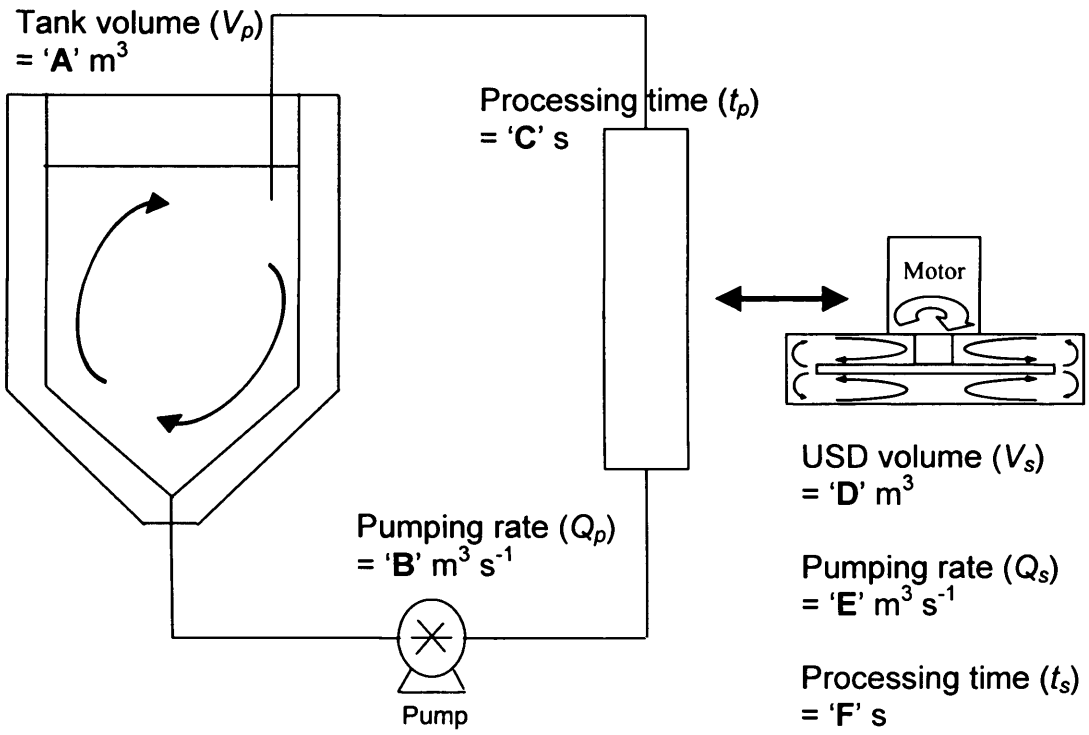

Q: How one could predict the breakage in this rig with time?

A: By using Equation 8.2: $t_p = t_s \cdot (V_p/V_s) \cdot (Q_s/Q_p) \cdot 5$

In this case, this becomes:
$t_p = F \cdot (A/D) \cdot (E/B) \cdot 5$ or
$t_s = C \cdot (D/A) \cdot (B/E) \cdot (1/5)$

Figure 8.6 How one could predict the breakage in this rig with time? This central challenge posed in the membrane filtration process can be answered using the given mathematical relationship, which was derived from the CFD-USD methodology described in this thesis study. Following the USD experiments, the large-scale prediction (particle size at t_p) can be achieved by using the above relationship between flow rates (Q_s and Q_p), USD processing time (t_s) and volume info (V_s and V_p). Likewise, if the processing time in the large scale is fixed, then USD processing time can be calculated and the USD experiment performed.

CHAPTER 9 FUTURE WORKS

The achievement and findings from this study suggest certain areas to be explored in greater detail laying the basics for future research. This chapter aims to propose the future works whose key objectives are to improve the performance of the current USD design and reduce the volume of expensive materials being tested and to apply this technology to differently configured systems used in the biotechnology industries. Business opportunities arisen in terms of knowledge transfer and technology exploitation are also presented.

9.1 Continuation of current study

The models developed to date, i.e. for the kinetics of cell aggregate break up and the translation of USD data to predict cell aggregate break up in large-scale system, need to be further refined. A wider range of pump types, flow rates and bioprocess materials would be invaluable, although it has to be recognised that the CFD analysis for each pump type will be very time consuming.

9.2 Design of future USD devices

The current design of shear device is capable of providing the information regarding the size of materials after being subjected to maximum EDR generated from the disc rotating between ~3000 to 15000 rpm. Due to the limitation of the power pack, which controls the electric current to the shear device, and the motor itself, the lower limit has been observed to be ~3000 rpm under which the rotational speed becomes fluctuated and unreliable. The problem associated with the current design also includes the settlement of suspensions containing solids at very low disc speed (<1000 rpm). This phenomenon has been observed when an opaque bottom is replaced by a transparent one and results in a heterogeneous condition of the sample within the device, which in turn gives unreliable data if material characteristic at a very low speed is to be studied.

Consequently, a few modifications need to be made to the USD system in order to broaden a range of the mimicked condition materials are subjected to in real processes.

Problems regarding capability in delivering low-speed rotation of the shear device can be overcome without any difficulties by replacing both power pack and motor with a newer model. Solutions to the design of the shear device itself may be achieved using the following modified proposed designs, especially those equipped with the impeller (Figure 9.1):

1. Prototype shear device: this is the prototype being used to mimic a few bioprocess equipment at the moment. The challenge here is to allow reliable operation for very short time process (< 1 s) to pick up early stages of break up.

2. Microwell shear device: a more scale-down version of the prototype shear device, which may be used where the biomaterial is in short supply or is very costly.

3. Capillary: a shear-generating device that generates uniform shear. This is proposed for dilute and small-sized samples and where very short times of exposure are required for early break up profiles.

4. Instron: a device that can be used to assess the combined effects of shear and impact together or to assess each parameter separately.

5. Impeller (in microwell): this is used to match low shear generated during formulation while the impeller propels sediments upwards.

6. Viscometer-shaped device: a shear-generating device that generates uniform shear for all materials inside. This is designed for higher-concentration and/or larger-sized (but non-precipitated) materials (compared to No.3).

7. Viscometer-shaped device with impeller at the bottom: a shear-generating device that generate uniform shear for all materials inside. This is designed for high-concentration, large-sized and *precipitated* materials.

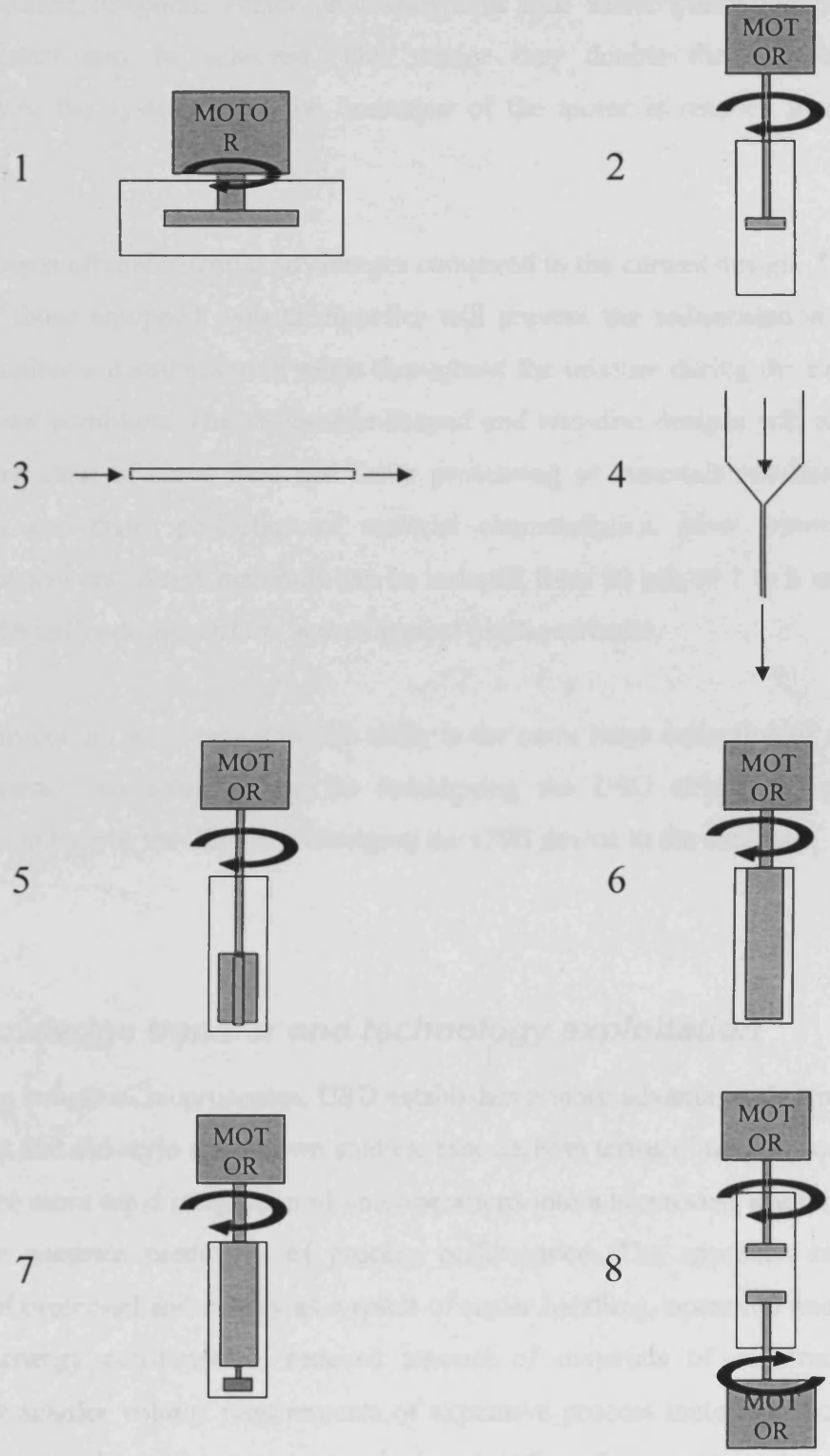

Figure 9.1 Proposed designs of the USD device for future work.

8. Two-disc device: the higher shear field may be generated with two discs operating in an opposite direction. Faster processing and thus faster prediction of material characteristics may be achieved. This device may double the maximum shear generated in the system when the limitation of the motor is reached in a one-disc prototype.

These designs offer substantial advantages compared to the current design. The stirring action of those equipped with an impeller will prevent the sedimentation of solids; promote uniform distribution of solids throughout the mixture during the experiments at low shear condition. The viscometer-shaped and two-disc designs will allow more even distribution of shear field and faster processing of materials resulting in more consistent and faster prediction of material characteristics. Most importantly the significant amount of test materials can be reduced from 20 mL to 1 to 3 mL or even less using smaller designs of the size of typical plastic cuvettes.

Another important issue raised in this study is the early stage collection of data in the USD system. The solution may be redesigning the USD device to include the recirculation loop in the design or changing the USD device to the capillary.

9.3 Knowledge transfer and technology exploitation

Regarding industrial bioprocesses, USD establishes a more advantageous strategy than pilot-plant and old-style scale-down studies, especially in terms of time-to-market, as it enables the more rapid integration of unit operations into a bioprocess leading to earlier and more accurate prediction of process performance. The approach saves time, number of personnel and money as a result of easier handling, operation and cleaning, reduced energy consumption, reduced amount of materials of construction, and especially smaller volume requirements of expensive process materials. Collectively, the USD approach enables very economical exploration of a greater number of process options compared to pilot-scale and old-style scale-down studies provided the same amount of time is used. As a result, the technology should be transferred to the biotechnology industries as well as academics.

USD could be commercialised to the industry by means of consultancy services as well as licensing verified USD techniques linked to specific unit operations. Predictions of what is happening in the process equipment can be done via USD approach facilitating validation of a manufacturing process, implementation of changes to the process, troubleshooting, process synthesis, process improvement and optimisation based on large-scale experiments, assessment of process sensitivity to changes in feed stocks, and even designing a new unit operation. Instead of operating large-scale units, which may have volumes up to 10000 L (Ma et al., 2002), one could run a USD mimic having volume of only 20 mL or less to obtain the same results saving process materials more than 10^5 times.

With recent innovations, the continued expansion of approved indications for existing products and the gradual uptake of biotech products outside the U.S., the global biotechnology market still have potential to grow (IMS-Health, 2008). In 2007 it was reported that the global prescription sales of biotech drugs increased 12.5% to more than $75 billion, i.e. a nearly double the rate of the global pharmaceutical market which increased 6.4% (IMS-Health, 2008). However, due to funding pressures and competition from biosimilars, its future growth is expected to be more moderate compared to those in the past five years until 2012 (Williams et al., 2008, IMS-Health, 2008). On the one hand, the lack of funding may slow down the market growth. On the other hand, this may become the driving force for an alternative approach for process design and development to which the USD technology may offer a solution. All these together with the fact that the process material costs can constitute up to 80% of the total operating cost (Harrison et al., 2003) especially manufacture of therapeutic monoclonal antibodies, whose trend is increasing (Business-Insights, 2005), the future for USD commercialisation to save costs of raw materials utilised as a result of these activities looks promising. Moreover, since R&D costs of biotechnology equipment may correspond to 6.8% of its market values (Sartorius, 2007) which are subjected to grow following the increasing growth of global biotechnology market, the environment for commercialising USD technologies for designing new biotechnology equipment becomes more favourable. However, there are some risks involved. Sometimes there may be too many factors affecting the performance of unit operations, or important engineering parameters of the system cannot be clearly determined. In such cases, it may not be possible to employ USD technology to make predictions on their

performances. Moreover, it may take a long time to identify engineering parameters mentioned, especially when CFD technique is employed, lengthening the time-to-market.

As the global biotechnology sector is still expected to grow and remain one of the most robust segments of the marketplace with a continued strong flow of innovative products to the market (IMS-Health, 2008) and USD technology would lay an more economic strategy for process design and prediction, the USD technology has potential to flourish in the biotechnology industries. Moreover, a particular unit operation which has already had USD technology linked can be patented. As an investor, I need to know how and when I would get my money back. To do so, I would firstly urge that the company is to be set up alone because there will be issues of IPR when the Department or University is involved. I would also ensure that recommended milestones are met. At later stages, the company may be merged with a larger company in order to get the money invested back.

REFERENCES

ABU-REESH, I. & KARGI, F. (1989) Biological Responses of Hybridoma Cells to Defined Hydrodynamic Shear Stress. *Journal of Biotechnology,* 9, 167-178.

AEA-TECHNOLOGY (1999) CFX-4 Documentation. Oxfordshire, UK.

AFSCHAR, A. S., SCHALLER, K. & SCHÜGERL, K. (1986) Continuous Production of Acetone and Butanol with Shear-Activated *Clostridium acetobutylicum. Applied Microbiology and Biotechnology,* 23, 315-321.

AHMAD, A. L., LAU, K. K., BAKAR, M. Z. A. & SHUKOR, S. R. A. (2005) Integrated CFD Simulation of Concentration Polarization in Narrow Membrane Channel. *Computers & Chemical Engineering,* 29, 2087-2095.

AIBA, S., KITAI, S. & HEIMA, H. (1964) Determination of Equivalent Size of Microbial Cells from Their Velocities in Hindered Settling. *Journal of General and Applied Microbiology,* 243-256.

AL-AKOUM, O., DING, L. H. & JAFFRIN, M. Y. (2002a) Microfiltration and Ultrafiltration of UHT Skim Milk with a Vibrating Membrane Module. *Separation and Purification Technology,* 28, 219-234.

AL-AKOUM, O., MERCIER-BONIN, M., DING, L., FONADE, C., APTEL, P. & JAFFRIN, M. (2002b) Comparison of Three Different Systems Used for Flux Enhancement: Application to Crossflow Filtration of Yeast Suspensions. *Desalination,* 147, 31-36.

AL-AKOUM, O., RICHFIELD, D., JAFFRIN, M. Y., DING, L. H. & SWART, P. (2006) Recovery of Trypsin Inhibitor and Soy Milk Protein Concentration by Dynamic Filtration. *Journal of Membrane Science,* 279, 291-300.

AL-RUBEAI, M., SINGH, R. P., GOLDMAN, M. H. & EMERY, A. N. (1995) Death Mechanisms of Animal Cells in Conditions of Intensive Agitation. *Biotechnology and Bioengineering,* 45, 463-472.

ALOI, L. E. & CHERRY, R. S. (1996) Cellular Response to Agitation Characterized by Energy Dissipation at the Impeller Tip. *Chemical Engineering Science,* 51, 1523-1529.

AMBLER, C. M. (1959) The Theory of Scaling up Laboratory Data for the Sedimentation Type Centrifuge. *Journal of Biochemical and Microbiological Technology and Engineering,* 1, 185-205.

ARNAUD, J. P., LACROIX, C., FOUSSEREAU, C. & CHOPLIN, L. (1993) Shear Stress Effects on Growth and Activity of *Lactobacillus delbrueckii* subsp. *Bulgaricus*. *Journal of Biotechnology,* 29, 157-175.

AUGENSTEIN, D. C., SINSKEY, A. J. & WANG, D. I. C. (1971) Effect of Shear on the Death of Two Strains of Mammalian Tissue Cells. *Biotechnology and Bioengineering,* 13, 409-418.

AUSTIN, L. G. (2002) A Treatment of Impact Breakage of Particles. *Powder Technology,* 126, 85-90.

AXELSSON, H. A. C. (1985) *Comprehensive biotechnology,* New York, USA, Pergamon Press.

BAILEY, F. J., WARF, R. T. & MAIGETTER, R. Z. (1990) Harvesting Recombinant Microbial Cells Using Crossflow Filtration. *Enzyme and Microbial Technology,* 12, 647-652.

BAKER, R. W., CUSSLER, E. L., EYKAMP, W., KOROS, W. J., RILEY, R. L. & STRATHMANN, H. (1991) *Membrane Separation Systems: Recent Developments and Future Directions,* New Jersey, USA, Noyes Data Corporation.

BARBOSA, M. J., ALBRECHT, M. & WIJFFELS, R. H. (2003) Hydrodynamic Stress and Lethal Events in Sparged Microalgae Cultures. *Biotechnology and Bioengineering,* 83, 112-120.

BATES, R., FONDY, P. & CORPSTEIN, R. (1963) An Examination of Some Geometrical Parameters of Impeller Power. *Industrial and Engineering Chemistry Product Research and Development,* 310-314.

BENTHAM, A. C., BONNERJEA, J., ORSBORN, C. B., WARD, P. N. & HOARE, M. (1990) The Separation of Affinity Flocculated Yeast Cell Debris Using a Pilot-Plant Scroll Decanter Centrifuge. *Biotechnology and Bioengineering,* 36, 397-401.

BISSEN, M. & FRIMMEL, F. H. (2003) Arsenic - a Review. Part II: Oxidation of Arsenic and its Removal in Water Treatment. *Acta hydrochimica et hydrobiologica,* 31, 97-107.

BJERKHOLT, J. T., CUMBY, T. R. & SCOTFORD, I. M. (2005) Pipeline Design Procedures for Cattle and Pig Slurries using a Large-scale Pipeline Apparatus. *Biosystems Engineering,* 91, 201-217.

BLUESTEIN, M. & MOCKROS, L. (1969) Hemolytic Effects of Energy Dissipation in Flowing Blood. *Medical and Biological Engineering and Computing,* 7, 1-16.

BORN, C., ZHANG, Z., AL-RUBEAI, M. & THOMAS, C. R. (1992) Estimation of Disruption of Animal Cells by Laminar Shear Stress. *Biotechnology and Bioengineering,* 40, 1004-1010.

BOULDING, N., YIM, S. S. S., KESHAVARZ-MOORE, E., AYAZI SHAMLOU, P. & BERRY, M. (2002) Ultra Scaledown to Predict Filtering Centrifugation of Secreted Antibody Fragments from Fungal Broth. *Biotechnology and Bioengineering,* 79, 381-388.

BOUZERAR, R., JAFFRIN, M. Y., LEFEVRE, A. & PAULLIER, P. (2000) Concentration of Ferric Hydroxide Suspensions in Saline Medium by Dynamic Cross-Flow Filtration. *Journal of Membrane Science,* 165, 111-123.

BOUZERAR, R., PAULLIER, P. & JAFFRIN, M. Y. (2003) Concentration of Mineral Suspensions and Industrial Effluents Using a Rotating Disk Dynamic Filtration Module. *Desalination,* 158, 79-85.

BOYCHYN, M., DOYLE, W., BULMER, M., MORE, J. & HOARE, M. (2000) Laboratory Scaledown of Protein Purification Processes Involving Fractional Precipitation and Centrifugal Recovery. *Biotechnology and Bioengineering,* 69, 1-10.

BOYCHYN, M., YIM, S. S. S., AYAZI SHAMLOU, P., BULMER, M., MORE, J. & HOARE, M. (2001) Characterization of Flow Intensity in Continuous Centrifuges for the Development of Laboratory Mimics. *Chemical Engineering Science,* 56, 4759-4770.

BOYCHYN, M., YIM, S. S. S., BULMER, M., MORE, J., BRACEWELL, D. G. & HOARE, M. (2004) Performance Prediction of Industrial Centrifuges Using Scale-Down Models. *Bioprocess and Biosystems Engineering,* 26, 385-391.

BRINDLEY ALÍAS, C., GARCÍA-MALEA LÓPEZ, M. C., ACIÉN FERNÁNDEZ, F. G., FERNÍNDEZ SEVILLA, J. M., GARCÍA SÁNCHEZ, J. L. & MOLINA GRIMA, E. (2004) Influence of Power Supply in the Feasibility of *Phaeodactylum tricornutum* Cultures. *Biotechnology and Bioengineering,* 87, 723-733.

BROWN, G. J., MILES, N. J. & JONES, T. F. (1996) A Fractal Description of the Progeny of Single Impact Single Particle Breakage. *Minerals Engineering,* 9, 715-726.

BUSINESS-INSIGHTS (2005) The Biotechnology Market Outlook: Growth Opportunities and Effective Strategies for Licensing and Collaborations. London, UK.

BYLUND, F., GUILLARD, F., ENFORS, S. O., TRÄGÅRDH, C. & LARSSON, G. (1999) Scale Down of Recombinant Protein Production: A Comparative Study of Scaling Performance. *Bioprocess and Biosystems Engineering,* 20, 377-389.

BYRNE, E. P., FITZPATRICK, J. J., PAMPEL, L. W. & TITCHENER-HOOKER, N. J. (2002) Influence of Shear on Particle Size and Fractal Dimension of Whey Protein

Precipitates: Implications for Scale-Up and Centrifugal Clarification Efficiency. *Chemical Engineering Science,* 57, 3767-3779.

CAO, Z., WILEY, D. E. & FANE, A. G. (2001) CFD Simulations of Net-Type Turbulence Promoters in a Narrow Channel. *Journal of Membrane Science,* 185, 157-176.

CHAN, G., BOOTH, A. J., MANNWEILER, K. & HOARE, M. (2006) Ultra Scale-Down Studies of the Effect of Flow and Impact Conditions During *E. coli* Cell Processing. *Biotechnology and Bioengineering,* 95, 671-683.

CHAN, W. K. Y., BELFORT, M. & BELFORT, G. (1991) Protein Overproduction in Escherichia Coli: RNA Stabilization, Cell Disruption and Recovery with a Cross-Flow Microfiltration Membrane. *Journal of Biotechnology,* 18, 225-242.

CHEMINEER, CO. & STAFF (1976) Liquid Agitation. *Chemical Engineering.*

CHERRY, R. S. & KWON, K. Y. (1990) Transient Shear Stresses on a Suspension Cell in Turbulence. *Biotechnology and Bioengineering,* 36, 563-571.

CHERRY, R. S. & PAPOUTSAKIS, E. T. (1986) Hydrodynamic Effects on Cells in Agitated Tissue Culture Reactors. *Bioprocess and Biosystems Engineering,* 1, 29-41.

CHERRY, R. S. & PAPOUTSAKIS, E. T. (1988) Physical Mechanisms of Cell Damage in Microcarrier Cell Culture Bioreactors. *Biotechnology and Bioengineering,* 32, 1001-1014.

CHERRY, R. S. & PAPOUTSAKIS, E. T. (1989) Growth and Death Rates of Bovine Embryonic Kidney Cells in Turbulent Microcarrier Bioreactors. *Bioprocess and Biosystems Engineering,* 4, 81-89.

CHISTI, Y. (1993) Animal Cell Culture in Stirred Bioreactors: Observations on Scale-Up. *Bioprocess and Biosystems Engineering,* 9, 191-196.

CHOO, K.-H. & LEE, C.-H. (1996) Membrane Fouling Mechanisms in the Membrane-Coupled Anaerobic Bioreactor. *Water Research,* 30, 1771-1780.

CLARKSON, A. I., BULMER, M. & TITCHENER-HOOKER, N. J. (1996) Pilot-Scale Verification of a Computer-Based Simulation for the Centrifugal Recovery of Biological Particles. *Bioprocess and Biosystems Engineering,* 14, 81-89.

CROUGHAN, M. S., HAMEL, J.-F. & WANG, D. I. C. (1987) Hydrodynamic Effects on Animal Cells Grown in Microcarrier Cultures. *Biotechnology and Bioengineering,* 29, 130-141.

DICKEY, D. S. (1984) *Handbook of Chemical Engineering Calculations,* New York, USA, McGraw-Hill.

DO, J. H., SHANG, L. A., KIM, D. H. & CHANG, H. N. (2002) Flow Pattern and Mixing in the Multi-Turbine Agitated Bioreactor Filled with Poly(γ-Glutamic Acid) Solution. *Engineering in Life Sciences,* 2, 345-352.

DOMBROWSKI, N., FOUMENY, E. A., OOKAWARA, S. & RIZA, A. (1993) The Influence of Reynolds Number on the Entry Length and Pressure Drop for Laminar Pipe Flow. *Canadian Journal of Chemical Engineering,* 71, 472-476.

DORAN, P. M. (1995) *Bioprocess Engineering Principles,* London, UK, Harcourt Brace & Company.

DUCLOS-ORSELLO, C., LI, W. & HO, C.-C. (2006) A Three Mechanism Model to Describe Fouling of Microfiltration Membranes. *Journal of Membrane Science,* 280, 856-866.

ERSSON, B., RYDÉN, L. & JANSON, J.-C. (1989) *Protein Purification,* New York, USA, VCH Publishers Inc.

EVEN, M. S., SANDUSKY, C. B. & BARNARD, N. D. (2006) Serum-Free Hybridoma Culture: Ethical, Scientific and Safety Considerations. *Trends in Biotechnology,* 24, 105-108.

FANE, A. G. & RODOVICH, J. M. (1990) Membrane Systems. IN ASENJO, J. A. (Ed.) *Separation Processes in Biotechnology.* New York, USA, Marcel Dekker Inc.

FENG, W., WEN, J., LIU, C., YUAN, Q., JIA, X. & SUN, Y. (2007) Modeling of Local Dynamic Behavior of Phenol Degradation in an Internal Loop Airlift Bioreactor by Yeast *Candida tropicalis. Biotechnology and Bioengineering,* 97, 251-264.

FORSTROM, R. J., BARTELT, K., BLACKSHEAR JR., P. L. & WOOD, T. (1975) Formed Element Reposition onto Filtering Walls. *Transactions - American Society for Artificial Internal Organs,* 21, 602-607.

FRANCIS, P., MARTINEZ, D. M., TAGHIPOUR, F., BOWEN, B. D. & HAYNES, C. A. (2006) Optimizing the Rotor Design for Controlled-Shear Affinity Filtration Using Computational Fluid Dynamics. *Biotechnology and Bioengineering,* 95, 1207-1217.

GABLER, F. R. (1985) Cell Processing Using Tangential Flow Filtration. IN COONEY, C. L. & HUMPHREY, A. E. (Eds.) *Comprehensive Biotechnology.* New York, USA, Pergamon Press.

GARCIA-BRIONES, M. A. & CHALMERS, J. J. (1994) Flow Parameters Associated with Hydrodynamic Cell Injury. *Biotechnology and Bioengineering,* 44, 1089-1098.

GOMME, P. T., HUNT, B. M., TATFORD, O. C., A., J. & J., B. (2006) Effect of Lobe Pumping on Human Albumin: Investigating the Underlying Mechanisms of Aggregate Formation. *Biotechnology and Applied Biochemistry,* 43, 103–111.

GRANDISON, A. S. & LEWIS, M. J. (1996) *Separation Processes in the Food and Biotechnology Industries: Principles and Applications,* Cambridge, UK, Woodhead Publishing Limited.

GRAY, P. P., DUNNILL, P. & LILLY, M. D. (1972) The Continuous-Flow Isolation of Enzymes. IN TERUI, G. (Ed.) *Fermentation Technology Today.* Osaka, Japan, Soc. Ferment. Technol.

HALLER, K. K., VENTIKOS, Y., POULIKAKOS, D. & MONKEWITZ, P. (2002) Computational Study of High-Speed Liquid Droplet Impact. *Journal of Applied Physics,* 92, 2821-2828.

HARNBY, N., EDWARDS, M. F. & NIENOW, A. W. (1997) *Mixing in the Process Industries* London, UK, Butterworth-Heinemann Ltd.

HARRISON, R. G., TODD, P., RUDGE, S. R. & PETRIDES, D. P. (2003) *Bioseparations Science and Engineering,* New York, USA, Oxford University Press Inc.

HARSCOAT, C., JAFFRIN, M. Y., BOUZERAR, R. & COURTOIS, J. (1999) Influence of Fermentation Conditions and Microfiltration Processes on Membrane Fouling During Recovery of Glucuronane Polysaccharides from Fermentation Broths. *Biotechnology and Bioengineering,* 65, 500-511.

HELLUNG-LARSEN, P., ASSAAD, F., PANKRATOVA, S., SAIETZ, B. L. & SKOVGAARD, L. T. (2000) Effects of Pluronic F-68 on Tetrahymena cells: protection against chemical and physical stress and prolongation of survival under toxic conditions. *Journal of Biotechnology,* 76, 185-195.

HENRY, J. D. & ALLRED, R. C. (1972) Concentration of Bacterial Cells by Cross Flow Filtration. *Developments in Industrial Microbiology,* 13, 177-190.

HOLLAND, F. A. & CHAPMAN, F. S. (1966) *Liquid Mixing and Processing in Stirred Tanks,* New York, USA, Reinhold Publishing Corporation.

HOWELL, J. A., SANCHEZ, V. & FIELD, R. W. (1993) *Membranes in Bioprocessing, Theory and Applications.* , London, UK, Chapman & Hall.

HUTCHINSON, N., BINGHAM, N., MURRELL, N., FARID, S. & HOARE, M. (2006) Shear Stress Analysis of Mammalian Cell Suspensions for Prediction of Industrial Centrifugation and its Verification. *Biotechnology and Bioengineering,* 95, 483-491.

IMS-HEALTH (2008) IMS 2008 Global Biotech Perspective. Connecticut, USA, IMS Health.

JACKSON, L. R., TRUDEL, L. J. & LIPMAN, N. S. (1999) Small Scale Monoclonal Antibody Production *in vitro*: Methods and Resources. *Lab Animal,* 28, 38-50.

JAOUEN, P., VANDANJON, L. & QUEMENEUR, F. (1999) The Shear Stress of Microalgal Cell Suspensions (*Tetraselmis suecica*) in Tangential Flow Filtration Systems: The Role of Pumps. *Bioresource Technology,* 68, 149-154.

JÜSTEN, P., PAUL, G. C., NIENOW, A. W. & THOMAS, C. R. (1996) Dependence of Mycelial Morphology on Impeller Type and Agitation Intensity. *Biotechnology and Bioengineering,* 52, 672-684.

KESHAVARZ-MOORE, E., HOARE, M. & DUNNILL, P. (1987) Biochemical Engineering Aspects of Cell Disruption. IN VERRALL, M. S. & HUDSON, M. J. (Eds.) *Separations for Biotechnology.* Chichester, UK, Ellis Harwood Ltd.

KESHAVARZ-MOORE, E., HOARE, M. & DUNNILL, P. (1990) Disruption of Baker's Yeast in a High-Pressure Homogenizer: New Evidence on Mechanism. *Enzyme and Microbial Technology,* 12, 764-770.

KIM, J.-S., LEE, C.-H. & CHANG, I.-S. (2001) Effect of Pump Shear on the Performance of a Crossflow Membrane Bioreactor. *Water Research,* 35, 2137-2144.

KIM, M.-M. & ZYDNEY, A. L. (2006) Theoretical Analysis of Particle Trajectories and Sieving in a Two-Dimensional Cross-Flow Filtration System. *Journal of Membrane Science,* 281, 666-675.

KING, A. T., DAVEY, M. R., MULLIGAN, B. J. & LOWE, K. C. (1990) Effects of Pluronic F-68 on Plant Cells in Suspension Culture. *Biotechnology Letters,* 12, 29-32.

KOBAYASHI, M. (2004) Breakup and Strength of Polystyrene Latex Flocs Subjected to a Converging Flow. *Colloids and Surfaces A: Physicochemical and Engineering Aspects,* 235, 73-78.

KRESTA, S. M. (1998) Turbulence in Stirred Tanks: Anisotropic, Approximate and Applied. *Canadian Journal of Chemical Engineering,* 76, 563-576.

KRESTA, S. M. & WOOD, P. E. (1991) Prediction of the Three-Dimensional Turbulent Flow in Stirred Tanks. *AIChE Journal,* 37, 448-460.

KUMAR, S., GANVIR, V., SATYANAND, C., KUMAR, R. & GANDHI, K. S. (1998) Alternative Mechanisms of Drop Breakup in Stirred Vessels. *Chemical Engineering Science,* 53, 3269-3280.

KUMARESAN, T. & JOSHI, J. B. (2006) Effect of impeller design on the flow pattern and mixing in stirred tanks. *Chemical Engineering Journal,* 115, 173-193.

KUNAS, K. T. & PAPOUTSAKIS, E. T. (1990) Damage Mechanisms of Suspended Animal Cells in Agitated Bioreactors With and Without Bubble Entrainment. *Biotechnology and Bioengineering,* 36, 476-483.

LAUNDER, B. E. & SPALDING, D. B. (1974) The Numerical Computation of Turbulent Flows. *Computer Methods in Applied Mechanics and Engineering,* 3, 269-289.

LAWRENCE, M. B., MCINTIRE, L. V. & G, E. S. (1987) Effect of Flow on Polymorphonuclear Leukocyte/Endothelial Cell Adhesion. *Blood,* 70, 1284–1290

LEE, S.-M. (1989) The Primary Stages of Protein Recovery. *Journal of Biotechnology,* 11, 103-117.

LEE, S. J., CHOO, K. H. & LEE, C. H. (2000) Conjunctive Use of Ultrafiltration with Powdered Activated Carbon Adsorption for Removal of Synthetic and Natural Organic Matter. *Journal of Industrial and Engineering Chemistry,* 6, 357-364.

LEHR, F., MILLIES, M. & MEWES, D. (2002) Bubble-Size Distributions and Flow Fields in Bubble Columns. *AIChE Journal,* 48, 2426-2443.

LEVY, M. S., CICCOLINI, L. A. S., YIM, S. S. S., TSAI, J. T., TITCHENER-HOOKER, N., AYAZI SHAMLOU, P. & DUNNILL, P. (1999) The Effects of Material Properties and Fluid Flow Intensity on Plasmid DNA Recovery During Cell Lysis. *Chemical Engineering Science,* 54, 3171-3178.

LI, J., WANG, Z., GE, Y., SUN, Q. & HU, X. (2006) Clarification and Sterilization of Raw Depectinized Apple Juice by Ceramic Ultrafiltration Membranes. *Journal of the Science of Food and Agriculture,* 86, 148-155.

MA, N., KOELLING, K. W. & CHALMERS, J. J. (2002) Fabrication and Use of a Transient Contractional Flow Device to Quantify the Sensitivity of Mammalian and Insect Cells to Hydrodynamic Forces. *Biotechnology and Bioengineering,* 80, 428-437.

MAIORELLA, B., DORIN, G., CARION, A. & HARANO, D. (1991) Crossflow Microfiltration of Animal Cells. *Biotechnology and Bioengineering,* 37, 121-126.

MANNWEILER, K. (1990) The Recovery of Biological Particles in High-Speed Continuous Centrifuges with Special Reference to Feed-Zone Break-Up Effects. PhD Thesis, University College London.

MANNWEILER, K. & HOARE, M. (1992) The Scale-Down of an Industrial Disc Stack Centrifuge. *Bioprocess and Biosystems Engineering,* 8, 19-25.

METZNER, A. B. & OTTO, R. E. (1957) Agitation of Non-Newtonian Fluids. *AIChE Journal,* 3, 3-10.

MEYER, F., GEHMLICH, I., GUTHKE, R., GÓRAK, A. & KNORRE, W. A. (1998) Analysis and Simulation of Complex Interactions During Dynamic Microfiltration of *Escherichia coli* Suspensions. *Biotechnology and Bioengineering,* 59, 189-202.

MICHAELS, J. D. & PAPOUTSAKIS, E. T. (1991) Polyvinyl Alcohol and Polyethylene Glycol as Protectants Against Fluid-Mechanical Injury of Freely-Suspended Animal Cells (CRL 8018). *Journal of Biotechnology,* 19, 241-257.

MICHAELS, J. D., PETERSEN, J. F., MCLNTIRE, L. V. & PAPOUTSAKIS, E. T. (1991) Protection Mechanisms of Freely Suspended Animal Cells (CRL 8018) from Fluid-Mechanical Injury. Viscometric and Bioreactor Studies Using Serum, Pluronic F68 and Polyethylene Glycol. *Biotechnology and Bioengineering,* 38, 169-180.

MILLWARD, H. R., BELLHOUSE, B. J., NICHOLSON, A. M., BEETON, S., JENKINS, N. & KNOWLES, C. J. (1994) Mammalian Cell Damage in a Novel Membrane Bioreactor. *Biotechnology and Bioengineering,* 43, 899-906.

MOLINA GRIMA, E., CHISTI, Y. & MOO-YOUNG, M. (1997) Characterization of shear rates in airlift bioreactors for animal cell culture. *Journal of Biotechnology,* 54, 195-210.

MORES, W. D. & DAVIS, R. H. (2002) Yeast Foulant Removal by Backpulses in Crossflow Microfiltration. *Journal of Membrane Science,* 208, 389-404.

MORRIS, C. B. & WARBURTON, S. (1994) Serum-Screening and Selection. IN DOYLE, A. & GRIFFITHS, J. B. (Eds.) *Cell & Tissue Culture: Laboratory Procedures in Biotechnology.* New Jersey, USA, Wiley.

NAGATA, S. (1975) *Mixing: Principles and Applications,* Tokyo, Japan, Kodansha.

NAILI, S. & THIRIET, M. (2005) Pressure Field in Flow through Uniform Straight Pipes with Varying Wall Cross Curvature. *Computers in Biology and Medicine,* 35, 645-663.

NAUMAN, E. B. (2004) Residence Time Distribution. IN PAUL, E. L., ATIEMO-OBENG, V. A. & KRESTA, S. M. (Eds.) *Handbook of Industrial Mixing.* New Jersey, USA, A John Wiley & Sons, Inc.

NEAL, G., CHRISTIE, J., KESHAVARZ-MOORE, E. & AYAZI SHAMLOU, P. (2003) Ultra Scale-Down Approach for the Prediction of Full-Scale Recovery of Ovine Polycolonal Immunoglobulins Used in the Manufacture of Snake Venom-Specific Fab Fragment. *Biotechnology and Bioengineering,* 81, 149-157.

NIPKOW, A., ZEIKUS, J. G. & GERHARDT, P. (1989) Microfiltration Cell-Recycle Pilot System for Continuous Thermoanaerobic Production of Exo-β-Amylase. *Biotechnology and Bioengineering,* 34, 1075-1084.

OLDSHUE, J. Y. (1983) *Fluid Mixing Technology,* New York, USA, McGraw-Hill.

PALOMARES, L. A., GONZALEZ, M. & RAMIREZ, O. T. (2000) Evidence of Pluronic F-68 Direct Interaction with Insect Cells: Impact on Shear Protection, Recombinant Protein, and Baculovirus Production. *Enzyme and Microbial Technology,* 26, 324-331.

PERNER, I., POSTEN, C. & BRONESKE, J. (2003) CFD Optimization of a Plate Photobioreactor Used for Cultivation of Microalgae. *Engineering in Life Sciences,* 3, 287-291.

PERRY, R. H. & GREEN, D. W. (1997) *Chemical Engineers' Handbook (7th Edition),* London, UK, McGraw-Hill.

PLACEK, J. & TAVLARIDES, L. L. (1985) Turbulent Flow in Stirred Tanks. Part I: Turbulent Flow in the Turbine Impeller Region. *AIChE Journal,* 31, 1113-1120.

RAMÍREZ, O. T. & MUTHARASAN, R. (1990) The Role of the Plasma Membrane Fluidity on the Shear Sensitivity of Hybridomas Grown under Hydrodynamic Stress. *Biotechnology and Bioengineering,* 36, 911-920.

REN, J., CHUNG, T.-S., LI, D., WANG, R. & LIU, Y. (2002) Development of Asymmetric 6FDA-2,6 DAT Hollow Fiber Membranes for CO_2/CH_4 Separation: 1. The Influence of Dope Composition and Rheology on Membrane Morphology and Separation Performance. *Journal of Membrane Science,* 207, 227-240.

ROBERTSON, B. & ULBRECHT, J. J. (1987) Measurement of Shear Rate on an Agitator in a Fermentation Broth. IN HO, C. S. & OLDSHUE, J. Y. (Eds.) *Biotechnology Processes: Scale-up and Mixing.* New York, USA, American Institute of Chemical Engineers.

ROY, D., LAGIMONIÈRE, M., HARDY, M.-J., BOURASSA, J.-F. & MOUROT, P. (1989) Viability of an Ectomycorrhizal Fungus During Cross-Flow Filtration. *Journal of Biotechnology,* 10, 227-240.

SARTORIUS (2007) Sartorius Reviews Results of Fiscal 2006. Goettingen, Germany.

SAVE, S. S., PANDIT, A. B. & JOSHI, J. B. (1994) Microbial Cell Disruption: Role of Cavitation. *Chemical Engineering Journal,* 55, 67-72.

SCHÄFER, M., YIANNESKIS, M., WÄCHTER, P. & DURST, F. (1998) Trailing Vortices around a 45° Pitched-Blade Impeller. *AIChE Journal,* 44, 1233-1246.

SCHLICHTING, H. (1979) *Boundary Layer Theory,* New York, USA, McGraw-Hill.

SCHUTTE, H. & KULA, M. R. (1990) Pilot- and Process-Scale Techniques for Cell Disruption. *Biotechnology and Applied Biochemistry,* 12, 599-620.

SCHWINGE, J., WILEY, D. E. & FLETCHER, D. F. (2002) A CFD Study of Unsteady Flow in Narrow Spacer-Filled Channels for Spiral-Wound Membrane Modules. *Desalination,* 146, 195-201.

SHAMLOU, P. A. (1993) *Processing of Solid-Liquid Suspensions,* London, UK, Butterworth Heinemann.

SMITH, C. G., GREENFIELD, P. F. & RANDERSON, D. H. (1987) A Technique for Determining the Shear Sensitivity of Mammalian Cells in Suspension Culture. *Biotechnology Techniques,* 1, 39-44.

SZALAI, E. S. & MUZZIO, F. J. (2003) Fundamental Approach to the Design and Optimization of Static Mixers. *AIChE Journal,* 49, 2687-2699.

TARABARA, V. V. & WIESNER, M. R. (2003) Computational Fluid Dynamics Modeling of the Flow in a Laboratory Membrane Filtration Cell Operated at Low Recoveries. *Chemical Engineering Science,* 58, 239-246.

THOMASSEN, J. K., FARADAY, D. B. F., UNDERWOOD, B. O. & CLEAVER, J. A. S. (2005) The Effect of Varying Transmembrane Pressure and Crossflow Velocity on the Microfiltration Fouling of a Model Beer. *Separation and Purification Technology,* 41, 91-100.

THORNTON, C., CIOMOCOS, M. T. & ADAMS, M. J. (1999) Numerical Simulations of Agglomerate Impact Breakage. *Powder Technology,* 105, 74-82.

TRAMPER, J., WILLIAMS, J. B., JOUSTRA, D. & VLAK, J. M. (1986) Shear Sensitivity of Insect Cells in Suspension. *Enzyme and Microbial Technology,* 8, 33-36.

VAN DER POL, L., BAKKER, W. A. M. & TRAMPER, J. (1992) Effect of Low Serum Concentrations (0%-2.5%) on Growth, Production, and Shear Sensitivity of Hybridoma Cells. *Biotechnology and Bioengineering,* 40, 179-182.

VAN REIS, R. & ZYDNEY, A. (2007) Bioprocess Membrane Technology. *Journal of Membrane Science,* 297, 16-50.

VANDANJON, L., ROSSIGNOL, N., JAOUEN, P., ROBERT, J. M. & QUÉMÉNEUR, F. (1999) Effects of Shear on Two Microalgae Species. Contribution of Pumps and Valves in Tangential Flow Filtration Systems. *Biotechnology and Bioengineering,* 63, 1-9.

VANE, L. M., ALVAREZ, F. R. & GIROUX, E. L. (1999) Reduction of Concentration Polarization in Pervaporation Using Vibrating Membrane Module. *Journal of Membrane Science,* 153, 233-241.

VASAN, S. S., GHOSH, R. & CUI, Z. (2002) Design of Cone-and-Plate Test Cell for Ultrafiltration. *Desalination,* 146, 219-224.

VERSTEEG, H. K. & MALALASEKERA, W. (1995) *An Introduction to Computational Fluid Dynamics: The Finite Volume Method,* London, UK, Longman.

VERSTEEG, H. K. & MALALASEKERA, W. (2007) *An Introduction to Computational Fluid Dynamics: The Finite Volume Method,* London, UK, Pearson Education Limited.

VIRKAR, P. D., NARENDRANATHAN, T. J., HOARE, M. & DUNNILL, P. (1981) Studies of the Effect of Shear on Globular Proteins: Extension to High Shear Fields and to Pumps. *Biotechnology and Bioengineering,* 23, 425-429.

WALAS, S. M. (1990) *Chemical Process Equipment - Selection and Design,* London, UK, Butterworth-Heinemann Ltd.

WALSH, G. (1998) *Biopharmaceuticals: Biochemistry and Biotechnology,* Chichester, UK, J. Wiley & Sons Ltd.

WANG, A., LEWUS, R. & RATHORE, A. S. (2006) Comparison of Different Options for Harvest of a Therapeutic Protein Product from High Cell Density Yeast Fermentation Broth. *Biotechnology and Bioengineering,* 94, 91-104.

WASE, D. A. J. & PATEL, Y. R. (1985) Variations in the Volumes of Microbial Cells with Change in the Agitation Rates of Chemostat Cultures. *Journal of General Microbiology,* 131, 725-736.

WICHTERLE, K., SOBOLIK, V., LUTZ, M. & DENK, V. (1996) Shear Rate on Centrifugal Pump Impeller. *Chemical Engineering Science,* 51, 5227-5228.

WILLIAMS, G., GILBERT, M. & IRVINE, C. (2008) Biotechnology 2008. London, UK, Marks & Clark

WU, Y. X., YU, H. W. & CHING, C. B. (2004) A Computational Fluid Dynamics Study of Binary Adsorption Separation in Chromatography. *Chemical Engineering & Technology,* 27, 955-961.

YIM, S. S. & SHAMLOU, P. A. (2000) The Engineering Effects of Fluids Flow on Freely Suspended Biological Macro-Materials and Macromolecules. *Advances in Biochemical Engineering/Biotechnology.* Berlin / Heidelberg, Germany, Springer Berlin / Heidelberg.

ZHANG, H., WILLIAMS-DALSON, W., KESHAVARZ-MOORE, E. & SHAMLOU, P. A. (2005) Computational Fluid Dynamics (CFD) Analysis of Mixing and Gas-Liquid Mass Transfer in Shake Flasks. 41, 1-8.

ZHANG, Z., AL-RUBEAI, M. & THOMAS, C. R. (1992) Effect of Pluronic F-68 on the Mechanical Properties of Mammalian cells. *Enzyme and Microbial Technology,* 14, 980-983.

ZHANG, Z., AL-RUBEAI, M. & THOMAS, C. R. (1993) Estimation of Disruption of Animal Cells by Turbulent Capillary Flow. *Biotechnology and Bioengineering,* 42, 987-993.

ZHOU, G. & KRESTA, S. M. (1996) Impact of Geometry on the Maximum Turbulence Energy Dissipation Rate for Various Impellers. *AIChE Journal,* 42, 2476-2490.

ZUMAETA, N., BYRNE, E. P. & FITZPATRICK, J. J. (2006) Predicting Precipitate Particle Breakage in a Pipeline: Effect of Agitation Intensity During Precipitate Formation. *Chemical Engineering Science,* 61, 7991-8003.

ZUMAETA, N., CARTLAND-GLOVER, G. M., HEFFERNAN, S. P., BYRNE, E. P. & FITZPATRICK, J. J. (2005) Breakage Model Development and Application with

CFD for Predicting Breakage of Whey Protein Precipitate Particles. *Chemical Engineering Science,* 60, 3443-3452.

ZYDNEY, A. L. & COLTON, C. K. (1984) A Red Cell Deformation Model for Hemolysis in Cross Flow Membrane Plasmapheresis. *Chemical Engineering Communications,* 30, 191-207.

APPENDIX I CFD commands and specifications

SHEAR DEVICE (command file)

```
>>CFX4
 #CALC
  PI=3.1415926 ;
  RPM=3260 ;
  OMEGA=2*PI*RPM/60 ;
  OMEGA = 1*OMEGA ;
  OMEGAM = -1*OMEGA ;
 #ENDCALC
 >>OPTIONS
  THREE DIMENSIONS
  TURBULENT FLOW
  CYLINDRICAL COORDINATES
  UNMATCHED GRIDS
  ROTATING COORDINATES
  USER SCALAR EQUATIONS 11
 >>VARIABLE NAMES
  USER SCALAR1 'MFR U VELOCITY'
  USER SCALAR2 'MFR V VELOCITY'
  USER SCALAR3 'MFR W VELOCITY'
  USER SCALAR4 'MFR SPEED'
  USER SCALAR5 'SHEAR RATE'
  USER SCALAR6 'X SHEAR STRESS'
  USER SCALAR7 'Y SHEAR STRESS'
  USER SCALAR8 'Z SHEAR STRESS'
  USER SCALAR9 'XY NODAL SHEAR STRESS'
  USER SCALAR10 'YZ NODAL SHEAR STRESS'
  USER SCALAR11 'ZX NODAL SHEAR STRESS'
 >>MODEL TOPOLOGY
  >>GLUE PATCHES FOR UNMATCHED GRIDS
   FIRST PATCH NAMES 'BLKBDYUMB-OUTER'
   SECOND PATCH NAMES 'BLKBDYUMB-INNER'
>>MODEL DATA
 >>PHYSICAL PROPERTIES
  #CALC
   DENL  = 1000.0;
        VALUE SET =  1.0000E+03
   VISL  = 1.0E-3;
        VALUE SET =  1.0000E-03
  #ENDCALC
  >>FLUID PARAMETERS
   DENSITY #DENL
   VISCOSITY #VISL
   END
  >>ROTATING COORDINATES PARAMETERS
   OMEGA #OMEGA 0.0 0.0
```

```
    PATCH NAME 'USER3D-ROTOR'
 >>SOLVER DATA
  >>PROGRAM CONTROL
   MAXIMUM NUMBER OF ITERATIONS 30000
   MASS SOURCE TOLERANCE 1.0000E-10
 >>WALL BOUNDARIES
   PATCH NAME 'WALL-BASE-INNER'
   ANGULAR VELOCITY #OMEGAM 0.0 0.0
 >>WALL BOUNDARIES
   PATCH NAME 'WALL-TOP-INNER'
   ANGULAR VELOCITY #OMEGAM 0.0 0.0
 >>STOP
```

PUMP (command file)

```
/* UMP MOVING VANE + ROTATING*/
     #CALC
      RPM=600;
      PI=3.1415926;
      DEG=PI/180.;
      ASTEP=2*DEG;
      OMEGA = RPM*2.0*PI/60.0;
      OMEGAM=-1.0*OMEGA;
      REVOLT = 2.0*PI/OMEGA;
      DT = REVOLT*ASTEP/(360.0*DEG);
     #ENDCALC
>>CFX4
 >>SET LIMITS
  TOTAL INTEGER WORK SPACE 100000000
  TOTAL REAL WORK SPACE 20000000
 >>OPTIONS
  THREE DIMENSIONS
  BODY FITTED GRID
  CYLINDRICAL COORDINATES
  AXIS INCLUDED
  turbulent FLOW
  ISOTHERMAL FLOW
  INCOMPRESSIBLE FLOW
  transient flow
  transient grid
  unmatched grids
  USER SCALAR EQUATIONS 1
 >>USER FORTRAN
  USRGRD
  USRTRN
 >>VARIABLE NAMES
  USER SCALAR1 'SHEAR RATE'
>>MODEL TOPOLOGY
 >>CREATE BLOCK
  BLOCK NAME 'BLOCK-NUMBER-1'
```

```
  BLOCK DIMENSIONS 3 40 45

>>CREATE PATCH
  PATCH NAME 'PERIODIC'
  BLOCK NAME 'BLOCK-NUMBER-1'
  PATCH TYPE 'PERIODIC'
  LOW K
  HIGH K */
 >>CREATE PATCH
  PATCH NAME 'blockage1'
  BLOCK NAME 'BLOCK-NUMBER-1'
  PATCH TYPE 'wall'
  LOW K
 >>CREATE PATCH
  PATCH NAME 'blockage2'
  BLOCK NAME 'BLOCK-NUMBER-1'
  PATCH TYPE 'wall'
  high K
 >>CREATE PATCH
  PATCH NAME 'INLET-OUTLET'
  BLOCK NAME 'BLOCK-NUMBER-1'
  PATCH TYPE 'SYMMETRY PLANE'
  LOW I
  HIGH I
 >>CREATE PATCH
  PATCH NAME 'INLET-SOURCE'
  BLOCK NAME 'BLOCK-NUMBER-1'
  PATCH TYPE 'USER2D'
  LOW I
 >>CREATE PATCH
  PATCH NAME 'OUTLET-SOURCE'
  BLOCK NAME 'BLOCK-NUMBER-1'
  PATCH TYPE 'USER2D'
  HIGH I
 >>CREATE PATCH
  PATCH NAME 'MOVING WALL'
  BLOCK NAME 'BLOCK-NUMBER-1'
  PATCH TYPE 'WALL'
  LOW J
 >>CREATE PATCH
  PATCH NAME 'STATIONARY WALL'
  BLOCK NAME 'BLOCK-NUMBER-1'
  PATCH TYPE 'WALL'
  HIGH J

>>MODEL DATA
 >>PHYSICAL PROPERTIES
  >>FLUID PARAMETERS
   VISCOSITY 1.000E-03
   DENSITY 1.00E+03
```

```
  >>TRANSIENT PARAMETERS
   >>FIXED TIME STEPPING
    TIME STEPS 125 * #DT
  >>TURBULENCE PARAMETERS
   >>TURBULENCE MODEL
    TURBULENCE MODEL 'K-EPSILON'
>>SOLVER DATA
 >>PROGRAM CONTROL
  MAXIMUM NUMBER OF ITERATIONS 200
  MASS SOURCE TOLERANCE 1.0000E-08
>>CREATE GRID
>>MODEL BOUNDARY CONDITIONS
 >>WALL BOUNDARY CONDITIONS
  PATCH NAME 'STATIONARY WALL'
  ANGULAR VELOCITY #OMEGAM 0.0 0.0
>>OUTPUT OPTIONS
 >>print options
 >>what
  all variables
 >>DUMP FILE OPTIONS
 INITIAL GUESS
 EACH TIME STEP
 GEOMETRY DATA
 ALL variables
>>STOP
```

PUMP (FORTRAN file)

```
      SUBROUTINE USRGRD(U,V,W,P,VFRAC,DEN,VIS,TE,ED,RS,T,H,RF,SCAL,
     +                  XP,YP,ZP,VOL,AREA,VPOR,ARPOR,WFACT,
     +                  XCOLD,YCOLD,ZCOLD,XC,YC,ZC,IPT,
     +                  IBLK,IPVERT,IPNODN,IPFACN,IPNODF,IPNODB,IPFACB,
     +                  WORK,IWORK,CWORK)
C
C***********************************************************************
C
C  USER SUBROUTINE TO ALLOW USERS TO GENERATE A GRID FOR CFX-4
C
C  >>> IMPORTANT                              <<<
C  >>>                                    <<<
C  >>> USERS MAY ONLY ADD OR ALTER PARTS OF THE SUBROUTINE WITHIN  <<<
C  >>> THE DESIGNATED USER AREAS                          <<<
C
C***********************************************************************
C
C  THIS SUBROUTINE IS CALLED BY THE FOLLOWING SUBROUTINES
C    CREATE  CUSR
C
C***********************************************************************
C  CREATED
```

```
C   27/04/90 ADB
C MODIFIED
C   05/08/91 IRH  NEW STRUCTURE
C   09/09/91 IRH  CORRECT EXAMPLE
C   01/10/91 DSC  REDUCE COMMENT LINE GOING OVER 72 COLUMNS.
C   29/11/91 PHA  UPDATE CALLED BY COMMENT, ADD RF ARGUMENT,
C             CHANGE LAST DIMENSION OF RS TO 6 AND IVERS TO 2
C   03/06/92 PHA  ADD PRECISION FLAG AND CHANGE IVERS TO 3
C   03/07/92 DSC  CORRECT COMMON MLTGRD.
C   23/11/93 CSH  EXPLICITLY DIMENSION IPVERT ETC.
C   03/02/94 PHA  CHANGE FLOW3D TO CFDS-FLOW3D
C   03/03/94 FHW  CORRECTION OF SPELLING MISTAKE
C   22/08/94 NSW  MOVE 'IF(IUSED.EQ.0) RETURN' OUT OF USER AREA
C   19/12/94 NSW  CHANGE FOR CFX-F3D
C   02/07/97 NSW  UPDATE FOR CFX-4
C
C*********************************************************************
C
C SUBROUTINE ARGUMENTS
C
C   U    - U COMPONENT OF VELOCITY
C   V    - V COMPONENT OF VELOCITY
C   W    - W COMPONENT OF VELOCITY
C   P    - PRESSURE
C   VFRAC  - VOLUME FRACTION
C   DEN    - DENSITY OF FLUID
C   VIS    - VISCOSITY OF FLUID
C   TE     - TURBULENT KINETIC ENERGY
C   ED     - EPSILON
C   RS     - REYNOLD STRESSES
C   T    - TEMPERATURE
C   H    - ENTHALPY
C   RF     - REYNOLD FLUXES
C   SCAL   - SCALARS (THE FIRST 'NCONC' OF THESE ARE MASS FRACTIONS)
C   XP     - X COORDINATES OF CELL CENTRES
C   YP     - Y COORDINATES OF CELL CENTRES
C   ZP     - Z COORDINATES OF CELL CENTRES
C   VOL    - VOLUME OF CELLS
C   AREA   - AREA OF CELLS
C   VPOR   - POROUS VOLUME
C   ARPOR  - POROUS AREA
C   WFACT  - WEIGHT FACTORS
C * XC     - X COORDINATES OF CELL VERTICES
C * YC     - Y COORDINATES OF CELL VERTICES
C * ZC     - Z COORDINATES OF CELL VERTICES
C   XCOLD  - X COORDINATES OF CELL VERTICES AT START OF TIME STEP
C   YCOLD  - Y COORDINATES OF CELL VERTICES AT START OF TIME STEP
C   ZCOLD  - Z COORDINATES OF CELL VERTICES AT START OF TIME STEP
C
C   IPT    - 1D POINTER ARRAY
```

```
C    IBLK   - BLOCK SIZE INFORMATION
C    IPVERT - POINTER FROM CELL CENTERS TO 8 NEIGHBOURING VERTICES
C    IPNODN - POINTER FROM CELL CENTERS TO 6 NEIGHBOURING CELLS
C    IPFACN - POINTER FROM CELL CENTERS TO 6 NEIGHBOURING FACES
C    IPNODF - POINTER FROM CELL FACES TO 2 NEIGHBOURING CELL CENTERS
C    IPNODB - POINTER FROM BOUNDARY CENTERS TO CELL CENTERS
C    IPFACB - POINTER FROM BOUNDARY CENTERS TO BOUNDARY FACESS
C
C    WORK   - REAL WORKSPACE ARRAY
C    IWORK  - INTEGER WORKSPACE ARRAY
C    CWORK  - CHARACTER WORKSPACE ARRAY
C
C  SUBROUTINE ARGUMENTS PRECEDED WITH A '*' ARE ARGUMENTS THAT MUST
C  BE SET  BY THE USER IN THIS ROUTINE.
C
C  NOTE THAT OTHER DATA MAY BE OBTAINED FROM CFX-4 USING THE
C  ROUTINE GETADD, FOR FURTHER DETAILS SEE THE VERSION 4
C  USER MANUAL.
C
C*********************************************************************
C
      LOGICAL LDEN,LVIS,LTURB,LTEMP,LBUOY,LSCAL,LCOMP
     +       ,LRECT,LCYN,LAXIS,LPOROS,LTRANS
C
      CHARACTER*(*) CWORK
C
C+++++++++++++++++ USER AREA 1 ++++++++++++++++++++++++++++++++++++++++
C---- AREA FOR USERS EXPLICITLY DECLARED VARIABLES
C
C+++++++++++++++++ END OF USER AREA 1 ++++++++++++++++++++++++++++++++
C
      COMMON
     + /ALL/    NBLOCK,NCELL,NBDRY,NNODE,NFACE,NVERT,NDIM
     + /ALLWRK/ NRWS,NIWS,NCWS,IWRFRE,IWIFRE,IWCFRE
     + /ADDIMS/ NPHASE,NSCAL,NVAR,NPROP
     +       ,NDVAR,NDPROP,NDXNN,NDGEOM,NDCOEF,NILIST,NRLIST,NTOPOL
     + /CHKUSR/ IVERS,IUCALL,IUSED
     + /CONC/   NCONC
     + /DEVICE/ NREAD,NWRITE,NRDISK,NWDISK
     + /IDUM/   ILEN,JLEN
     + /LOGIC/  LDEN,LVIS,LTURB,LTEMP,LBUOY,LSCAL,LCOMP
     +       ,LRECT,LCYN,LAXIS,LPOROS,LTRANS
     + /MLTGRD/ MLEVEL,NLEVEL,ILEVEL
     + /SGLDBL/ IFLGPR,ICHKPR
     + /SPARM/  SMALL,SORMAX,NITER,INDPRI,MAXIT,NODREF,NODMON
     + /TIMUSR/ DTUSR
     + /TRANSI/ NSTEP,KSTEP,MF,INCORE
     + /TRANSR/ TIME,DT,DTINVF,TPARM
C
C+++++++++++++++++ USER AREA 2 ++++++++++++++++++++++++++++++++++++++++
```

```
C---- AREA FOR USERS TO DECLARE THEIR OWN COMMON BLOCKS
C    THESE SHOULD START WITH THE CHARACTERS 'UC' TO ENSURE
C    NO CONFLICT WITH NON-USER COMMON BLOCKS
C
C+++++++++++++++++ END OF USER AREA 2 +++++++++++++++++++++++++++++++++
C
     DIMENSION
    + U(NNODE,NPHASE),V(NNODE,NPHASE),W(NNODE,NPHASE),P(NNODE,NPHASE)
    +,VFRAC(NNODE,NPHASE),DEN(NNODE,NPHASE),VIS(NNODE,NPHASE)
    +,TE(NNODE,NPHASE),ED(NNODE,NPHASE),RS(NNODE,NPHASE,6)
    +,T(NNODE,NPHASE),H(NNODE,NPHASE),RF(NNODE,NPHASE,4)
    +,SCAL(NNODE,NPHASE,NSCAL)
     DIMENSION
    + XP(NNODE),YP(NNODE),ZP(NNODE),XC(NVERT),YC(NVERT),ZC(NVERT)
    +,XCOLD(NVERT),YCOLD(NVERT),ZCOLD(NVERT)
    +,VOL(NCELL),AREA(NFACE,3),VPOR(NCELL),ARPOR(NFACE,3)
    +,WFACT(NFACE)
    +,IPT(*),IBLK(5,NBLOCK)
    +,IPVERT(NCELL,8),IPNODN(NCELL,6),IPFACN(NCELL,6),IPNODF(NFACE,4)
    +,IPNODB(NBDRY,4),IPFACB(NBDRY)
    +,IWORK(*),WORK(*),CWORK(*)
C
C++++++++++++++++ USER AREA 3 +++++++++++++++++++++++++++++++++++++++++
C---- AREA FOR USERS TO DIMENSION THEIR ARRAYS
     DIMENSION YA1(1000)
C
C---- AREA FOR USERS TO DEFINE DATA STATEMENTS
C
C+++++++++++++++++ END OF USER AREA 3 +++++++++++++++++++++++++++++++++
C
C---- STATEMENT FUNCTION FOR ADDRESSING
     IP(I,J,K)=IPT((K-1)*ILEN*JLEN+(J-1)*ILEN+I)
C
C---- VERSION NUMBER OF USER ROUTINE AND PRECISION FLAG
C
     IVERS=3
     ICHKPR = 1
C
C+++++++++++++++++ USER AREA 4 +++++++++++++++++++++++++++++++++++++++++
C---- TO USE THIS USER ROUTINE FIRST SET IUSED=1
C
     IUSED=1
C
C+++++++++++++++++ END OF USER AREA 4 +++++++++++++++++++++++++++++++++
C
     IF (IUSED.EQ.0) RETURN
C
C---- FRONTEND CHECKING OF USER ROUTINE
     IF (IUCALL.EQ.0) RETURN
C
```

```
C+++++++++++++++++ USER AREA 5 ++++++++++++++++++++++++++++++++++++++++
C
      RPM=120.
      PI=3.1415926
      ZLEN=PI/2.
      Y0=1.0E-05
      Y1=0.02
      Y2=0.04
      Y3=Y1
      YLEN1=0.04
      XLEN1=0.01
      IF (KSTEP.EQ.0) THEN

C
C###################################################################
C DEFINE THE INTTIAL MESH
C###################################################################
C
C
       CALL IPREC('BLOCK-NUMBER-1','BLOCK','VERTICES',IPT,ILEN,JLEN,
     +         KLEN,CWORK,IWORK)
       KK=KLEN-1
       KK2=KK*2
       KK4=KK*4
       KK43=KK*3/4
       DO 10 I=1, KK4
         IF (I.LE.KK2) THEN
           YA1(I)=(Y2-Y0)/KK2*I
         ELSE
           YA1(I)=Y2-(Y2-Y0)/KK2*(I-KK2)
         ENDIF
C        WRITE(*,*)YA1(I)
10     CONTINUE
C-- LOOP OVER BLOCK
      DO 100 I=1,ILEN
        DO 120 J=1,JLEN
          DO 130 K=1,KLEN
C-- USE STATEMENT FUNCTION IP TO GET ADDRESSES
          INODE = IP(I,J,K)

C-- DEFINE LOCATION OF GRID VERTICES
          XC(INODE)=XLEN1*FLOAT(I-1)/FLOAT(ILEN-1)
          ZC(INODE)=-zlen+ZLEN*FLOAT(K-1)/FLOAT(KLEN-1)
          YC(INODE)=YLEN1+YA1(K)*FLOAT(J-1)/FLOAT(JLEN-1)


  130     CONTINUE
  120   CONTINUE
  100 CONTINUE
CCCCC  THE TRASIENT FLOW NOW ###################
```

```
      ELSEIF (KSTEP.LE.NSTEP ) THEN
      CALL IPREC('BLOCK-NUMBER-1','BLOCK','VERTICES',IPT,ILEN,JLEN,
     +         KLEN,CWORK,IWORK)
C-- LOOP OVER BLOCK
      DO 200 I=1,ILEN
       DO 220 J=1,JLEN
         DO 230 K=1,KLEN
C-- USE STATEMENT FUNCTION IP TO GET ADDRESSES
         INODE = IP(I,J,K)

C-- DEFINE LOCATION OF GRID VERTICES
         XC(INODE)=XCOLD(INODE)
         YC(INODE)=YLEN1+YA1(K+KSTEP)*FLOAT(J-1)/FLOAT(JLEN-1)
         ZC(INODE)=ZCOLD(INODE)+RPM/60*2*PI*DT
  230     CONTINUE
  220   CONTINUE
  200  CONTINUE


      ENDIF
C
C---- END OF EXAMPLE
C
C+++++++++++++++++ END OF USER AREA 5 +++++++++++++++++++++++++++++++++
C
      RETURN
      END
      SUBROUTINE USRSRC(IEQN,ICALL,CNAME,CALIAS,AM,SP,SU,CONV
     +            ,U,V,W,P,VFRAC,DEN,VIS,TE,ED,RS,T,H,RF,SCAL
     +            ,XP,YP,ZP,VOL,AREA,VPOR,ARPOR,WFACT,IPT
     +            ,IBLK,IPVERT,IPNODN,IPFACN,IPNODF,IPNODB,IPFACB
     +            ,WORK,IWORK,CWORK)
C
C**************************************************************************
C
C  UTILITY SUBROUTINE FOR USER-SUPPLIED SOURCES
C
C  >>> IMPORTANT                              <<<
C  >>>                                        <<<
C  >>> USERS MAY ONLY ADD OR ALTER PARTS OF THE SUBROUTINE WITHIN <<<
C  >>> THE DESIGNATED USER AREAS                          <<<
C
C**************************************************************************
C
C  THIS SUBROUTINE IS CALLED BY THE FOLLOWING SUBROUTINES
C    CUSR SCDF SCDS SCED SCENRG SCHF SCMOM SCPCE SCSCAL
C    SCTE SCVF
C
C**************************************************************************
```

```
C  CREATED
C    08/03/90  ADB
C  MODIFIED
C    04/03/91  ADB  ALTERED ARGUMENT LIST.
C    28/08/91  IRH  NEW STRUCTURE
C    28/09/91  IRH  CHANGE EXAMPLE + ADD COMMON BLOCKS
C    10/02/92  PHA  UPDATE CALLED BY COMMENT, ADD RF ARGUMENT,
C                   CHANGE LAST DIMENSION OF RS TO 6 AND IVERS TO 2
C    03/06/92  PHA  ADD PRECISION FLAG AND CHANGE IVERS TO 3
C    23/11/93  CSH  EXPLICITLY DIMENSION IPVERT ETC.
C    07/12/93  NSW  INCLUDE CONV IN ARGUMENT LIST AND CHANGE IVERS
C                   TO 4
C    03/02/94  PHA  CHANGE FLOW3D TO CFDS-FLOW3D
C    03/03/94  FHW  CORRECTION OF SPELLING MISTAKE
C    08/03/94  NSW  CORRECT SPELLING
C    09/08/94  NSW  CORRECT SPELLING.
C                   MOVE 'IF(IUSED.EQ.0) RETURN' OUT OF USER AREA.
C                   INCLUDE COMMENT ON MASS SOURCES.
C    19/12/94  NSW  CHANGE FOR CFX-F3D
C    02/07/97  NSW  UPDATE FOR CFX-4
C
C*************************************************************************
C
C  SUBROUTINE ARGUMENTS
C
C    IEQN   - EQUATION NUMBER
C    ICALL  - SUBROUTINE CALL
C    CNAME  - EQUATION NAME
C    CALIAS - ALIAS OF EQUATION NAME
C    AM     - OFF DIAGONAL MATRIX COEFFICIENTS
C    SU     - SU IN LINEARISATION OF SOURCE TERM
C    SP     - SP IN LINEARISATION OF SOURCE TERM
C    CONV   - CONVECTION COEFFICIENTS
C    U      - U COMPONENT OF VELOCITY
C    V      - V COMPONENT OF VELOCITY
C    W      - W COMPONENT OF VELOCITY
C    P      - PRESSURE
C    VFRAC  - VOLUME FRACTION
C    DEN    - DENSITY OF FLUID
C    VIS    - VISCOSITY OF FLUID
C    TE     - TURBULENT KINETIC ENERGY
C    ED     - EPSILON
C    RS     - REYNOLD STRESSES
C    T      - TEMPERATURE
C    H      - ENTHALPY
C    RF     - REYNOLD FLUXES
C    SCAL   - SCALARS (THE FIRST 'NCONC' OF THESE ARE MASS FRACTIONS)
C    XP     - X COORDINATES OF CELL CENTRES
C    YP     - Y COORDINATES OF CELL CENTRES
C    ZP     - Z COORDINATES OF CELL CENTRES
```

```
C    VOL   - VOLUME OF CELLS
C    AREA  - AREA OF CELLS
C    VPOR  - POROUS VOLUME
C    ARPOR - POROUS AREA
C    WFACT - WEIGHT FACTORS
C
C    IPT   - 1D POINTER ARRAY
C    IBLK  - BLOCK SIZE INFORMATION
C    IPVERT - POINTER FROM CELL CENTERS TO 8 NEIGHBOURING VERTICES
C    IPNODN - POINTER FROM CELL CENTERS TO 6 NEIGHBOURING CELLS
C    IPFACN - POINTER FROM CELL CENTERS TO 6 NEIGHBOURING FACES
C    IPNODF - POINTER FROM CELL FACES TO 2 NEIGHBOURING CELL CENTERS
C    IPNODB - POINTER FROM BOUNDARY CENTERS TO CELL CENTERS
C    IPFACB - POINTER FROM BOUNDARY CENTERS TO BOUNDARY FACESS
C
C    WORK  - REAL WORKSPACE ARRAY
C    IWORK - INTEGER WORKSPACE ARRAY
C    CWORK - CHARACTER WORKSPACE ARRAY
C
C  SUBROUTINE ARGUMENTS PRECEDED WITH A '*' ARE ARGUMENTS THAT MUST
C  BE SET  BY THE USER IN THIS ROUTINE.
C
C  NOTE THAT WHEN USING MASS SOURCES, THE FLOWS THROUGH MASS FLOW
C  BOUNDARIES ARE UNCHANGED. THE USER SHOULD THEREFORE INCLUDE AT
C  LEAST ONE PRESSURE BOUNDARY FOR SUCH A CALCULATION.
C
C  NOTE THAT OTHER DATA MAY BE OBTAINED FROM CFX-4 USING THE
C  ROUTINE GETADD, FOR FURTHER DETAILS SEE THE VERSION 4
C  USER MANUAL.
C
C***********************************************************************
C
      LOGICAL LDEN,LVIS,LTURB,LTEMP,LBUOY,LSCAL,LCOMP
     +     ,LRECT,LCYN,LAXIS,LPOROS,LTRANS
C
      CHARACTER*(*) CWORK
      CHARACTER    CNAME*6, CALIAS*24
C
C+++++++++++++++++ USER AREA 1 ++++++++++++++++++++++++++++++++++++++++
C---- AREA FOR USERS EXPLICITLY DECLARED VARIABLES
C
C+++++++++++++++++ END OF USER AREA 1 ++++++++++++++++++++++++++++++++++
C
      COMMON
     + /ALL/   NBLOCK,NCELL,NBDRY,NNODE,NFACE,NVERT,NDIM
     + /ALLWRK/ NRWS,NIWS,NCWS,IWRFRE,IWIFRE,IWCFRE
     + /ADDIMS/ NPHASE,NSCAL,NVAR,NPROP
     +       ,NDVAR,NDPROP,NDXNN,NDGEOM,NDCOEF,NILIST,NRLIST,NTOPOL
     + /CHKUSR/ IVERS,IUCALL,IUSED
     + /DEVICE/ NREAD,NWRITE,NRDISK,NWDISK
```

```
     + /IDUM/  ILEN,JLEN
     + /LOGIC/ LDEN,LVIS,LTURB,LTEMP,LBUOY,LSCAL,LCOMP
     +       ,LRECT,LCYN,LAXIS,LPOROS,LTRANS
     + /MLTGRD/ MLEVEL,NLEVEL,ILEVEL
     + /SGLDBL/ IFLGPR,ICHKPR
     + /SPARM/  SMALL,SORMAX,NITER,INDPRI,MAXIT,NODREF,NODMON
     + /TRANSI/ NSTEP,KSTEP,MF,INCORE
     + /TRANSR/ TIME,DT,DTINVF,TPARM
C
C+++++++++++++++++ USER AREA 2 ++++++++++++++++++++++++++++++++++++++++++
C---- AREA FOR USERS TO DECLARE THEIR OWN COMMON BLOCKS
C    THESE SHOULD START WITH THE CHARACTERS 'UC' TO ENSURE
C    NO CONFLICT WITH NON-USER COMMON BLOCKS
      COMMON /UCVOL/ VOLTOT
C
C
C+++++++++++++++++ END OF USER AREA 2 ++++++++++++++++++++++++++++++++++
C
      DIMENSION AM(NCELL,6,NPHASE),SP(NCELL,NPHASE),SU(NCELL,NPHASE)
     +,CONV(NFACE,NPHASE)
C
      DIMENSION
     + U(NNODE,NPHASE),V(NNODE,NPHASE),W(NNODE,NPHASE),P(NNODE,NPHASE)
     +,VFRAC(NNODE,NPHASE),DEN(NNODE,NPHASE),VIS(NNODE,NPHASE)
     +,TE(NNODE,NPHASE),ED(NNODE,NPHASE),RS(NNODE,NPHASE,6)
     +,T(NNODE,NPHASE),H(NNODE,NPHASE),RF(NNODE,NPHASE,4)
     +,SCAL(NNODE,NPHASE,NSCAL)
C
      DIMENSION
     + XP(NNODE),YP(NNODE),ZP(NNODE)
     +,VOL(NCELL),AREA(NFACE,3),VPOR(NCELL),ARPOR(NFACE,3)
     +,WFACT(NFACE)
     +,IPT(*),IBLK(5,NBLOCK)
     +,IPVERT(NCELL,8),IPNODN(NCELL,6),IPFACN(NCELL,6),IPNODF(NFACE,4)
     +,IPNODB(NBDRY,4),IPFACB(NBDRY)
     +,IWORK(*),WORK(*),CWORK(*)
C
C+++++++++++++++++ USER AREA 3 ++++++++++++++++++++++++++++++++++++++++++
C---- AREA FOR USERS TO DIMENSION THEIR ARRAYS
C
      DIMENSION VOLTOT(1000)
C---- AREA FOR USERS TO DEFINE DATA STATEMENTS
C
C+++++++++++++++++ END OF USER AREA 3 ++++++++++++++++++++++++++++++++++
C
C---- STATEMENT FUNCTION FOR ADDRESSING
      IP(I,J,K)=IPT((K-1)*ILEN*JLEN+(J-1)*ILEN+I)
C
C----VERSION NUMBER OF USER ROUTINE AND PRECISION FLAG
C
```

```
      IVERS=4
      ICHKPR = 1
C
C+++++++++++++++++ USER AREA 4 ++++++++++++++++++++++++++++++++++++++++
C---- TO USE THIS USER ROUTINE FIRST SET IUSED=1
C
      IUSED=0
C
C+++++++++++++++++ END OF USER AREA 4 ++++++++++++++++++++++++++++++++
C
      IF (IUSED.EQ.0) RETURN
C
C---- FRONTEND CHECKING OF USER ROUTINE
      IF (IUCALL.EQ.0) RETURN
C
C---- ADD TO SOURCE TERMS
      IF (ICALL.EQ.1) THEN
C
C+++++++++++++++++ USER AREA 5 ++++++++++++++++++++++++++++++++++++++++

CC TRASIENT FLOW CONDITION

        IF (KSTEP.LE.NSTEP) THEN
          totv=0.0
          CALL IPREC('BLOCK-NUMBER-1','BLOCK','CENTRES',IPT,ILEN,
     +               JLEN,KLEN,CWORK,IWORK)
          DO 201 I=1,ILEN
            DO 201 J=1, JLEN
              DO 201 K=1, KLEN
                INODE=IP(I,J,K)
                totv=totv+vol(inode)
201       CONTINUE
          voltot(kstep+1)=totv
          TOTV=VOLTOT(KSTEP+1)-VOLTOT(KSTEP)
          write(*,*)kstep,voltot(kstep+1), voltot(kstep)
          FLUX=TOTV/DT/VOLTOT(KSTEP+1)*1000.0
          write(*,*)'flux:', flux
          IF (FLUX.GT.0) THEN
C
C#################################################################
C
C  PRESSURE EQUATION
C
           IF(CALIAS.EQ.'PRESSURE') THEN
             CALL IPALL('INLET-SOURCE', 'USER2D', 'PATCH'
     +                 ,'CENTRES', IPT,NPT,CWORK,IWORK)
C  LOOP OVER PATCH
             do 300 I=1,NPT
              INODE = IPT(I)
              SU(INODE,1)=SU(INODE,1)+FLUX*VOL(INODE)
```

```
 300        CONTINUE
C
C
          ENDIF
         ELSE
          IF(CALIAS.EQ.'PRESSURE') THEN
            CALL IPALL('OUTLET-SOURCE', 'USER2D', 'PATCH'
   +              ,'CENTRES', IPT,NPT,CWORK,IWORK)
C  LOOP OVER PATCH
            do 301 I=1,NPT
             INODE = IPT(I)
             SU(INODE,1)=SU(INODE,1)-FLUX*VOL(INODE)
 301         CONTINUE
C
C
          ENDIF
         ENDIF

C
C
       ENDIF
C
C----------------------------------------------------------------
C----------------------------------------------------------------
C
C---- END
C
C+++++++++++++++++ END OF USER AREA 5 +++++++++++++++++++++++++++++++++++
    ENDIF
C
C---- OVERWRITE SOURCE TERMS
    IF (ICALL.EQ.2) THEN
C
C+++++++++++++++++ USER AREA 6 +++++++++++++++++++++++++++++++++++++++++
C
C+++++++++++++++++ END OF USER AREA 6 +++++++++++++++++++++++++++++++++++
C
    ENDIF
    RETURN
    END

    SUBROUTINE USRTRN(U,V,W,P,VFRAC,DEN,VIS,TE,ED,RS,T,H,RF,SCAL,
   +              XP,YP,ZP,VOL,AREA,VPOR,ARPOR,WFACT,CONV,IPT,
   +              IBLK,IPVERT,IPNODN,IPFACN,IPNODF,IPNODB,IPFACB,
   +              WORK,IWORK,CWORK)
C
C**********************************************************************
C
C  USER SUBROUTINE TO ALLOW USERS TO MODIFY OR MONITOR THE SOLUTION AT
C  THE END OF EACH TIME STEP
```

```
C  THIS SUBROUTINE IS CALLED BEFORE THE START OF THE RUN AS WELL AS AT
C  THE END OF EACH TIME STEP
C
C  >>> IMPORTANT                              <<<
C  >>>                                       <<<
C  >>> USERS MAY ONLY ADD OR ALTER PARTS OF THE SUBROUTINE WITHIN  <<<
C  >>> THE DESIGNATED USER AREAS                          <<<
C
C***********************************************************************
C
C  THIS SUBROUTINE IS CALLED BY THE FOLLOWING SUBROUTINES
C    CUSR  TRNMOD
C
C***********************************************************************
C  CREATED
C    27/04/90  ADB
C  MODIFIED
C    05/08/91  IRH  NEW STRUCTURE
C    01/10/91  DSC  REDUCE COMMENT LINE GOING OVER COLUMN 72.
C    29/11/91  PHA  UPDATE CALLED BY COMMENT, ADD RF ARGUMENT,
C               CHANGE LAST DIMENSION OF RS TO 6 AND IVERS TO 2
C    05/06/92  PHA  ADD PRECISION FLAG AND CHANGE IVERS TO 3
C    03/07/92  DSC  CORRECT COMMON MLTGRD.
C    23/11/93  CSH  EXPLICITLY DIMENSION IPVERT ETC.
C    03/02/94  PHA  CHANGE FLOW3D TO CFDS-FLOW3D
C
C***********************************************************************
C
C  SUBROUTINE ARGUMENTS
C
C    U     - U COMPONENT OF VELOCITY
C    V     - V COMPONENT OF VELOCITY
C    W     - W COMPONENT OF VELOCITY
C    P     - PRESSURE
C    VFRAC  - VOLUME FRACTION
C    DEN    - DENSITY OF FLUID
C    VIS    - VISCOSITY OF FLUID
C    TE     - TURBULENT KINETIC ENERGY
C    ED     - EPSILON
C    RS     - REYNOLD STRESSES
C    T      - TEMPERATURE
C    H      - ENTHALPY
C    RF     - REYNOLD FLUXES
C    SCAL   - SCALARS (THE FIRST 'NCONC' OF THESE ARE MASS FRACTIONS)
C    XP     - X COORDINATES OF CELL CENTRES
C    YP     - Y COORDINATES OF CELL CENTRES
C    ZP     - Z COORDINATES OF CELL CENTRES
C    VOL    - VOLUME OF CELLS
C    AREA   - AREA OF CELLS
C    VPOR   - POROUS VOLUME
```

```
C   ARPOR  - POROUS AREA
C   WFACT  - WEIGHT FACTORS
C   CONV   - CONVECTION COEFFICIENTS
C
C   IPT    - 1D POINTER ARRAY
C   IBLK   - BLOCK SIZE INFORMATION
C   IPVERT - POINTER FROM CELL CENTERS TO 8 NEIGHBOURING VERTICES
C   IPNODN - POINTER FROM CELL CENTERS TO 6 NEIGHBOURING CELLS
C   IPFACN - POINTER FROM CELL CENTERS TO 6 NEIGHBOURING FACES
C   IPNODF - POINTER FROM CELL FACES TO 2 NEIGHBOURING CELL CENTERS
C   IPNODB - POINTER FROM BOUNDARY CENTERS TO CELL CENTERS
C   IPFACB - POINTER FROM BOUNDARY CENTERS TO BOUNDARY FACESS
C
C   WORK   - REAL WORKSPACE ARRAY
C   IWORK  - INTEGER WORKSPACE ARRAY
C   CWORK  - CHARACTER WORKSPACE ARRAY
C
C  SUBROUTINE ARGUMENTS PRECEDED WITH A '*' ARE ARGUMENTS THAT MUST
C  BE SET  BY THE USER IN THIS ROUTINE.
C
C  NOTE THAT OTHER DATA MAY BE OBTAINED FROM CFDS-FLOW3D USING THE
C  ROUTINE GETADD, FOR FURTHER DETAILS SEE THE RELEASE 3
C  USER MANUAL.
C
C*************************************************************************
C
C
      LOGICAL LDEN,LVIS,LTURB,LTEMP,LBUOY,LSCAL,LCOMP
     +     ,LRECT,LCYN,LAXIS,LPOROS,LTRANS
C
      CHARACTER*(*) CWORK
C
C+++++++++++++++++ USER AREA 1 ++++++++++++++++++++++++++++++++++++++++
C---- AREA FOR USERS EXPLICITLY DECLARED VARIABLES
C
C+++++++++++++++++ END OF USER AREA 1 ++++++++++++++++++++++++++++++++++
C
      COMMON
     + /ALL/   NBLOCK,NCELL,NBDRY,NNODE,NFACE,NVERT,NDIM
     + /ALLWRK/ NRWS,NIWS,NCWS,IWRFRE,IWIFRE,IWCFRE
     + /ADDIMS/ NPHASE,NSCAL,NVAR,NPROP
     +      ,NDVAR,NDPROP,NDXNN,NDGEOM,NDCOEF,NILIST,NRLIST,NTOPOL
     + /CHKUSR/ IVERS,IUCALL,IUSED
     + /CONC/  NCONC
     + /DEVICE/ NREAD,NWRITE,NRDISK,NWDISK
     + /IDUM/  ILEN,JLEN
     + /LOGIC/  LDEN,LVIS,LTURB,LTEMP,LBUOY,LSCAL,LCOMP
     +      ,LRECT,LCYN,LAXIS,LPOROS,LTRANS
     + /MLTGRD/ MLEVEL,NLEVEL,ILEVEL
     + /SGLDBL/ IFLGPR,ICHKPR
```

```
     + /SPARM/  SMALL,SORMAX,NITER,INDPRI,MAXIT,NODREF,NODMON
     + /TIMUSR/ DTUSR
     + /TRANSI/ NSTEP,KSTEP,MF,INCORE
     + /TRANSR/ TIME,DT,DTINVF,TPARM
C
C+++++++++++++++++ USER AREA 2 ++++++++++++++++++++++++++++++++++++++++
C---- AREA FOR USERS TO DECLARE THEIR OWN COMMON BLOCKS
C    THESE SHOULD START WITH THE CHARACTERS 'UC' TO ENSURE
C    NO CONFLICT WITH NON-USER COMMON BLOCKS
C
     COMMON /UCVOL/ VOLTOT
C
C+++++++++++++++++ END OF USER AREA 2 +++++++++++++++++++++++++++++++++
C
     DIMENSION
     + U(NNODE,NPHASE),V(NNODE,NPHASE),W(NNODE,NPHASE),P(NNODE,NPHASE)
     +,VFRAC(NNODE,NPHASE),DEN(NNODE,NPHASE),VIS(NNODE,NPHASE)
     +,TE(NNODE,NPHASE),ED(NNODE,NPHASE),RS(NNODE,NPHASE,6)
     +,T(NNODE,NPHASE),H(NNODE,NPHASE),RF(NNODE,NPHASE,4)
     +,SCAL(NNODE,NPHASE,NSCAL)
     DIMENSION
     + XP(NNODE),YP(NNODE),ZP(NNODE)
     +,VOL(NCELL),AREA(NFACE,3),VPOR(NCELL),ARPOR(NFACE,3)
     +,WFACT(NFACE),CONV(NFACE,NPHASE)
     +,IPT(*),IBLK(5,NBLOCK)
     +,IPVERT(NCELL,8),IPNODN(NCELL,6),IPFACN(NCELL,6),IPNODF(NFACE,4)
     +,IPNODB(NBDRY,4),IPFACB(NBDRY)
     +,IWORK(*),WORK(*),CWORK(*)
C
C+++++++++++++++++ USER AREA 3 ++++++++++++++++++++++++++++++++++++++++
C---- AREA FOR USERS TO DIMENSION THEIR ARRAYS
      DIMENSION VOLTOT(1000)
C
C---- AREA FOR USERS TO DEFINE DATA STATEMENTS
C
C+++++++++++++++++ END OF USER AREA 3 +++++++++++++++++++++++++++++++++
C
C---- STATEMENT FUNCTION FOR ADDRESSING
     IP(I,J,K)=IPT((K-1)*ILEN*JLEN+(J-1)*ILEN+I)
C
C----VERSION NUMBER OF USER ROUTINE AND PRECISION FLAG
C
     IVERS=3
     ICHKPR = 1
C
C+++++++++++++++++ USER AREA 4 ++++++++++++++++++++++++++++++++++++++++
C---- TO USE THIS USER ROUTINE FIRST SET IUSED=1
C
     IUSED=1
     IF (IUSED.EQ.0) RETURN
```

```
C+++++++++++++++++ END OF USER AREA 4 +++++++++++++++++++++++++++++++++
C
C---- FRONTEND CHECKING OF USER ROUTINE
      IF (IUCALL.EQ.0) RETURN
       totv=0.0
       vs1=0.0
       vs5=0.0
       vs10=0.0
       vs25=0.0
       vs50=0.0
       vs75=0.0
       vs100=0.0
       vs250=0.0
       vs500=0.0
       vs750=0.0
       vs1000=0.0
       crited=1000.0
C
C+++++++++++++++++ USER AREA 5 +++++++++++++++++++++++++++++++++++++++++
C
      IF (KSTEP.LE.NSTEP) THEN
C

      CALL IPREC('BLOCK-NUMBER-1','BLOCK','CENTRES',IPT,ILEN,
     +    JLEN,KLEN,CWORK,IWORK)
      DO 101 I=1,ILEN
       DO 101 J=1, JLEN
        DO 101 K=1, KLEN
         INODE=IP(I,J,K)
         if (ed(INODE,1).GE.1.0) then
           vs1=vs1+vol(inode)
         endif
         if (ed(INODE,1).GE.5.0) then
           vs5=vs5+vol(inode)
         endif
         if (ed(INODE,1).GE.10.0) then
           vs10=vs10+vol(inode)
         endif
         if (ed(INODE,1).GE.25.0) then
           vs25=vs25+vol(inode)
         endif
         if (ed(INODE,1).GE.50.0) then
           vs50=vs50+vol(inode)
         endif
         if (ed(INODE,1).GE.75.0) then
           vs75=vs75+vol(inode)
         endif
         if (ed(INODE,1).GE.100.0) then
           vs100=vs100+vol(inode)
         endif
```

```
        if (ed(INODE,1).GE.250.0) then
          vs250=vs250+vol(inode)
        endif
        if (ed(INODE,1).GE.500.0) then
          vs500=vs500+vol(inode)
        endif
        if (ed(INODE,1).GE.750.0) then
          vs750=vs750+vol(inode)
        endif
        if (ed(INODE,1).GE.1000.0) then
          vs1000=vs1000+vol(inode)
        endif
CC  to calculate the first element in k direction for all time step.
        if (k.eq.1) then
          totv=totv+vol(inode)
        endif

101    CONTINUE
c
     ENDIF
     IF (KSTEP.EQ.NSTEP) THEN
C
      vs2=0.0
      vs3=0.0
      CALL IPREC('BLOCK-NUMBER-1','BLOCK','CENTRES',IPT,ILEN,
   +    JLEN,KLEN,CWORK,IWORK)
      DO 102 I=1,ILEN
       DO 102 J=1, JLEN
        DO 102 K=1, KLEN
         INODE=IP(I,J,K)

        if (k.eq.1) then
          vs3=vs3+vol(inode)
        else
          vs2=vs2+vol(inode)
        endif

102    CONTINUE
      totv=totv+vs2
      vs1=vs1/float(nstep)
      vs5=vs5/float(nstep)
      vs10=vs10/float(nstep)
      vs25=vs25/float(nstep)
      vs50=vs50/float(nstep)
      vs75=vs75/float(nstep)
      vs100=vs100/float(nstep)
      vs250=vs250/float(nstep)
      vs500=vs500/float(nstep)
      vs750=vs750/float(nstep)
      vs1000=vs1000/float(nstep)
```

```
      write(nwrite,*)'total volume is: ', totv
      write(nwrite,*)vs1,vs5,vs10, vs25, vs50,vs75, vs100
      write(nwrite,*)vs250, vs500, vs750, vs1000
c
      ENDIF

C
C+++++++++++++++++ END OF USER AREA 5 +++++++++++++++++++++++++++++++++++
C
      RETURN
      END
```

APPENDIX II: Volume fraction data from USD experiment

Shear device at 3260 rpm

Size	Bandwidth	Mean size	Control	15 s	30 s	1 min	2 min	5 min
0.02								
0.02244	0.0024404	0.021185	0	0	0	0	0	0
0.025179	0.0027381	0.02377	0	0	0	0	0	0
0.028251	0.0030722	0.02667	0	0	0	0	0	0
0.031698	0.0034471	0.029925	0	0	0	0	0	0
0.035566	0.0038677	0.033576	0	0	0	0	0	0
0.039905	0.0043397	0.037673	0	0	0	0	0	0
0.044774	0.0048692	0.04227	0	0	0	0	0	0
0.050238	0.0054633	0.047427	0	0	0	0	0	0
0.056368	0.0061299	0.053215	0	0	0	0	0	0
0.063246	0.0068779	0.059708	0	0	0	0	0	0
0.070963	0.0077171	0.066993	0	0	0	0	0	0
0.079621	0.0086588	0.075167	0	0	0	0	0	0
0.089337	0.0097153	0.084339	0	0	0	0	0	0
0.100237	0.0109007	0.09463	0	0	0	0	0	0
0.112468	0.0122308	0.106177	0	0	0	0	0	0
0.126191	0.0137232	0.119132	0	0	0	0	0	0
0.141589	0.0153977	0.133669	0	0	0	0	0	0
0.158866	0.0172765	0.149979	0	0	0	0	0	0
0.17825	0.0193845	0.168279	0	0	0	0	0	0
0.2	0.0217498	0.188812	0	0	0	0	0	0
0.224404	0.0244037	0.211851	0	0	0	0	0	0
0.251785	0.0273814	0.2377	0	0	0	0	0	0
0.282508	0.0307224	0.266704	0	0	0	0	0	0
0.316979	0.0344711	0.299247	0	0	0	0	0	0
0.355656	0.0386772	0.335761	0	0	0	0	0	0
0.399052	0.0433966	0.37673	0	0	0	0	0	0
0.447744	0.0486918	0.422698	0	0	0	0	0	0
0.502377	0.0546331	0.474275	0	0	0	0	0	0
0.563677	0.0612993	0.532145	0	0	0	0	0	0
0.632456	0.0687789	0.597077	0	0	0	0	0	0
0.709627	0.0771713	0.669931	0	0	0	0	0	0
0.796214	0.0865876	0.751675	0	0	0	0	0	0
0.893367	0.0971528	0.843393	0	0	0	0	0	0
1.002374	0.1090073	0.946303	0	0	0	0	0	0
1.124683	0.1223082	1.061769	0	0	0	0	0	0
1.261915	0.137232	1.191324	0	0	0	0	0.015103	0.016673
1.415892	0.1539769	1.336688	0	0.004073	0.004139	0.005155	0.06188	0.067267

1.588656	0.1727649	1.499788	0	0.059182	0.060442	0.070645	0.078876	0.083783
1.782502	0.1938454	1.68279	0.040925	0.073303	0.076061	0.085067	0.096746	0.101651
2	0.2174981	1.888122	0.067654	0.083388	0.087145	0.097394	0.109266	0.11336
2.244037	0.2440369	2.118507	0.071122	0.087379	0.09222	0.102378	0.112336	0.11613
2.517851	0.2738139	2.377004	0.073209	0.088954	0.094254	0.101624	0.106685	0.110059
2.825075	0.3072243	2.667043	0.074042	0.087237	0.092894	0.096957	0.094565	0.097724
3.169786	0.3447113	2.992471	0.077551	0.088158	0.094394	0.094866	0.083099	0.086383
3.556559	0.3867724	3.357608	0.088546	0.100487	0.107963	0.105714	0.08457	0.088653
3.990525	0.4339658	3.767298	0.118162	0.136501	0.146545	0.144321	0.116057	0.122201
4.477442	0.4869177	4.226978	0.17608	0.209349	0.223843	0.226523	0.197012	0.207038
5.023773	0.5463306	4.742747	0.27615	0.336324	0.357911	0.372873	0.351791	0.368288
5.636766	0.612993	5.32145	0.427792	0.529019	0.560724	0.597301	0.598012	0.624007
6.324555	0.6877895	5.970765	0.638465	0.796388	0.841502	0.910465	0.949212	0.987972
7.096268	0.7717125	6.699309	0.911996	1.14255	1.204408	1.317279	1.412345	1.467016
7.962143	0.8658756	7.516748	1.236543	1.551715	1.632816	1.799109	1.966917	2.039475
8.933672	0.9715284	8.43393	1.607279	2.016943	2.119479	2.347671	2.60374	2.695201
10.02374	1.0900728	9.463025	1.988633	2.492829	2.617028	2.9093	3.260339	3.369061
11.24683	1.2230818	10.61769	2.366981	2.961663	3.107188	3.462967	3.911509	4.034141
12.61915	1.3723204	11.91324	2.70306	3.37419	3.538781	3.950344	4.487519	4.617898
14.15892	1.5397688	13.36688	2.980458	3.70996	3.890706	4.34693	4.957513	5.087749
15.88656	1.727649	14.99788	3.183303	3.949487	4.142705	4.628998	5.290785	5.41161
17.82502	1.9384541	16.8279	3.309581	4.090643	4.292351	4.792817	5.479627	5.58154
20	2.1749812	18.88122	3.372204	4.148961	4.355298	4.85455	5.539029	5.612584
22.44037	2.4403691	21.18507	3.391059	4.14868	4.355751	4.840141	5.496271	5.534345
25.17851	2.7381392	23.77004	3.39167	4.118423	4.322205	4.77915	5.381804	5.378097
28.25075	3.0722427	26.67043	3.397287	4.08498	4.281141	4.700135	5.228287	5.180672
31.69786	3.447113	29.92471	3.425971	4.065553	4.248852	4.618594	5.051312	4.95967
35.56559	3.8677244	33.57608	3.485511	4.066067	4.230494	4.539557	4.858795	4.727329
39.90525	4.3396581	37.67298	3.574276	4.080618	4.219445	4.455351	4.644729	4.481019
44.77442	4.8691765	42.26978	3.684049	4.095504	4.201403	4.350632	4.395597	4.210534
50.23773	5.4633059	47.42747	3.797115	4.09133	4.158082	4.210146	4.103912	3.911368
56.36766	6.12993	53.2145	3.897758	4.047115	4.068414	4.013184	3.751259	3.566335
63.24555	6.8778946	59.70765	3.963565	3.948697	3.921959	3.759113	3.351677	3.188466
70.96268	7.7171247	66.99309	3.980256	3.782722	3.706271	3.438728	2.900357	2.771049
79.62143	8.6587563	75.16748	3.933623	3.550334	3.426926	3.067924	2.426476	2.338191
89.33672	9.7152843	84.3393	3.81649	3.255532	3.090574	2.658151	1.947465	1.902316
100.2374	10.900728	94.63025	3.627914	2.912974	2.715359	2.232066	1.491464	1.485859
112.4683	12.230818	106.1769	3.376434	2.545165	2.326565	1.816405	1.085772	1.111239
126.1915	13.723204	119.1324	3.067995	2.165883	1.939457	1.424953	0.741522	0.787071
141.5892	15.397688	133.6688	2.72924	1.807103	1.586522	1.086607	0.478222	0.531833
158.8656	17.27649	149.9788	2.367361	1.471879	1.270015	0.799238	0.286264	0.338039
178.2502	19.384541	168.279	2.013779	1.181773	1.008711	0.575931	0.164472	0.208283
200	21.749812	188.8122	1.675936	0.983551	0.795332	0.406015	0.094687	0.128113
224.4037	24.403691	211.8507	1.371978	0.786639	0.627829	0.283319	0.061341	0.084731

251.7851	27.381392	237.7004	1.107927	0.646323	0.496119	0.199031	0.054052	0.067976
282.5075	30.722427	266.7043	0.884158	0.513871	0.39005	0.136135	0.039728	0
316.9786	34.47113	299.2471	0.703263	0.417479	0.303061	0.094976	0	0
355.6559	38.677244	335.7608	0.555167	0.320004	0.225777	0.071294	0	0
399.0525	43.396581	376.7298	0.441075	0.242404	0.163406	0.021974	0	0
447.7442	48.691765	422.6978	0.352215	0.180696	0.10418	0	0	0
502.3773	54.633059	474.2747	0.287543	0.125812	0.068382	0	0	0
563.6766	61.2993	532.145	0.242792	0.086159	0.00692	0	0	0
632.4555	68.778946	597.0765	0.215098	0.055581	0	0	0	0
709.6268	77.171246	669.9309	0.199679	0.048529	0	0	0	0
796.2143	86.587563	751.6748	0.190717	0.032626	0	0	0	0
893.3672	97.152843	843.393	0.183751	0.011816	0	0	0	0
1002.374	109.00728	946.3025	0.17571	0.009499	0	0	0	0
1124.683	122.30818	1061.769	0.166018	0	0	0	0	0
1261.915	137.23204	1191.324	0.153187	0	0	0	0	0
1415.892	153.97688	1336.688	0.136	0	0	0	0	0
1588.656	172.7649	1499.788	0.116941	0	0	0	0	0
1782.502	193.84541	1682.79	0.078297	0	0	0	0	0
2000	217.49812	1888.122	0.051458	0	0	0	0	0

Because the smallest particle size being detected during the USD experiment (at 15000 rpm) is 0.299 μm, only data of those equal to and larger than this cut-off size will be shown.

Shear device at 5000 rpm

Size	Bandwidth	Mean size	Control	15 s	30 s	1 min	2 min	5 min
0.316979	0.0344711	0.299247	0	0	0	0	0	0
0.355656	0.0386772	0.335761	0	0	0	0	0	0
0.399052	0.0433966	0.37673	0	0	0	0	0	0
0.447744	0.0486918	0.422698	0	0	0	0	0	0
0.502377	0.0546331	0.474275	0	0	0	0	0	0
0.563677	0.0612993	0.532145	0	0	0	0	0	0
0.632456	0.0687789	0.597077	0	0	0	0	0	0
0.709627	0.0771713	0.669931	0	0	0	0	0	0
0.796214	0.0865876	0.751675	0	0	0	0	0	0
0.893367	0.0971528	0.843393	0	0	0	0	0	0
1.002374	0.1090073	0.946303	0	0	0	0	0	0
1.124683	0.1223082	1.061769	0	0	0	0	0.023901	0.047806
1.261915	0.137232	1.191324	0	0.021116	0.023548	0.048266	0.077864	0.107466
1.415892	0.1539769	1.336688	0	0.074545	0.08299	0.099753	0.123991	0.148233
1.588656	0.1727649	1.499788	0	0.102434	0.112826	0.136663	0.163144	0.189628
1.782502	0.1938454	1.68279	0.040925	0.12789	0.139713	0.170546	0.196267	0.221991

2	0.2174981	1.888122	0.067654	0.14166	0.153401	0.189076	0.215761	0.242448
2.244037	0.2440369	2.118507	0.071122	0.143891	0.153925	0.192322	0.219986	0.247653
2.517851	0.2738139	2.377004	0.073209	0.130298	0.136716	0.174348	0.203096	0.231846
2.825075	0.3072243	2.667043	0.074042	0.104659	0.105974	0.139588	0.16358	0.187574
3.169786	0.3447113	2.992471	0.077551	0.075579	0.071143	0.098374	0.122621	0.146871
3.556559	0.3867724	3.357608	0.088546	0.059769	0.050612	0.071408	0.075937	0.080465
3.990525	0.4339658	3.767298	0.118162	0.079989	0.069083	0.086444	0.085908	0.085372
4.477442	0.4869177	4.226978	0.17608	0.164217	0.157076	0.178271	0.170542	0.162809
5.023773	0.5463306	4.742747	0.27615	0.346243	0.350997	0.387895	0.398083	0.408267
5.636766	0.612993	5.32145	0.427792	0.652478	0.679183	0.74736	0.774664	0.801963
6.324555	0.6877895	5.970765	0.638465	1.103377	1.163191	1.280469	1.347084	1.413693
7.096268	0.7717125	6.699309	0.911996	1.710542	1.81471	1.999246	2.110051	2.220847
7.962143	0.8658756	7.516748	1.236543	2.448097	2.604807	2.869548	3.028663	3.187765
8.933672	0.9715284	8.43393	1.607279	3.303417	3.518395	3.871055	4.07963	4.288186
10.02374	1.0900728	9.463025	1.988633	4.190297	4.46162	4.896098	5.147334	5.398544
11.24683	1.2230818	10.61769	2.366981	5.070071	5.391264	5.891645	6.164687	6.457693
12.61915	1.3723204	11.91324	2.70306	5.840798	6.197219	6.732682	7.03016	7.327592
14.15892	1.5397688	13.36688	2.980458	6.450219	6.82272	7.353713	7.694917	7.936075
15.88656	1.727649	14.99788	3.183303	6.844387	7.210232	7.691685	7.953917	8.216084
17.82502	1.9384541	16.8279	3.309581	7.000995	7.337122	7.725655	7.937322	8.148913
20	2.1749812	18.88122	3.372204	6.926272	7.210905	7.468097	7.609728	7.751273
22.44037	2.4403691	21.18507	3.391059	6.655802	6.873251	6.977002	7.036926	7.096758
25.17851	2.7381392	23.77004	3.39167	6.223862	6.361664	6.29933	6.270089	6.240748
28.25075	3.0722427	26.67043	3.397287	5.694298	5.748948	5.529467	5.414622	5.299673
31.69786	3.447113	29.92471	3.425971	5.099813	5.071477	4.713899	4.522341	4.330676
35.56559	3.8677244	33.57608	3.485511	4.486021	4.38134	3.918631	3.667122	3.415508
39.90525	4.3396581	37.67298	3.574276	3.876582	3.705657	3.176696	2.885755	2.594714
44.77442	4.8691765	42.26978	3.684049	3.28561	3.061107	2.507346	2.199471	1.891502
50.23773	5.4633059	47.42747	3.797115	2.736636	2.47395	1.934662	1.631756	1.328766
56.36766	6.12993	53.2145	3.897758	2.221228	1.935673	1.44452	1.165775	0.886957
63.24555	6.8778946	59.70765	3.963565	1.765476	1.473057	1.052632	0.811719	0.570746
70.96268	7.7171247	66.99309	3.980256	1.357343	1.072957	0.737259	0.543594	0.349883
79.62143	8.6587563	75.16748	3.933623	1.011608	0.748363	0.498277	0.354493	0.210674
89.33672	9.7152843	84.3393	3.81649	0.723724	0.490233	0.319589	0.222975	0.126339
100.2374	10.900728	94.63025	3.627914	0.495648	0.30297	0.1961	0.09806	0
112.4683	12.230818	106.1769	3.376434	0.326319	0.169407	0.11291	0.056461	0
126.1915	13.723204	119.1324	3.067995	0.208081	0.091588	0.067313	0	0
141.5892	15.397688	133.6688	2.72924	0.136098	0.01899	0.014161	0	0
158.8656	17.27649	149.9788	2.367361	0.097472	0	0	0	0
178.2502	19.384541	168.279	2.013779	0.083169	0	0	0	0
200	21.749812	188.8122	1.675936	0.081619	0	0	0	0
224.4037	24.403691	211.8507	1.371978	0.082421	0	0	0	0
251.7851	27.381392	237.7004	1.107927	0.08525	0	0	0	0
282.5075	30.722427	266.7043	0.884158	0.076852	0	0	0	0

316.9786	34.47113	299.2471	0.703263	0.067292	0	0	0	0
355.6559	38.677244	335.7608	0.555167	0.008535	0	0	0	0
399.0525	43.396581	376.7298	0.441075	0	0	0	0	0
447.7442	48.691765	422.6978	0.352215	0	0	0	0	0
502.3773	54.633059	474.2747	0.287543	0	0	0	0	0
563.6766	61.2993	532.145	0.242792	0	0	0	0	0
632.4555	68.778946	597.0765	0.215098	0	0	0	0	0
709.6268	77.171246	669.9309	0.199679	0	0	0	0	0
796.2143	86.587563	751.6748	0.190717	0	0	0	0	0
893.3672	97.152843	843.393	0.183751	0	0	0	0	0
1002.374	109.00728	946.3025	0.17571	0	0	0	0	0
1124.683	122.30818	1061.769	0.166018	0	0	0	0	0
1261.915	137.23204	1191.324	0.153187	0	0	0	0	0
1415.892	153.97688	1336.688	0.136	0	0	0	0	0
1588.656	172.7649	1499.788	0.116941	0	0	0	0	0
1782.502	193.84541	1682.79	0.078297	0	0	0	0	0
2000	217.49812	1888.122	0.051458	0	0	0	0	0

Shear device at 7000 rpm

Size	Bandwidth	Mean size	Control	15 s	30 s	1 min	2 min	5 min
0.316979	0.0344711	0.299247	0	0	0	0	0	0
0.355656	0.0386772	0.335761	0	0	0	0	0	0
0.399052	0.0433966	0.37673	0	0	0	0	0	0
0.447744	0.0486918	0.422698	0	0	0	0	0	0
0.502377	0.0546331	0.474275	0	0	0	0	0	0
0.563677	0.0612993	0.532145	0	0	0	0	0	0
0.632456	0.0687789	0.597077	0	0	0	0	0	0
0.709627	0.0771713	0.669931	0	0	0	0	0	0
0.796214	0.0865876	0.751675	0	0	0	0.007711	0.01394	0.020164
0.893367	0.0971528	0.843393	0	0	0.007964	0.020411	0.031344	0.042264
1.002374	0.1090073	0.946303	0	0.010413	0.026159	0.04096	0.056227	0.071473
1.124683	0.1223082	1.061769	0	0.039513	0.052998	0.070856	0.086807	0.102725
1.261915	0.137232	1.191324	0	0.07616	0.090283	0.103959	0.120718	0.13743
1.415892	0.1539769	1.336688	0	0.114568	0.128321	0.13979	0.155876	0.171902
1.588656	0.1727649	1.499788	0	0.146493	0.155977	0.170569	0.18876	0.206877
1.782502	0.1938454	1.68279	0.040925	0.174529	0.182753	0.196497	0.217324	0.238067
2	0.2174981	1.888122	0.067654	0.184224	0.196316	0.20963	0.233481	0.257242
2.244037	0.2440369	2.118507	0.071122	0.175562	0.19566	0.208995	0.23771	0.266333
2.517851	0.2738139	2.377004	0.073209	0.156446	0.1797	0.19354	0.225543	0.257458
2.825075	0.3072243	2.667043	0.074042	0.133576	0.162002	0.176403	0.199995	0.223509
3.169786	0.3447113	2.992471	0.077551	0.104816	0.133518	0.148823	0.159541	0.170196
3.556559	0.3867724	3.357608	0.088546	0.089455	0.116324	0.132174	0.140187	0.148146
3.990525	0.4339658	3.767298	0.118162	0.119912	0.1247	0.159822	0.174847	0.189805
4.477442	0.4869177	4.226978	0.17608	0.226433	0.196872	0.276211	0.345563	0.414781

5.023773	0.5463306	4.742747	0.27615	0.473019	0.45916	0.579221	0.722661	0.865822
5.636766	0.612993	5.32145	0.427792	0.896122	0.979347	1.031516	1.252942	1.473884
6.324555	0.6877895	5.970765	0.638465	1.43983	1.666436	1.733703	2.028424	2.322361
7.096268	0.7717125	6.699309	0.911996	2.301118	2.617198	2.72654	3.089949	3.452164
7.962143	0.8658756	7.516748	1.236543	3.335708	3.739972	3.892993	4.30882	4.722982
8.933672	0.9715284	8.43393	1.607279	4.512641	4.994456	5.188265	5.630682	6.070923
10.02374	1.0900728	9.463025	1.988633	5.696669	6.229959	6.454323	6.887969	7.318953
11.24683	1.2230818	10.61769	2.366981	6.817417	7.366778	7.606405	7.990673	8.371854
12.61915	1.3723204	11.91324	2.70306	7.722911	8.244212	8.478466	8.77426	9.066664
14.15892	1.5397688	13.36688	2.980458	8.33232	8.779709	8.985974	9.160064	9.330614
15.88656	1.727649	14.99788	3.183303	8.571712	8.904586	9.060874	9.09215	9.119912
17.82502	1.9384541	16.8279	3.309581	8.426079	8.612643	8.701363	8.58504	8.465398
20	2.1749812	18.88122	3.372204	7.913403	7.93794	7.946821	7.692153	7.434512
22.44037	2.4403691	21.18507	3.391059	7.125434	6.992042	6.919508	6.553762	6.185483
25.17851	2.7381392	23.77004	3.39167	6.128221	5.852042	5.702362	5.259047	4.813699
28.25075	3.0722427	26.67043	3.397287	5.056941	4.674388	4.462339	3.982987	3.502096
31.69786	3.447113	29.92471	3.425971	3.982916	3.532521	3.276656	2.800797	2.323857
35.56559	3.8677244	33.57608	3.485511	3.000212	2.524727	2.248791	1.809956	1.370421
39.90525	4.3396581	37.67298	3.574276	2.150665	1.691353	1.414886	1.040189	0.665091
44.77442	4.8691765	42.26978	3.684049	1.460266	1.04814	0.793402	0.496966	0.200338
50.23773	5.4633059	47.42747	3.797115	0.945089	0.599153	0.389671	0.197175	0.004603
56.36766	6.12993	53.2145	3.897758	0.57482	0.30693	0.110926	0.055474	0
63.24555	6.8778946	59.70765	3.963565	0.340058	0.148636	0.038642	0	0
70.96268	7.7171247	66.99309	3.980256	0.201884	0.079996	0	0	0
79.62143	8.6587563	75.16748	3.933623	0.133523	0.068131	0	0	0
89.33672	9.7152843	84.3393	3.81649	0.105681	0	0	0	0
100.2374	10.900728	94.63025	3.627914	0.098675	0	0	0	0
112.4683	12.230818	106.1769	3.376434	0.098693	0	0	0	0
126.1915	13.723204	119.1324	3.067995	0.097775	0	0	0	0
141.5892	15.397688	133.6688	2.72924	0.09244	0	0	0	0
158.8656	17.27649	149.9788	2.367361	0.082451	0	0	0	0
178.2502	19.384541	168.279	2.013779	0.068986	0	0	0	0
200	21.749812	188.8122	1.675936	0.055401	0	0	0	0
224.4037	24.403691	211.8507	1.371978	0.008854	0	0	0	0
251.7851	27.381392	237.7004	1.107927	0	0	0	0	0
282.5075	30.722427	266.7043	0.884158	0	0	0	0	0
316.9786	34.47113	299.2471	0.703263	0	0	0	0	0
355.6559	38.677244	335.7608	0.555167	0	0	0	0	0
399.0525	43.396581	376.7298	0.441075	0	0	0	0	0
447.7442	48.691765	422.6978	0.352215	0	0	0	0	0
502.3773	54.633059	474.2747	0.287543	0	0	0	0	0
563.6766	61.2993	532.145	0.242792	0	0	0	0	0
632.4555	68.778946	597.0765	0.215098	0	0	0	0	0
709.6268	77.171246	669.9309	0.199679	0	0	0	0	0

796.2143	86.587563	751.6748	0.190717	0	0	0	0	0
893.3672	97.152843	843.393	0.183751	0	0	0	0	0
1002.374	109.00728	946.3025	0.17571	0	0	0	0	0
1124.683	122.30818	1061.769	0.166018	0	0	0	0	0
1261.915	137.23204	1191.324	0.153187	0	0	0	0	0
1415.892	153.97688	1336.688	0.136	0	0	0	0	0
1588.656	172.7649	1499.788	0.116941	0	0	0	0	0
1782.502	193.84541	1682.79	0.078297	0	0	0	0	0
2000	217.49812	1888.122	0.051458	0	0	0	0	0

Shear device at 10000 rpm

Size	Bandwidth	Mean size	Control	15 s	30 s	1 min	2 min	5 min
0.316979	0.0344711	0.299247	0	0	0	0	0	0
0.355656	0.0386772	0.335761	0	0	0	0	0	0
0.399052	0.0433966	0.37673	0	0	0	0	0	0
0.447744	0.0486918	0.422698	0	0	0	0	0	0
0.502377	0.0546331	0.474275	0	0	0	0	0	0
0.563677	0.0612993	0.532145	0	0	0	0	0	0
0.632456	0.0687789	0.597077	0	0	0	0	0	0
0.709627	0.0771713	0.669931	0	0	0	0	0	0.038348
0.796214	0.0865876	0.751675	0	0	0	0.013392	0.022494	0.083332
0.893367	0.0971528	0.843393	0	0.015032	0.025409	0.057195	0.093249	0.136201
1.002374	0.1090073	0.946303	0	0.047217	0.060727	0.10664	0.145736	0.187671
1.124683	0.1223082	1.061769	0	0.085351	0.10771	0.164318	0.206897	0.243165
1.261915	0.137232	1.191324	0	0.126402	0.152658	0.217206	0.261175	0.29505
1.415892	0.1539769	1.336688	0	0.16928	0.194509	0.267901	0.310797	0.335647
1.588656	0.1727649	1.499788	0	0.201391	0.235612	0.300853	0.340459	0.358002
1.782502	0.1938454	1.68279	0.040925	0.238488	0.265965	0.310431	0.345162	0.357691
2	0.2174981	1.888122	0.067654	0.257697	0.29057	0.290861	0.320832	0.334442
2.244037	0.2440369	2.118507	0.071122	0.259977	0.291819	0.24294	0.270527	0.295125
2.517851	0.2738139	2.377004	0.073209	0.242308	0.26579	0.175844	0.206488	0.255422
2.825075	0.3072243	2.667043	0.074042	0.2083	0.195505	0.109891	0.152374	0.241316
3.169786	0.3447113	2.992471	0.077551	0.168547	0.142895	0.077139	0.143916	0.29007
3.556559	0.3867724	3.357608	0.088546	0.176972	0.137668	0.119944	0.224955	0.441763
3.990525	0.4339658	3.767298	0.118162	0.246623	0.215141	0.289857	0.449276	0.747743
4.477442	0.4869177	4.226978	0.17608	0.418937	0.474553	0.630494	0.856877	1.236663
5.023773	0.5463306	4.742747	0.27615	0.782706	0.978491	1.191624	1.49462	1.946449
5.636766	0.612993	5.32145	0.427792	1.455059	1.731451	1.985779	2.365898	2.866321
6.324555	0.6877895	5.970765	0.638465	2.392796	2.719062	3.007086	3.455218	3.96924
7.096268	0.7717125	6.699309	0.911996	3.552765	3.921406	4.221199	4.716575	5.198634
7.962143	0.8658756	7.516748	1.236543	4.849009	5.236319	5.521216	6.03093	6.431737
8.933672	0.9715284	8.43393	1.607279	6.214171	6.589012	6.828785	7.310899	7.580574
10.02374	1.0900728	9.463025	1.988633	7.467102	7.796683	7.963962	8.373449	8.476897
11.24683	1.2230818	10.61769	2.366981	8.510673	8.760979	8.832105	9.123132	9.03652

12.61915	1.3723204	11.91324	2.70306	9.181773	9.326984	9.291462	9.429805	9.156872
14.15892	1.5397688	13.36688	2.980458	9.409452	9.432874	9.291728	9.255605	8.819465
15.88656	1.727649	14.99788	3.183303	9.153931	9.052279	8.820422	8.606941	8.051439
17.82502	1.9384541	16.8279	3.309581	8.451863	8.236143	7.94	7.565961	6.947726
20	2.1749812	18.88122	3.372204	7.376146	7.067707	6.740094	6.235854	5.614303
22.44037	2.4403691	21.18507	3.391059	6.091661	5.720959	5.396481	4.809745	4.2437
25.17851	2.7381392	23.77004	3.39167	4.696729	4.29823	4.008585	3.379848	2.904972
28.25075	3.0722427	26.67043	3.397287	3.376442	2.981696	2.749976	2.128516	1.77645
31.69786	3.447113	29.92471	3.425971	2.20166	1.828656	1.668725	1.12033	0.948273
35.56559	3.8677244	33.57608	3.485511	1.26637	0.980392	0.902169	0.245464	0.152777
39.90525	4.3396581	37.67298	3.574276	0.572836	0.284146	0.263698	0	0
44.77442	4.8691765	42.26978	3.684049	0.132406	0	0	0	0
50.23773	5.4633059	47.42747	3.797115	0.001928	0	0	0	0
56.36766	6.12993	53.2145	3.897758	0	0	0	0	0
63.24555	6.8778946	59.70765	3.963565	0	0	0	0	0
70.96268	7.7171247	66.99309	3.980256	0	0	0	0	0
79.62143	8.6587563	75.16748	3.933623	0	0	0	0	0
89.33672	9.7152843	84.3393	3.81649	0	0	0	0	0
100.2374	10.900728	94.63025	3.627914	0	0	0	0	0
112.4683	12.230818	106.1769	3.376434	0	0	0	0	0
126.1915	13.723204	119.1324	3.067995	0	0	0	0	0
141.5892	15.397688	133.6688	2.72924	0	0	0	0	0
158.8656	17.27649	149.9788	2.367361	0	0	0	0	0
178.2502	19.384541	168.279	2.013779	0	0	0	0	0
200	21.749812	188.8122	1.675936	0	0	0	0	0
224.4037	24.403691	211.8507	1.371978	0	0	0	0	0
251.7851	27.381392	237.7004	1.107927	0	0	0	0	0
282.5075	30.722427	266.7043	0.884158	0	0	0	0	0
316.9786	34.47113	299.2471	0.703263	0	0	0	0	0
355.6559	38.677244	335.7608	0.555167	0	0	0	0	0
399.0525	43.396581	376.7298	0.441075	0	0	0	0	0
447.7442	48.691765	422.6978	0.352215	0	0	0	0	0
502.3773	54.633059	474.2747	0.287543	0	0	0	0	0
563.6766	61.2993	532.145	0.242792	0	0	0	0	0
632.4555	68.778946	597.0765	0.215098	0	0	0	0	0
709.6268	77.171246	669.9309	0.199679	0	0	0	0	0
796.2143	86.587563	751.6748	0.190717	0	0	0	0	0
893.3672	97.152843	843.393	0.183751	0	0	0	0	0
1002.374	109.00728	946.3025	0.17571	0	0	0	0	0
1124.683	122.30818	1061.769	0.166018	0	0	0	0	0
1261.915	137.23204	1191.324	0.153187	0	0	0	0	0
1415.892	153.97688	1336.688	0.136	0	0	0	0	0
1588.656	172.7649	1499.788	0.116941	0	0	0	0	0
1782.502	193.84541	1682.79	0.078297	0	0	0	0	0

2000	217.49812	1888.122	0.051458	0	0	0	0	0

Shear device at 15000 rpm

Size	Bandwidth	Mean size	Control	15 s	30 s	1 min	2 min	5 min
0.316979	0.0344711	0.299247	0	0	0	0	0	0.012531
0.355656	0.0386772	0.335761	0	0	0	0	0	0.075794
0.399052	0.0433966	0.37673	0	0	0	0	0.060933	0.102673
0.447744	0.0486918	0.422698	0	0	0	0	0.088921	0.136557
0.502377	0.0546331	0.474275	0	0	0	0	0.104521	0.168657
0.563677	0.0612993	0.532145	0	0	0	0.000154	0.128872	0.204938
0.632456	0.0687789	0.597077	0	0	0	0.071528	0.157609	0.244287
0.709627	0.0771713	0.669931	0	0.033825	0.055223	0.106412	0.190814	0.28604
0.796214	0.0865876	0.751675	0	0.074723	0.115332	0.161203	0.229317	0.331313
0.893367	0.0971528	0.843393	0	0.127017	0.169258	0.21131	0.271394	0.37835
1.002374	0.1090073	0.946303	0	0.177476	0.22112	0.267164	0.315346	0.426379
1.124683	0.1223082	1.061769	0	0.232075	0.274524	0.320343	0.358403	0.474017
1.261915	0.137232	1.191324	0	0.283137	0.322367	0.365254	0.396682	0.519339
1.415892	0.1539769	1.336688	0	0.322796	0.357895	0.398776	0.428508	0.563619
1.588656	0.1727649	1.499788	0	0.343902	0.375834	0.416267	0.451903	0.60752
1.782502	0.1938454	1.68279	0.040925	0.341585	0.373764	0.41826	0.470312	0.658669
2	0.2174981	1.888122	0.067654	0.31509	0.35399	0.409764	0.491247	0.726747
2.244037	0.2440369	2.118507	0.071122	0.270626	0.32586	0.402842	0.529576	0.829182
2.517851	0.2738139	2.377004	0.073209	0.223289	0.307199	0.41732	0.606245	0.986541
2.825075	0.3072243	2.667043	0.074042	0.198684	0.325013	0.480659	0.747389	1.22141
3.169786	0.3447113	2.992471	0.077551	0.233789	0.416976	0.630197	0.987806	1.563387
3.556559	0.3867724	3.357608	0.088546	0.369578	0.619742	0.897322	1.349084	2.020941
3.990525	0.4339658	3.767298	0.118162	0.657978	0.982379	1.327388	1.86951	2.622137
4.477442	0.4869177	4.226978	0.17608	1.130207	1.525272	1.929887	2.542169	3.341306
5.023773	0.5463306	4.742747	0.27615	1.82633	2.280166	2.728299	3.3786	4.175882
5.636766	0.612993	5.32145	0.427792	2.738862	3.227097	3.691486	4.333816	5.067562
6.324555	0.6877895	5.970765	0.638465	3.84351	4.332043	4.777333	5.357319	5.959119
7.096268	0.7717125	6.699309	0.911996	5.086172	5.532427	5.916953	6.375724	6.775934
7.962143	0.8658756	7.516748	1.236543	6.344595	6.704369	6.987626	7.274146	7.418368
8.933672	0.9715284	8.43393	1.607279	7.530559	7.760205	7.904071	7.975378	7.822108
10.02374	1.0900728	9.463025	1.988633	8.471251	8.542031	8.525073	8.366446	7.913084
11.24683	1.2230818	10.61769	2.366981	9.078936	8.972574	8.784186	8.3979	7.663808
12.61915	1.3723204	11.91324	2.70306	9.243395	8.966551	8.620241	8.04085	7.085749
14.15892	1.5397688	13.36688	2.980458	8.941187	8.517222	8.041698	7.320263	6.223635
15.88656	1.727649	14.99788	3.183303	8.194866	7.664447	7.103258	6.304286	5.161272
17.82502	1.9384541	16.8279	3.309581	7.097813	6.511872	5.916437	5.1064	4.012126
20	2.1749812	18.88122	3.372204	5.757754	5.169238	4.592067	3.830571	2.86919
22.44037	2.4403691	21.18507	3.391059	4.368632	3.823588	3.304014	2.632235	1.861412
25.17851	2.7381392	23.77004	3.39167	3.010721	2.546621	2.126702	1.577417	1.026654
28.25075	3.0722427	26.67043	3.397287	1.860018	1.495424	1.185158	0.766722	0.430329

31.69786	3.447113	29.92471	3.425971	0.988855	0.725394	0.485177	0.185374	0.031438
35.56559	3.8677244	33.57608	3.485511	0.247344	0.106982	0.078168	0	0
39.90525	4.3396581	37.67298	3.574276	0.03342	0	0	0	0
44.77442	4.8691765	42.26978	3.684049	0	0	0	0	0
50.23773	5.4633059	47.42747	3.797115	0	0	0	0	0
56.36766	6.12993	53.2145	3.897758	0	0	0	0	0
63.24555	6.8778946	59.70765	3.963565	0	0	0	0	0
70.96268	7.7171247	66.99309	3.980256	0	0	0	0	0
79.62143	8.6587563	75.16748	3.933623	0	0	0	0	0
89.33672	9.7152843	84.3393	3.81649	0	0	0	0	0
100.2374	10.900728	94.63025	3.627914	0	0	0	0	0
112.4683	12.230818	106.1769	3.376434	0	0	0	0	0
126.1915	13.723204	119.1324	3.067995	0	0	0	0	0
141.5892	15.397688	133.6688	2.72924	0	0	0	0	0
158.8656	17.27649	149.9788	2.367361	0	0	0	0	0
178.2502	19.384541	168.279	2.013779	0	0	0	0	0
200	21.749812	188.8122	1.675936	0	0	0	0	0
224.4037	24.403691	211.8507	1.371978	0	0	0	0	0
251.7851	27.381392	237.7004	1.107927	0	0	0	0	0
282.5075	30.722427	266.7043	0.884158	0	0	0	0	0
316.9786	34.47113	299.2471	0.703263	0	0	0	0	0
355.6559	38.677244	335.7608	0.555167	0	0	0	0	0
399.0525	43.396581	376.7298	0.441075	0	0	0	0	0
447.7442	48.691765	422.6978	0.352215	0	0	0	0	0
502.3773	54.633059	474.2747	0.287543	0	0	0	0	0
563.6766	61.2993	532.145	0.242792	0	0	0	0	0
632.4555	68.778946	597.0765	0.215098	0	0	0	0	0
709.6268	77.171246	669.9309	0.199679	0	0	0	0	0
796.2143	86.587563	751.6748	0.190717	0	0	0	0	0
893.3672	97.152843	843.393	0.183751	0	0	0	0	0
1002.374	109.00728	946.3025	0.17571	0	0	0	0	0
1124.683	122.30818	1061.769	0.166018	0	0	0	0	0
1261.915	137.23204	1191.324	0.153187	0	0	0	0	0
1415.892	153.97688	1336.688	0.136	0	0	0	0	0
1588.656	172.7649	1499.788	0.116941	0	0	0	0	0
1782.502	193.84541	1682.79	0.078297	0	0	0	0	0
2000	217.49812	1888.122	0.051458	0	0	0	0	0

APPENDIX III: Volume fraction data from pump experiment

Pump at 600 rpm

Size	Bandwidth	Mean size	Control	10 min	1 h	2 h	3 h	4 h
0.632456	0.0687789	0.597077	0	0	0	0	0	0
0.709627	0.0771713	0.669931	0	0	0	0	0	0
0.796214	0.0865876	0.751675	0	0	0	0	0	0
0.893367	0.0971528	0.843393	0	0	0	0	0	0
1.002374	0.1090073	0.946303	0	0	0	0	0	0
1.124683	0.1223082	1.061769	0	0	0	0	0	0
1.261915	0.137232	1.191324	0	0	0	0	0	0
1.415892	0.1539769	1.336688	0	0	0	0	0	0
1.588656	0.1727649	1.499788	0	0	0	0	0	0
1.782502	0.1938454	1.68279	0.040925	0.04145	0.0571426	0.061694	0.065942	0.073366
2	0.2174981	1.888122	0.067654	0.070069	0.0886696	0.095732	0.108263	0.113844
2.244037	0.2440369	2.118507	0.071122	0.08778	0.1113296	0.120196	0.131391	0.142937
2.517851	0.2738139	2.377004	0.073209	0.10278	0.1290635	0.139343	0.156489	0.165706
2.825075	0.3072243	2.667043	0.074042	0.115427	0.1458122	0.157425	0.172236	0.18721
3.169786	0.3447113	2.992471	0.077551	0.118321	0.153694	0.165935	0.186015	0.197329
3.556559	0.3867724	3.357608	0.088546	0.120401	0.1556644	0.176669	0.19192	0.210095
3.990525	0.4339658	3.767298	0.118162	0.117075	0.1292231	0.159161	0.178301	0.214412
4.477442	0.4869177	4.226978	0.17608	0.159287	0.1332261	0.165847	0.190066	0.217701
5.023773	0.5463306	4.742747	0.27615	0.277847	0.2918462	0.348405	0.329823	0.29436
5.636766	0.612993	5.32145	0.427792	0.482718	0.5508018	0.700833	0.639	0.52534
6.324555	0.6877895	5.970765	0.638465	0.812108	0.9780307	1.143993	1.178827	1.061526
7.096268	0.7717125	6.699309	0.911996	1.232614	1.5860461	1.901049	1.984778	1.848425
7.962143	0.8658756	7.516748	1.236543	1.865652	2.4279512	2.735096	2.964873	2.819621
8.933672	0.9715284	8.43393	1.607279	2.609809	3.4164548	3.817747	4.088497	3.949522
10.02374	1.0900728	9.463025	1.988633	3.395523	4.452766	4.939722	5.240197	5.120033
11.24683	1.2230818	10.61769	2.366981	4.183724	5.4821877	6.036922	6.349995	6.263496
12.61915	1.3723204	11.91324	2.70306	4.880952	6.3762433	6.967624	7.27203	7.23017
14.15892	1.5397688	13.36688	2.980458	5.436852	7.0632535	7.652953	7.926285	7.935869
15.88656	1.727649	14.99788	3.183303	5.800667	7.4714352	8.01652	8.237661	8.29926
17.82502	1.9384541	16.8279	3.309581	5.952944	7.571485	8.030709	8.183214	8.290625
20	2.1749812	18.88122	3.372204	5.905013	7.3721567	7.708254	7.780518	7.922504
22.44037	2.4403691	21.18507	3.391059	5.698641	6.9305328	7.120206	7.110072	7.271042
25.17851	2.7381392	23.77004	3.39167	5.379191	6.3004318	6.327456	6.236647	6.400615
28.25075	3.0722427	26.67043	3.397287	5.013762	5.5816257	5.448655	5.287611	5.439799
31.69786	3.447113	29.92471	3.425971	4.641906	4.8285459	4.546314	4.327654	4.456674
35.56559	3.8677244	33.57608	3.485511	4.300666	4.108258	3.700739	3.44067	3.540091
39.90525	4.3396581	37.67298	3.574276	3.999742	3.4503817	2.948263	2.663407	2.731523
44.77442	4.8691765	42.26978	3.684049	3.733616	2.8664973	2.304896	2.011582	2.050691
50.23773	5.4633059	47.42747	3.797115	3.491542	2.3673899	1.783391	1.496623	1.512578
56.36766	6.12993	53.2145	3.897758	3.245095	1.9290339	1.357224	1.090517	1.08985
63.24555	6.8778946	59.70765	3.963565	2.986369	1.5570038	1.026195	0.790408	0.779831
70.96268	7.7171247	66.99309	3.980256	2.694711	1.2267775	0.760054	0.564652	0.548835
79.62143	8.6587563	75.16748	3.933623	2.37487	0.9402683	0.550915	0.401674	0.383097

89.33672	9.7152843	84.3393	3.81649	2.029721	0.6901835	0.381519	0.28325	0.261602
100.2374	10.900728	94.63025	3.627914	1.675251	0.4769844	0.252903	0.199672	0.175823
112.4683	12.230818	106.1769	3.376434	1.332873	0.3078067	0.150303	0.143363	0.114679
126.1915	13.723204	119.1324	3.067995	1.014758	0.1808141	0.082072	0.106972	0.074254
141.5892	15.397688	133.6688	2.72924	0.745654	0.0818017	0.017084	0.084505	0.060833
158.8656	17.27649	149.9788	2.367361	0.525007	0.0311793	0	0.073204	0.024864
178.2502	19.384541	168.279	2.013779	0.363032	0	0	0.063105	0
200	21.749812	188.8122	1.675936	0.250641	0	0	0.058229	0
224.4037	24.403691	211.8507	1.371978	0.180904	0	0	0.009863	0
251.7851	27.381392	237.7004	1.107927	0.141041	0	0	0	0
282.5075	30.722427	266.7043	0.884158	0.118817	0	0	0	0
316.9786	34.47113	299.2471	0.703263	0.10328	0	0	0	0
355.6559	38.677244	335.7608	0.555167	0.085272	0	0	0	0
399.0525	43.396581	376.7298	0.441075	0.06866	0	0	0	0
447.7442	48.691765	422.6978	0.352215	0.035962	0	0	0	0
502.3773	54.633059	474.2747	0.287543	0	0	0	0	0
563.6766	61.2993	532.145	0.242792	0	0	0	0	0
632.4555	68.778946	597.0765	0.215098	0	0	0	0	0
709.6268	77.171246	669.9309	0.199679	0	0	0	0	0
796.2143	86.587563	751.6748	0.190717	0	0	0	0	0
893.3672	97.152843	843.393	0.183751	0	0	0	0	0
1002.374	109.00728	946.3025	0.17571	0	0	0	0	0
1124.683	122.30818	1061.769	0.166018	0	0	0	0	0
1261.915	137.23204	1191.324	0.153187	0	0	0	0	0
1415.892	153.97688	1336.688	0.136	0	0	0	0	0
1588.656	172.7649	1499.788	0.116941	0	0	0	0	0
1782.502	193.84541	1682.79	0.078297	0	0	0	0	0
2000	217.49812	1888.122	0.051458	0	0	0	0	0

Pump at 1500 rpm

Size	Bandwidth	Mean size	Control	10 min	1 h	2 h	3 h	4 h
0.632456	0.0687789	0.597077	0	0	0	0	0	0
0.709627	0.0771713	0.669931	0	0	0	0	0.029638	0.038161
0.796214	0.0865876	0.751675	0	0	0	0	0.066666	0.083034
0.893367	0.0971528	0.843393	0	0	0	0	0.118248	0.136121
1.002374	0.1090073	0.946303	0	0	0	0	0.16852	0.187513
1.124683	0.1223082	1.061769	0	0	0	0	0.223336	0.242254
1.261915	0.137232	1.191324	0	0	0	0.04878	0.274455	0.292117
1.415892	0.1539769	1.336688	0	0	0	0.098536	0.313228	0.32862
1.588656	0.1727649	1.499788	0	0	0	0.141463	0.331585	0.344281
1.782502	0.1938454	1.68279	0.040925	0.049063	0.078689	0.175609	0.323566	0.33389
2	0.2174981	1.888122	0.067654	0.088766	0.137705	0.209755	0.287814	0.29733
2.244037	0.2440369	2.118507	0.071122	0.118355	0.17705	0.235121	0.230206	0.241796
2.517851	0.2738139	2.377004	0.073209	0.136109	0.206558	0.25756	0.166461	0.184432

2.825075	0.3072243	2.667043	0.074042	0.143013	0.221312	0.278047	0.123907	0.153691
3.169786	0.3447113	2.992471	0.077551	0.131177	0.22623	0.284389	0.142095	0.190075
3.556559	0.3867724	3.357608	0.088546	0.143013	0.217378	0.303901	0.266184	0.337967
3.990525	0.4339658	3.767298	0.118162	0.168656	0.252788	0.409754	0.552132	0.652938
4.477442	0.4869177	4.226978	0.17608	0.272296	0.483031	0.875711	1.035641	1.167095
5.023773	0.5463306	4.742747	0.27615	0.518935	1.052447	1.555774	1.760408	1.921186
5.636766	0.612993	5.32145	0.427792	1.010136	1.894832	2.543269	2.719986	2.903538
6.324555	0.6877895	5.970765	0.638465	1.83043	3.068487	3.661924	3.888799	4.083994
7.096268	0.7717125	6.699309	0.911996	2.954605	4.444594	5.05293	5.20872	5.399877
7.962143	0.8658756	7.516748	1.236543	4.265616	5.908244	6.473099	6.54786	6.716683
8.933672	0.9715284	8.43393	1.607279	5.703248	7.361687	7.816621	7.809515	7.936383
10.02374	1.0900728	9.463025	1.988633	7.094222	8.592425	8.883775	8.806563	8.875793
11.24683	1.2230818	10.61769	2.366981	8.333545	9.491546	9.572927	9.442217	9.441346
12.61915	1.3723204	11.91324	2.70306	9.234015	9.906045	9.760588	9.59693	9.523104
14.15892	1.5397688	13.36688	2.980458	9.699497	9.789719	9.424704	9.245001	9.102907
15.88656	1.727649	14.99788	3.183303	9.657255	9.145862	8.596508	8.411382	8.214253
17.82502	1.9384541	16.8279	3.309581	9.1143	8.063137	7.386822	7.199387	6.966992
20	2.1749812	18.88122	3.372204	8.125213	6.656285	5.921592	5.729583	5.485016
22.44037	2.4403691	21.18507	3.391059	6.847429	5.141834	4.414812	4.206058	3.970124
25.17851	2.7381392	23.77004	3.39167	5.386901	3.613888	2.959721	2.741773	2.537138
28.25075	3.0722427	26.67043	3.397287	3.948355	2.282535	1.737773	1.502263	1.339337
31.69786	3.447113	29.92471	3.425971	2.62425	1.248775	0.806384	0.495271	0.363672
35.56559	3.8677244	33.57608	3.485511	1.53848	0.305188	0.112169	0.034604	0.007342
39.90525	4.3396581	37.67298	3.574276	0.703939	0.03176	0	0	0
44.77442	4.8691765	42.26978	3.684049	0.157173	0	0	0	0
50.23773	5.4633059	47.42747	3.797115	0.002011	0	0	0	0
56.36766	6.12993	53.2145	3.897758	0	0	0	0	0
63.24555	6.8778946	59.70765	3.963565	0	0	0	0	0
70.96268	7.7171247	66.99309	3.980256	0	0	0	0	0
79.62143	8.6587563	75.16748	3.933623	0	0	0	0	0
89.33672	9.7152843	84.3393	3.81649	0	0	0	0	0
100.2374	10.900728	94.63025	3.627914	0	0	0	0	0
112.4683	12.230818	106.1769	3.376434	0	0	0	0	0
126.1915	13.723204	119.1324	3.067995	0	0	0	0	0
141.5892	15.397688	133.6688	2.72924	0	0	0	0	0
158.8656	17.27649	149.9788	2.367361	0	0	0	0	0
178.2502	19.384541	168.279	2.013779	0	0	0	0	0
200	21.749812	188.8122	1.675936	0	0	0	0	0
224.4037	24.403691	211.8507	1.371978	0	0	0	0	0
251.7851	27.381392	237.7004	1.107927	0	0	0	0	0
282.5075	30.722427	266.7043	0.884158	0	0	0	0	0
316.9786	34.47113	299.2471	0.703263	0	0	0	0	0
355.6559	38.677244	335.7608	0.555167	0	0	0	0	0
399.0525	43.396581	376.7298	0.441075	0	0	0	0	0

447.7442	48.691765	422.6978	0.352215	0	0	0	0	0
502.3773	54.633059	474.2747	0.287543	0	0	0	0	0
563.6766	61.2993	532.145	0.242792	0	0	0	0	0
632.4555	68.778946	597.0765	0.215098	0	0	0	0	0
709.6268	77.171246	669.9309	0.199679	0	0	0	0	0
796.2143	86.587563	751.6748	0.190717	0	0	0	0	0
893.3672	97.152843	843.393	0.183751	0	0	0	0	0
1002.374	109.00728	946.3025	0.17571	0	0	0	0	0
1124.683	122.30818	1061.769	0.166018	0	0	0	0	0
1261.915	137.23204	1191.324	0.153187	0	0	0	0	0
1415.892	153.97688	1336.688	0.136	0	0	0	0	0
1588.656	172.7649	1499.788	0.116941	0	0	0	0	0
1782.502	193.84541	1682.79	0.078297	0	0	0	0	0
2000	217.49812	1888.122	0.051458	0	0	0	0	0